Drug-Device Development:

Cancer Immunotherapy with Therapeutic, Ultrasound-Mediated Delivery



Lincoln College, University of Oxford

January 2020

Prateek S. Katti

A thesis submitted for the degree of Doctor of Philosophy

Abstract

Tumour and tumour microenvironment exploitation of immunologic checkpoints like PD-L1 can enable immune evasion. Recent advances in oncology, have brought forward antibody drugs, such as anti-PD-L1, capable of blocking and/or mediating the eradication of cells that express PD-L1. Despite promise across a wide range of indications, clinically such agents meaningfully extend survival only in a fraction of patients treated.

Immature, heterogenous blood vessels, elevated interstitial pressures, and stromal barriers severely limit the accumulation and extravasation of drugs within the tumour microenvironment. We hypothesize that the physical size of antibody therapeutics, such as anti-PD-L1, compounded by delivery barriers could be a factor limiting their efficacy.

Recently, submicron cavitation nucleation agents, sonosensitive particles (SSPs), activated by focused ultrasound have been shown to improve the delivery of large, anti-cancer therapeutics via microstreaming-mediated transport. Our aim was to pre-clinically investigate whether systemically-dosed anti-PD-L1 followed by SSPs and the application of focused ultrasound could improve the intratumoural delivery and therapeutic efficacy of anti-PD-L1.

Efficacy studies revealed that pairing anti-PD-L1 with ultrasound-mediated cavitation can significantly extend median survival time. Cavitation was also found to enhance the intratumoural accumulation of anti-PD-L1 and three other antibodies. Further, the binding intensity and distribution of anti-PD-L1 improved in cavitation-treated tumours. Immunological analysis suggests that anti-PD-L1 paired with cavitation enables the innate and adaptive immune system to leverage the modest cavitation-induced inflammation and improved anti-PD-L1 delivery to facilitate tumour attack. Taken in a broader context, this pre-clinical work suggests that ultrasound-mediated cavitation warrants further investigation as viable tool to improve drug delivery clinically.

Acknowledgments

I feel incredibly privileged to have had the opportunity to work on this project with individuals across so many different fields—it was truly these friends and mentors whose dedication and passion made this work possible. In addition to my supervisors both formal and informal, I cannot begin to put to words how grateful I am for the support I have received from my friends and colleagues in the Biomedical Ultrasonics, Biotherapy, and Biopharmaceuticals Laboratory (BUBBL), the Transplantation Research and Immunology Group (TRIG), and at the National Institutes of Health. Lastly, I must also acknowledge the love and support of my family and friends outside of lab.

Abbreviations & Acronyms **11**

1 Introduction **12**

1.1 Cancer **12**

1.1.1 Cancer immunotherapy 12

1.1.2 Principles of immunotherapy 13

1.2 Mechanisms of Checkpoint Blockade **14**

1.2.1 CTLA-4 15

1.2.2 PD1/PDL1 16

1.2.3 PD1/PDL1 axis blockade in clinic 18

1.2.4 Strategies to improve PD1/PDL1 blockade therapeutic outcomes 20

1.3 Drug Delivery Barriers in Tumours **21**

1.3.1 Tumour vasculature is a poor drug conduit 22

1.3.2 Elevated interstitial pressures and stromal barriers 23

1.3.3 Relevance of drug delivery barriers to aPDL1 therapy 24

1.4 Strategies to Overcome Delivery Barriers **25**

1.4.1 Principles of ultrasound & ultrasound-mediated cavitation 26

1.4.2 Cavitation as a tool for drug delivery 26

1.4.3 Cavitation with microbubble contrast agents 27

1.4.4 Cavitation with sub-micrometre nuclei 28

1.4.5 Monitoring and Mapping of Cavitation Activity 29

1.5 Summary of Background **30**

2 Methods and Materials **31**

2.1 Statement of Contributions and Assistance **31**

2.2 Ultrasound Apparatus & Exposure Parameters **32**

2.2.1 Treatment Monitoring (Passive Acoustic Mapping) 33

2.2.2 Acoustic Parameters and Rationale 33
2.2.3 Retrospective Cavitation Analysis 35
2.3 In vivo models 36
2.3.1 Cell Culture 36
2.3.3 Tumour propagation & monitoring 36
2.4 Interventions 38
2.4.1 Survival Study Analysis Censorship Criteria 38
2.5 Imaging Methods 40
2.5.1 IVIS Imaging of Near-Infrared Antibody Conjugates 40
2.5.2 Microscopy 42
2.6 Flow Cytometry Methods 43
2.6.1 Drug Delivery Query 43
2.6.2 Immunophenotyping 45
2.7 RNA Nanostring 46
2.8 Statistics 47
3 Efficacy Studies 48
3.1 Pilot Study: Low-Dose aPDL1 with Cavitation 51
3.1.1 Experimental Overview 52
3.1.2 Results 53
3.1.3 Discussion 56
3.2 PD1/PDL1 Axis Blockade with US-mediated Cavitation-Enhanced Delivery of Antibody-based Therapeutics 61
3.2.1 Experimental overview 64
3.2.2 Results 66
3.2.3 Discussion 70

3.3 Impact of Inertial Cavitation Dose on aPDL1 Efficacy Enhancement 74

3.4 Feedback-Optimized, Cavitation-Mediated Drug Delivery 78

3.4.1 Experimental Overview 78

3.4.2 Results 79

3.4.3 Discussion 82

3.5 Pilot Evaluation of aPDL1 with Cavitation in EMT6 Tumour Bearing Mice 86

3.5.1 Experimental Overview 86

3.5.2 Results 87

3.5.3 Discussion 88

3.6 Chapter Summary 89

3.6.1 Future Directions 91

Chapter 4: Drug Delivery Studies 93

4.1 *In vitro* and *in vivo* IVIS imaging of therapeutic antibodies 95

4.2 IVIS as a potential tool to quantify changes in drug delivery *in vivo* 97

4.2.1 Experimental Overview 97

4.2.2 Results 97

4.2.3 Discussion 99

4.3 Cavitation-enhanced intratumoural accumulation of a range of therapeutic antibodies 101

4.3.1 Experimental Overview 101

4.3.2 Results 102

4.3.3 Discussion 106

4.4 Cavitation-enhanced aPDL1 accumulation in EMT6 tumours 108

4.4.1 Experimental Overview 108

4.4.2 Results 109

4.4.3 Discussion 110
4.5 Detection of *ex vivo* tumour-bound therapeutic antibody 112
4.5.1 Experimental Overview 112
4.5.2 Results: 113
4.5.3 Discussion: 114
4.6 Flow cytometry characterization of aPDL1 binding intensity and frequency with or without intratumoural cavitation 115
4.6.1 Experimental Overview 115
4.6.2 Results & Discussion 116
4.7 Comparative FCM of antibody binding frequency and intensity with respect to US treatment across the PD1/PDL1 axis 122
4.7.1 Experimental Overview 122
4.7.2 Results 124
4.7.3 Discussion 127
4.8 Quantitative microscopy of aPDL1-treated, bilateral CT26 tumour bearing mice .. 133
4.8.1 Experimental Overview: 133
4.8.2 Results 134
4.8.3 Discussion 137
4.9 Chapter Summary, Limitations, and Future Directions 139
Future Directions 140
5 Immunologic Correlates of Response 142
5.1 Gene-Level Changes Driven by aPDL1 Paired with Cavitation 142
5.1.1 Experimental Setup 143
5.2 Gene-Level Changes 24hrs After Intervention 145
5.2.1 Results Overview 145

5.2.2 Discussion 149
5.3 Most Differentially Expressed Genes, 24hr-Post Intervention 150
5.4 Effector-Response Related Genes 24hrs After Intervention 153
5.5 Cell Type Profiling 24hrs After Intervention 154
Summary of gene-level changes 24hr-after intervention 156
Limitations & the impact of cavitation to DEG expression 156
5.6 Gene-Level Changes 5d After Intervention 158
5.6.1 Results & Discussion 158
5.7 Top DEGs 5d Post-Intervention 163
5.8 Shared genes between aPDL1 and aPDL1+US 166
5.8.1 Innate immune system effector function (Fig. 5.8a) 166
5.8.2 Adaptive immune system activity (Fig. 5.8b) 168
5.8.3 Leukocyte activation and recruitment (Fig. 5.8c) 169
5.8.4 Unclear role (Fig. 5.8d) 170
5.8.5 Summary 171
5.9 Effector-response related genes 5d after intervention 172
5.9.1 Activation (Fig. 5.9a) 172
5.9.2 Dysfunction and Resistance (Fig. 5.9b) 173
5.9.3 Effector function (Fig. 5.9c) 173
5.9.4 Summary 175
5.10 *Nanostring* Cell Scores 5d-Post Intervention 176
5.10 Summary of Gene-Level Changes 5d After Intervention 178
5.10.2 Summary of *Nanostring* Data 179
5.10.3 Time-Course of Biomarkers, A Working Hypothesis 180
5.11 Flow Cytometry of 5-Day Tissue 182
5.11.1 Experimental Overview 182

5.11.2 FCM Panel Design 182
5.12 Distribution of Leukocytes Populations 184
5.12.1 Phenotypic comparisons across tissue-types irrespective of treatment 184
5.12.2 Phenotypic comparisons by treatment-group & tissue-type 185
5.13 Frequencies of T Regulatory Cells 188
5.13.1 T regulatory cells irrespective of treatment arm : 188
5.13.2 T Regulatory cells compared by treatment group 189
5.14 & 5.15 T Cell Memory Marker Expression: CD62L vs. CD44 Expression 191
5.16 & 5.17 T Cell Exhaustion: TIM3 vs. PD1 Expression 196
5.18 T Cell Activation 201
5.18.1 CD69, OX40, ICOS, and GITR 201
5.18.2 Tumour-tissue changes in CD69, OX40, and ICOS Expression 201
5.18.3 Tumour-tissue changes in GITR Expression 203
5.19 Cytotoxic Function: GranzymeB 205
5.20 Summary of FCM Data 207
5.21 Chapter Summary 209
5.21.1 Nanostring Analysis 209
5.21.2 Flow Cytometry with Additional Tumour Tissue 211
5.21.3 Future Directions 213
6 Conclusion 215
6.1 Efficacy Studies Chapter Summary 216
6.2 Drug Delivery Studies Chapter Summary 217
6.3 Immunologic Correlates of Response Chapter Summary 218
6.4 Limitations 220
6.5 Future Work 221

6.6 Synthesis and Proposed Mechanism 222

References: 224

Appendices 244

Appendix 3.1 - Extended Data Related to 3.1 245

Appendix 3.2 - Extended Data Related to 3.2 247

Appendix 3.3 - Extended Data Related to 3.3 250

Appendix 3.4 - Extended Data Related to 3.4 251

Appendix 3.5 - Extended Data Related to 3.5 253

Appendix 4.2 - Extended Data Related to 4.2 254

Appendix 4.3 - Extended Data Related to 4.3 255

Appendix 4.4 - Extended Data Related to 4.4 256

Appendix 4.5 - Extended Data Related to 4.5 257

Appendix 4.6 - Extended Data Related to 4.6 258

Appendix 4.7 - Extended Data Related to 4.7 260

Appendix 4.8 - Extended Data Related to 4.8 264

Appendix 5.11 - Extended Data Related to 5.11 265

Abbreviations & Acronyms

ADCC	antibody-dependent cell-mediated cytotoxicity
APC	antigen presenting cell
aPD1	anti-PD-1 blocking antibody
aPDL1	anti-PD-L1 blocking antibody
CAF	cancer-associated fibroblast
CTLA-4	cytotoxic T lymphocyte-associated protein 4
ECM	extracellular matrix
FBS	foetal bovine serum
FUS	focused ultrasound
i.v.	intravenous (injection)
IFNg	interferon gamma
IFP	interstitial fluid pressure
IVIS	in vivo imaging system
MAR	microautoradiography
MFI	median fluorescence intensity
MHC	major histocompatibility complex
NSCLC	non-small cell lung cancer
PAM	passive acoustic mapping
PD	pharmacodynamics
PD1	programmed cell death protein 1
PDL1	programmed death-ligand 1 (also known as B7-H1 and CD274)
PDL2	programmed death-ligand 2 (also known as B7-H2, CD273)
PK	pharmacokinetics
s.c.	subcutaneous (injection)
SCLC	small cell lung cancer
SSP	sonosensitive particles
TME	tumour microenvironment
US	ultrasound

1 Introduction

1.1 Cancer

Across the globe, cancer has become the 2nd-leading cause of death, with the World Health Organization attributing 1 in 6 deaths to cancer [WHO 2018]. Over decades, researchers have worked to identify shared features of cancer, synthesized by Hanahan and Weinberg in 2000 as "*The Hallmarks of Cancer*" [Hanahan & Weinberg 2000] and later summarized by Hanahan and Weinberg who wrote that "[t]hey include sustaining proliferative signaling, evading growth suppressors, resisting cell death, enabling replicative immortality, inducing angiogenesis, and activating invasion and metastasis." [Hanahan & Weinberg 2011]. In addition to summarizing their previous work, in 2011 Hanahan & Weinberg "added two emerging hallmarks …reprogramming of energy metabolism and evading immune destruction" [Hanahan & Weinberg 2011].

1.1.1 Cancer immunotherapy

Cancer immunotherapy describes various therapeutic strategies designed to overcome immune evasion. These therapies were recognized in 2013 as *Science's Breakthrough of the Year* and they have continued to revolutionize and improve oncology's approach to cancer [Couzin-Frankel 2013]. Cancer immunotherapies have grown to include a variety of therapies including antibodies, vaccines, oncolytic viruses (OVs), and engineered, cell-based therapies [Skeate et. al 2016, Kaufman et. al 2015, Maude et. al 2018]. Checkpoint inhibitors hold particular promise. These antibodies act to block immunologic checkpoints that tumours, and/or the environments that they shape, exploit in order to suppress anti-tumour immunity [Ribas & Wolchok 2018]. Over just eight years the percentage of patients in the United States eligible for treatment with checkpoint inhibitors expanded from 1.54% in 2011 to 43.6% in 2018 [Haslam & Prasad 2019].

Presently approved indications for checkpoint inhibitor drugs include: "…melanoma, hepatocellular carcinoma, SCLC, NSCLC, renal cell carcinoma, urothelial carcinoma, Hodgkin lymphoma, head and neck squamous cell carcinoma, Merkel cell carcinoma, microsatellite instability–high colorectal cancer, gastric cancer, microsatellite instability–high cancers (noncolorectal), primary mediastinal large B-cell lymphoma, and cervical cancer", where SCLC is small cell lung cancer and NSCLC refers to non-small cell lung cancer [Haslam & Prasad 2019]. This wide range of target indications and the fact that in many cases checkpoint inhibitors have provided compelling improvements in clinical outcomes without the toxicity profile of conventional chemotherapeutics, has given checkpoint inhibitors commercial importance.

Indeed, in 2014 Webster wrote that: "[t]he immune checkpoint inhibitor market will experience considerable growth over the 2013–2020 forecast period, increasing from approximately US$1 billion in 2013 to in excess of $7 billion in 2020 (corresponding to 33% annual growth), across the seven major markets…" [Webster 2014]. Despite the incredible growth of these agents both clinically and commercially, checkpoint inhibitors drive responses in less than 13% of patients (across all indications) [Haslam & Prasad 2019]. It is therefore critical to understand how to and what can be done to further improve the efficacy of these agents, so first the principles of immunotherapy and checkpoint blockade are reviewed.

1.1.2 Principles of immunotherapy

The immune system can eradicate malignancy by recognizing differences between tumour cells and their non-malignant counterparts [Tian et al. 2011,Gajewski et al. 2013]. However, anti-tumour immune responses require a number of events to occur in a stepwise fashion, under the regulation of checkpoints intended to prevent autoimmune attack, coined by Chen & Mellman as the *cancer-immunity cycle* [Chen & Mellman 2013], as shown in Fig. 1.1 (with permission).

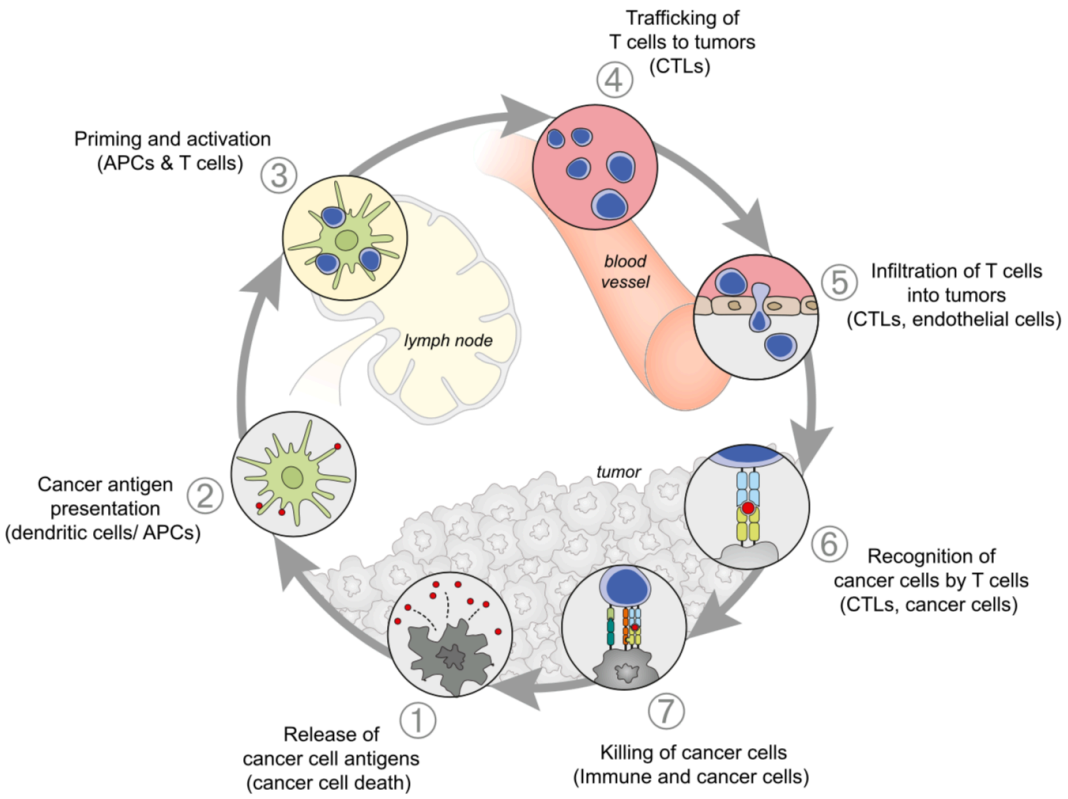


Figure 1: The Cancer-Immunity Cycle as adopted from Chen & Mellman 2013 with permission from Elsevier

Critical steps of adaptive T cell-mediated immunity include a) the activation of antigen presenting cells (APCs) by a pro-inflammatory milieu, b) the priming and clonal expansion of lymphocytes under the direction mature APCs, c) the trafficking and infiltration of anti-tumour lymphocytes to the local tumour environment, and d) cytotoxic attack of target cells [Chen & Mellman 2013]. However, anti-tumour immunity is often unable to control tumour burden, in part due to tumour-mediated exploitation of regulatory processes intended to maintain immunologic homeostasis [Van der Vlist et. al 2016, Ribas & Wolchok 2018].

1.2 Mechanisms of Checkpoint Blockade

Through decades of basic scientific research, two key pathways of modulation have emerged that have translated to the clinic: the cytotoxic T lymphocyte-associated protein 4 (CTLA-4) and programmed cell death protein 1 (PD1) pathways [Ribas & Wolchok 2018]. Here

the key discoveries and mechanisms of CTLA-4, PD1, and PDL1 (programmed death-ligand 1) blockade are briefly reviewed.

1.2.1 CTLA-4

CTLA-4 was initially discovered as a new immunoglobulin superfamily member by Brunet et al. in 1987 [Brunet et al. 1987]. Subsequent work to knock-out CTLA-4 in preclinical models, suggested that "CTLA-4 acts as a negative regulator of T cell activation" [Waterhouse et. al 1995]. This was corroborated by 1995 report by Tivol and colleagues titled: *"Loss of CTLA-4 Leads to Massive Lymphoproliferation and Fatal Multiorgan Tissue Destruction, Revealing a Critical Negative Regulatory Role of CTLA-4."* [Tivol et. al 1995]

Naïve T cell activation requires not only T cell receptor engagement with APC-major histocompatibility complex (MHC) presented cognate antigen (signal 1), but also costimulatory signals like T cell CD28 receptor engagement with APC expressed B7 ligands (CD80/CD86) [Lenschow et. al 1996]. CTLA-4 can outcompete T cell expressed CD28 for B7 ligands (CD80/CD86), resulting in a lack of sufficient T cell co-stimulation, thereby suppressing T cell activation and clonal expansion [Krummel et. al 1996, Ribas & Wolchok 2018].

Although CTLA-4 knockout resulted in lethality, fortunately investigation of CTLA-4 as a therapeutic target continued with preclinical work by Leach et. al identifying that CTLA-4 blockade with an antibody could drive durable tumour regression in vivo and protect the mice from tumour re-challenge [Leach et. al 1996]. In addition to promoting CD28-B7 interactions by blocking CTLA-4, anti-CTLA-4 antibodies (aCTLA-4) may facilitate the depletion of immunosuppressive populations, such as T regulatory cells, through antibody-dependent cell-mediated cytotoxicity (ADCC) [Selby et al 2013, Simpson et al 2013, Grosso & Jure-Kunkel 2013, Vargas et. al 2018].

The clinical evaluation of CTLA-4 blockade ultimately lead to 2011 FDA approval of ipilimumab [Khalil et. al 2016], a fully-humanized aCTLA-4 for advanced melanoma based on results of a phase 3 study that improved the overall survival of advanced melanoma patients [Hodi et. al 2010]. While CTLA-4 blockade remains within oncology's arsenal and is an agent of active investigation, checkpoint inhibitors targeting the PD1/PDL1 axis represent an area of substantial growth, from just one trial in 2006 to over 2,250 active trials in Sept. of 2018 [Tang et. al 2018]. In fact, the Cancer Research Institute in collaboration with IQVIA found that clinical investigation of the PD1/PDL1 axis grew by nearly 150% between September of 2017 (1,502 trials) to September of 2018 (2,250 trials) [Tang et. al 2018]. The incredible excitement over the PD1/PDL1 axis may relate to its favourable toxicity profile over CTLA-4.

1.2.2 PD1/PDL1

PD1 was discovered by Tasuku Honjo's group, who first suspected its role in programmed T cell death [Ishida et al. 1992]. By 2002, Iwai et. al explored the utility of PD1/PDL1 blockade in cancer, observing that administration of an anti-PD-L1 antibody (aPDL1) could significantly suppress tumour growth [Iwai et. al 2002]. Similar to CTLA-4, PD1 engagement acts to negatively regulate immune responses [Freeman et. al 2000, Dong et. al 2002, Parry et. al 2005]. However, in contrast to CTLA-4 knockout, PD1 knockout mice bear a milder, non-lethal phenotype marked by "autoimmune diseases" [Nishimura et. al 1999] including proliferative arthritis, glomerulonephritis, and dilated cardiomyopathy [Nishimura et. al 1999, Nishimura et. al 2001]. The differences may be tied to CTLA-4's primary role within lymphoid-tissue to regulate T cell activation and proliferation, in contrast to PD1's role to suppress already active T cell responses, such as the suppression of anti-tumour T cells within the tumour bed by PDL1 engagement (canonically, *Step 7* of the *Cancer-Immunity Cycle* shown in Fig. 1.1) [Chen & Mellman 2013, Chen & Mellman 2017, Ribas & Wolchok 2018].

Mechanistically, PD1 ligation results in cytoplasmic reorganization (including phosphatase SHP-2 recruitment) that ultimately suppresses T cell receptor (TCR) signalling pathway phosphorylation driving downregulation of phosphatidylinositol 3-kinase (PI3K) and Akt [Chemnitz et. al 2004, Parry et. al 2005, Nurieva et. al 2006, Okazaki & Honjo 2007, Patsoukis et. al 2013].

PD1 has two well-defined ligands, PDL1 (B7-H1, CD274) and PDL2 (B7-H2, CD273). In contrast to PDL2, whose expression is thought to be restricted to APCs, PDL1 is expressed by a wide variety of somatic cells, including tumour cells and cells of the tumour microenvironment—including endothelial cells [Dieterich et. al 2017], tumour-associated macrophages, myeloid derived suppressor cells (MDSCs) [Lu et. al 2016], T regulatory cells, and other leukocytes [Yamazaki et. al 2002, Jiang et. al 2019].

T cells begin expressing PD1 on their cell surface upon activation [Chen & Mellman 2017]. PD1's main ligand in the human tumour microenvironment hypothesized to be PDL1, and to date, whereas PD1-blocking and PDL1-blocking antibodies hold FDA-approval to address a broad range of malignancies, there is no approved anti-PDL2 agent [Sun et al 2018]. PDL1's expression can be constitutive [Tang & Zheng 2018], facilitated by genetic mutation (for example EGFR activation [Parsa et al 2007] or p10 loss of function mutation [Azuma et. al 2014]), and/or stimulated by pro-inflammatory factors like IFNg [Keir et. al 2008, Chen & Mellman 2017]. Put simply, the interaction of PD1 on T cells with tumour or TME expressed PDL1 can drive the T cells toward a dysfunctional, exhausted state rendering them unable to eliminate malignancy [Ribas & Wolchok 2018].

Although mechanistically both aPD1 and aPDL1 agents block PD1/PDL1 engagement, aPD1 agents can also block PD1's interaction with PDL2 [Zitvogel & Kroemer 2012]. This can be advantageous, but, it has been proposed that this could also lead to worse toxicity, owing to PDL2's expression in the lung, where PDL2 is known to play a role in mediating physiologic

respiratory T cell tolerance [Xiao et al. 2014, Lee et al. 2019]. Blockade with aPDL1 may be attractive over aPD1 for other reasons as well.

Firstly, in addition to PDL1's interaction with PD1 leading to T cell dysfunction and exhaustion, PDL1 has been reported to inhibit T cell proliferation by binding to CD80 at a higher affinity than CD28, effectively rendering CD80 sequestered due to the overlapping nature of the PDL1-CD80 interaction—a mechanism of action similar in effect to that of CD80/86 capture by CTLA-4 [Butte et. al 2007]. Therefore, administration of aPDL1 agents, may enable the blocking PDL1-CD80 interactions which can thereby reduce T cell anergy induction and enhance clonal expansion [Park et al 2010]. PDL1 can also function as an "antiapoptotic receptor" for the cancer cell expressing it—empowering the cancer cell to resist immune attack [Azuma et. al 2008]. PDL1 targeting is not only rational for the aforementioned reasons, but also because PDL1 targeted antibodies mediate target cell depletion through ADCC. Hence, aPDL1 agents can mediate eradication of the tumour or TME cells expressing PDL1 by direct mechanisms triggered by clustering of antibody Fc regions [Boyerinas et. al 2015, Juliá et. al 2018]. In brief, the general consensus is that aPD1's primary mechanism of action is to bind T cell expressed PD1, whereas aPDL1 agents are thought to bind tumour or tumour microenvironment expressed PDL1 in order to mediate anti-tumour responses.

1.2.3 PD1/PDL1 axis blockade in clinic

Pembrolizumab, a humanized aPD1 IgG4-kappa antibody, was the first FDA approved PD1/PDL1 agent [FDA 2014]. Since Pembrolizumab's 2014 approval, five additional aPD1 agents have been approved (Nivolumab, Cemiplimab, Sintilimab, Toripalimab, and Camrelizumab) and three aPDL1 agents have been approved (Atezolizumab, Durvalumab, and Avelumab) [Yu et al. 2019]. Together these agents hold indications across a broad spectrum of malignancies

In addition to more conventional tumour-specific indications, Pembrolizumab was also granted FDA approval across all types of solid tumours marked by high levels genomic instability (microsatellite instability-high (MSI-H) or mismatch repair deficient (dMMR) solid tumours) on the basis of five clinical trials [FDA 2017, Keytruda Label 2017]. This 2017 accelerated approval was considered a turning-point in drug translation—"the FDA's first tissue/site-agnostic approval" [FDA 2017].

Mild adverse effects (fatigue, diarrhoea, rash, and pruritus) are the most common treatment-related adverse effects, though 10-15% of patients receiving single-agent PD1/PDL1 axis blockade present with a grade 3 or 4 toxicity over the course of therapy [Ribas & Wolchok 2018]. Some of the most serious immune-related adverse events (irAREs) driven by PD1/PDL1 axis blockade are endocrinopathies, where autoimmune attack unleashed by checkpoint inhibition results in irreversible destruction of a hormone-secreting gland (including thyroid, pituitary, adrenal, and pancreatic disorders) [Girotra et. al 2018, Iglesias 2018]. These toxicities can be particularly bothersome given their contribution to morbidity, requiring life-long hormone replacement, not to mention its associated cost.

According to a 2018 meta-analysis of 12 PD1/PDL1 axis blockade randomized clinical trials in advanced solid tumours, only 2.19% of patients were complete responders (CR), and 18.9% were partial responders (PR) to PD1/PDL1 axis blockade [Carretero-González et al. 2018]. While this compares favourably to the 0.54% CR and 8.9% PR rates provided by standard of care [Carretero-González et al. 2018], given the financial and physical burden these agents can create Kelly & Davar 2019, improvements to response rates is clearly desired. To this end, enormous efforts are underway to understand which patients are promising candidates for therapy, why some tumours are outright refractory to therapy, and why others through immunoediting and other resistance mechanisms ultimately progress regardless of therapy [Sharma et. al 2017, Chen & Mellman 2017, Ribas & Wolchok 2018].

1.2.4 Strategies to improve PD1/PDL1 blockade therapeutic outcomes

There is a growing appreciation that PD1/PDL1 blockade is most effective in cancers where pre-existing immunity exists, but has been restrained [Bourgeois-Daigneault et al. 2018, Chen & Mellman 2017, Ribas & Wolchok 2018], such as in immunologically “hot” tumours marked by T cell inflammation, interferons, chemokines [Samson et al. 2018, Trujilo et al 2019], a high mutational burden (neoantigen load) [Schumacher & Schreiber 2015], and/or robust PDL1 expression [Yarchoan et al. 2019]. Such information is helping to stratify patients more effectively. Furthermore, a number of strategies, at varying stages of preclinical and clinical development, aim to improve the response rates of PD1/PDL1 therapy in all patients. These include the combinatorial use of chemotherapeutics, adjuvants [Wang et al. 2016, Takeda et al. 2017, Wang et al. 2018], oncolytic viruses [Samson et al. 2018, Bourgeois-Daigneault et al. 2018], loco-regional ablation [Shi et al. 2016, Zhao et al. 2019] or radiotherapy [Zeng et al. 2013, Deng et al. 2014, Haymaker et al. 2017], or other immunomodulatory agents, like anti-TGFb [Mariathasan et al. 2018, Lan et al. 2018]. Beyond tissue-debulking, the central thesis underlying the use of chemotherapeutics, adjuvants, oncolytic viruses, and loco-regional therapies (ablation or radiotherapy) is to create immunogenic stimuli and/or injury within the tumour microenvironment that renders the environment stimulatory for APC maturation and subsequent T cell activation and expansion, infiltration, and attack.

The combinatorial use of PD1/PDL1 axis blockade with other immunomodulatory agents has also proven promising. In fact, the remarkable improvements provided by the combination of aPD1 with aCTLA-4 over aCTLA-4 alone [Wolchok et al. 2013, Postow et al. 2015], lead to an accelerated FDA approval of this combination for advanced melanoma in 2015 [Tontonoz 2015]. Of note, strategies to combine aPDL1 agents with TGFb inhibitors have proven particularly intriguing, with two recent papers identifying that the combination of these two agents suppresses stromal factors that seem to block T cell infiltration and anti-tumour immunity

[Mariathasan et al. 2018, Lan et al. 2018]. Exploration of the dual-targeting of PDL1 and TGFb was driven by the rationale that PDL1 and TGFb play non-redundant roles in immunosuppression and/or that the TGFb tumour-signature marks poor outcomes [Mariathasan et al. 2018, Lan et al. 2018]. One, underexplored and perhaps overlooked consequence of TGFb signalling disruption may in fact be a change in the tumour's drug-delivery environment, discussed in greater detail in the subsequent section. The improvements to drug-delivery conferred by TGFb disruption perhaps were also a contributing factor to the combinatorial approach, enhancing aPDL1's efficacy. This naturally raises questions of whether, more broadly, drug delivery is a barrier to the efficacy of aPDL1. Notably, "meta-analysis suggests that anti–PD-1 exhibited better survival outcomes than anti–PD-L1 in patients with solid tumours in either overall, monotherapy, or combination therapy settings, with comparable safety profiles" [Duan et al. 2019]. Taken together, aPDL1 agents may be particularly susceptible to drug delivery barriers. It is from this perspective we briefly review some of the barriers that systemically administered drugs encounter on their passage into and throughout tumour microenvironments.

1.3 Drug Delivery Barriers in Tumours

There is a strong body of evidence that intratumoural drug delivery can dictate the efficacy of anti-cancer chemotherapeutics which must navigate to tumour-areas, breach endothelial walls, and traverse extravascular space in order to reach their target [Minchton & Tannock 2006, Brown & Giaccia 1998, Dewhirst and Secomb 2017]. Although checkpoint inhibitors are not known to function in a directly cytotoxic capacity, there is reason to suspect that improving their delivery may also improve their efficacy—particularly in the case of aPDL1, a drug targeting a tumour-bed expressed target. Therefore factors which influence and stymie intratumoural drug delivery and accumulation are reviewed here.

1.3.1 Tumour vasculature is a poor drug conduit

Vasculature supplying physiologic tissue is highly structured, marked by branching [McDonald & Choyke 2003] that maximizes the efficiency of oxygen and nutrient transport between systemic circulation and the extravascular space. Conversely, tumour vasculature is disorganized and patchy [Dwhirst & Secomb 2017, Ribatti et al. 2007]. Notably, when tumours grow beyond "approximately 1-2 mm^3" they can no longer rely on their existing vascular supply [Hillen and Griffioen 2007]. In response, like an "angiogenic switch", the tumour drives vessel growth with proangiogenic signalling (e.g. secretion of vascular endothelial cell growth factor family factors) to overcome angiostatic cues like endostatin and angiostatin [Hanahan & Folkman 1996, Hillen & Griffioen 2007, Baeriswyl et al 2009]. The aberrant vessels that sprout in tumours grow in a patchy, tortuous manner and are marked by morphological and phenotypic heterogeneity in terms of diameter and composition [Carlisle & Coussios 2013, Fukumura et al 2007].

The new microvasculature can also lack order with feeding vessels smaller in diameter than daughter vessels [Less et al 1991, Dewhirst and Secomb 2017]. The disorganized growth of vessels can result in shunting, which can occur when a new vessel provides a quicker route for blood to travel between the arterial and venous systems, thereby choking off tissue that would have otherwise be feed by a different vessel [Pries et al 2010]. Further, the new vessels can be structurally immature, with larger endothelial gaps, increased pore sizes, and less pericyte coverage to support the thinner endothelial wall [Hashizume et al. 2000, Maeda et al 2000]. Adding to insult, tumour-driven matrix metalloproteinase (MMP) activity, can further drive vessel wall disintegration [Utoguchi et al. 1996]. Altogether, tumour vasculature is markedly disorganized, tortuous, and patchy, and therefore fails to serve as an effective conduit to enable homogenous tumour-drug delivery.

1.3.2 Elevated interstitial pressures and stromal barriers

While macromolecules may be favoured in getting to the tumour's perivascular space, owing to the increased pore size and leakiness of tumour vasculature compared to that physiologic tissue [Maeda 2001], the increased size of these agents can restrict their ability to diffuse interstitially [Nichols & Bae 2014], an important problem when we consider that "...the peak distance between a cell and the nearest blood vessel in healthy tissues rarely exceeds 100 microns…" but in tumours "…this distance almost doubles to 180 microns…" [Carlisle & Coussios 2013]. Likewise, the leakiness of tumour vessels does not solely favour the deposition of the desired agent, other circulating macromolecules will also accumulate, which ultimately can drive elevations in interstitial fluid pressure (IFP), further compromising drug delivery [Nichols & Bae 2014]. Such raised IFP can cause the collapse of lymphatic vessels and the lymphatic drainage of tumours can therefore also be comprised, creating a vicious cycle that further exacerbates the elevation of IFP. Taken together, the pressures within tumour microenvironments can exceed or equilibrate to that of the venous system (~20mmHg), further comprising the ability of convective flow to bring a systemically administered drug to the local tumour environment [Carlisle & Coussios 2013].

Once a drug has breached the endothelial wall to reach the perivascular space, it still must diffuse throughout the tumour's interstitial space—here it also encounters challenges. The cellularity of tumour microenvironments [Lu et al. 2007], extent of stromal activity (e.g. cancer associated fibroblasts) [Truffi et al. 2019], and consistency of the extracellular matrix (ECM) can act to limit interstitial diffusion [Alexandrakis et al. 2004]. For example, work by Netti et al. has shown that collagenase treatment to address ECM-stiffness mediated transport resistance, could significantly improve IgG interstitial diffusion rate [Netti et al 2000]. In summary, pathophysiologic changes to the tumour's vasculature, lymphatic drainage, and

microenvironment in addition to other factors challenge the delivery and distribution of systemically administered drugs.

1.3.3 Relevance of drug delivery barriers to aPDL1 therapy

Over the past few decades oncology research has shifted away from small molecule chemotherapeutics toward biologic class agents, such as aPDL1, that can target protein-protein interactions in an exacting manner. Taking into account the diffusion-limited nature of drug delivery in cancer treatment, it is likely that drug delivery barriers are making it very difficult for these biologic agents to distribute and accumulate within the tumour interstitium. Of note, recent work has highlighted that aPDL1 is limited in its ability to escape the perivascular space. Working with microautoradiography (MAR) to characterize the intratumoural localization of a radiolabelled aPDL1, Deng and colleagues report that radiolabelled aPDL1 was “primarily associated with tumor vasculature with little or no diffusion into the tumor parenchyma” [Deng et al. 2016].

As referred to in 1.2.3, the work by Mariathasan et al. 2018 and Lan et al. 2018 combining PDL1 targeting with TGFb disruption is pertinent to the discussion of delivery [Mariathasan et al. 2018 and Lan et al. 2018]. Cancer associated fibroblasts, are key modifiers of the extracellular environment of tumours that can “secrete ECM proteins” [Gascard & Tlsty 2016] which may hinder drug delivery throughout the tumour. Mariathasan et al. 2018 and Lan et al. 2018 worked to disrupt TGFb, an important regulator of CAF activity. Put in the context of Deng et al., they have, albeit unintentionally, addressed one of the barriers to delivery—the tumour stroma—and observed that aPDL1 is more effective [Mariathasan et al. 2018, Lan et al. 2018]. Taken together, this points to a strong likelihood that improving aPDL1 delivery outright may improve the efficacy of the agent.

It is for these reasons, that in the next section, other approaches to improve systemically administered drug delivery are explored, with special attention to ultrasound-mediated cavitation, a tool capable of pushing and propelling intravenous drug into and around tumour.

1.4 Strategies to Overcome Delivery Barriers

The possibility of enhancing the local delivery and distribution of a systemically administered agent, holds great promise. Several strategies are gaining traction, notably vessel normalization and focused, therapeutic ultrasound. Proposed in 2001, vessel normalization aims to restore, “normalize,” vasculature in order to decrease tumour interstitial pressure and thereby improve intratumoural drug delivery, typically through the use of anti-vascular agents like bevacizumab [Jain 2001, Tong et al 2004, Nakahara et al. 2006]. Despite growing traction, challenges remain in the translation of vascular normalization including a need to better understand mechanism and define/address resistance mechanisms [Goel et al. 2011, Martin et al 2019].

Other technologies also in development include plasmonic photothermal therapy [Gormley et al. 2012], magnetic force-driven technology [McBain et al. 2008], and ultrasound [Graham et al. 2014], however ultrasound is perhaps safest and most clinically-relevant approach Therapeutic ultrasound can mediate a variety of thermal and mechanical bioeffects, including the generation of tumour-targeted hyperthermia which can improve intratumoural drug delivery and even trigger chemotherapeutic-drug release from a carrier [ter Haar & Coussios 2007, Lyon et al 2018].

Therapeutic ultrasound has also been shown to have immunomodulatory and radiosenitizing qualities, likely linked an ability to drive stress-responses [Czarnota et al. 2012, Skalina et al. 2019]. For example, work by Czarnota et al. 2012 has shown that therapeutic ultrasound paired with microbubbles can drive ceramide production (a stress response), compromise vasculature, and ultimately "enhance tumor responses to radiation in vivo”

[Czarnota et al. 2012]. Therapeutic focused ultrasound (FUS) can also be used to drive intratumoural cavitation [Mitragotri 2005], an approach discussed in more detail subsequently.

1.4.1 Principles of ultrasound & ultrasound-mediated cavitation

Ultrasound refers to sound waves greater than 20 kHz in frequency that travel in a longitudinal fashion resulting in cycles of compression and rarefaction. Typically, therapeutic ultrasound is operated between frequencies of “0.5 to 3 MHz” corresponding to “millimetre-length scales” [Gray et al. 2019]. When such acoustic waves interact with bubbles the bioeffects at length-scales relevant to drug delivery can be generated [Gray et al. 2019]. This is important considering the small size of antibodies (~0.016 μm in length) [Hanley et al. 2007].

Acoustic cavitation is defined as the response of a gas or vapour-filled bubble to acoustic excitation and can be classified as inertial and non-inertial. Any mention of cavitation in this thesis refers to acoustic cavitation. Inertial cavitation describes a regime whereby the bubble grows unstably during the rarefactional half-cycle of the acoustic wave, subsequently collapsing violently during compression owing to the inertia of the surrounding fluid. On the other hand, non-inertial cavitation describes the linear or non-linear periodic expansion and contraction of a bubble driven by ultrasonic excitation without the occurrence of inertial collapses [Stride & Coussios 2019].

1.4.2 Cavitation as a tool for drug delivery

Both inertial and non-inertial cavitation can aid drug delivery. Bubble-wave interactions enable highly efficient conversion of acoustic energy to heat and kinetic energy that is capable of bringing about thermal, mechanical, and even chemical effects such as sonoluminescence [Gray et al. 2019]. Of particular relevance to drug delivery is the ability of ultrasound-mediated cavitation to generate net fluid motion, also known as microstreaming, which arises from

momentum transfer from the oscillating bubble to the surrounding liquid [Stride & Coussios 2019]. Proximity of the bubble to a tissue boundary, such as a vessel wall, can drive non-spherical oscillations that can result in microstreaming velocities on the order of 1 mm/s [Pereno et al. 2018]. Additionally, shear forces can be generated against the tissue boundaries that may perturb the wall and support transport [Gray et al. 2019]. Finally, in the context of inertial cavitation, the violent bubble collapse can generate jetting and shockwaves which can also support drug delivery [Stride & Coussios 2019].

The ultrasound waves required to drive acoustic cavitation can be generated through the piezoelectric effect, whereby electrical energy is converted to mechanical energy [Hunt 1983]. The ultrasound transducer can focus the acoustic energy toward an intratumoural target, enabling non-invasive therapy [ter Haar 2001]. The bubbles can either form “spontaneously” or be provided to the environment exogenously. Specifically, at high acoustic peak rarefactional pressures, bubbles can “spontaneously” form through mechanical and/or thermal means [Gray et al. 2019]. These “spontaneous” bubbles are thought to originate from the presence of bubble-stabilizing surfactants or defects in tissue, such as surfaces featuring crevices, that can thermodynamically favour nucleation [Atchley & Prosperetti 1989]. Irrespective of aetiology, bubbles that are created in such a fashion in vivo require the application of relatively high peak pressures, which hinders clinical translation owing to safety concerns. To lower the pressure level required (i.e. the cavitation threshold), exogenous bubbles can be introduced, such as ultrasound contrast agents (microbubbles).

1.4.3 Cavitation with microbubble contrast agents

Microbubbles were intended for use as contrast agents to aid in diagnostic ultrasound applications, wherein the microbubble reflects incoming sound waves. Commercial microbubble contrast agents consist of an inert gas encapsulated within a shell ranging in size between 1

and 10μm. As of 2016 there were seven commercially marketed ultrasound contrast agents [Ignee et al. 2016, Gray et al. 2019].

When used as cavitation nuclei, these agents can improve the delivery of anti-cancer therapies including chemotherapeutics [Chen & Hwang 2013], chemotherapeutic-loaded liposomes [Graham et al. 2014], and oncolytic viruses, achieving intratumoural delivery to more than one hundred microns from the nearest blood vessel [Carlisle et al. 2013, Bazan-Peregrino et al 2013]. Despite their considerable promise as drug-pumps, these agents have several limitations. Notably, they have a short half-life and are physically too large to extravasate from tumour vessels, limiting their ability to provide a nucleus for sustained cavitation that spreads and facilitates fluid-mixing throughout the TME [Radhakrishnan et al. 2013, Graham et al. 2014, Gray et al. 2019]. A smaller, submicron nuclei would be better suited as it may co-extravasate and thereby provide a stimulus beyond the vessels [Oeffinger & Wheatley 2004, Paefgen et al. 2015].

1.4.4 Cavitation with sub-micrometre nuclei

Work by Kwan and others has recently brought forward the promise of sub-micrometre (submicron) sonosensitive particles (SSPs) (~480nm), “capable of seeding cavitation within the tumour microenvironment” [Kwan et al. 2015]. Additionally, these particles were tailored to sustain cavitation, from durations on the order of 30 seconds for microbubbles to several tens of minutes [Kwan et al 2015].

When compared to the sonication of microbubbles, SSP cavitation has also proven superior in improving delivery of macromolecular agents in vivo. Work by Myers et al. 2016 reports that ultrasound paired with SSPs but not SonoVue® microbubbles (SV), significantly improves vaccinia virus (VV) delivery in HepG2 tumours. Further, Myers and colleagues have shown that infectivity of VV is significantly greater when ultrasound-treated CT26 tumour-

bearing mice are administered SSPs compared to SV [Myers et al. 2016]. Likewise, Kwan et al. have shown some promising, albeit preliminary qualitative data that suggests that SSP-cavitation can improve the distribution of antibodies in vivo [Kwan et al. 2015]. Recent work has further confirmed that SSP-mediated cavitation does not detrimentally impact the activity of small molecules, oncolytic viruses (OVs), or antibodies [Myers et al. 2018]. Since 2014, SSPs have been developed and manufactured for clinical translation by *OxSonics Therapeutics Ltd*. (Oxford, UK), under the trade name *SonoTran® Particles*.

1.4.5 Monitoring and Mapping of Cavitation Activity

Another powerful feature of cavitation as a therapeutic tool, it its ability to be monitored *in vivo,* in real time—in short, the acoustic emissions generated by cavitation can be monitored. Non-inertial bubble collapse results in narrow-band emissions at multiples of the excitation frequency, whereas inertial bubble collapse generates broadband emissions [Stride & Coussios 2019]. While ablative therapeutic ultrasound can be monitored by B-mode ultrasound and magnetic resonance imaging (MRI) these modalities alone are not well suited to capture inertial cavitation [Coviello et al. 2015], such as that generated by the sonication of SSPs. Passive acoustic mapping (PAM), an approach first proposed by Gyöngy and Coussios in 2010, addresses such limitations [Gyöngy & Coussios 2010]. In brief, PAM employs conventional arrays of US receivers to passively capture acoustic emissions generated during therapy. A beamforming algorithm which exploits the differences in the time that acoustic emissions arrive to a given element allows for the translation of the acoustic emissions into information about the intensity and spatiotemporal distribution of cavitation [Stride & Coussios 2019].

1.5 Summary of Background

Cancer immunotherapy agents that disrupt the PD1/PDL1 axis are changing the course of oncology. However, despite the tremendous excitement, benefits so far extend only to a small subset of patients. We hypothesize that the physical size of the antibody therapeutics compounded by the drug delivery barriers presented by the tumour microenvironment may be limiting the efficacy of such agents. In particular, aPDL1 drugs, which bind tumour or TME expressed PDL1 may be particularly sensitive to the drug delivery barriers of the TME.

Recently, acoustic cavitation seeded by submicron nucleation agents has emerged as an attractive tool to improve the delivery of large, macromolecular anti-cancer agents. This US-mediated cavitation approach is attractive given that it is non-ionizing, relatively inexpensive, capable of deep tissue penetration, and can be monitored in real-time. Taken together, in this thesis the potential of pairing aPDL1 with cavitation to improve the delivery and efficacy of aPDL1 therapy is evaluated. The aims of this thesis are to:

1. Pair aPDL1 with submicron, tumour-penetrating cavitation nucleation agents (SSPs) and focused ultrasound to improve the efficacy of aPDL1
2. Enhance the intratumoural delivery of immunotherapy with SSP-nucleated cavitation
3. Characterize the biological and immunological changes induced by intratumoural cavitation in the absence or in the presence of a checkpoint inhibitor

2 Methods and Materials

2.1 Statement of Contributions and Assistance

The work described in my thesis is my own work but involved multidisciplinary experiments and intricate procedures which could not have been carried out without contributions of others. In particular, I would like to acknowledge the following individuals for their significant contributions to:

- Acoustic apparatus operation: Dr. Christophoros Mannaris, Catherine Paverd, and Claudia Hill
- Mouse cannulation and dosing: Sheena Wallington and Prof. Robert Carlisle
- Post-procedural cavitation analysis: Cameron Smith and Dr. Christophoros Mannaris
- Immunofluorescent microscopy and tissue preparation (cryosectioning, staining, and image analysis): Andras Miklosi and others of *Oxford Nanoimaging Ltd*
- RNA Extraction, *Nanostring*, and *nSolver* analysis: Dr. Joanna Hester
- *Nanostring* data analysis and FCM data plotting: Dr. Luca Bau

Additionally, I would like to acknowledge the assistance I received in: Cancer cell preparation and culture for tumour inoculation by Dr. Joanna Hester and Dr. Kate Milward, aid in mouse monitoring by Prof. Robert Carlisle and others of *IBME*/*BUBBL*, and assistance in tissue harvesting and processing for flow cytometry by Jamie Wallis, Dr. Joanna Hester, Kento Kawai, Alexander Martin, and others of *NDS*/*TRIG*

2.2 Ultrasound Apparatus & Exposure Parameters

Figure 2.2: Ultrasound Apparatus

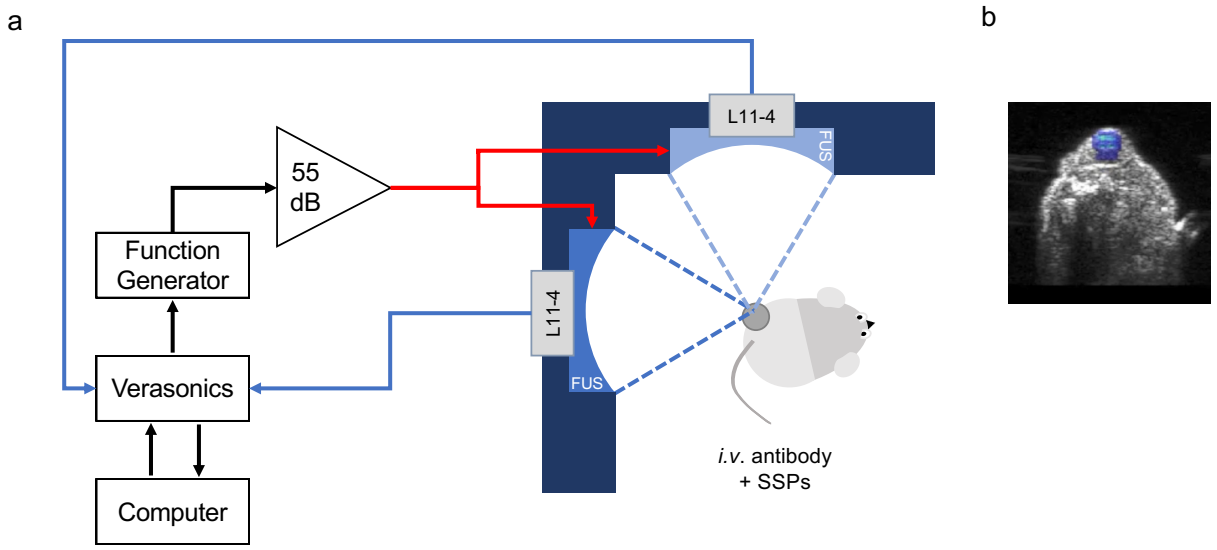


Figure 2.2: a) Treated tumours were aligned to the focus of two orthogonally positioned focused ultrasound (FUS) transducers B-mode guidance provided by the linear array diagnostic US transducers embedded within each therapeutic transducer. Following intravenous co-administration of therapeutic antibody and sonosensitive particles (SSPs), therapeutic ultrasound was triggered. Intratumoural cavitation generated by acoustic tumour excitation following the intravenous sequential dosing of therapeutic antibody and SSPs was monitored in real time in with passive acoustic mapping overlaid upon B-mode imaging of the tumour. b) An example image of passive acoustic mapping data overlaid upon B-mode tumour imaging kindly provided by Cameron Smith & Constantin Coussios

An overview of the experimental apparatus is provided in Fig. 2.1a. In brief, two therapeutic, single-element, spherical FUS transducers of a 63mm focal length (H107D, Sonic Concepts) were orthogonally and confocally aligned. L11-4v diagnostic US probes (Verasonics) were mounted within each FUS transducer, allowing for B-mode imaging and acoustic emission capture in a co-planar fashion. The therapeutic transducers were driven by a 55-dB, RF power amplified (A300 Power Amplifier, 017098, Electronics and Innovation) function generator (33250A; Agilent Technologies), directly connected to the matching network of each transducer. Acoustic output was calibrated by a hydrophone (HNA400, Onda Corporation).

2.2.1 Treatment Monitoring (Passive Acoustic Mapping)

Passive acoustic mapping was utilized to monitor therapy in manner refined from initial work by Gyöngy & Coussios in 2010 [Gyöngy & Coussios 2010]. To improve the axial and lateral resolution (down to 400μm), two coplanar arrays were utilized (a dual-transducer setup). Therefore, the experimental setup consists of a set of therapeutic US transducer arrays each fitted with a coaxial L11-5 diagnostic US probe that produces both B-mode images and is suitable to capture a cavitation activity from a coplanar perspective, enabling mapping of cavitation activity with high spatial resolution in real time. PAM data was generated by the robust Capon beamformer (RCB) algorithm [Coviello et al. 2015] as implemented and kindly provided by OxSonics Therapeutics Ltd.

2.2.2 Acoustic Parameters and Rationale

Frequency, Pulse Repetition Frequency and Pulse Duration

Pre-clinical therapeutic US frequencies reported in literature vary widely, ranging from a few hundred kHz to several MHz, though typically “0.5 to 3 MHz” in pre-clinical applications [Gray et al. 2019]. For example, Bulner et al. utilized US at a 1 MHz frequency in combination with microbubbles to generate vascular damage [Bulner et al. 2019] and work by Silvestrini et al. thermally ablated tumours at a 3 MHz frequency [Silvestrini et al 2017]. Previous studies completed in the BUBBL group since 2009 have demonstrated that a 0.5 MHz frequency allows for reasonable spatial specificity and cavitation at modest pressures, while minimizing risks related to thermal injury. In short, a 0.5 MHz frequency was utilized in this work. A pulse repetition frequency of 0.5 Hz was used in order to allow for SSP and drug replenishment within the region of interest between each burst [Bazan-Peregrino et al. 2013]. A 50,000-cycle pulse duration was selected in order to maximize the total acoustic energy delivered while maintaining

a 5% duty cycle which minimizes ultrasound induced heating [Graham et al. 2014 and unpublished, Mannaris *et al*].

Peak Rarefactional Pressure

Initial studies utilized a fixed peak rarefactional pressure of 1.7MPa. This fixed-pressure strategy was utilized in the experiments described in Sections 3.1, 3.2, and 3.3. However, in Section 3.3 the fixed-pressure strategy generated cavitation levels that were lower than expected, associated with efficacy outcomes that did not fit with previous observations. The initial approach to overcome this reduction in cavitation activity was to increase the incident pressure. In a subsequent study (Section 4.2) a fixed-pressure cavitation strategy was utilized at a pressure of approximately 1.9MPa. However, in an improvement over fixed-pressure strategies altogether, a better means of addressing such inconsistency was implemented—a strategy in which the real-time PAM was used to inform the pressure applied, so called "adjustable pressure strategy." In adjustable pressure studies, the therapeutic pressure was initially set to 1.5 MPa at the beginning of sonication and gradually increased or decreased from 1.5 to 2.1 MPa to sustain cavitation intratumorally between a range of peak cavitation intensity values 10 to 20 arbitrary units of power (AUP).

Summary of Acoustic Parameters

Strategy	Approximate Peak Negative Pressure	Pulse Duration	Pulse Repetition Frequency (PRF)	Duty Cycle	Sections
Fixed	1.5 MPa	50,000 Cycles	0.5 Hz	5%	3.1, 3.2, and 3.3
Fixed	1.9 MPa	50,000 Cycles	0.5 Hz	5%	4.2
Adjustable	1.5 to 2.1 MPa	50,000 Cycles	0.5 Hz	5%	All other sections

2.2.3 Retrospective Cavitation Analysis

The integrated cavitation dose, in arbitrary units of energy (AUC), was retrospectively quantified by one of two different methods, abbreviated CC-G1 and CC-G2 analysis, developed by Dr. Christophoros Mannaris and Mr. Cameron Smith. The first generation of analysis (CC-G1), calculates the integrated cavitation dose by summating the peak intensity pixel on a frame by frame basis across the sonication duration—in essence, integrating the power of acoustic emissions over time. CC-G1 analysis was utilized only in Section 3.1, an experiment where second generation (CC-G2) analysis was not feasible. CC-G2 analysis re-processes acoustic data with improved beamforming, enabling better estimation of the distribution of energy within each frame rather than just the peak pixel's intensity, yielding an improved calculation of the integrated cavitation dose, again measured in arbitrary units (AUC). PAM data was also characterized in Section 3.3 for "persistence" – a value ranging between 0 and 1 representing the fraction of sonication time of which cavitation activity was above a certain threshold.

2.3 In vivo models

The CT26 tumour model was selected given that it is "…a widely used murine model of colon adenocarcinoma…" [Kuai et al. 2018], is rather immunogenic [Lau et al. 2017], and that it expresses PDL1 [Kleinovink et al. 2017]. EMT6 (mammary) cancer was also utilized; this model is syngeneic to the BALB/c background and exhibits an aPDL1-refractory, immune excluded phenotype rich in stromal elements [Mariathasan et. al 2018]. Animal studies were carried out to UK Home Office guidelines per 3R (Replacement, Reduction, and Refinement) principles.

2.3.1 Cell Culture

CT26 and EMT6 cells were cultured *in vitro* at 37C° with 5% CO_2 in an aseptic manner. EMT6 cells were purchased from ATCC. CT26 cells were kindly provided by the research group of Prof. Len Seymour, Dept. of Oncology, University of Oxford (all sections except 4.7 and 4.8) or purchased from ATCC (Sections 4.7 and 4.8) and maintained in a manner similar to that advised by ATCC. In brief, cells were maintained in complete media consisting of RPMI-1640 (Sigma or equivalent) supplemented with approximately 2mM L-glutamine (Sigma or equivalent), 8.9-10% foetal bovine serum (FBS) (Gibco or equivalent), +/- 1mM sodium pyruvate (Gibco or equivalent). EMT6 cells were maintained in manner similar to that advised by ATCC: Weymouth's Medium (Gibco) with 2mM L-glutamine and 15% FBS (Gibco or equivalent).

2.3.3 Tumour propagation & monitoring

Immunocompetent, wildtype Balb/c mice (BALB/cAnNCrl) were purchased from Charles River Laboratories and acclimated with the local animal housing facility prior to tumour inoculation. Each CT26 tumour was propagated by the implantation of 5E5 CT26 tumour cells suspended in FBS-free PBS (Gibco or equivalent). Each EMT6 tumour was propagated by the injection of 5E5 (Section 3.5) or 1E6 (Section 4.4) EMT6 cells suspended a 1:1 ratio of Matrigel

(Corning) to PBS. Tumours were propagated subcutaneously to single flank or bilateral flanks as per study design. Mice were monitored at least every 2-3 days when tumours were palpable. 90-days represented the experimental endpoint in studies (unless otherwise noted), though mice were sacrificed earlier in case of welfare concern or a tumour burden exceeding 1000mm^3 (e.g. ≥ 950mm^3 if expected to exceed 1000mm^3 prior to next measurement). Tumour volumes were calculated as: ½*a*b^2, where 'a' represents the largest axis of the tumour and b represents the smaller axis of the tumour. In the case of multi-nodular tumours, the tumour volume was calculated as the sum of each measurable mass.

2.4 Interventions

Mice under isoflurane induced (~5%) and maintained (~2-3%) anaesthesia were depilated about the tumour (when required) to prevent bubble trapping within hair, minimize ultrasound reflection, and cavitation about the skin. On a bench top, a tail-vein catheter was implanted. Mice were then intravenously *(i.v.)* dosed injectables as outlined in each study (typically a drug, then sonosensitive particles (SSP) in 5% glucose, followed by a 5% glucose flush. Therapeutic antibodies were sourced from BioXCell and/or BioLegend: IgG2b (Clone LTF-2 or RTK4530), IgG2a (Clone 2A3 or RTK2758), aPD1 (Clone RMP1-14), aPDL1 (Clone 10F.9G2), and aICOS (Clone 7E.17G9). SSPs were kindly provided by OxSonics Therapeutics Ltd. (Oxford, UK).

Each ultrasound-assigned mouse was secured to a custom holder and lowered into a 37C° water bath fitted with therapeutic and diagnostic ultrasound equipment. Tumours were aligned to the focus of two orthogonally focused ultrasound (FUS) transducers using linear translation stages of micro-meter accuracy (Newport Corporation) under B-mode guidance.

Therapy was initiated upon intravenous injection. Following injection of drug and 50μL of sonosensitive particles (SSPs) suspended in 5% glucose, the catheter was cleared via 5% glucose flush. The SSPs injection corresponds to an approximate injection of 0.875-1.094mg of SSPs per intervention. Throughout sonication, passive acoustic mapping (PAM) provided real-time treatment feedback (in APU), allowing for confirmation of cavitation activity within the tumour [Coviello et. al 2015]. Each sonication was carried out for approximately 10 minutes except for the EMT6 study of (3.5) where a 5-minute cavitation duration was intended. The CT26 treatment strategy was informed by previous work in the BUBBL group with CT26-tumour bearing mice (pressure, duty cycle, circulation time of SSP)

2.4.1 Survival Study Analysis Censorship Criteria

Owing to procedural deviations that may have arisen over the course of survival studies, the following censorship criteria were applied. Censorship does not refer to the sacrifice of the mouse, rather it refers to the mouse's censorship from a survival curve plot during survival curve analysis. Mice were not censored unless there was clear rationale for why a mouse should be censored from the study. The complications (listed below) group problems into three core areas: cannulation, ultrasound/therapy, and welfare. *WNL = Within Normal Limits

Possible Procedural Complications:

- cannulation issue
  - do not censor mice when:
    - >50% of intended drug dose is injected
    - >50% of intended SSP volume injected and cavitation is WNL of group
  - censor mouse on day of originating procedure if:
    - Unclear or <50% drug or SSP injection
    - Documented cannulation issue & poor subsequent cavitation
- ultrasound deviation
  - do not censor mice when:
    - Sonication is interrupted but >50% of sonication duration takes place
    - Sonication is delayed from time drug and/or SSP injection, but cavitation is WNL
  - censor mouse on day of originating procedure if:
    - Incorrect burst parameter initially utilized
- mice sacrificed per procedure-related welfare issues
  - do not censor mice sacrificed due to
    - excessive skin ulceration about tumour
  - censor mouse on day of originating procedure for mouse sacrificed for:
    - skin ulceration/bioeffect distal to tumour capsule
    - hunched posture (despite total tumour regression)
    - ambulation issues that do not resolve

2.5 Imaging Methods

2.5.1 IVIS Imaging of Near-Infrared Antibody Conjugates

Antibody conjugation

aPDL1, aPD1, aICOS, and IgG2b were each conjugated to a near-infrared fluorochrome (680nm) via NHS linker chemistry as guided by manufacturer protocol (PerkinElmer 2010) in order to enable direct imaging of therapeutic within tumour. The fluorophore's maximal absorbance and emission is at 688nm in 1x PBS as reported by the manufacturer, making ideal for imaging by IVIS.

In brief, antibody and sodium bicarbonate were mixed at a ratio of 50µL (1M, 8.3 pH) sodium bicarbonate per 500µL of drug and 2uL of reconstituted VivoTag 680XL dye per each mg of (unconjugated, parent) drug. The reaction mixture was then shaken at room temperature for at least 2-hours. A size-exclusion column (7kDa molecular weight cut-off) was utilized to remove unconjugated fluorophore. Drugs were made on several occasions with minor batch-to-batch variations in manufacturing protocol (i.e. an additional centrifugation of the purification column, during column preparation), but these deviations were unlikely to make an impact. Following conjugation, collected conjugate protein was characterized by absorbance 280nm (A280) and 668nm (A668) measurement (NanoDrop and/or NanoDropOne, ThermoFisher).

Degree of ligation (DOL) and concentration were determined by the formulas shown below, derived from manufacturer recommendations [PerkinElmer 2010]. The DOL relates the molar ratio of dye to protein and the concentration calculation scales the drug-conjugate's A668-corrected, A280 to its unconjugated parent of concentration.

Degree of Ligation

$$DOL = A668_{conjugate} / (A280_{conjugate} - 0.16 \times A668_{conjugate})$$

Drug Concentration:

$$\text{Conjugate Drug Concentration} = \Theta * [A280_{conjugate} - (0.16 \times A668_{conjugate})]$$

$$\text{where: } \Theta = \text{Parent Drug Concentration} / ([A280_{parent} - (0.16 \times A668_{parent})]$$

Please see additional batch-specific details regarding synthesis and characterization below:

Characterization of conjugates used in Figures 4.1 and 4.2

The aPDL1 conjugate used in Fig. 4.1 was prepared as described above. aPDL1-bonus used in Fig. 4.2, unlike all other drug-conjugate, was reacted at a ratio of 1uL dye to protein instead of 2uL dye per mg of protein and was purified on an already utilized purification column (the column utilized to prepare the drug conjugate of 4.1). The DOL and concentration of agents administered in Figures 4.1 & 4.2 is summarized in Table 1. For these two drug-conjugates, A280 and A668 were acquired with a 340nm baseline correction, with automated path length correction. Likewise, drug and unconjugated parent drug were likely not diluted prior to absorbance acquisition, which limits the reliability of the concentration and degree of ligation (DOL) values (later studies addressed these limitations). Please see text and figure legend for the actual administered drug-dose.

Table 1

Drug Conjugate	DOL	Concentration (mg/mL)
aPDL1	2.18	4.10
aPDL1-bonus	1.44	5.51

Characterization of conjugates used in Figures 4.3 and 4.4

The range of DOL and concentration of agents administered in Figures 4.3 and 4.4 is summarized in Table 2. Please see the text and figure legend for the actual administered drug-dose. Drug characterization was completed by NanoDrop with the collection of 280nm and

668nm absorbance (A280 and A668) with an 800nm baseline correction, and no automated path length correction. Drug and unconjugated parent drug were diluted to 1:4 or 1:5 prior to absorbance acquisition to better fit the maximum tolerated ranges of drug concentration the NanoDrop is capable of accurately reporting.

Table 2

Drug Conjugate	DOL	Concentration (mg/mL)
aPDL1	1.48 to 2.85	3.03 to 5.32
aPD1	0.69	4.01
aICOS	1.11	4.03
IgG2b	1.83	6.26

Imaging of conjugated antibodies

Live animal imaging and excised tumour imaging of NIR-conjugate drugs administered to CT26 or EMT6 tumour bearing mice was conducted via IVIS Lumina II (PerkinElmer). Please see the text and/or each figure caption, for details regarding the acquisition parameters utilized. Captured images were manually traced to mark tumour boundaries and then analysed by LivingImage (PerkinElmer) to quantify average fluorescent counts per unit area, termed counts by area (CBA). The count scales of representative images were adjusted in order to accommodate the range of counts, see each image for further detail.

2.5.2 Microscopy

Haematoxylin & Eosin Microscopy

After intervention, excision, and IVIS imaging, the paired tumours of a subset of mice (6 mice) were OCT-embedded, then flash-frozen for H&E evaluation. Following 10um

cryosectioning, the tissue was rehydrated, haematoxylin-incubated (Mayer's Modified Hematoxylin Solution, Abcam), then washed prior to the application of ammonium hydroxide (Sigma or equivalent) for blueing, then counterstaining in 1% aqueous eosin (Raymond) followed by dehydration and mounting. Slides were scanned on a conventional light microscope (DM2000, Lecia) at 20x and 5x with matched exposure settings used for each pair of tumours.

Quantitative Immunofluorescent Microscopy

After tumours of bilateral, CT26 tumour-bearing mice treated with unconjugated aPDL1 were cryopreserved in OCT they were processed by *Oxford Nanoimaging Ltd.* (Oxford, UK). In brief they were 1) cryosectioned, 2) stained to detect unconjugated aPDL1 (by anti-IgG2b), blood vessels (by anti-CD31), and nuclei (by DAPI), imaged by *NanoImager*, then analysed for stain intensity and distribution.

2.6 Flow Cytometry Methods

All flow cytometry (FCM) data presented in this thesis was completed on a BD FACS Canto II configured with a blue, red, and violet laser with filters to enabling detection of 8 fluorescent channels: FITC, PE, PE-TexasRed, PerCp, PE-Cy7, APC, APC-Cy7, and PacificBlue. A number of the commercially purchased FCM antibodies utilized throughout the work presented here feature FCM-optimized spectral properties (e.g. "AlexaFluor" and "eFluor"). In the sake of clarity and brevity instead of referring to dye by its proprietary name, each dye is referred to by the channel it is recognized by. For example, the AlexaFluor647-aIgG2b is referred to as an APC-aIgG2b.

2.6.1 Drug Delivery Query

Detection of Tumour-Bound Antibody *Ex Vivo*

Four tumours were excised from sacrificed, tumour-bearing BALB/c mice. Tumours were enzymatically digested in tumour digestion media, mechanically disassociated in gentleMACS C

Tubes by gentleMACS Octo Dissociator (Miltenyi Biotec), then and mashed through a 70um cell strainer (VWR or equivalent) to yield a single-cell suspension. Aliquots of the suspensions were then incubated (~30min) with or without unconjugated aPDL1 (Clone 10F.9G2, an IgG2b antibody), then washed, prior to the application of APC-aIgG2b (Clone MRG2b-85, BioLegend 408208/9) to detect, bound unconjugated therapeutic aPDL1to all samples. After an approximately 30-minute incubation, cells were washed and resuspended in 7AAD (BioLegend or equivalent) for determination of cell viability. After at least 30-minutes of 7AAD staining, the samples were acquired on the BD FACS Canto II and analysed in FlowJo (BD) per gating hierarchies shown in 4.1.

aPDL1-binding queried ~24hr post-intervention

Approximately 24-hours post-intervention, tumours were excised and prepared to a single-cell suspension. Subsequently, tumour suspensions were blocked (2.5% Fc Block, BioLegend or equivalent) for approximately thirty minutes, followed by staining with 1:600 dilution of APC-aIgG2b (BioLegend). After an approximate 30-minute incubation at 4C, cells were thoroughly washed and stained in 1:600 dilution of aCD45 (eBioscience or equivalent) in FACS buffer. After a 30-minute incubation at 4C, samples were then washed and resuspended in 7AAD (3:100 dilution in FACS buffer) prior to acquisition via BD FACS Canto II (BD).

aPDL1, aPD1, and IgG2b binding queried 1.5hrs-post intervention

BALB/c mice bearing bilateral CT26 tumours (n=4/group) were either dosed 200μg of unconjugated (therapeutic) aPD1, aPDL1, or IgG2b, then SSPs followed by single-tumour sonication. Approximately 1.5hrs after therapy, mice were sacrificed, and their bilateral tumours were collected and weighted. Tumours were subsequently processed to a single-cell suspension. In brief, tumours were loaded to a gentleMACS C-Tubes (Miltenyi Biotec) and mechanically disassociated in FACS buffer with 2mM EDTA a gentleMACS Octo Dissociator (Miltenyi Biotec). Tumour suspensions were then mashed thru a 70um cell strainer (VWR or

equivalent) to yield a single-cell suspension. The single-cell suspension was washed in PBS with 2mM EDTA then each tumour was re-suspended in volume scaled to its weight (weight-normalizing the concentration of each sample). Red blood cells (RBC), a contaminant, were then eliminated by 1x RBC lysis buffer (Invitrogen or equivalent) incubation. Cells were subsequently resuspended in a Zombie Violet Fixable (BioLegend) live/dead stain at a dilution of 1:400. After approximately 25 minutes of live/dead staining, the stain was removed, and cells were blocked at least 2.5% normal goat serum (ThermoFisher Scientific) for at least 25 minutes. Cells were subsequently stained with APC-aIgG2a (BioLegend 407511/2; for aPD1-administered mice samples) or APC-aIgG2b (BioLegend 408208/9; for aPDL1 or IgG2b administered mice samples) antibody at a dilution of 1:600 for about 30 minutes on ice. Of note, the aIgG2a stain was accidentally applied to one aPDL1 treated, non-US tumour sample, however, the error was quickly corrected (thorough washing, re-application of the correct stain). The error would be expected to raise the APC signal of the sample, but it did not, so the sample was not excluded from analysis. After incubation in aIgG2a or aIgG2b, samples were washed, and stained at a 1:1200 dilution of PE-Cy7-aCD11b (eBioscience 25-0112-82), and a 1:600 dilution of PE-aCD45.2 (eBioscience 12-0454-81) and FITC-aCD3 (eBioscience 11-0032-82). Stained suspensions were then fixed in 2% fixation buffer and acquired by FACS Canto II (BD).

2.6.2 Immunophenotyping

Staining of whole-tissue suspensions

Three different kinds of tissue (tumour, tumour-draining lymph node, and tumour non-draining lymph node) tissue were collected then subdivided for staining by 3-different FCM panels. Data presented here represents stained tissue from mice that were sacrificed 5-day post-intervention mice for RNA analysis then subdivided & appropriately stained—a total of 198

individual samples (i.e. there were n=5-6/group/tissue for FCM1 and FCM2, and n=5/group/tissue appropriately stained by FCM3).

Excised tumours were placed into C-tubes (Miltenyi Biotec) filled with approximately 5mL of tumour digestion media then mechanically dissociated. The suspension was then mashed through thru a 70um cell strainer (VWR or equivalent) to yield a single-cell tumour suspension. Excised lymph node tissue was similarly mashed through a 70um cell strainer to yield a single-cell suspension. The single-cell suspensions were then directly utilized in downstream immunostaining. After samples were blocked in at least 2.5% Fc block (BioLegend 101301/2 or equivalent), the appropriate cocktail of extracellular antibodies was applied—the extracellular markers of the FCM1, FCM2, FCM3 panels as shown in Fig. 5.11 and Appx. 5.11. All extracellular antibodies were at an approximate 1:600 dilution (assuming entrenched well volume was negligible) in FACS buffer.

Following, extracellular staining, samples of all panels were then fixed and permeabilized in a prepared 1x solution of Fixation/Permeabilization buffer (Invitrogen or equivalent). Because samples were collected on consecutive days (days 14-16) they were incubated in Fixation/Perm. buffer for slightly different times. Once all samples collected had been fixed and permeabilized, intracellular stains were applied at an 1:10 dilution (assuming no entrenched well volume). Samples were subsequently acquired via BD FACS Canto II and analysed in FlowJo.

2.7 RNA Nanostring

RNA was isolated, quantified, then queried for gene expression by *Nanostring.* RNALater-stored tumour samples were thawed in lysis buffer (RNeasy kit, Qiagen) and placed into Gentle MACS M tubes (Miltenyi) for disassociation. Total RNA isolated was isolated (RNeasy, Qiagen) then measured via Quant-IT RNA Assay Kit (Invitrogen). Nanostring *PanCancer Mouse Immune Profiling* reagents and were utilized in the remainder of the work.

50ng RNA tumour samples were hybridized (18-hours) then loaded to *nCounter PanCancer Mouse Immune Profiling* cartridges, which were then acquired on *nCounter Sprint* (Nanostring). Pathway and cell scores were generated in nSolver (Nanostring) with assistance from Dr. Joanna Hester. Nanostring data was prepared and analysed by Dr. Luca Bau using *R* (R Foundation for Statistical Computing). Other than pathway and cell scores, all other data was sourced from RCC output files of the *nCounter* and imported to *R* for processing (normalization, error checking, statistical testing, and plotting). Statistics shown in gene boxplots (e.g. Fig. 5.3b) were calculated from a linear model fitted to normalized data by limma-trend [Ritchie et al. 2015] with intervention as a covariate. Technical variation was addressed by positive normalization (using the geometric mean of positive controls) followed by mRNA content normalization with housekeeping genes selected using the geNorm algorithm (*Eef1g, Tubb5, Sf3a3, Sap130* for t=5d and *Rpl19, Abcf1, Eef1g, Hprt* for t=24hrs). Genes were excluded from analysis if their raw count was below background in more than 20% of samples.

2.8 Statistics

Statistics were completed in GraphPad *Prism* 6 and/or 8.4. Typical testing conducted in *Prism* included unpaired t tests, paired t tests, ordinary one-way ANOVA, ordinary two-way ANOVA, repeated measures (RM) two-way ANOVA, and log-rank (Mantel-Cox) survival analysis. Throughout this thesis: * = $p < 0.05$, ** = $p < 0.01$, *** = $p < 0.001$, **** = $p < 0.0001$.

3 Efficacy Studies

Expression of programmed death ligand 1 (PDL1) by the tumour and its microenvironment acts to suppress T-cell mediated anti-tumour immunity through PD1, a T cell receptor. Anti-PDL1 (aPDL1) is an immunomodulatory antibody which acts to disrupt PD1/PDL1 interactions thereby reducing T cell exhaustion and dysfunction [Khalil et al 2016]. In addition to a blocking functionality, aPDL1 can act to deplete PDL1 positive cells through antibody-dependent cell toxicity (ADCC) [Boyerinas et a. 2015]. Depletion of PDL1-expressing cells is thought to be advantageous because PDL1 is often expressed by tumour cells and immunosuppressive populations within the tumour, whose elimination would contribute toward anti-tumour immunity in a direct and indirect manner. Directly, by eliminating cancer cells that express PDL1, and indirectly by eliminating immunosuppressive cells which could be dampening an anti-tumour immune response. Highlighting both of these features, work by Dahan et al. with ADCC-incompetent and competent engineered aPDL1 has shown that ADCC-competent aPDL1 has better anti-tumour activity which correlated with favourable changes in the myeloid compartment (i.e. monocyte elimination) [Dahan et al. 2015]. aPDL1 can also act through other mechanisms as reviewed in Section 1.2.

PDL1 as a clinical target has proven to be safe and effective with three aPDL1 agents holding FDA approval, though it is worth noting that only one, Avelumab is ADCC-competent [Kaufman et al. 2016, Apolo et al 2017, Chen et al 2019]. Despite its unique mechanistic potential Avelumab “response rates have been modest, similar to other PD-L1 and PD-1 targeted antibodies” [Collins and Gulley 2019]. Meta-analysis of Atezolizumab, an aPDL1 therapeutic with perhaps the greatest amount of data available, revealed that when its used as a monotherapy 16% of patients were partial responders and only 6% of patients were complete responders [Tie et al 2019]. It is evident that there is room to improve the efficacy of PDL1-targeted agents, especially an agent akin to Avelumab that can mediate anti-cancer activity

through multiple mechanisms. Drug delivery barriers, including the malformed vasculature, elevated interstitial pressures, dense extracellular matrix, and lack of convective flow of tumour microenvironments [Minchinton & Tannock 2006, Chauhan et al. 2011], could be a factor limiting the efficacy of aPDL1 agents.

There has been a considerable body of work investigating whether therapeutic ultrasound can improve anti-tumour immunity, though work to date has primarily focused on using an acoustic strategy to create vascular damage or tissue injury. In brief, Silvestrini et al. 2017 investigated the sequencing of FUS-mediated thermal tumour ablation with immunotherapy and Han et al. 2019 have demonstrated that HIFU-mediated tumour ablation paired with checkpoint inhibition can yield strong anti-tumour immune responses that can protect mice from tumour re-challenge [Silvestrini et al 2017, Han et al 2019]. Likewise, work by Bulner et. al has demonstrated that pairing aPD1 with vascular damage generated by US excitation of microbubbles can improve the aPD1 efficacy and work by Yue et al. has shown that nanosonosensitizer-mediated sonotoxicity paired with checkpoint-blockade “not only arrests primary tumour progression, but also prevents lung metastasis” [Bulner et. al 2019, Yue et al. 2019]. Work by Eranki et al. has shown that cavitation histotripsy paired with dual-checkpoint (both aPDL1 and aCTLA4) blockade can drive tumour regression [Eranki et al. 2019].

US-mediated cavitation of sonosensitive particles (SSPs) has recently emerged as an attractive, non-invasive strategy to improve anti-cancer agent delivery to tumours [Kwan et al. 2015, Myers et al. 2016]. Studies presented in this chapter assess whether improving aPDL1 delivery by applying US-mediated cavitation can improve the efficacy of pre-clinical, Fc-competent aPDL1. Given that:

1) tumour microenvironments limit the extravasation of large, biologic drugs,

2) US-mediated cavitation may enhance the delivery of intratumoural drug, and

3) aPDL1’s function may require its intratumoural delivery,

We hypothesize that US-mediated cavitation may increase aPDL1 efficacy. This chapter, therefore, explores the biological ramifications of enhancing PD1/PDL1 axis inhibition *in vivo* in immunocompetent mouse models. Additionally, work is extended to explore whether this same approach may improve the efficacy of an aPD1 whose mechanism is thought to be reliant on binding PD1 expressed by T cells; T cells which could be intratumoural or extra-tumoral (i.e. in systemic circulation) and not as limited by drug delivery barriers.

3.1 Pilot Study: Low-Dose aPDL1 with Cavitation

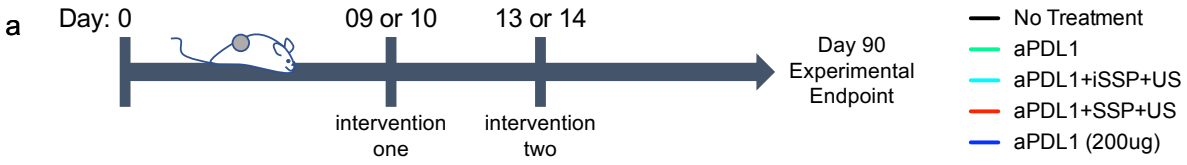
In this study, the potential of US-mediated cavitation to enhance the therapeutic efficacy of an aPDL1 at a low dose is explored. Clinically aPDL1 therapeutics are often dosed at 10mg/kg, for example Avelumab is dosed at 10mg/kg *i.v.* every 2-weeks [Collins & Gulley 2019]. This dose in humans approximately corresponds to a 200μg dose in mice. Owing to potential safety and cost advantages in lowering the systemically administered drug dose, the present study investigates whether comparable tumour growth and survival outcomes can be achieved between mice dosed at 200μg of aPDL1 (200μg aPDL1) without cavitation and mice receiving 100μg of aPDL1 paired with SSP-nucleated cavitation (aPDL1+SSP+US). A group of mice dosed at 100μg of aPDL1 (aPDL1) without cavitation is also included for comparison, as is a no-treatment control group.

In addition, the present study also sought to evaluate the impact of the presence of ultrasound alone and of the introduction of polymeric SSPs nanoparticles in the absence of cavitation activity. This was achieved by sonicating a group of mice having received 100μg aPDL1 and cavitation-inactivated SSPs (aPDL1+iSSP+US), and comparing the results both to the group receiving 100μg aPDL1 without ultrasound (aPDL1) and the group receiving 100μg of aPDL1 paired with SSP-nucleated cavitation (aPDL1+SSP+US).

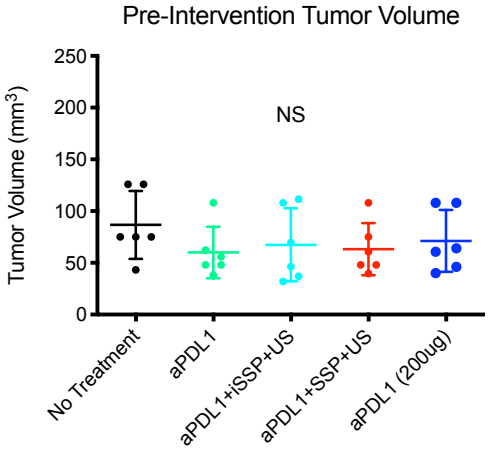
3.1.1 Experimental Overview

As illustrated in Fig. 3.1a, CT26 tumour bearing BALB/c mice were assigned to 1 of 5 intervention groups (n=6/group) 9 or 10 days following tumour inoculation (no treatment, 100µg aPDL1, 100µg aPDL1+iSSP+US, 100µg aPDL1+SSP+US, and 200µg aPDL1). Pre-intervention tumour volumes were NS different between groups as determined by ordinary, one-way ANOVA with Tukey multiple comparisons among groups (Fig. 3.1b). The average overall tumour volume of study enrolled mice was 69.7mm^3 with a standard deviation of 29.3mm^3. Mice with tumours deemed too difficult to target with therapeutic ultrasound were assigned to injection-only groups. The rationale for doing so was that the total tumour burden in non-spheroid or bi-lobed tumour bearing mice was identical to that of mice bearing spherical tumours.

Figure 3.1: Pilot Evaluation of aPDL1 +/- SSPs +/- US (1/3)



b



Group	Mean (mm^3)	Std. Deviation (mm^3)
No Treatment (NT)	86.7	32.8
aPDL1	60.1	24.9
aPDL1+iSSP+US	67.4	35.3
aPDL1+SSP+US	63.2	25.2
aPDL1 (200ug)	71.2	29.9
Overall	69.7	29.3

Figure 3.1
a) Schematic of survival study. BALB/c mice were implanted with single CT26 tumours. 9 or 10 days following tumour inoculation mice were assigned to 1 of 5 intervention groups. Each mouse received two identical interventions spaced 4 days apart. Mice were monitored to day 90 or sacrificed earlier owing to tumour burden or welfare concern. In this study the standard dose of aPDL1 administered was 100µg (all groups except 'no treatment' and '200µg aPDL1'). Cavitation-incompetent sonosensitive particles (SSPs) are denoted as 'iSSP'
b) Comparison of pre-intervention tumour volumes by ordinary one-way ANOVA with Tukey's multiple comparisons test (single pooled variance) with adjacent tabulation of mean and standard deviation by group

Treatment was initiated once the tumours were established so as to model cancer treatment in humans, in whom therapy is initiated only after tumour burden is established. 4-days following their first intervention, each mouse received a second, identical intervention, or no treatment in the case of no-treatment mice. Fixed acoustic pressures and parameters were utilized across all mice in this study. Acoustic parameters and the rationale underpinning their selection are also detailed in Chapter 2.

Cavitation was monitored in real-time by passive acoustic mapping (PAM) overlaid upon B-mode imaging (see Section 2.2.1). Due to a data storage error, PAM data recorded in this study was not readable and suitable for CC-G2 analysis. As a result, cavitation analysis was limited to CC-G1 analysis (Section 2.2.3). Mice were monitored at least every 2-3 days when tumours were palpable. 90 days was the experimental endpoint of the study, with mice sacrificed earlier in case of welfare concerns or tumour burden (Section 2.3).

3.1.2 Results

The total cavitation dose of the 1st intervention, as quantified by CC-G1 analysis was greater in tumours of mice receiving SSPs compared to those receiving iSSPs. Tumours in the SSP and iSSP groups were exposed to the same polymer cup concentration and the same US parameters, yet significantly ($p<0.01$) higher levels of cavitation were detected in the SSP group during the first intervention (Fig. 3.1c). Surprisingly, the integrated cavitation dose at the second intervention tended to be greater in SSP administered mice, however the difference was not statistically significantly different (Fig. 3.1c).

Average tumour growth, shown in Fig. 3.1d, reveals that mice in the aPDL1+SSP+US group consistently had the lowest average tumour volumes compared to all other study groups beginning on day 12. Average tumour growth curves are shown until day 17, which marks the

last measurement before study-enrolled mice were sacrificed. Ordinary two-way ANOVA with Tukey's multiple comparisons test to assess simple differences in mean tumour volume between intervention groups revealed a number of non-significant comparisons between groups (Appx. 3.1a). Notably, average tumour volume was significantly lower on days 16 ($p<0.001$) and 17 ($p<0.0001$) in mice that received 100µg of aPDL1+SSP+US compared to control mice not receiving treatment. Analysis revealed no other significant comparisons over days tested. In short, analysis of early tumour growth data suggests that paring aPDL1 with SSPs and US yields a more robust therapy.

Figure 3.1: Pilot Evaluation of aPDL1 +/- SSP +/- US (2/3)

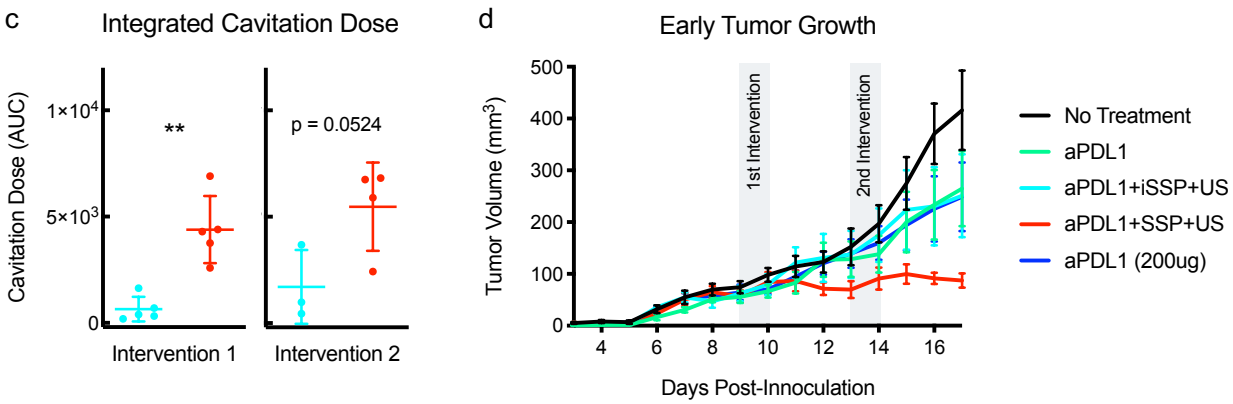


Figure 3.1 Continued
c) Comparison of CC-G1 calculated integrated cavitation dose at intervention 1 and 2 by unpaired t test
d) Early tumour growth curves. Lines connect the average of tumour volumes measured (by group) on a given day (mean and SEM shown). Different colours correspond to each of the groups

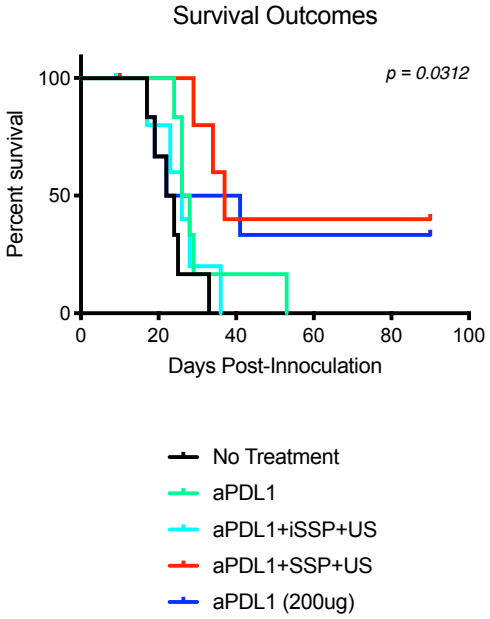
Survival data observed that there were highly significant differences among groups by log-rank (mantel-cox) testing ($p<0.05$). Median survival time was longest in mice administered the combination of aPDL1+SSP+US. Indeed, the 37 days achieved by aPDL1+SSP+US treatment compared favourably to the 23, 27, 26, and 31.5 days achieved with no treatment, aPDL1, aPDL1+iSSP+US, and aPDL1 (200µg) mice respectively (Fig. 3.1e).

Uncorrected, pairwise log-rank comparisons between groups revealed no significant pairwise differences between the outcomes of mice receiving aPDL1, aPDL1+iSSP+US, no treatment, or 200µg of aPDL1 (Fig. 3.1e). In contrast, mice receiving aPDL1+SSP+US had

significantly better survival outcomes compared to mice that received no treatment, aPDL1, or aPDL1+iSSP+US (Fig. 3.1e). At study termination, day 90 (d90), the experimental endpoint of the study, two mice in the aPDL1+SSP+US group were in fact completely tumour free.

Figure 3.1: Pilot Evaluation of aPDL1 +/- SSP +/- US (3/3)

e



Summary Outcomes

Group	Number Tumor-Free	Percent Tumor-Free	Median Survival (Days)
No Treatment	0/6	0%	23
aPDL1	0/6	0%	27
aPDL1+iSSP+US	0/5	0%	26
aPDL1+SSP+US	2/5	40%	37
aPDL1 (200ug)	2/6	33.3%	31.5

Uncorrected, Log-Rank Pairwise Comparisons

Comparison	P-Value	Symbol
No Treatment vs. aPDL1	0.1259	ns
No Treatment vs. aPDL1+iSSP+US	0.3458	ns
No Treatment vs. aPDL1+SSP+US	0.0042	**
No Treatment vs. aPDL1 (200ug)	0.1914	ns
aPDL1 vs. aPDL1+iSSP+US	0.4611	ns
aPDL1 vs. aPDL1+SSP+US	0.0444	*
aPDL1 vs. aPDL1 (200ug)	0.5256	ns
aPDL1+iSSP+US vs. aPDL1+SSP+US	0.0198	*
aPDL1+iSSP+US vs. aPDL1 (200ug)	0.2968	ns
aPDL1+SSP+US vs. aPDL1 (200ug)	0.6432	ns

Figure 3.1 Continued
e) Survival curves with log-rank (Mantel-Cox) testing of survival outcomes. Adjacent to the survival curves is a tabulation of key summary outcomes and a table of pairwise, uncorrected comparisons of survival outcomes between groups by log-rank (Mantel-Cox) testing. See Appx. 3.1b for plots of pairwise comparisons

Intriguingly, two mice in the aPDL1 (200µg) group were also tumour free at the end of the study, however, it is notable that the survival outcomes of this group as compared by log-rank pairwise testing were not significantly different compared to no treatment and other groups owing to a very similar pattern of early deaths of mice in this group and the early deaths found the 100µg aPDL1 drug-only and no treatment mice. Individual tumour growth curves are shown in Appx. 3.1c. No significant deviations in weight (rapid weight loss exceeding 20% or sustained weight loss exceeding 15%) were observed in any mouse.

3.1.3 Discussion

Limitations & Deviations

One mouse in the aPDL1+SSP+US group was sacrificed and censored owing to skin ulceration that was physically distal to the tumour capsule and likely unrelated to the tumour burden of the mouse. The ulceration's aetiology was likely off-target cavitation or other procedural error. Additionally, one mouse in the aPDL1+iSSP+US group was censored from the study due to a cannulation issue on its first day of intervention (i.e. it was unclear whether the majority of iSSP had been successfully injected). An experimental error occurred in this study, wherein one mouse in the 100μg aPDL1 group was dosed with 200μg instead of 100μg of aPDL1 on its 2nd intervention. Given that this mouse was in a control group and the error would be expected to improve outcomes, this mouse was not censored. Cavitation data could not be analysed for a few interventions owing to incomplete recording and/or storage error of the PAM data, an issue that was addressed in subsequent experiments.

Additionally, in this study to simplify the procedural workflow, all mice in a given group received consecutive interventions. In other words, on a given intervention day all aPDL1+US mice were treated consecutively, followed by all iSSP+US mice. This ordering, made organizing the procedures easier, but it may also introduce a bias, similar to that observed by Kelz et al. who observed that surgical outcomes (morbidity and mortality) were worse at later times of the day (though other factors could have also played a role) [Kelz et al. 2009]. Future studies should look to spread out intervention types with respect to time of day. Future work should consider including also 'cavitation only' and 'isotype antibody control' groups. Inclusion of these groups would enable assessment of the role the introduction of exogenous biologic protein (i.e. isotype antibody) can make to the mouse's tumour burden and help clarify what (if any) role cavitation alone can play in the impact of pairing cavitation with aPDL1. Although previous work by *BUBBL* with similar acoustic parameters suggests the therapeutic value of cavitation alone is

insignificant, it could be important to introduce a cavitation control group in future studies given the variations observed in cavitation response across mice. Furthermore, the immunological effect of intratumoural cavitation alone has not been previously assessed.

Implications

This study highlights that pairing aPDL1 with cavitation significantly improved drug efficacy over drug administration alone or with US and inactivated SSPs (iSSPs). Mice receiving aPDL1+SSP+US accumulated greater cavitation than mice receiving aPDL1+iSSP+US at both intervention one and two, though the comparison was only statistically significant at the 1st intervention. The observed cavitation of iSSP could be attributed to a manufacturing issue. Future work should consider inactivating the iSSPs immediately before injection. This could be accomplished by sonicating the iSSPs until they no longer cavitate prior to injection—a process that was not considered or conducted in this study.

Several key findings can be drawn from comparisons of groups evaluated in this study. Comparing between 100μg-dosed aPDL1 groups we observed that survival curves of mice administered aPDL1 and those administered aPDL1+iSSPs are very similar with nearly identical median survival times (27 and 26 days respectively). This demonstrates that the presence or absence of polymeric cups makes little impact on the efficacy outcomes, suggesting that polymeric cups alone do not alter the pharmacokinetics (PK) or pharmacodynamics (PD) of the antibody. This finding suggests the efficacy of aPDL1 + SSP (no US) control warrants no further investigation, reducing the number of groups and thereby reducing the complexity of the experiments and the number of mice needed in future studies.

The observation that outcomes with 100μg of aPDL1 improve when it is administered along with SSPs and US compared to aPDL1 alone, suggests that either ultrasound and/or SSPs or the combination thereof drives the improvement in therapeutic response achieved. Further clarifying whether cavitation was core to improving outcomes, the comparison of the outcomes in aPDL1+SSP+US treated mice to those treated with aPDL1+iSSP+US mice reveals

that ultrasound alone does not improve outcomes—as the aPDL1+iSSP+US did not do much better than mice administered aPDL1 alone. Although US is applied in both the aPDL1+SSP+US and aPDL1+iSSP+US groups, a differential response is observed only when SSPs are administered in tandem with US—mice administered aPDL1+SSP+US had greater AUC cavitation compared to those administered iSSP+US. Put simply, the greater level of cavitation in aPDL1+SSP+US mice vs. aPDL1+iSSP+US mice likely underpins the improved efficacy outcomes of aPDL1+SSP+US mice. In short, US and polymeric cups independently did not improve the efficacy of aPDL1, rather it is the presence of SSPs and US together (cavitation) which improves aPDL1 efficacy.

The outcomes of mice receiving 200μg of aPDL1 without ultrasound or SSPs, were also assessed in this study. Notably, the doubling of the systemic dose did not drive statistically meaningful improvements in survival outcomes compared to no treatment, whereas utilizing US-mediated cavitation to enhance drug delivery did provide a means of achieving improved efficacy. This observation is consistent with a hypothesis that a bottleneck in aPDL1 efficacy is not systemic drug concentration, but rather tumour-level drug transport barriers which can be addressed with cavitation. In other words, this work suggests that paring aPDL1 with cavitation is a better way to target and enhance local drug delivery over simply increasing the systemically administered dose. This observation has important implications because it could be very attractive means to lower cost by reducing the quantity of drug a patient needs to be administered. Furthermore, reducing systemic dose could be advantageous because although immunotherapy agents are generally well-tolerated as monotherapy regimens, the increasing use of these agents in combinatorial regimens where adverse events are more likely, could mean that lower systemic doses, enabled by cavitation, provide valuable safety benefits.

Summary & Implications for Next Steps:

aPDL1 alone dosed either at 100μg or 200μg did not provide statistically significant improvement in survival compared to no treatment in this CT26 tumour study. aPDL1 administered with SSPs and US significantly reduced tumour burden and extended survival of mice compared to mice administered the same dose of aPDL1 without cavitation. Survival curves were similar and median survival times nearly identical between mice administered aPDL1 and those administered aPDL1 with iSSPs and US. This suggests that neither the presence of polymeric particles nor the application of ultrasound alone provided therapeutic value.

Exploration of whether paring cavitation with other immunomodulatory agents will improve their efficacy is an important direction to further this work. It would be especially interesting to assess whether cavitation paired with aPD1 would enhance its efficacy. While both aPD1 and aPDL1 agents can block the same signalling pathway, these agents target complementary parts of the PD1/PDL1 interaction. aPDL1 is thought to block and target PDL1, a ligand which when expressed in the tumour microenvironment by immune cells and tumour cells is thought to drive T cell exhaustion [Tang & Zheng 2018]. In fact, the FDA has cleared or approved two companion diagnostic devices for the detection of tumoural PDL1 expression—i.e. intratumoural PDL1 expression informs clinical practice and patient management [FDA 2019]. aPD1 is mechanistically thought to act on T cells which can be found in systemic circulation but also within tumour microenvironments (TME) [Khalil et al 2016, Chen & Mellman 2013]. It would therefore be worthwhile to explore whether pairing cavitation with aPD1 improves aPD1 efficacy, as it would clarify the fundamental mechanism of action of aPD1 from an immunologic perspective, i.e. help answer the question is aPD1 co-localization within the TME important or does its function lie outside of the TME?

Although this study did control for the presence or absence of polymeric particles, it did not clarify the therapeutic value of cavitation alone. In other words, while it was clear that the

presence or absence of cavitation improved survival outcomes over no treatment, it is possible that the benefits observed are also simply the result of cavitation alone rather than the presence of aPDL1 with cavitation. Such query of cavitation alone given recent reports that other modalities of focused ultrasound including acoustic stress [Skalina et al. 2019], ablation [Han et al. 2019], vascular injury [Bulner et al 2019], and histotripsy [Eranki et al. 2019, Pahk et al. 2019] can bolster anti-tumour immunity. Future work could explore the role of cavitation alone by including a cavitation control group.

In this study, it is reasoned that the presence of aPDL1 and cavitation are important in driving responses. However, it remains unclear from this study whether the order of delivery of drug and instigation of cavitation impact on the success achieved. Future work could address the question of whether the temporal sequencing of the cavitation with respect to the drug administration is important to the therapeutic benefit of cavitation and aPDL1. Future work could address this question by administering cavitation before drug administration.

Additionally, in this study the no treatment group did not control for introduction of antibodies to treatment-group mice. The introduction of exogenous biologic material to these mice (i.e. antibody irrespective of its binding specificity) could have influenced their tumour growth, and general physiology. For example, the introduction of an exogenous antibody could result in non-specific immune activation which could act to benefit the therapeutic efficacy in a non-PDL1/PD1 related manner. To address this limitation, future work should introduce administration of IgG, nonspecific isotype-controlled antibodies administered with or without tumour targeted cavitation.

Lastly, owing to the observation that even 200μg of aPDL1 could not generate a significant efficacy improvement compared to no treatment, the question of whether paring cavitation with a higher systemic drug dose might also confer a benefit to the drug's efficacy, was raised.

3.2 PD1/PDL1 Axis Blockade with US-mediated Cavitation-Enhanced Delivery of Antibody-based Therapeutics

Previous work demonstrated that pairing aPDL1 antibody with tumour-targeted cavitation could significantly improve survival outcomes compared to the use of aPDL1 at the same dose without cavitation, in mice bearing CT26 tumours. To develop the work further four critical aims are addressed in this subsection:

1) defining the therapeutic value of cavitation alone
2) characterizing whether or not the sequence of drug administration and cavitation is important
3) examining whether pairing cavitation with PD1/PDL1 axis blockade works irrespective of particular biologic target along this pathway
4) assessing whether benefits conferred by pairing immunomodulation with cavitation exist even when drug dose more closely aligns with clinically administered drug doses schedules (a higher drug dose)

Therapeutic value of cavitation alone

Previous work identified that the sonication of cavitation-inactive polymeric particles did not significantly impact efficacy (3.1), however such work motivated interest in learning what the therapeutic value of cavitation alone might be. This is addressed here by the introduction of an IgG+SSP+US treatment group. Although ultrasound is able to create tissue-damage [Sheybani & Price 2019], in these previous studies ultrasound was applied with the intention to fractionate, thermally ablate, or generate vascular injury within the tissue. In the parameter space of this work, in the vein of work by Carlisle et al 2013 and Myers et al 2016, cavitation had little if any therapeutic value alone [Carlisle et al 2013 and Myers et al 2016]. For further detail regarding the parameters selected please see Section 2.2.2.

Temporal sequencing

Previously, drug and SSPs were administered consecutively followed by US. Doing so maximized the systemic drug dose in circulation at the time cavitation activity. This was thought to maximize the potential for cavitation to push and propel drug throughout the tumour microenvironment, as cavitation would be present as the drug was at its maximal systemic concentration. While our initial work suggests that this strategy holds therapeutic promise, it remains interesting to explore whether cavitation timing with respect to drug administration is tuneable factor of therapy success. In an extension of the previous experimental design, in this study groups are also included where drug is dosed only after cavitation is complete. These groups are intended to segregate the potential effect of transient or permanent tumour or vasculature permeation due to cavitation from cavitation-mediated drug transport by microstreaming.

Role of the specific checkpoint inhibitor used

In the first study of this chapter, the ability of US-mediated cavitation to enhance aPDL1 efficacy was queried. However, it remains unclear whether a similar benefit would be conferred by pairing aPD1 with US. Both aPD1 and aPDL1 target the same immunoregulatory PD1/PDL1 axis, albeit from opposite flanks. Unlike aPDL1 thought to bind tumour- and TME-expressed PDL1, aPD1's engagement with T cell expressed PD1 is thought to be mechanistically important to its function. Notably, T cells exist not only in TMEs but also within the systemic circulation. It is therefore less clear if pairing aPD1 with US-mediated cavitation may also enhance this agents efficacy. In this study, we extend our previous work and explore whether pairing aPD1 with US may improve the efficacy of this immunotherapeutic too.

Increasing systemic drug-dose

We sought to query what level of benefit adding cavitation to higher, more clinically aligned drug doses would provide. In the last study, no significant differences between the

survival outcomes between 100μg and 200μg aPDL1-dosed mice were observed (Fig. 3.1e), which suggests that limitations in drug efficacy, and perhaps those related to “last-mile” drug delivery cannot simply be overcome by increasing systemic drug dose. In other words, perhaps, cavitation could further improve the efficacy outcomes of mice, if the initial systemic drug-dose were to be doubled. Likewise, immunotherapeutic agents administered clinically are often administered at the pre-clinical equivalent of a 200μg dose (a ~10mg/kg human dose [Durvalumab label 2018, Avelumab label 2019] and still fail to create therapeutic value for the majority of patients [Collins & Gulley 2019]. Taken together, in this study it was desirable to increase the baseline drug-dose to 200μg of antibody per mouse for each group evaluated, in the hope of capturing even larger drug-device related benefits.

In summary, this experiment set out to query four aims: 1) understanding the therapeutic value of cavitation alone, 2) clarifying the importance of procedural sequence with respect to ultrasound and injectable (antibody and SSP) administration, 3) evaluating the target-agnostic or target-specific benefit of pairing cavitation with immunotherapy, and 4) appreciating benefits of pairing cavitation with clinically-equivalent, higher drug doses.

3.2.1 Experimental overview

BALB/c mice were inoculated in two batches with an injection of 5E5 CT26 tumour cells as per Section 2.3.3. This study pools together the data from two batches of 48 mice, yielding 96-study enrolled mice. Study personnel, injectables, CT26 cell line passage, and equipment were nearly identical between cohorts. Mice were assigned to one of eight intervention groups on a per-batch basis (n=6/group), to yield an overall group size of n=12/group overall. The outward appearance of the tumour was not a criterion of inclusion or exclusion from study enrolment.

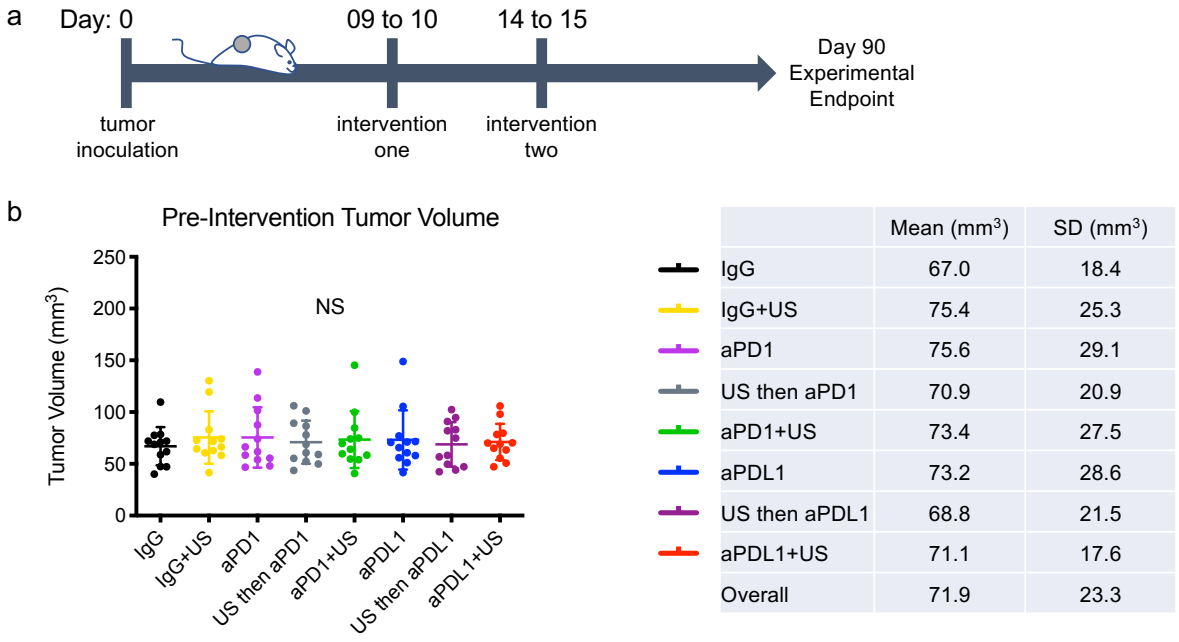
In order to comply with the 3Rs, cavitation inactive SSPs (iSSPs) were not explored further. Indeed, in the previous study, aPDL1+iSSP+US treated mice survived comparably to the aPDL1+SSP (no US) group in the last study, with nearly identical median survivals (Fig. 3.1e). Similarly, on the basis that administration of polymeric SSPs was shown to have no impact on survival outcomes, SSPs were administered to all study-enrolled mice irrespective of treatment or control group assignment. As such, in this study and all studies moving forward, SSPs are not explicitly stated in the treatment description.

To improve the robustness of the study, the ‘no-treatment group’, was replaced with a group of mice which received isotype antibodies (a mixture of 200μg of IgG2a and 200μg of IgG2b). The IgGs match the isotypes of therapeutic agents administered, wherein aPD1 is an IgG2a antibody, and aPDL1 is an IgG2b antibody. This change more appropriately controls for the fact that each mouse is injected with exogenous biologic material; the isotype antibodies are physically similar to the therapeutic antibodies, yet they lack target specificity.

On day of first intervention (9 or 10 days after tumour inoculation), mice were assigned to 1 of 8 groups (IgG, IgG+US, aPD1, US then aPD1, aPD1+US, aPDL1, US then aPDL1, or aPDL1+US). Pre-intervention tumour volumes were NS different between groups as confirmed by one-way ANOVA with Tukey multiple comparisons (Fig. 3.2b). Irrespective of assignment the

average overall tumour pre-intervention tumour volume was 71.9mm^3 with an SD of 23.3mm^3. Interventions were then repeated 5-days following the first intervention for each mouse. Each IgG control injection consisted of 200µg of IgG2a mixed with 200µg of IgG2b to control for the 200µg of aPD1 (an IgG2a antibody) or 200µg of aPDL1 (an IgG2b antibody) that was administered in the other intervention groups. In this study and all other studies unless otherwise noted, mice in every group were dosed SSPs at each intervention.

Figure 3.2: PD1/PDL1 Axis Blockade with US (1/4)



	Mean (mm^3)	SD (mm^3)
IgG	67.0	18.4
IgG+US	75.4	25.3
aPD1	75.6	29.1
US then aPD1	70.9	20.9
aPD1+US	73.4	27.5
aPDL1	73.2	28.6
US then aPDL1	68.8	21.5
aPDL1+US	71.1	17.6
Overall	71.9	23.3

Figure 3.2
a) Overview of experimental design. BALB/c mice were implanted with single CT26 tumours. 9 to 10 days later mice were assigned to 1 of 8 intervention groups. Each mouse received two identical interventions spaced 5 days apart. Mice were monitored to day 90 or sacrificed earlier owing to tumour burden or welfare concern. In this study and all other studies unless otherwise noted studies, mice in every group were dosed SSPs at each intervention
b) Comparison of pre-intervention tumour volumes by ordinary one-way ANOVA with Tukey's multiple comparisons test (single pooled variance); pre-intervention tumour volume mean and standard deviation are tabulated adjacent to the plot of tumour volumes

Fixed acoustic pressure and consistent acoustic parameters were utilized across all mice in this study as Section 2.2.2. Mice were monitored at least every 2-3 days and monitored to 90-days or sacrificed prior to the experimental endpoint owing to welfare/tumour burden (Section 2.3.3).

3.2.2 Results

The integrated cavitation dose, calculated by CC-G2 analysis (Section 2.2.3), showed no significant difference between US treated groups by one-way ANOVA with Tukey's multiple comparisons testing at the 1st and 2nd interventions (Fig. 3.2c & 3.2d). On intervention one the average integrated cavitation doses were 1.950e-006, 2.744e-006, 2.185e-006, 2.245e-006, and 2.332e-006 arbitrary units (AUC) with standard deviations of 1.091e-006, 1.529e-006, 1.648e-006, 1.646e-006, and 1.371e-006 for groups IgG+US, US then aPD1, aPD1+US, US then aPDL1, and aPDL1+US respectively. At intervention two, the average integrated cavitation doses were 1.310e-006, 1.794e-006, 1.678e-006, 2.259e-006, and 1.772e-006 AUC with an SDs of 6.618e-007, 9.340e-007, 1.054e-006, 1.010e-006, and 9.861e-007 AUC for groups IgG+US, US then aPD1, aPD1+US, US then aPDL1, and aPDL1+US respectively.

Figure 3.2: PD1/PDL1 Axis Blockade with US (2/4)

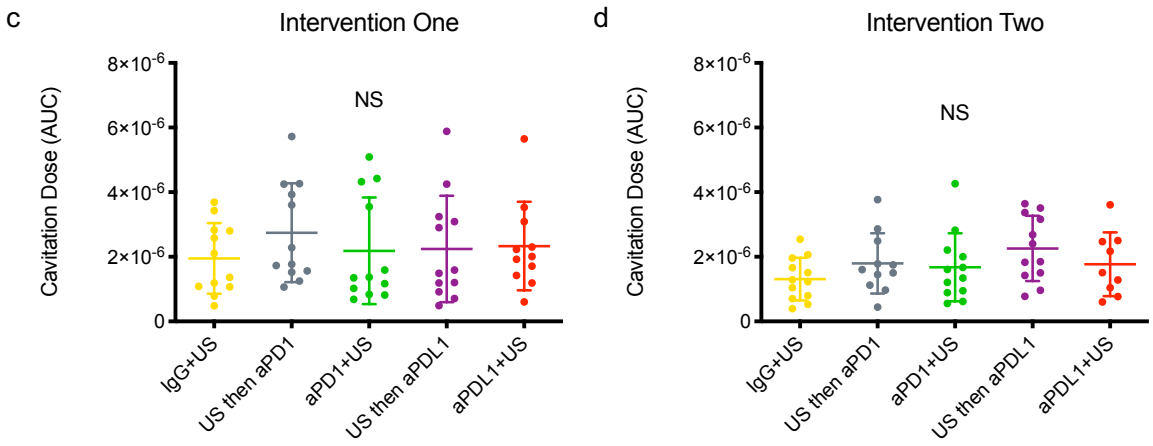


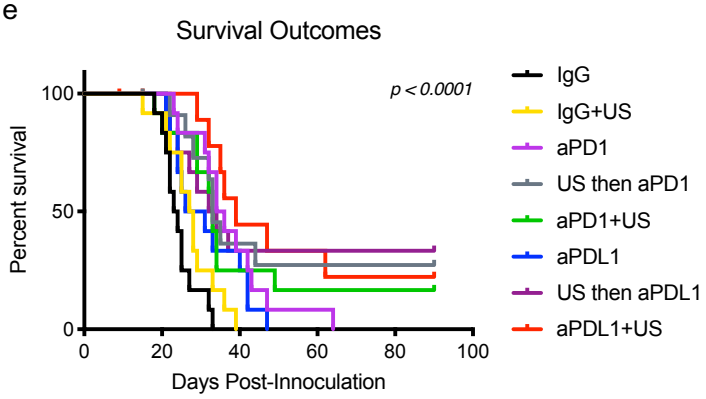
Figure 3.2 continued
c-d) The CC-G2 calculated integrated cavitation dose (AUC) for each group at each intervention. Differences between groups were assessed by ordinary one-way ANOVA with Tukey's multiple comparisons test (single pooled variance)

Average tumour burden is shown in Appx. 3.2a, however, statistical differences are not shown given the nature of data collected (i.e. only about half of the mice in each group were measured on a given day) in this study.

Log-rank (Mantel-Cox) analysis of survival outcomes, revealed highly significant differences between survival curves of groups evaluated in this study ($p<0.0001$). The median survival time of mice administered IgG+US was longer than that of mice dosed IgG alone (27.5 vs. 23.5 days), although log-rank (Mantel-Cox) pairwise testing revealed that difference was not statistically significant ($p=.098$) by uncorrected, pairwise comparison. Uncorrected, pairwise log-rank (Mantel-Cox) comparisons are tabulated in Fig. 3.2e and shown in Appx 3.2b.

Figure 3.2: PD1/PDL1 Axis Blockade with US (3/4)

e



Summary Outcomes

Group	# Tumor-Free	% Tumor-Free	Median Survival
IgG	0/12	0%	23.5
IgG+US	0/12	0%	27.5
aPD1	0/12	0%	35
US then aPD1	3/11	27.3%	33
aPD1+US	2/12	16.7%	33
aPDL1	0/12	0%	28.5
US then aPDL1	4/12	33.3%	33
aPDL1+US	2/9	22.2%	39

Uncorrected, Log-Rank Pairwise Comparisons

Comparison	P-Value	Symbol
IgG vs. IgG+US	0.098	ns
IgG vs. aPD1	0.0002	***
IgG vs. US then aPD1	0.0006	***
IgG vs. aPD1+US	0.0021	**
IgG vs. aPDL1	0.0245	*
IgG vs. US then aPDL1	0.0034	**
IgG vs. aPDL1+US	<0.0001	****
IgG+US vs. US then aPD1	0.0188	*
IgG+US vs. aPD1+US	0.0479	*
IgG+US vs. US then aPDL1	0.0451	*
IgG+US vs. aPDL1+US	0.0014	**
aPD1 vs. US then aPD1	0.3932	ns
aPD1 vs. aPD1+US	0.8504	ns
US then aPD1 vs. aPD1+US	0.6013	ns
aPDL1 vs. US then aPDL1	0.1601	ns
aPDL1 vs. aPDL1+US	0.0315	*
US then aPDL1 vs. aPDL1+US	0.742	ns

Figure 3.2 continued
e) Survival curves with log-rank (Mantel-Cox) testing of survival outcomes. Key summary outcomes are tabulated below the plot. Located adjacent to the plot is a table of pairwise, uncorrected comparisons of survival outcomes between meaningful groups by log-rank (Mantel-Cox) testing. See Appx. 3.2b for plots of pairwise comparisons

Uncorrected, pairwise comparison revealed all mice administered aPD1 (aPD1 alone, US then aPD1, or aPD1+US) lived significantly ($p<.01$) longer than IgG control mice, with median survival times of 35, 34, and 33 days respectively in aPD1 administered groups compared to 23.5 days in IgG control mice. Despite the similarity in median survival time and significance compared to IgG control across aPD1 administered mice, more mice were tumour free at the end of the 90-day period in the US then aPD1 group (33% tumour-free, 4 tumour free

mice) and aPD1+US (16.7% tumour-free, 2 tumour free mice) treated mice compared to mice that received aPD1 alone (0% cured, no tumour free mice). However, no significant difference was observed between the survival curves of any of the groups where aPD1 was dosed—i.e. the survival curves of aPD1 vs. US then aPD1 or aPD1+US were not significantly different.

Pairwise comparison of aPDL1 administered mice revealed that aPDL1 alone, US then aPDL1, and aPDL1+US treated mice showed significantly enhanced survival compared to IgG mice, with uncorrected p-values of $p<.05$, $p<.01$, and $p<0.0001$ respectively. The extensions in median survival time (28.5, 33, and 39 days) paralleled the pattern of increasing statistical significance of pairwise comparisons of IgG to aPDL1 alone, IgG vs US then aPDL1, or IgG vs aPDL1+US ($p<.05$, $p<.01$, $p<.0001$ respectively). Whereas no mice were tumour free in the aPDL1 or US then aPDL1 groups, 22.2% of mice were tumour free in the aPDL1+US group (2 tumour-free mice). A comparison of survival curves within aPDL1 administered groups revealed NS between the survival curves of aPDL1 vs. US then aPDL1 administered mice, however the difference between aPDL1 and aPDL1+US treated mice was statistically significant ($p<0.05$).

Subgroup analyses of study outcomes, where the survival curves are shown and analysed without inclusion of the US then aPD1 and US then aPDL1 groups are shown Fig. 3.2f. Subsets of Fig. 3.2f are shown in Fig. 3.2g-i, where survival curves are shown on an agent specific basis (IgG, aPD1, or aPDL1) along with the IgG control. Tumour growth curves of study-enrolled mice are shown in Appx. 3.2c.

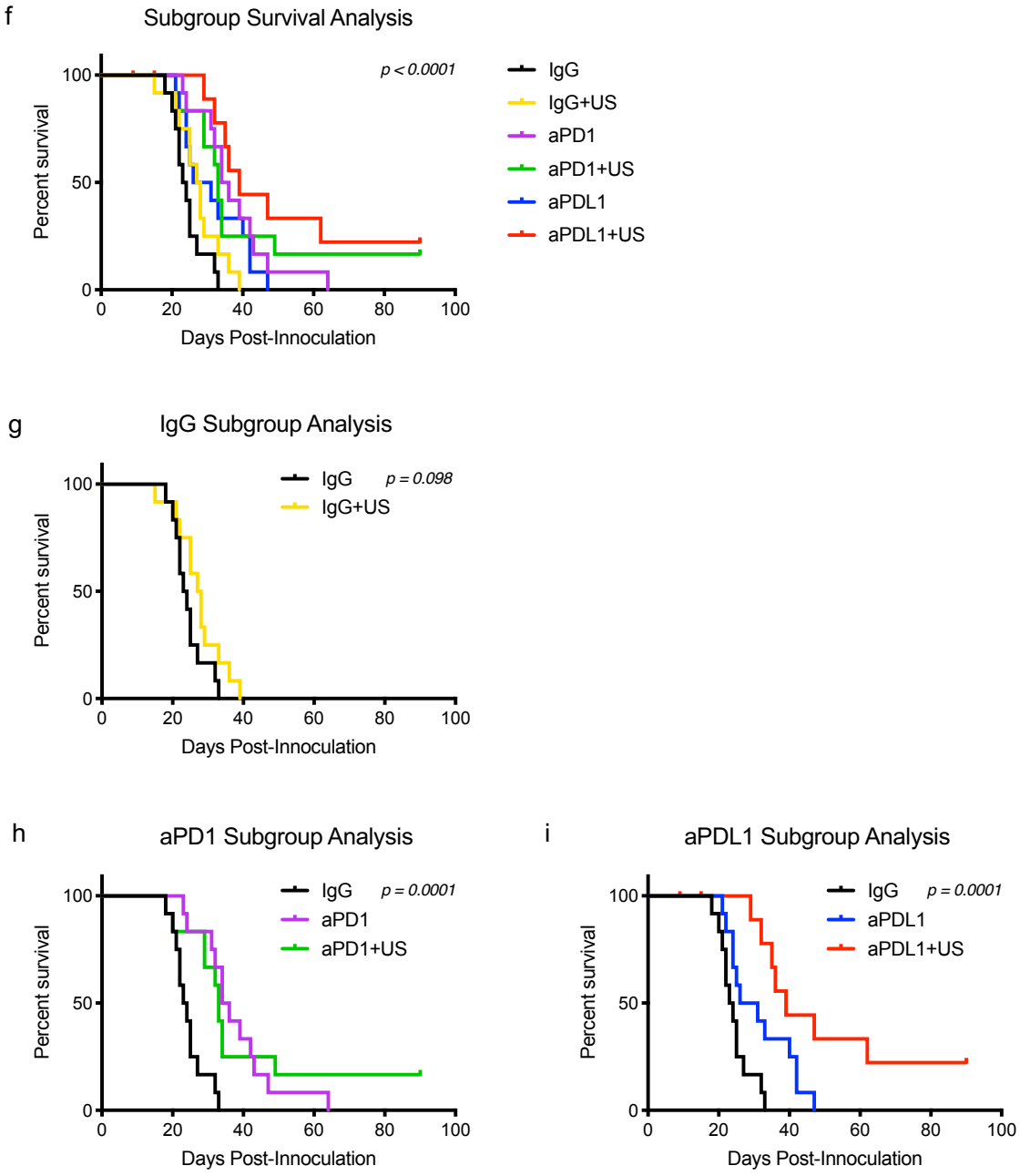


Figure 3.2 continued
f) Subgroup analysis of survival outcomes (cavitation before drug-injection groups omitted), assessed by log-rank Mantel-Cox testing
g-i) Subsets of (f) are shown in g (IgG groups), h (aPD1 groups), and i (aPDL1 groups). Significance (uncorrected) calculated by log-rank (Mantel-Cox) testing.

3.2.3 Discussion

Limitations

In this is study four mice were censored owing to procedural complications related to *i.v.* injection, acoustic parameter mismatch, and an off-target US bioeffect. One of these procedural complications involved failure to recover post-anaesthesia, one involved failure to thrive post-recovery (despite total tumour regression), and one mouse was excluded after the second dosing due to uncertainty over the dose injected. A fourth mouse was censored because of an error made in the ultrasound exposure. Specifically, the mouse was exposed for the first 150s at 10,000 cycles per pulse instead of the intended 50,000 cycles per pulse. Taken together although 4 serious deviations occurred, when we consider that over 192 procedures took place, this represents an error rate of less than 2.1%. Unfortunately, three of those mice came from the same group, aPDL1+US. The fact that so many censorship events happened in the same group is problematic because it decreases the study power. For further detail regarding censorship criteria utilized, including a review of minor deviations that were deemed unlikely to impact study outcomes, please refer to Section: 2.4.1.

Implications

This study sought to address four key aims, in brief understanding 1) the therapeutic value of cavitation alone, 2) the importance of the sequence in which drug and cavitation is delivered, 3) the capability of cavitation to enhance not only aPDL1 efficacy but also aPD1 efficacy, and 4) the impact of the approach at clinically-aligned drug-doses.

Findings indicate that cavitation alone provides minor therapeutic value as IgG+US treated mice had an only marginally increased median survival time that did not translate into significantly improved survival outcomes compared to mice treated with IgG alone. The data therefore suggests that cavitation alone (IgG+US) may play a small role in the benefits conferred by pairing cavitation with immunomodulation. This observation is consistent with

previous which showed that similar acoustic parameters & cavitation nuclei in mice do not generate appreciable levels of tissue damage that have a measurable impact on survival [Carlisle et. al 2013 and Myers et. al 2016].

Attempts to address the question as to whether drug needs to be present while cavitation is taking place or whether the benefits of cavitation are evident even if drug is administered after cavitation is triggered, could not be clearly addressed in this study. Within aPDL1 groups, US then aPDL1 was not significantly better than aPDL1, but aPDL1 dosing timed with immediately sequential US targeting (aPDL1+US) did significantly improve survival outcomes compared to aPDL1 alone. Mice dosed with aPDL1 alone survived an average of 28.5 days, US then aPDL1 33 days, and aPDL1+US 39 days. Likewise, pairwise survival comparisons aPDL1 groups to IgG control became increasingly significant going from aPDL1 ($p<.05$) to US then aPDL1 ($p<0.01$), to aPDL1+US ($p<0.0001$). Although the survival data suggests that aPDL1+US is more effective than US then aPDL1, the direct comparison between these two groups was not statistically significant (likewise, statistically differential survival outcomes between US then aPD1 v. aPD1+US treatments were not observed, Fig. 3.2e). Taken together the ability of cavitation to generate lasting, non-transient improvements in drug delivery that delay tumour growth or drive tumour regression appear unlikely.

However, it is important to consider that the study perhaps was confounded by the long-circulation time of antibody drugs—a problem, considering that mice in the US then aPDL1 and US then aPD1 groups may have had a significant quantity of antibody present in their circulation prior to the instigation of cavitation during the 2nd intervention. Particularly relevant is work by Deng et. al who dosed mice with aPDL1 at a concentration of (10mg/kg) *i.v.* and showed that approximately 1/3^{rd*} of the injected dose remains in systemic circulation 5-days post-injection (*estimated from Figure 1 of the paper) [Deng et al 2016]. Although the intention was to interrogate the relationship between temporal sequencing of drug administration and cavitation, by the 2nd intervention/dosing of drug it is likely that too much drug was present in systemic

circulation from the 1st dosing to cleanly separate out the effects of drug being present while there is intratumoural cavitation and drug being present only after cavitation has been generated. Put simply, the US then aPDL1 or US then aPD1 groups as assessed in this study may not have enabled a true delineation of whether or not simultaneous presence of cavitation and drug was important or whether the two effects were independent of each other.

Given that the US then aPD1 or US then aPDL1 were unable to discern the temporal or non-temporal benefit to pairing cavitation with drug delivery, survival curves were re-rendered removing the US then aPD1 and US then aPDL1 groups. This subgroup analysis is shown in Figures 3.2f-i.

This study inadvertently also provided interesting insight with regard to the behaviour of SSPs. Notably, the levels of cavitation between mice administered SSP+US then drug were comparable to those that received, drug+SSP+US. There was a potential worry that SSPs can aggregate in charged solutions—like the PBS buffer the antibodies are suspended in. Although in drug+SSP+US groups drug and SSPs are not pre-mixed, there was a concern that mixing within the intravenous line could have diminished SSP-activity. Fortunately, in this study, no significant increase in cavitation was observed in mice that received cavitation first followed by drug injection cavitation vs. those that received drug and SSPs consecutively, indicating that this concern was unfounded.

Lastly, this study sought to query whether pairing cavitation with PD1/PDL1 axis inhibition on either side of the cascade would offer similar or dissimilar improvements to drug function. The data here suggests that pairing aPDL1 with US-mediated cavitation significantly improves efficacy outcomes over aPDL1 alone, however, a similar significant benefit was not observed for aPD1 (Fig. 3.2h-i). However, it is worthwhile to note that 27.3% and 16.7% of study-enrolled mice were tumour free at study termination in US then aPD1 and aPD1+US groups, warranting further consideration & testing (Fig. 3.2e). In contrast, in this study, as in the pilot study (3.1), pairing aPDL1 with US did favourably compare to aPDL1 alone (Fig. 3.2i). This

discrepancy in outcomes, could be explained by inadequate or excessive cavitation (perhaps aPD1 requires greater or lesser cavitation than aPDL1). Alternatively, the differential targets of the antibodies with respect to their physical place of binding, could be a contributing factor: In brief review here, aPDL1 targets PDL1, the expression of which has been shown to be predominately within the tumour and tumour microenvironment, whereas aPD1 targets PD-1, a marker predominately expressed by T cells [Khalil et al. 2016]. Unlike PDL1 which likely must be intratumorally accessed, T cells are not necessarily confined to TME. For example, T cells circulate in blood and in fact aPD1 has been shown to bind T cells with 98% receptor occupancy in peripheral blood after drug injection [Pluim et al 2019]. The results of this survival study suggest that some sort of a barrier is unlocked by pairing cavitation with aPDL1.

Key next steps:

Consistent with previous work, we observed that pairing cavitation with aPDL1, even when administered at a higher, more clinically aligned dose, improved the drug's efficacy compared to drug alone. Notably, the same US-mediated cavitation strategy did not significantly improve aPD1 efficacy compared to drug alone, an observation worth further investigation/confirmation. We also observed in this study that cavitation alone had a limited therapeutic value. Critical future survival study work should aim to corroborate the observations made in this study with greater statistical power and significance.

3.3 Impact of Inertial Cavitation Dose on aPDL1 Efficacy Enhancement

3.1 and 3.2 demonstrated that cavitation levels achieved during treatment could be measured and quantified. To confirm our observation that pairing a 200µg dose of aPDL1 with cavitation (aPDL1+US) improves drug efficacy compared to drug alone, a study was performed with 200µg IgG2b (n=9), 200µg aPDL1 (n=11), and 200µg aPDL1+US groups (n=11 per group), as shown in Fig. 3.3a. Pre-intervention tumour volumes were not significantly different between groups (Fig. 3.3b). The integrated cavitation doses were remarkably lower than expected. On the first intervention, the average integrated cavitation dose was 1.575e-006 AUC with an SD of 1.024e-006 as calculated by CC-G2 analysis. At the second intervention, the average integrated cavitation dose was 7.524e-007 AUC with an SD of 4.073e-007, calculated by CC-G2 analysis (Fig. 3.3c).

Figure 3.3: Impact of Inertial Cavitation Dose to aPDL1 Efficacy Enhancement (1/3)

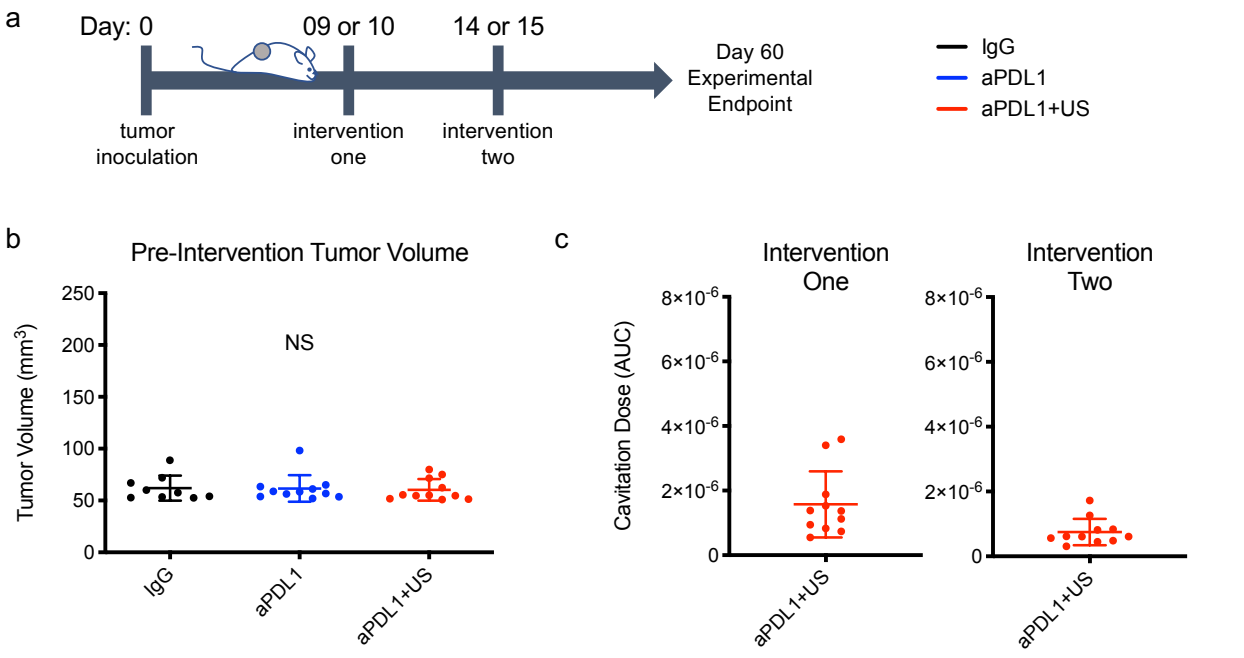
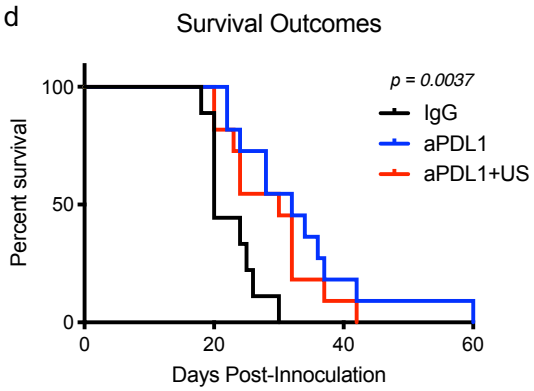


Figure 3.3
a) Illustrative representation of experiment. BALB/c mice were assigned to 1 of 3 intervention groups 9 or 10 days after implantation of CT26 cells. Mice not suitable for US treatment were assigned to the IgG control group (n=9) and mice ideal for US (i.e. those with more a more uniform, spherical/ellipsoid shape), were assigned to either aPDL1 or aPDL1+US groups (n=11 each)
b) Pre-intervention tumour volumes assessed by ordinary one-way ANOVA with Tukey's multiple comparisons testing (single pooled variance). Mean and SD shown; pre-intervention volume statistics tabulated in Appx. 3.3a
c) The CC-G2 calculated integrated cavitation dose (AUC) for intervention 1 and 2

Despite efforts to match equipment consumables and personnel, the levels of cavitation achieved in this study (Fig. 3.3c) were much lower than those of Fig. 3.2c-d and perhaps as a consequence, no efficacy benefit was observed between aPDL1 and aPDL1+US treatment (Fig. 3.3d). Average tumour growth by group and individual mouse tumour growth curves are shown in Appx. 3.3b-c.

Figure 3.3: Impact of Inertial Cavitation Dose to aPDL1 Efficacy Enhancement (2/3)

d



Uncorrected, Pairwise Log-Rank Comparisons

Comparison	P-Value	Symbol
IgG v. aPDL1	0.0019	**
IgG v. aPDL1+US	0.0187	*
aPDL1 v. aPDL1+US	0.3501	ns

Summary Outcomes

Group	# Tumor-Free	Median Survival
IgG	0/9	20
aPDL1	0/11	32
aPDL1+US	0/11	30

Figure 3.3 continued
d) Survival analysis by log-rank (Mantel-Cox) testing with adjacent tabulation of key summary outcomes and uncorrected, pairwise log-rank (Mantel-Cox) testing results

A calculation of the average integrated dose across both interventions any given mouse received (excluding mice where CC-G2 analysis could not be completed for both interventions), observed that the average integrated cavitation dose in this study, shown in Fig. 3.3e, were significantly ($p<0.01$) lower than those of Fig. 3.2, a mean of 1.165e-006 AUC vs. 2.007e-006 AUC. Further analysis was performed whereby cavitation was assessed with relation to the duration it occurred at levels above a given threshold (i.e. ‘persistence’ metric). Specifically, ‘persistence’ refers to the fraction of sonication time (ranging from 0 to 1) that the cavitation exceeded a threshold designated as useful. A comparison of average persistence calculated on a per-mouse basis revealed a highly significant ($p<0.01$) decrease in the persistence of cavitation in mice in this study compared to previous work (9.2% vs. 2.8% of sonication time) (Fig. 3.3f).

Figure 3.3: Impact of Inertial Cavitation Dose to aPDL1 Efficacy Enhancement (3/3)

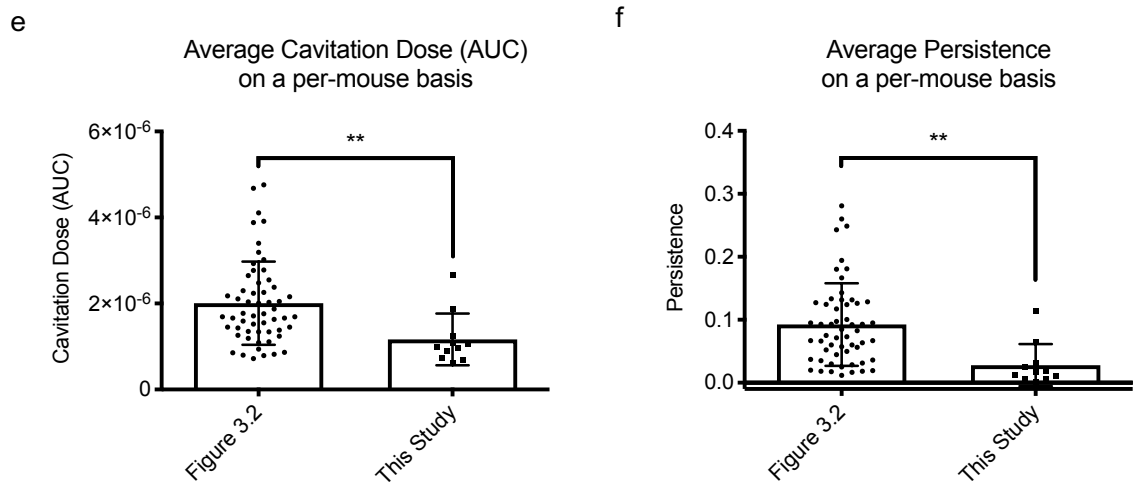


Figure 3.3 continued
g) The average integrated cavitation dose (AUC), as calculated by taking the average of intervention one and intervention two integrated cavitation dose (AUC) on a per mouse basis. An unpaired t test comparing the average integrated cavitation dose of mice in this study compared to mice in receipt of US & cavitation of Figure 3.2 reveals a highly significant ($p<0.01$) drop in the cavitation dose (AUC)
h) Persistence, a metric referring to the fraction of sonication time (ranging from 0 to 1) that the cavitation exceeded a designated level as useful, was calculated for each mouse at each intervention. The average of these two interventions was then calculated on a per mouse basis. Unpaired t test comparison of persistence values from this study compared to mice of Fig. 3.2 reveals highly significant differences in the persistence between the two studies ($p<0.01$)

A parallel survival study with aPD1 also yielded low-cavitation levels, averaging 1.053e-006 AUC with an SD of 6.014e-007 AUC as per CC-G2 analysis of cavitation-treated mice. This study evaluated IgG2a, aPD1, aPD1+US, and US then aPD1 (200μg drug per dose, n=6/group) in follow-up of the interesting, but statistically insignificant finding that US then aPD1 works best out of these three therapies, with a 27.6% cure-rate. The results of this study seemed to conflict with those of Fig. 3.2, suggesting aPD1+US works best out of the three (though again insignificantly in terms of survival). The findings were likely stochastic, but more importantly, given the sub-threshold cavitation levels they cannot be used to conclusively confirm the observations of Fig. 3.2, which, like here, found that there was no statistically meaningful benefit in paring aPD1 with cavitation.

While it remains unclear exactly why lower cavitation was registered in these experiments, it reinforced the importance of generating and monitoring sufficient cavitation

intratumorally. Hence, although these results provided negative therapy data it motivated a shift in sonication strategy, whereby instead of exposing tumours at a fixed pressure, PAM feedback was incorporated in real time to adjust pressure within a range allowing for cavitation to be sustained within a range of 10-20 arbitrary power units (APU) throughout the duration of exposure (see Section 2.2.2).

3.4 Feedback-Optimized, Cavitation-Mediated Drug Delivery

Previous studies highlighted the role that cavitation dose and persistence can play in dictating the outcomes of pairing immunotherapy with ultrasound-mediated drug delivery. In all previous studies, the incident acoustic pressure was kept constant during treatment, yielding variable instant and cumulative levels of cavitation activity as monitored in real-time by passive acoustic mapping (PAM). In the present study, to improve the consistency of cavitation activity, continuous adjustment of the acoustic pressure within a range of 1.5 to 2.1 MPa was used to maintain the real-time PAM signal to between 0-20 arbitrary power units (APU), so as to yield a cumulative cavitation dose of at least of 2e-006 AUC, which was found to be effective across the three previous studies. The groups in the present study included IgG+US, aPD1+US, or aDPL1+US and were compared to controls receiving IgGs, aPD1, or aPDL1 alone.

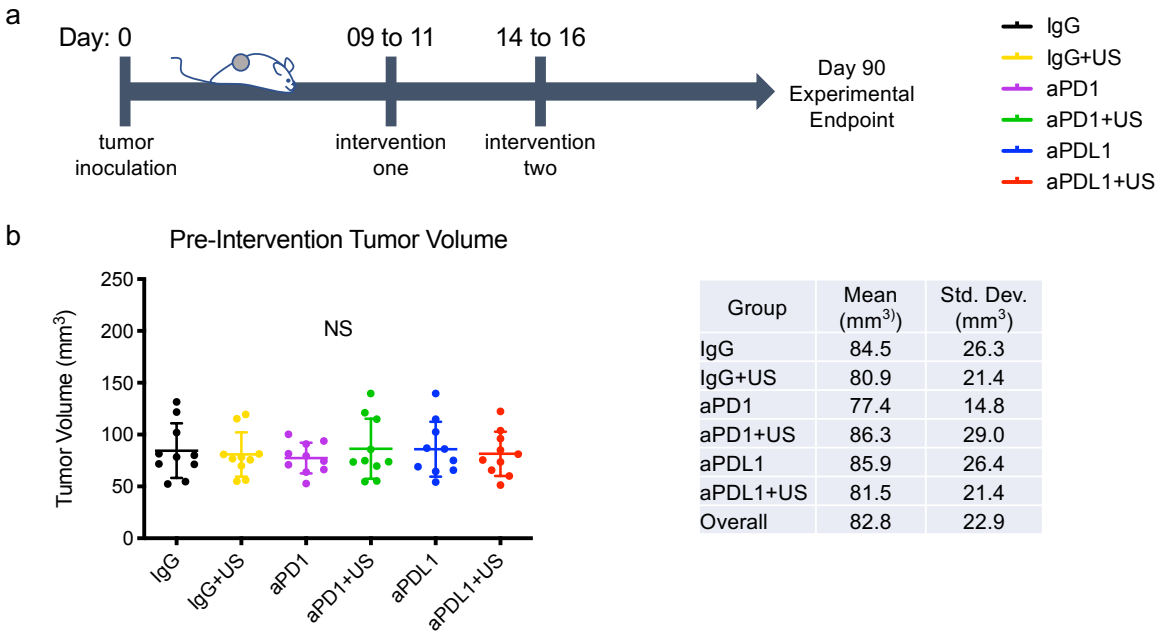
New acoustic strategy in hand, pairing this cavitation-optimized strategy with PD1/PDL1 axis blockade was deployed to assess whether efficacy benefits could be realized by pairing drug with cavitation. Although in previous work it was demonstrated that IgG+US is conferring NS differences in survival compared to IgG alone, owing to the change in acoustic strategy of this study, an IgG+US control was also evaluated.

3.4.1 Experimental Overview

As previous, Balb/c mice were inoculated with single CT26 tumours, and assigned to 1 of 6 interventions (IgGs, IgGs+US, aPD1, aPD1+US, aPDL1, aPDL1+US), Fig. 3.4a. One-way ANOVA with Tukey's multiple comparisons revealed no significant differences between pre-intervention tumour volumes (Fig. 3.4b). Irrespective of assignment the mean tumour volume was 82.8mm^3 with a standard deviation of 22.9mm^3. Pre-intervention tumour volumes ranged from a minimum of 51.3mm^3 to a maximum of 139.7mm^3 with median of 77.5mm^3. See Section 2.3 and 2.4 for additional detail. aPD1 and aPDL1 were dosed at 200μg per mouse. IgG dose

consisted of a mixture of 200µg of IgG2a and 200µg of IgG2b. Five days after first intervention, mice received a second, identical intervention. Mice were monitored at least every 2-3 days and were survived to 90 days unless they were sacrificed earlier owing to welfare concern or tumour burden (Fig. 3.4a).

Figure 3.4: Feedback-Optimized, Cavitation-Mediated Drug Delivery (1/4)



Group	Mean ($mm^{3)}$)	Std. Dev. (mm^3)
IgG	84.5	26.3
IgG+US	80.9	21.4
aPD1	77.4	14.8
aPD1+US	86.3	29.0
aPDL1	85.9	26.4
aPDL1+US	81.5	21.4
Overall	82.8	22.9

Figure 3.4:
a) BALB/c mice were assigned to 1 of 6 intervention groups (n=10/group) 9, 10, or 11 days after CT26 tumour cell implantation and monitored to 90 days (or sacrificed earlier owing to tumour burden or welfare concern)
b) Comparison of pre-intervention tumour volumes by one-way ANOVA with Tukey's multiple comparisons testing (single pooled variance). *Adjacent the plot is a tabulation of mean and standard deviations of pre-intervention tumour volumes*

3.4.2 Results

The integrated cavitation dose, calculated by CC-G2 analysis and analysed by one-way ANOVA with Tukey's multiple comparisons test identified no significant difference in the integrated cavitation dose between groups on the 1st day of intervention (Fig. 3.4c), confirming that the real-time cavitation control strategy had been successful in eliminating both variability and sub-threshold generation of cavitation. At the 1st intervention, the mean integrated cavitation doses per group was 3.497e-006, 3.079e-006, and 4.147e-006 AUC for IgG+US, aPD1+US,

and aPDL1+US mice with standard deviations of 1.190e-006, 1.471e-006, and 9.970e-007 AUC respectively. These cavitation dose figures are substantially raised compared to the previous unsuccessful experiment of Section 3.3 and comparable to the therapeutically successful interventions of Sections 3.1 and 3.2.

On the 2nd set of interventions, the CC-G2 calculated, average integrated cavitation doses were 6.017e-006, 2.758e-006, and 3.783e-006 AUC with standard deviations of 2.453e-006, 9.352e-007, and 2.078e-006 AUC for IgG+US, aPD1+US, and aPDL1+US mice respectively. Of note, the integrated cavitation dose of aPD1+US mice was significantly lower ($p<.01$) than that of IgG+US treated mice at the time of the 2nd intervention, as detected by one-way ANOVA with Tukey's multiple comparisons (Fig. 3.4d). No other significant differences of integrated cavitation dose between groups were detected for other pairwise comparisons.

Figure 3.4: Feedback-Optimized, Cavitation-Mediated Drug Delivery (2/4)

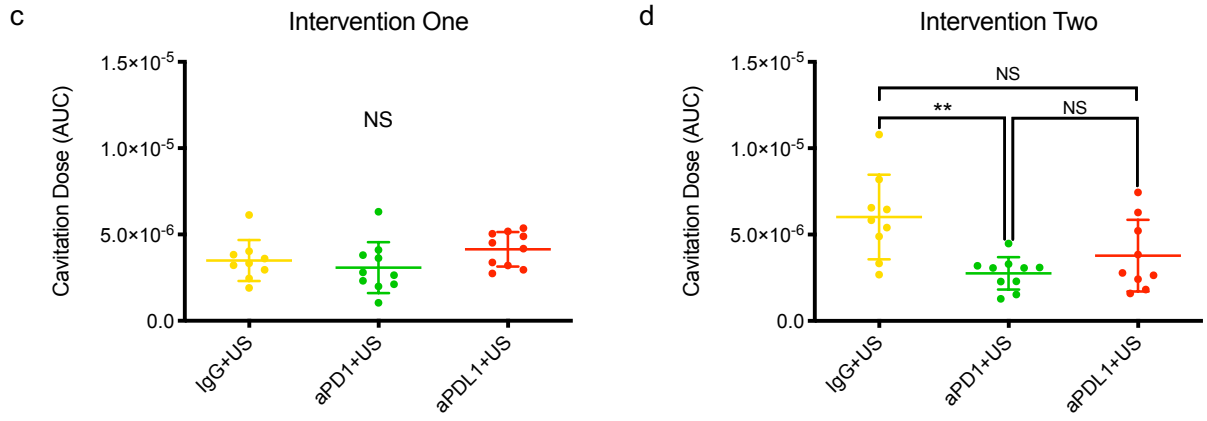


Figure 3.4 continued
c-d) The CC-G2-calculated integrated cavitation dose for each group at each intervention. Differences between groups assessed by ordinary one-way ANOVA with Tukey's multiple comparison test (single pooled variance)

Average tumour volumes measured on even days on a per group basis are shown in Fig. 3.4e. Differences in tumour volumes on even days from day 12 to day 20 were assessed by two-way ANOVA with Tukey multiple comparisons testing. On day 18 there was a significant decrease in the average tumour volume of aPDL1+US mice compared to IgG control mice, however, no other significant differences were observed on day 18 (Appx. 3.4a). On day 20,

significant decreases in average tumour volume of IgG+US, aPD1+US, and aPDL1+US treated mice compared to IgG treated mice were observed (see Appx. 3.4a for other comparisons).

Figure 3.4: Feedback-Optimized, Cavitation-Mediated Drug Delivery (3/4)

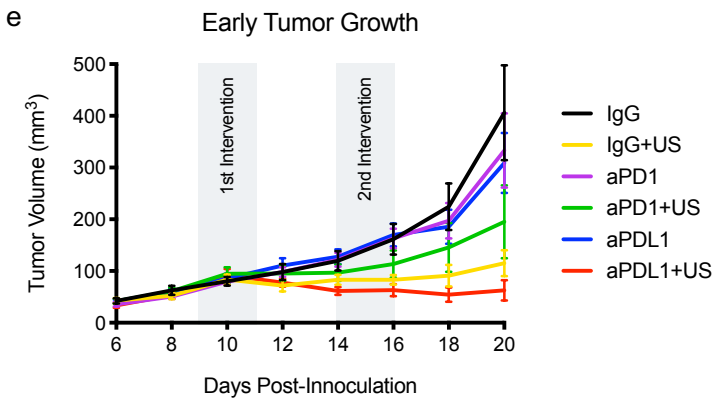


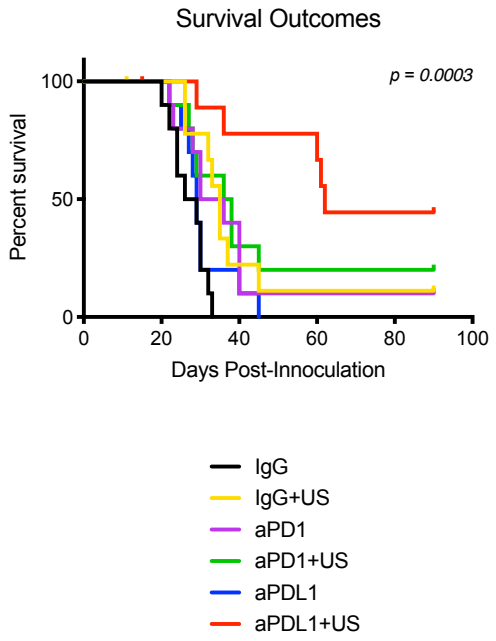
Figure 3.4 continued
e) Early tumour growth curves of mice (mean and SEM) constructed using measurements collected on even-days. Lines connect the average of tumour volumes measured (by group) on a given day (mean and SEM shown). Different colours correspond to each of the groups

Log-rank (Mantel-Cox) testing across all groups revealed highly significant differences in the survival curves ($p = 0.0003$) (Fig. 3.4f). Uncorrected, pairwise analysis of the survival data confirmed several striking observations. Notably, the combination of aPDL1 with cavitation abrogated tumour growth and doubled the median survival time (62 vs. 29 days) compared to aPDL1 without US, with uncorrected, pairwise log-rank (Mantel-Cox) revealing a highly significant ($p<.001$) difference in survival between the two groups (Fig. 3.4f). Pairwise log-rank comparison of aPDL1+US to IgG+US mice revealed a significant ($p<0.05$) increase in survival, including a marked extension of median survival from 35 to 62 days. Notably, around day 36 the majority of mice (7 of 9, 77%) of aPDL1+US treated mice had no apparent tumour burden. However, tumours in three of these mice subsequently returned, necessitating humane sacrifice owing to tumour burden around 60 days post-inoculation. Regardless, the benefit conferred by pairing aPDL1 with cavitation was striking, with 44% mice tumour-free in the aPDL1+US group compared to no tumour-mice in the aPDL1 treatment group (Fig. 3.4f).

In contrast to the results of aPDL1 paired with US, pairwise log-rank comparison of aPD1 vs. aPD1+US did not reveal a significant improvement in survival (p = 0.7198), with median survival times of 33 and 37 days respectively. Similarly, pairwise, log-rank comparison of survival between IgG+US and aPD1+US was not significant with median survivals of 35 vs. 37 days respectively. Intriguingly, log-rank pairwise comparison of IgG vs. IgG+US revealed a small (27.5 vs. 35 days) but significant (p <0.01) median survival benefit. (Fig. 3.4f).

Figure 3.4: Feedback-Optimized, Cavitation-Mediated Drug Delivery (4/4)

f



Summary Outcomes

Group	# Tumor-Free	% Tumor-Free	Median Survival (Days)
IgG	0/10	0%	27.5
IgG+US	1/9	11.1%	35
aPD1	1/10	10%	33
aPD1+US	2/10	20%	37
aPDL1	0/10	0%	29
aPDL1+US	4/9	44.4%	62

Uncorrected, pairwise log-rank comparisons

Comparison	P-Value	Symbol
IgG v. IgG+US	0.0028	**
IgG v. aPD1	0.0263	*
IgG v. aPD1+US	0.0112	*
IgG v. aPDL1	0.3594	ns
IgG v. aPDL1+US	<0.0001	****
IgG+US v. aPD1+US	0.5621	ns
IgG+US v. aPDL1+US	0.0228	*
aPD1 v. aPD1+US	0.7198	ns
aPDL1 v. aPDL1+US	0.0003	***

Figure 3.4 Continued:
f) Survival analysis by log-rank (Mantel-Cox) testing with adjacent tabulation of key summary outcomes and uncorrected, pairwise log-rank (Mantel-Cox) testing results. Uncorrected, pairwise survival curve comparisons are shown in Appx. 3.4b.

3.4.3 Discussion

Consistent with results of Figure 3.2, pairing aPDL1 with US enhanced the efficacy of the aPDL1. Curiously, pairing cavitation with aPD1 did not provide a significant nor meaningful

increase in median survival time. Future work leveraging this finding may help guide future work that explores how these two very similar drugs face different similar or dissimilar limitations in patients. Surprisingly, although both PD1 and PDL1 targeting agents are FDA approved, fundamental mechanistic questions regarding these drugs are still unclear [Munn et al. 2019, Duan et al. 2019].

Limitations:

Of note, two mice were censored in this study owing to ambulation issues as a result of procedural complications unrelated to drug or cavitation. In this study, no mice were culled owing to tumour ulceration, however, it is worthwhile to note that the majority of mice on day of assignment had small lesions that were uncovered after hair was removed (days 9-11). Consistent sacrifice criteria were utilized throughout this study to carefully ensure animal welfare and uphold ethical rationale per supervisor guidance.

Tumour Regrowth & Resistance

One intriguing observation from this work, was the number of mice in the aPDL1+US treatment arm that appeared to be tumour free but suffered tumour re-growth at a later time-point. Notably, no tumour burden was apparent in 7 of 9 mice around day 36, however palpable tumours later developed in 3 of the mice, ultimately requiring their sacrifice. This observation suggests that tumour resistance to therapy may develop via immune escape through an immunoediting mechanism—several mechanisms have been reported. For example, loss-of-function JAK1/2 mutations can enable PD-1 blockade resistance [Shin et al. 2017, Zaretsky et al. 2016]. Others, have also suggested that the interferon-gamma pathway plays a critical role in driving epigenomic changes that drive resistance to PD1 blockade [Benci et al. 2016]. In short, the observation that tumours regressed then re-grew suggests that aPDL1 worked as intended yet failed to drive a curable response owing resistance pathways not addressed by the therapeutic.

It is suspected that the tumours' regrowth represents resistance given they grew approximately where the originally planted tumours were; this suggests that the tumours were not of a primary (*de novo*) origin. The presence of resistance to therapy is not surprising given that it is not suspected that cavitation fundamentally changes the drug mechanism. Just as Myers et. al reported that cavitation does not decrease the activity of antibody drugs, it likely does not favourably alter drug structure [Myers et al 2018]. Put simply, it is suspected that cavitation improves drug delivery—playing no role in altering drug mechanism or addressing genetic drug-resistance programs that might emerge as a consequence of drug. However, there is a possibility that cavitation per-se does alter the local immune environment of the tumour, an aspect which is explored in depth in Chapter 5. In summary, the observed regression and regrowth observed in aPDL1+US treatment, warrants future investigation of strategies to combine with aPDL1+US therapy suitable to address resistance mechanisms.

Therapeutic value of cavitation alone:

The survival difference and the observed consistent, significant tumour burden reduction of IgG+US treated mice on day 20 compared to the IgG only treated group, indicates that the high level of cavitation generated in these studies may have driven tumour growth delay not previously observed. Indeed, one mouse in the IgG+US group was tumour free at study termination. Interestingly although this mouse did not have a particularly high overall average cavitation dose, its first intervention integrated cavitation dose was 6.13e-006 AUC, the highest AUC value of any mouse in its treatment group for intervention one. The higher levels of cavitation observed in certain mice of this study, in tandem with the observed drug-agnostic delay in tumour growth of cavitation treated mice on day 20, raise the possibility that high levels of cavitation do create direct cell-injury within the TME, drive acoustic stress, and/or generate intratumoural inflammation that plays a role in slowing tumour growth.

A preliminary investigation of the relationship between cavitation dose and survival revealed no clear correlation (Appx. 3.4d-e). Scatter plots comparing survival outcome to

integrated cavitation dose or persistence (at either intervention one, intervention two, or an average of both of these interventions on a per mouse basis), reveal no clear correlation. However, it is worthwhile to note the lack of correlation observed here could be due to inadequacy of PAM analysis to date to exclusively capture cavitation occurring intratumorally, as opposed to on the skin surface or in muscle behind the tumour. As such, future work to improve PAM treatment monitoring is urgently warranted.

Cavitation analysis

Overall, it was observed that cavitation levels were often lower on the second day of intervention compared to the first. To an extent this observation may contradict work by Zheng et al 2018 who explored the relationship between tumour vessel perfusion and checkpoint inhibitor efficacy [Zheng et al. 2018]. Zheng et al's report that checkpoint inhibitor therapy increased tumour perfusion in checkpoint inhibitor-responsive mouse models, including the CT26 animal model utilized here. Their work appears to contradict what was observed here, in that it might be expected that improved tumour permeability would lead to better intratumoural cavitation owing to the improved penetration of SSPs into the TME, yet in this study cavitation was lower on the 2nd day of intervention. Among several explanations for this difference, one might be that cavitation is simply damaging tumour vasculature during the 1st interventions such that tumour perfusion by the 2nd intervention is impeded, a hypothesis further explored in Section 4.8.

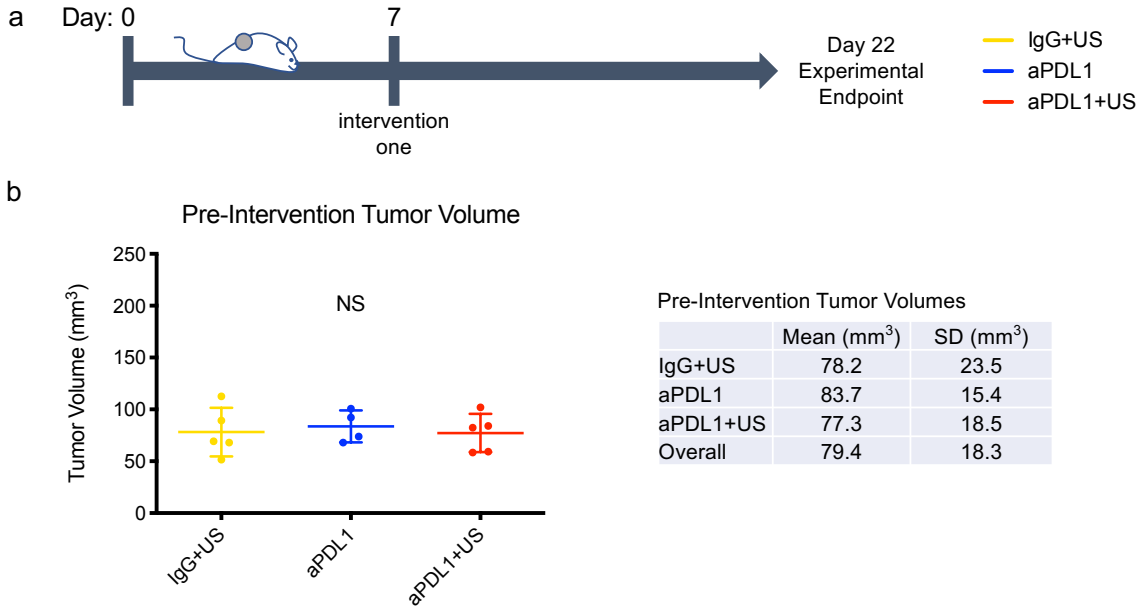
3.5 Pilot Evaluation of aPDL1 with Cavitation in EMT6 Tumour Bearing Mice

All previous work in this chapter was completed in BALB/c mice bearing CT26 colon cancer tumours. Therefore, to extend the generalizability of the aPDL1 plus cavitation approach, this study sought to query whether US-mediated cavitation could improve aPDL1 efficacy in a different tumour model. In this study, efficacy outcomes of aPDL1 alone were compared to aPDL1+US in *s.c.* implanted EMT6 tumours (mammary cancer origin). This model is particularly relevant, given recent reports that EMT6 tumours can feature an 'immune excluded' phenotype, marked by rich stromal infiltrate which restricts lymphocyte and likely drug delivery into and throughout the tumour [Mariathasan et al 2018].

3.5.1 Experimental Overview

BALB/c mice were *s.c.* inoculated with EMT6 cells suspended in FBS-free, PBS-diluted mixed 1:1 in *Matrigel*, a mixture of basement membrane proteins to support and foster stromal growth [Passaniti et al 1992]. Reaching a volume of approximately 80mm^3 on average, 7-days following inoculation a total of 14 mice were assigned to one of three groups: IgG+US (n=5), aPDL1 (n=4), and aPDL1+US (n=5). Each drug dose was likely 200μg, however, it is unclear whether the IgG injectable consisted of IgG2b alone or a mixture of IgG2b and IgG2a. Owing to a limited number of mice fitting the defined tumour size inclusion criteria in this study, no IgG control group could be included (Fig. 3.5a). One-way ANOVA with Tukey post-hoc correction observed no statistically significant difference between pre-intervention tumour volume between the 3 groups (Fig. 3.5b). Mice received only one intervention, and a 5-minute sonication (instead of 10-minutes). Mice were monitored at least every 2-3 days for welfare, tumour burden, and weight. Mice were culled 22 days after tumour inoculation and excised tumour weights were measured.

Figure 3.5: Pilot Evaluation of aPDL1 with Cavitation in EMT6 Tumour Bearing Mice (1/2)



Pre-Intervention Tumor Volumes

	Mean (mm^3)	SD (mm^3)
IgG+US	78.2	23.5
aPDL1	83.7	15.4
aPDL1+US	77.3	18.5
Overall	79.4	18.3

Figure 3.5:
a) Schematic of experiment. PBS-suspended EMT6 tumour cells were mixed at a 1:1 ratio with Matrigel and injected s.c. into BALB/c mice. 7 days post-inoculation mice were assigned to 1 of 3 intervention groups: IgG+US (n=5), aPDL1 (n=4), and aPDL1+US (n=5). Mice received only a single intervention in this study
b) Pre-intervention tumour volumes were not significantly different between groups as determined by ordinary one-way ANOVA with Tukey's multiple comparisons test (single pooled variance)

3.5.2 Results

CC-G2 cavitation analysis revealed no significant difference between the integrated cavitation dose of IgG+US and aPDL1+US administered mice, with mean values of 3.300e-006 (SD: 1.18e-006) and 2.782e-006 (SD: 1.02e-006) AUC respectively (Fig. 3.5c). Excised tumour weights were lowest on average in aPDL1+US treated mice (40.4mg with an SD of 77.5mg) compared to aPDL1 treated mice (83.3mg with an SD of 134mg) and IgG+US treated mice (154mg with an SD of 174mg), Fig. 3.5d. The median weights were 8mg, 20mg, and 91mg for aPDL1+US, aPDL1, and IgG+US treated mice respectively. However, one-way ordinary ANOVA revealed NS differences between excised tumour weights (Fig. 3.5d).

Figure 3.5: Pilot Evaluation of aPDL1 with Cavitation in EMT6 Tumour Bearing Mice (2/2)

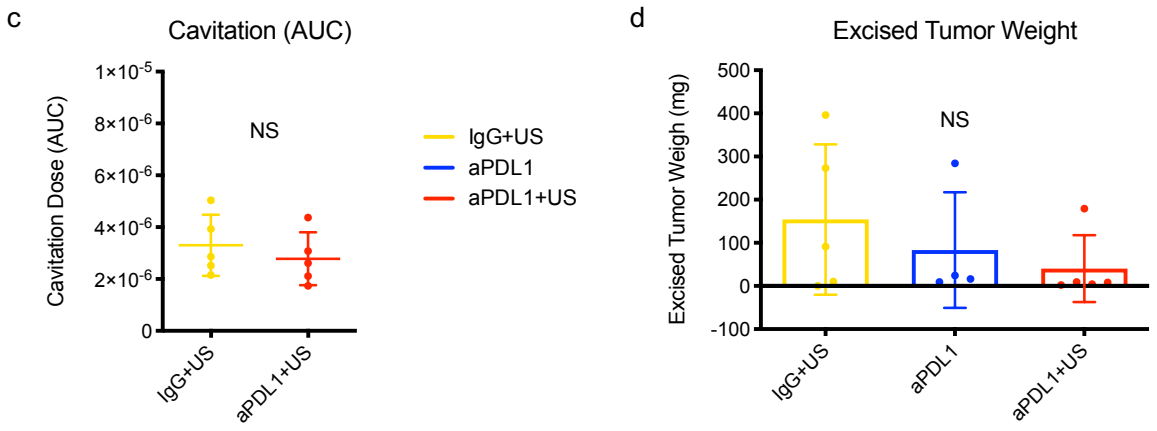


Figure 3.5 continued:
c) Unpaired t test of the CC-G2-calculated integrated cavitation doses were not significantly different between groups
d) All mice were sacrificed on d22 in this study and excised tumours were weighed. Ordinary one-way ANOVA with Tukey's multiple comparisons test (single pooled variance) *revealed no significant differences between excised tumour volumes.*

3.5.3 Discussion

Although d22 excised tumour weights were not statistically different in this study there was a trend observed that suggested that pairing aPDL1 with US best controlled tumour burden compared to IgG+US and aPDL1 drug alone. Comparison of average tumour burden as measured by callipers revealed a similar tumour burden reduction (Appx. 3.5a). Of note, because EMT6 tumours were propagated by the injection of cells that were suspended in Matrigel, as informed by the practices reported in the literature [Mariathasan et al 2018, Lau et al 2017], the absolute measurement of tumour volume vs. Matrigel is unclear, especially at earlier time-points. However, this would represent a systematic measurement error and not a treatment-specific issue and as such it is unlikely to impact high-level study findings.

Taken together it seems that aPDL1 with cavitation may provide a degree of benefit over cavitation alone (IgG+US) as well as over aPDL1 alone. In short, the results from this pilot study suggest that a study with greater statistical power and with an appropriate survival study design is strongly warranted—possibly confirming a model-agnostic benefit to pairing aPDL1 with SSP-mediated cavitation.

3.6 Chapter Summary

Efficacy studies presented in this chapter revealed that cavitation can improve drug efficacy. Across CT26 studies where sufficient cavitation was generated, it was repeatedly observed that pairing cavitation with aPDL1 enhanced efficacy compared to drug alone. Core findings in this chapter began in Section 3.1, where it was revealed that pairing aPDL1 with cavitation could improve the drug efficacy, whereas the sonication of cavitation-incompetent particles would not deliver improvements in survival. Later work in Section 3.2 explored whether or not cavitation could also benefit the efficacy of aPD1, which it did not. In Section 3.3 and related studies, the importance of maintaining sufficient cavitation was recognized; informing a change in practice wherein the ultrasound exposure strategy was refined, incorporating continuous adjustment of incident pressure in response to real-time PAM feedback to sustain intratumoural cavitation levels to within a pre-defined range. Section 3.4 put this new acoustic strategy to the test and confirmed previous findings that cavitation paired with aPDL1. Pairing aPD1 with cavitation in this study did not yield a statistically meaningful extension in survival. Lastly, the results of a pilot study, though not significant, suggest that pairing aPDL1 with cavitation can improve aPDL1 efficacy in cancer models beyond CT26, the cancer model utilized in all other studies.

The expression of PDL1 within the tumour, either by tumour cells, stromal elements, or suppressive immune populations residing in the tumour provides a clear, mechanistic rationale for why cavitation-improved aPDL1 delivery may improve aPDL1 efficacy. Three of the aPDL1 proposed mechanisms of action, a) driving intracellular, pro-apoptotic changes in PDL1 expressing cells through cell-intrinsic means, b) binding PDL1 to block PD1/PDL1 signalling, and c) depleting PDL1-expressing cells through ADCC, likely require the presence of aPDL1 within the tumour-bed. In the survival studies presented here, ultrasound-mediated cavitation paired with aPDL1 improved the function of aPDL1. Kwan et al. 2015 and Myers et al. 2016

have recently shown that ultrasound-mediated cavitation can improve drug delivery. As such, a likely reason aPDL1 paired with cavitation improves the efficacy of aPDL1 is that its delivery and distribution can be improved with US-mediated cavitation. The next chapter, directly queries and quantifies how US-mediated cavitation can enhance the immunotherapeutic delivery.

In contrast to aPDL1, in the majority of studies where aPD1 administration was paired with cavitation, no significant benefits were realized as compared to aPD1 alone. The only exception to this pattern was in one study (associated with Section 3.3) where a near-significant improvement in survival was observed in aPD1+US treated mice. However, in this study, cavitation levels were very low—similar in magnitude to those of the only study where aPDL1+US failed to deliver a survival benefit. Likewise, the number of mice in this anomalous study was small (n=6/group). A more definitive answer as to whether or not cavitation can enhance aPD1 efficacy was sought in the last study where aPD1 was paired with cavitation in a feedback-adjusted manner. In this study, aPD1 with cavitation conferred no statistically significant survival advantage as compared to aPD1 alone. Taken together, the data as currently understood suggests that the combination of aPD1 with cavitation does not yield significant improvements in survival.

Analysis of passive acoustic mapping data highlighted that the level of intratumoural cavitation can have a marked impact on therapy outcomes. While analysis comparing cavitation (either by total cavitation dose delivered or persistence) did not strongly correlate with survival, it is clear that poor cavitation results correlated strongly with no extension of survival compared to drug alone. These observations might suggest that the benefits of cavitation for efficacy and/or drug delivery act not in a dose-dependent manner but rather act in a binary, threshold manner whereby upon reaching a certain threshold level, cavitation helps improve efficacy outcomes if paired with the correct agent (i.e. aPDL1). Alternatively, improvements in the manner in which cavitation is captured, processed, and analysed may one day improve spatial and temporal resolution such that a relationship between cavitation dose and outcome can be revealed. For

example, while CC-G2 technique captures the spatial intensity of cavitation on a frame by frame basis, it may be currently confounded by capture of a significant amount of 'noise' from extra-tumoural cavitation occurring in the skin or elsewhere. The implementation of B-mode imaging to assist in the exclusion of extramural cavitation may improve the signal to noise ratio of the PAM data and thereby help the relationship between cavitation dose and outcome to be better defined.

3.6.1 Future Directions

Taken together it is robustly demonstrated here that pairing cavitation with aPDL1 can improve drug efficacy. Subsequent chapters in this thesis address questions related to drug delivery (Chapter 4) and the biological mechanism at play (Chapter 5). Beyond these two areas of investigation, future researchers may consider future work that aims to: 1) improve study quality & generalizability and/or 2) better understand the relationship between aPDL1, cavitation, and survival enhancement.

To improve study quality and generalizability, future studies should consider at least three possibilities. 1) Testing of the technology in alternate subcutaneous (like EMT6, MC38, and B16) models, genetically engineered (GEM) models (such as the KPC-model of pancreatic cancer), or spontaneous/virally driven pre-clinical cancer models like the hepatitis-driven Woodchuck hepatocellular carcinoma. GEM and spontaneous/viral driven cancer models are particularly attractive given their ability to better recapitulate human disease [Lee et al. 2017 and Tennant et al. 2004]. 2) Conducting studies such that intervention operators are blinded to agent administered and mouse monitoring is completed by a 3rd party external to the procedure team. Lastly, 3) evaluating whether cavitation as a tool to is useful in boosting the efficacy of other immunomodulatory agents, like IL-2 and toll-like-receptor agonists whose intratumoural placement may improve their efficacy or at least tolerability [Marabelle et al. 2017].

Several approaches can be undertaken to deepen the understanding of how cavitation improves aPDL1 efficacy. 1) Studies could be designed to query what intentionally changing the cavitation dose administered does to survival outcomes. 2) Querying the impact ADCC plays in the benefits of aPDL1 plus cavitation efficacy. This could be accomplished by administering Fc-tailored aPDL1 featuring differential ADCC competency or utilizing mice engineered with differential Fc receptor expression patterns, leveraging an approach similar to that of Dahan et al. to understand the importance of Fc function and checkpoint blockade [Dahan et al 2015]. 3) Evaluating the role initial tumour burden plays in dictating responses; in particular, assessing how cavitation may or may not improve outcomes in smaller tumours—tumours in volume more aligned with those that patients present with. Clinically, it has been reported that the average Stage 4b colon cancer has a volume of 71.1cm^3 [Park et al. 2017], which would correspond to a weight of approximately 71.1g assuming each cm^3 of tumour weighs one gram. Assuming the average human weights 70kg, the tumour burden of an extremely advanced-stage colon cancer would make up only 0.10% of human bodyweight. On the other hand, in studies completed here, pre-intervention tumour burden averaged ~75mm^3. Assuming mice weigh an average of 20g, a given mouse's tumour burden is 0.375% of its body weight on day of initial intervention—more than three times the relative volume of a patient with very advanced cancer. Lastly, 4) studies to evaluate the immunologic memory or abscopal potency of pairing aPDL1 with cavitation are warranted. One particularly unique experimental design, worthy of emulation, is perhaps work by Han et al. 2019, where bilateral tumours were planted of differing density. Following treatment of the larger tumour, the contralateral tumour was assessed for regression—in effect allowing for evaluation of the immunologic potency generated by the treatment strategy [Han et al. 2019]. 5) Different drug dosing regimens (i.e. higher or lower drug doses and/or adjustment of dose frequency) can be explored.

Chapter 4: Drug Delivery Studies

Haslam & Prasad reported in 2019 that about 44% of US cancer patients are eligible for checkpoint inhibitors, but only ~13% of those individuals would respond to therapy [Haslam & Prasad 2019]. Drug delivery barriers may be a factor restricting the efficacy of such agents. In this chapter, we assess whether ultrasound mediated cavitation of submicron nuclei can enhance the intratumoural delivery of antibody (biologic) checkpoint inhibitor drugs.

Previous work by Myers et al 2016 has confirmed that the intratumoural cavitation of submicron sonosensitive particles (SSP) can enhance the delivery of anti-cancer therapy *in vivo* [Myers et al. 2016]. In this study the enhanced delivery of oncolytic viruses (OVs), which at 140nm are an order of magnitude larger than therapeutic antibodies, was confirmed by polymerase chain reaction (PCR) measurement of viral nucleic acid. Assessment of delivery and infectivity via PCR was completed after euthanasia of the mice. Viral delivery was also assessed in a non-terminal fashion via *in vivo* imaging of luciferin, a bioluminescent substrate activated by luciferase, a viral-encoded gene [Myers et al 2016]. Non-terminal visualization of drug delivery is advantageous given that it enables tracking of the delivery benefit over a biologically relevant time period in the same mouse, reducing error and potentially reducing the number of mice required.

Unfortunately, antibody delivery does not naturally lend itself to the incorporation of a reporter vector like luciferase. Alternatively, antibodies can be radiolabelled and tracked, such as work by Deng et al. [Deng et al. 2016]. However, safety and cost barriers exist with such an approach. Previous work to assess the delivery of antibodies paired with SSP cavitation has employed microscopy to qualitatively describe drug delivery. Kwan et. al administered IgG antibody *in vivo* and qualitatively described how the IgG's distribution changed (increased) with or without sonication of the tumour [Kwan et al. 2015]. While microscopy was able to provide limited qualitative evidence of enhanced antibody distribution, the lack of quantitative data in

Kwan's paper speaks to the challenge of quantifying antibody delivery via microscopy. Although technically feasible, microscopy can be a labour intensive, multi-step process with ample opportunity for the introduction of error and artefact, from tumour excision and storage, to sectioning, staining, and image acquisition. Truly objective analysis of acquired microscopy data is also challenging because it is not feasible to scan every single section of every tumour with analysis typically limited to 3-4 spatially distinct tumour regions. Microscopy is therefore a strong tool to enable illustrative distribution in a low-throughput manner, but its utility in understanding and quantifying delivery across a large number of animals in a large number of studies is limited.

For these reasons, alternate high throughput means of assessing antibody delivery and binding were implemented in the present Chapter. Specifically, the use of two techniques 1) IVIS imaging of therapeutic antibodies conjugated to near-infrared fluorochromes, and 2) flow cytometric quantification of therapeutic antibody binding through secondary antibody detection. In addition to these two methods of assessing delivery, 3) microscopy of antibody distribution was qualitatively and quantitatively characterized in collaboration with ONI. In summary, this chapter leverages multi-modal approaches to characterize drug delivery and describe the improvements of drug delivery that can be observed in pre-clinical models of ultrasound-mediated submicron-nuclei cavitation.

4.1 *In vitro* and *in vivo* IVIS imaging of therapeutic antibodies

Near-infrared (NIR) imaging can enable the *ex vivo* and *in vivo* visualization of fluorophores within tissue owing to the spectral properties of light within this wavelength range [Smith et al. 2009]. The so-called NIR window, spanning wavelengths approximately 650nm to 900nm, 1) allows for tissue penetration beyond 500μm, 2) minimizes absorbance by water (<650nm light), and 3) reduces haemoglobin absorbance (>900nm light) [Weissleder et al. 2001]. To permit in vivo and ex vivo assessment of intratumoural drug accumulation, in this subsection the conjugation of a checkpoint inhibitor to a NIR-fluorophore is tested.

A checkpoint inhibitor, aPDL1, was conjugated to a near-infrared fluorochrome (680nm) via n-hydroxysuccinimide (NHS) linker chemistry. In brief, the fluorochrome dye's reactive succinimidyl ester reacts with free-amines, resulting in a stable amide linkage between the fluorochrome and the antibody [PerkinElmer 2010], as described in Section 2.5.1. IVIS imaging of the NIR-aPDL1 fluorescent signature only in the tube containing the conjugate but not for parent, unconjugated antibody, or a tube containing the SSP nuclei (Fig. 4.1a).

Figure 4.1: IVIS Imaging of NIR-aPDL1 *in vitro* and *in vivo*

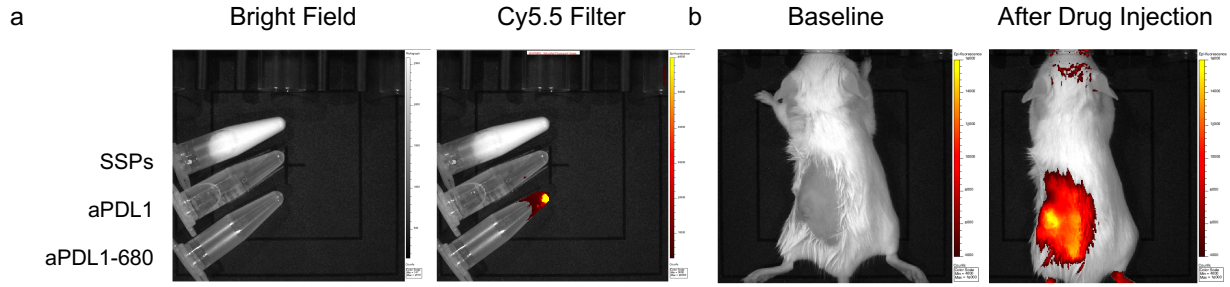


Figure 4.1:
a) IVIS imaging of SSPs, unconjugated therapeutic an aliquot of aPDL1-680 on bright field and a Cy5.5 filter reveals strong florescent signal specifically in the aPDL1-680 tube but not the others.
b) A mouse imaged after i.v. aPDL1-AF680 dosing. Imaging Settings: FOV: 7.5, f-stop:4, exposure = 0.25s, Ex = 675, Em: Cy5.5

Having established the detection limit for the antibody and confirmed the SSPs would provide no confounding fluorescence, dosing and imaging of tumour bearing mice could be performed. A comparison of imaging before and after administration of ~164ug of NIR-aPDL1

conjugate to a CT26-tumour bearing mouse revealed a sharp increase in florescent signal after drug administration, with particular accumulation of the signal about the tumour (Fig. 4.1b). For further clarification regarding the tumour model and drug conjugate administered, as described in Sections 2.3 and 2.5.1.

Intravenous, *in vivo* administration of the conjugate did not result in welfare issues. Subsequent studies (not shown) confirmed that other immunomodulatory antibodies (aPD1, aICOS) and isotype antibody (IgG2b) were similarly amenable to conjugation and suitable for in vivo administration and IVIS visualization. In summary, these data demonstrate that checkpoint inhibitors are amenable to conjugation, in vivo administration, imaging, and therefore are likely appropriate for assessing changes to intratumoural drug accumulation.

4.2 IVIS as a potential tool to quantify changes in drug delivery *in vivo*

To address the hypothesis that US-mediated cavitation may enhance intratumoural drug accumulation, a preliminary study was performed using NIR-conjugated aPDL1 in mice.

4.2.1 Experimental Overview

In brief, BALB/c mice bearing a single CT26 tumour were dosed intravenously with 220ug of NIR-conjugated aPDL1 and sonosensitive particles (SSPs), see Section 2.5.1. Tumours of 3 of the 6 mice were exposed to US directly after dosing (Fig. 4.2a). Unpaired student's t test revealed NS difference in pre-intervention tumour volumes between groups. The average tumour volumes across all mice was 55.1mm^3 with a standard deviation of 7.3mm^3 (Fig. 4.2b). Details regarding the interventions can be found in Section 2.4. Unlike all other studies presented later in this chapter where a variable pressure strategy was utilized (ranging from 1.5 to 1.9MPa), a ~1.9MPa fixed-pressure acoustic strategy was utilized in this initial study. It is worthwhile to note, however, that although a fixed-pressure strategy was used in this study, it was higher than that of other 1.5MPa fixed-pressure studies (Sections 3.1-3.3). For further detail, please see Section 2.2. Mice were anesthetized and live-imaged about 1-hr-post dosing then sacrificed. Fluorescent intensity, related to concentration of antibody per unit area, was quantified in *LivingImage* after manual-tumour tracing of the tumour boundaries, yielding the fluorescent counts per unit area (tumour area imaged), herein termed 'counts by area' (CBA). For further detail regarding methodology of IVIS imaging, refer to Section 2.5.1.

4.2.2 Results

Cavitation was monitored throughout ultrasound exposure in all three mice treated with US and is quantified and tabulated in Appx. 4.2a. The integrated cavitation dose as calculated by CC-G2 analysis averaged 3.367e-006 AUC with an SD of 2.486e-006 AUC. Please see

Section 2.2.3 for further detail. On average, live animal imaging revealed CBA was marginally greater in US treated tumours compared to tumours in mice that received drug alone, (3979 vs 3664 CBA, respectively), though not statistically significant (Appx. 4.2b-c). Approximately 1hr-after therapy mice were humanely sacrificed, and their tumours were excised and imaged (Fig. 4.2c). CBA quantification of excised tumours demonstrated a significant increase ($p<.01$) in the florescence of tumours treated with ultrasound, as determined by an unpaired t testing of natural log-transformed CBA (Fig. 4.2d). CBA increased on average from 2467 to 5137 (~2-fold) in mice administered NIR-aPDL1 alone versus those that received NIR-aPDL1 paired with ultrasound-mediated cavitation.

Figure 4.2: Pilot In Vivo aPDL1-680 Dosing +/- US

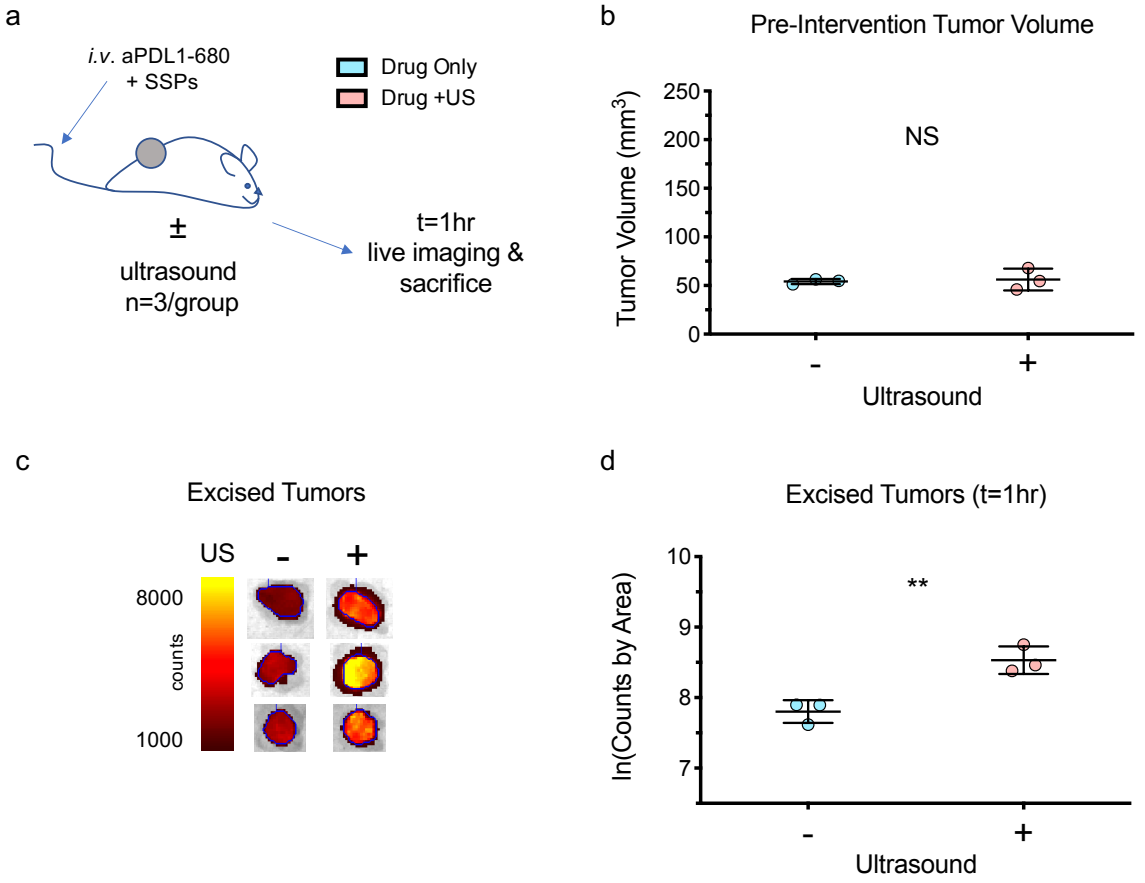


Figure 4.2:
a) Single tumour bearing CT26 mice were dosed SSPs and NIR-conjugated aPDL1 ("aPDL1-680"). Following i.v. injection, 3 out of the 6 tumours were sonicated. Mice were later imaged for assessment of aPDL1-680 accumulation
b) Pre-intervention tumour volumes analysed by unpaired t test. Mean and SD shown
c) IVIS imaging of excised tumours with parameters: FOV: 7.5; f-stop:8, exposure: 0.25s; Em=Cy5.5; Ex=675
d) Natural log transformed CBA of excised tumours. Significance determined by unpaired t test of ln(CBA)

4.2.3 Discussion

Taken together, the preliminary data of this study suggests that drug delivery is enhanced by US-mediated cavitation, as apparent through IVIS imaging of excised tumours. However, IVIS imaging of live animals, i.e. without excision of the tumours, did not reveal a difference in the CBA of tumours with respect to US treatment. Several factors may explain the apparent inability of live animal imaging to capture the difference in CBA observed by excised tumour imaging in this study including, two key driving factors are considered.

It was evident that urine on paws and skin/fur wetting, a common issue considering mice are placed into a water bath for their US-procedures, result in large fluorescent noise when imaged under 675nm excitation. Likewise, intrinsic differences between mice could be present including slight differences in the anaesthetic depth of the mice being imaged, which could play a role either increasing or decreasing measured CBA. Likewise, although operator variability was kept at a minimum, it is possible that, given the minute injection volumes (~50μL), slightly different doses of drug and SSPs may have been administered to the mice.

To address many of these issues, future studies adopted a bilateral tumour model, wherein following systemic drug and SSP administration, ultrasound-treatment of one tumour is applied. Such a model effectively ensures that each US-treated tumour can be compared to a contralateral tumour, that will have been exposed to the same systemic drug and SSP dose, in a single mouse experiencing a certain anaesthetic depth. In effect this reduces biological variability owing to the shared systemic drug supply and global anaesthetic depth.

4.2.4 Summary:

Efficacy work completed in Chapter 3 revealed that pairing cavitation with aPDL1 improved efficacy outcomes compared to aPDL1 administered without US. This preliminary study provides the first proof that cavitation is able to increase the antibody dose present in cavitation treated tumours. Taken together this begins to suggest that cavitation can enhance

local aPDL1 accumulation, and that this increase in accumulation is likely tied to the survival benefits generated.

4.3 Cavitation-enhanced intratumoural accumulation of a range of therapeutic antibodies

In this set of studies, the excised bilateral tumours of mice administered NIR-conjugated antibodies and treated on a single-side with US were assessed to query the impact of SSP-mediated cavitation on intratumoral drug-delivery (Fig. 4.3a). In an effort to establish the consistency and generalizability of the drug-device strategy, four different antibodies were evaluated. Additionally, to further establish and query the degree of physical damage potentially generated by cavitation, a subset of excised tumours of bilateral tumour bearing mice were sectioned and haematoxylin and eosin (H&E) stained.

4.3.1 Experimental Overview

BALB/c mice were bilaterally inoculated with CT26 tumours (Section 2.3). The average pre-intervention tumour volume across all tumours irrespective of assignment was 61.6mm^3 with an SD of 15.6mm^3. The mean (absolute value) of the difference between bilateral tumour volumes was 15.9mm^3 with a standard deviation of 11.3mm^3. The median (absolute value) of the difference between bilateral tumour volumes was 13.4mm^3 (ranging from 0.6mm^3 to 38.5mm^3). Repeated measures (RM) two-way ANOVA (drug and 'US status' as factors; matching by mouse—bilateral tumours) with Sidak's multiple comparisons test (single pooled variance), found no significant difference between mean pre-intervention tumour volumes in non-US vs. US-targeted tumours in any given drug group (Fig. 4.3b). In all RM two-way ANOVA analysis "*US status"* refers to whether or not a tumour has been US treated or not; see 2.8 for further clarification**.**

Mice were intravenously administered with NIR-labelled antibody (either 200μg aPDL1, 200μg IgG2b, 194μg aPD1, or 200μg aICOS) along with SSPs. IgG2b is the isotype control of aPDL1. In other words, IgG2b is structurally similar to aPDL1 except in its antigen binding

domain, which is functionally incompetent, thereby providing a means to assess drug delivery of an agent that does not specifically bind yet, behaves otherwise identical manner to aPDL1. Antibody conjugation and characterization is described in Section 2.5.1. Following *i.v.* drug and SSP administration, one of the two tumours of each mouse was sonicated for 10min as per Section 2.4 with an adjustable-PAM inform cavitation strategy as per Section 2.2.2. Mice were sacrificed on the same day of intervention and tumours were excised and imaged for quantification of florescence according to the imaging parameters defined in the figure legend (Fig. 4.3c). After intervention, excision, and IVIS imaging, the paired tumours of a subset of mice (6 mice) were OCT-embedded, frozen, then sectioned for H&E evaluation (Section 2.5.2).

4.3.2 Results

The integrated cavitation doses, calculated by CC-G2 analysis, averaged at 4.237e-006, 4.357e-006, 5.674e-006, 4.160e-006 AUC with SDs of 4.167e-007, 1.925e-006, 2.167e-006, 9.929e-007 AUC for IgG2b+US, aPD1+US, aPDL1+US, and aICOS+US treated mice respectively. Comparison of AUC between US-exposed mice identified no significant differences between cavitation dose recorded within tumours during exposure on an agent-specific basis by one-way ANOVA with Tukey's multiple comparisons post-hoc test (Appx. 4.3a).

Irrespective of agent administered, ultrasound exposed tumours had greater CBA than their sister, contralateral tumours for every antibody, in every mouse studied (Fig. 4.3c & d). CBA quantification corroborated gross observations of excised, IVIS-imaged tumours.

The paired fold changes (FCs) in CBA were 3.01, 3.00, 2.15, and 2.44 for IgG2b, aPD1, aPDL1, and aICOS dosed mice respectively. Paired FC was determined by first calculating the FC in CBA on a per-mouse basis ('mFC'), then calculating the mean of 'mFCs' for all mice of a given drug-group. The FCs in CBA on a per-mouse basis ('mFCs') were calculated by dividing the CBA of a given mouse's US-treated tumour by the CBA of its contralateral, non-US treated

tumour. Overall, the unpaired FCs in CBA were 2.97, 2.85, 2.09, and 2.24-fold in IgG2b, aPD1, aPDL1, and aICOS dosed mice respectively. Unpaired FCs were calculated by dividing the sum of US-treated tumour CBAs by the sum of non-US treated CBAs.

Figure 4.3: Ig2b, aPD1, aPDL1, and aICOS delivery in bilateral CT26 tumours (1/2)

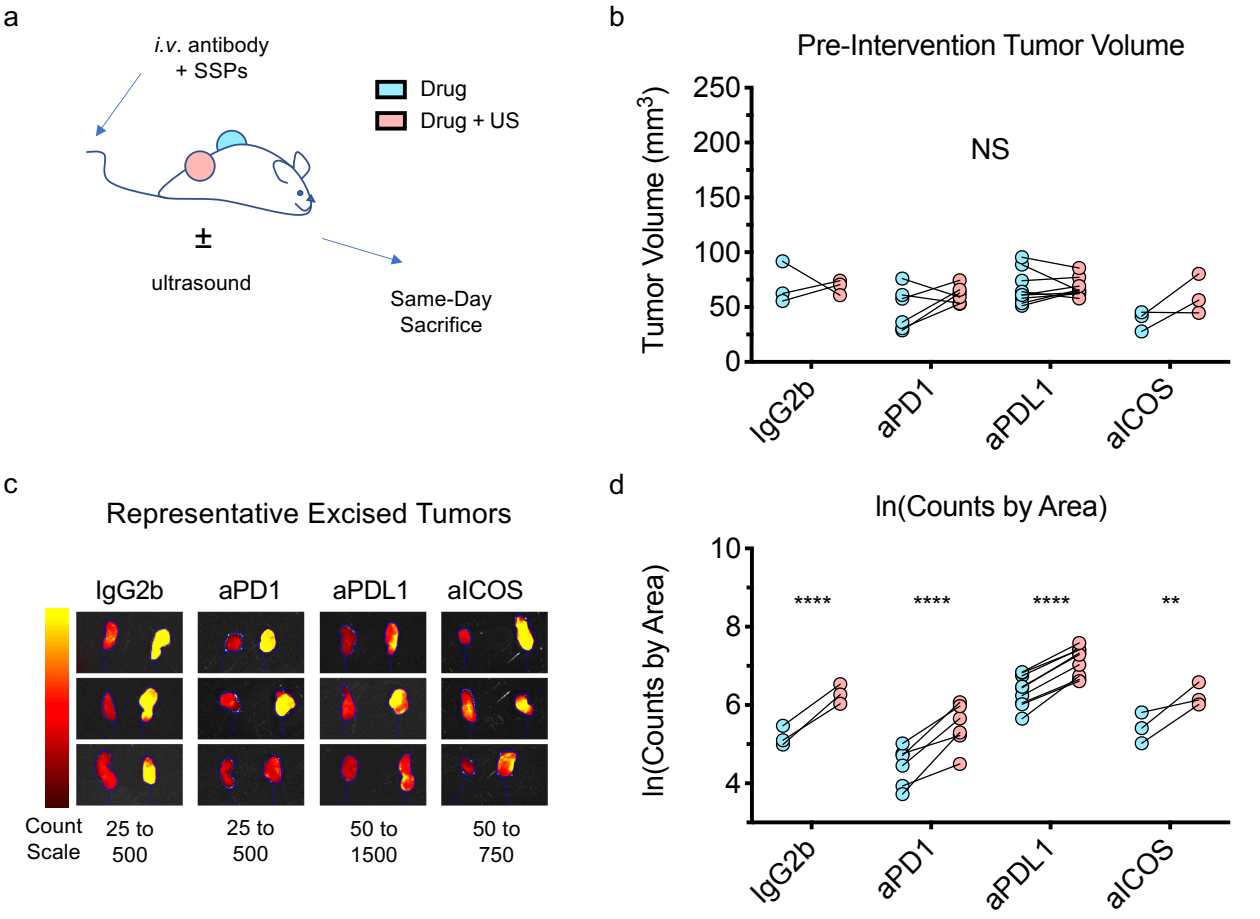


Figure 4.3
a) NIR-conjugated IgG2b (n=3), aPD1 (n=6), aPDL1 (n=9), and aICOS (n=3) were administered to bilateral CT26 tumour-bearing BALB/c mice. 1 of 2 tumours were US-targeted then mice were same-day sacrificed for assessment of excised tumour CBA by IVIS.
b) Pre-intervention tumour volumes were assessed by RM two-way ANOVA (US status and drug as factors; matching by mouse) with Sidak's multiple comparisons test (single pooled variance)
c) Representative IVIS images (FOV: 7.5, Exposure: 0.25, f-Stop: 4) of excised, bilateral tumours (US treated tumour on the right). The heat scale of representative mice was adjusted in order to accommodate the range of counts as per the different agents administered.
d) Tumours were manually traced, and the average florescence counts by area (CBA) quantified for IgG2b, aPD1, aPDL1, and aICOS administered mice. Natural log transformed CBA shown. Ln(CBA) assessed by RM two-way ANOVA (US status and drug as factors; matching by mouse) with Sidak's multiple comparisons test (single pooled variance)

Analysis of the natural-log transformed CBA by RM two-way ANOVA with Sidak's multiple comparisons test (see 2.8) appreciated highly significant ln(CBA) increases in US-

treated compared to contralateral control tumours for every drug evaluated (Fig. 4.3d). Given that tumour volume, vascularity, degree of necrosis, and permeability are closely linked it was important to evaluate whether initial tumour volume may confound or complicate the study. To best address this concern, mice with a very tight range of tumour volumes and limited absolute difference in bilateral tumour volumes were used. A comparison of initial tumour volume vs. ln(CBA) revealed no apparent clustering patterns between initial tumour volume and ln(CBA), Appx. 4.3b. This suggests mouse enrolment criteria were appropriately selective and that tumours evaluated had very similar baseline vasculature enabling similar levels of passive drug transport.

An absolute comparison of CBA between mice was not appropriate in this study given the variability in agent and production batch administered for a given agent given the variability in antibody degree of labelling (Section 2.5.1). Two-way repeated measures ANOVA analysis of revealed that both ‘US status’ (yes or no US) and ‘drug’ independently were strong, significant sources of variation, whereas the interaction between US and drug was not statistically significant. This observation that there is no significant interaction between US and drug is perhaps consistent with a hypothesis that US-mediated cavitation acts in a drug-agnostic manner to improve drug accumulation. Biologically one might assume that the mechanical bioeffects exerted by US-mediated drug delivery would be similar to all agents administered owing to the similarity across the agents’ physical sizes and molecular weights (150-180 kDa).

H&E staining of a subset of tumours from this study revealed no striking differences in gross histopathologic appearance between US-treated tumours and their contralateral, non-US treated tumours (Fig. 4.3e).

Figure 4.3: Ig2b, aPD1, aPDL1, and aICOS delivery in bilateral CT26 tumours (2/2)

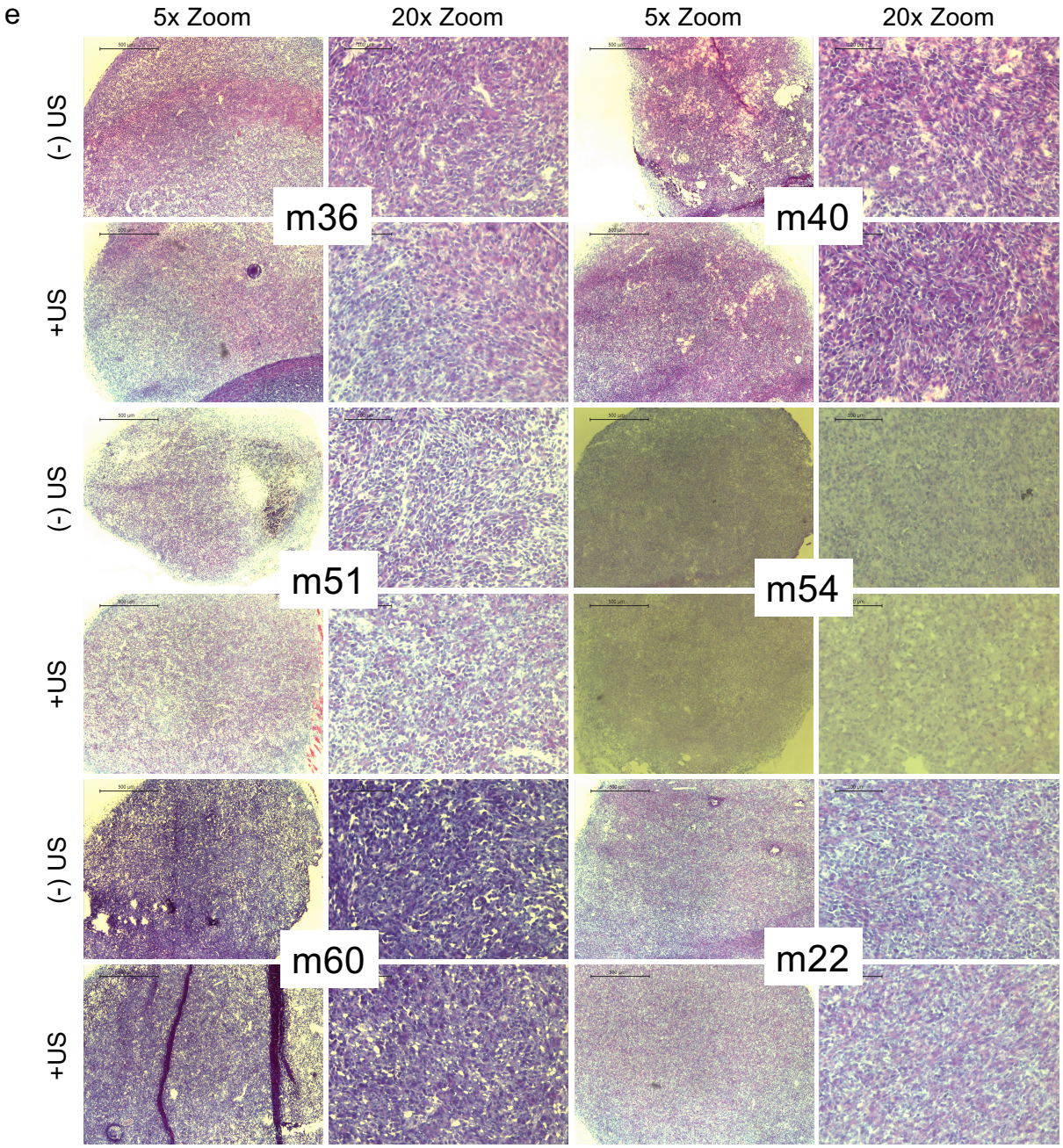


Figure 4.3 continued:
e) A subset of paired tumours were also processed for H&E staining. Images were acquired on a light microscope at 5x and 20x.

4.3.3 Discussion

Highly significant ($p<0.001$) increases in aPDL1, aPD1, aICOS, and isotype control antibody accumulation in ultrasound treated tumours compared to their contralateral controls was observed. Fluorescent counts by area increased on average by ~2 to 3-fold. These observations suggest that US-mediated cavitation is able to improve antibody-delivery in an antibody-agnostic manner. Beyond the cancer immunotherapeutics evaluated here, this work is meaningful more broadly considering the rapid growth and utilization of antibody-based agents in clinic—biologics including cancer drugs like trastuzmab, pertuzmab, ramucirumab, cetuximab, olaratumab, necitumumab, and denosumab [Grilo & Mantalaris 2019]. Grilo & Mantalaris write that: “Past market data (2012–2017) indicated a doubling of the mAb market, a trend that is anticipated to continue to 2022 when mAb sales are expected to reach US$130–200 billion…” [Grilo & Mantalaris 2019]. The ability of US-mediated cavitation to work across the diversity of agents evaluated here, suggests that this technology may be adapted and useful in supporting the delivery of other agents in clinic or in development.

The lack of observed, consistent differences per H&E between US-treated and contralateral control tumours, suggests that negligible direct tissue damage is generated by cavitation. While preserving tumour integrity is not a chief concern, the absence of direct-tissue damage shown here, suggests that this cavitation approach could potentially be safe in both cancer and non-oncological applications. However, future analysis should consider more specifically the impact cavitation may have at a later time point, as only a single time point was assessed by imaging in the current study. Likewise, it may be useful in the future to use more sophisticated stains to visualize tissue injury or death, for example the use of terminal deoxynucleotidyl transferase dUTP nick end labelling (TUNEL), tetrazolium, or Annexin-V staining.

Limitations & Future Work

The studies presented in this subsection utilized methodology that enabled the generation of internally controlled data. The ability to control for mouse-to-mouse variability (i.e. true injected dose or anaesthetic depth) in tandem with the screening of four different antibodies suggests US-mediated cavitation is a powerful capable of improving antibody delivery. However, the scope of work is limited by the fact that all studies were completed in a single mouse model. It is therefore unclear whether this device-strategy would yield a similar effect in other animal models or whether there is any relevance to clinical translation. To begin addressing the concern of generalizability, work in the next subsection evaluates the potential of ultrasound mediated cavitation to enhance drug delivery in subcutaneous EMT6 tumour bearing mice. Other limitations of the IVIS completed here and in 4.4 are discussed in more depth at the end of 4.4.

4.4 Cavitation-enhanced aPDL1 accumulation in EMT6 tumours

The studies described in Figures 4.2-3 demonstrated that ultrasound mediated cavitation may enhance intratumoural antibody accumulation in CT26 tumours, however, it is unclear whether such an approach would yield similar effects in other tumour models, or moreover in humans. To query the generalizability of this delivery strategy, the accumulation of NIR-aPDL1 in mice bearing bilateral EMT6 tumours, an aPDL1 refractory model, was assessed [Mariathasan et. al 2018].

4.4.1 Experimental Overview

Bilateral EMT6 tumour bearing mice (n=4) were administered NIR-aPDL1 (200μg) with SSPs. Subsequently one of the two tumours was US-targeted for a total of ten minutes. An adjustable-pressure acoustic strategy was utilized, as consistent with 4.3 (see Section 2.2.2). All tumours were imaged following intervention, on the same day of therapy. Excised tumours were IVIS scanned under imaging parameters as shown in the caption (Fig. 4.4a).

The average overall tumour volume irrespective of assignment was 108.8mm^3 with a standard deviation of 25.1mm^3. The mean non-US treated tumour volume was 108.8 mm^3 with an SD of 37.2mm^3 and the average US-treated tumour volume was 108.7mm^3 with an SD of 9.1mm^3. The mean, absolute value of the difference between bilateral tumour volumes was 32.0mm^3 with a standard deviation of 25.8mm^3. The median absolute value difference between contralateral tumour volumes was 28.3mm^3 ranging from 7.3 mm^3 to 64.1mm^3. Paired t test of pre-intervention tumour volumes revealed no significant difference between sonicated and non-sonicated tumours (Fig. 4.4b).

4.4.2 Results

The mean integrated cavitation dose of US-treated tumours was 3.203e-006 AUC with a standard deviation of 1.278e-006 AUC (Appx. 4.4a). Quantification of IVIS scanned, excised tumours (Fig. 4.5c and d) revealed a significant increase in ln(CBA) in ultrasound treated tumours compared to paired, contralateral control tumours. On average CBA increased from a mean of 471 CBA to a mean of 1545 CBA upon application of US, a ~3.28x increase (overall, irrespective of pairing) in intratumoural accumulation of aPDL1 by CBA.

Figure 4.4: aPDL1 delivery in bilateral EMT6 tumour-bearing mice

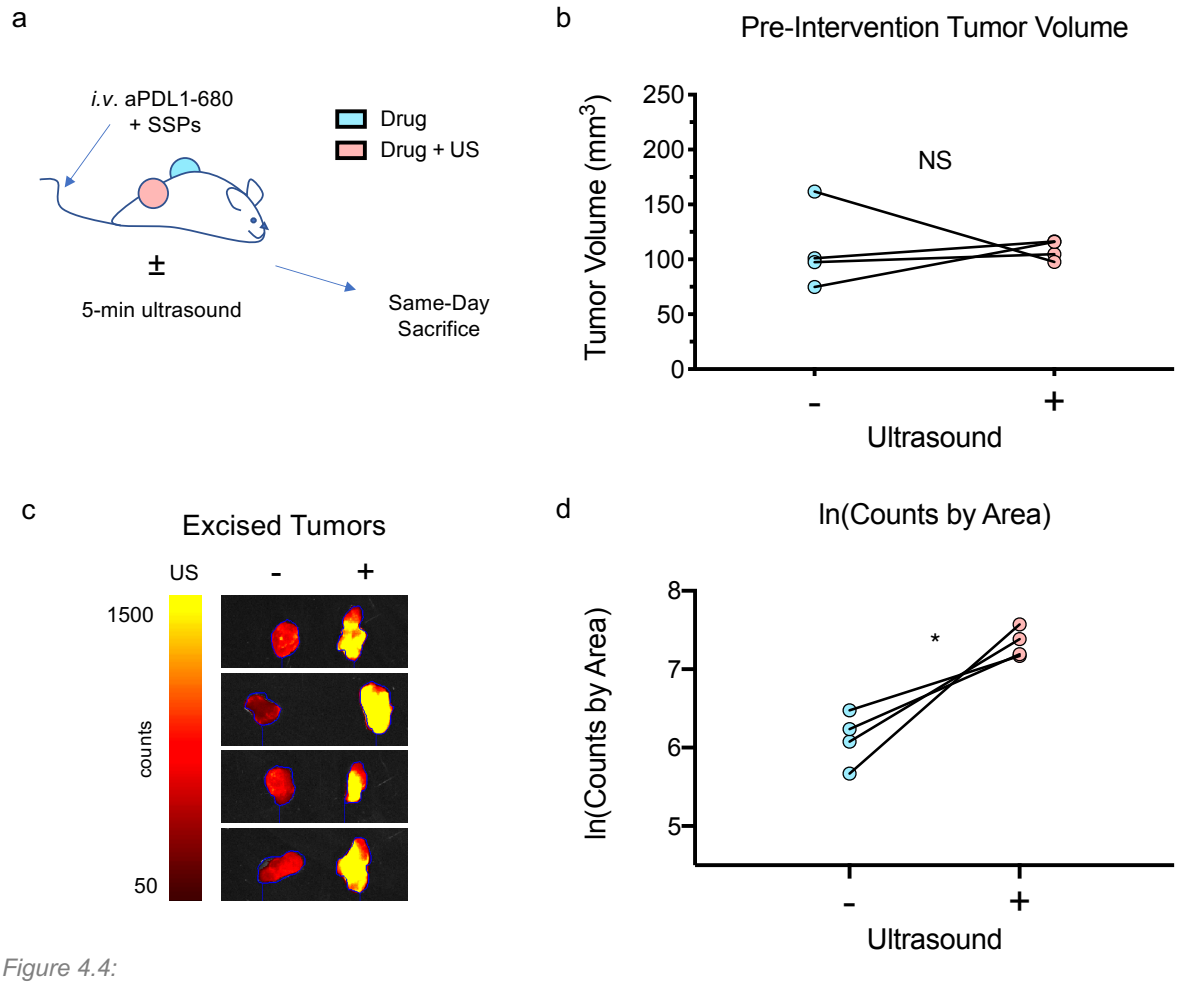


Figure 4.4:
a) BALB/c mice bearing bilateral EMT6 tumours were administered 200μg of NIR-aPDL1 and SSPs i.v. Following i.v. administration, 1 of 2 tumours were sonicated for 10-minutes.
b) Pre-intervention tumour volumes statistically assessed by paired t test. Bilateral tumours connected by a line
c) IVIS imaging of excised tumours. (Em = Cy5.5, Ex=675nm, F-Stop 4, exposure .25s, FOV: 7.5)
d) Quantified and ln transformed CBA of excised tumours. Significance determined by paired t test of ln(CBA)

4.4.3 Discussion

Implications

Ultrasound-mediated cavitation enhanced intratumoural aPDL1 delivery in EMT6 tumours as observed in mice bearing bilateral EMT6 tumours where one of two tumours was US-exposed. This observation is consistent with our findings of a similar phenomenon in CT26 tumour bearing mice. It was also noteworthy that the average integrated cavitation dose (AUC) in this study of 3.20e-6 AUC was comparable to that of Fig. 4.3 for aPDL1-NIR treated mice (5.67e-6 AUC).

Despite the lower average integrated cavitation dose, delivery in this study was still robust. A number of factors could explain the difference—two key reasons could be: 1) Unlike CT26 tumours, EMT6 tumours were propagated in Matrigel, as described in the literature [Mariathasan et al 2018, Lau et al 2017]. This difference in tumour propagation technique may motivate future investigation. Future work could further investigate the impact Matrigel alone plays in supporting or attenuating intratumoural cavitation and/or drug delivery. Related to tumour propagation, (2) the stroma of EMT6 tumours could render them especially drug restrictive. Although not comparative to CT26, work by Mariathasan has already suggested that stromal barriers in the EMT6 model can restrict aPDL1-mediated anti-tumour responses [Mariathasan et al. 2018]. Further highlighting the ability of EMT6 tumours to exclude drug-delivery is work by Schütze et al. who was able to significantly improve doxorubicin drug diffusion in 3D EMT6 tumour models by inhibiting lysyl oxidases (exploited by EMT6 tumours) [Schütze et al 2015].

While passive aPDL1 accumulation in CT26 vs. EMT6 was not directly compared here, the results of this study may indicate that passive drug delivery is more restricted in the EMT6 model, given that larger delivery-benefits can be appreciated when US-is applied to EMT6 tumours compared to CT26 tumours. Future work should consider more broadly evaluating the

passive permeability of pre-clinical clinical models commonly used in cancer-immunotherapy research and development, similar to work by Adkins et al to characterize the permeability of brain-metastatic pre-clinical models [Adkins et al. 2016]. Such work may prove to be a useful adjunct characteristic to the body of work to characterize the mutational burden, cytokines, and immunogenicity of such models [Yu et al. 2018].

Limitations & Future Directions

Taken together the results of this EMT6 study and previous work in CT26 bilateral mice showcase the ability of US-mediated cavitation to enhance intratumoural antibody delivery through IVIS imaging of NIR-conjugate antibodies.

Efficacy work completed in Chapter 3 revealed that pairing cavitation with aPDL1 improved efficacy outcomes. In this study, it was observed that cavitation did not act in a drug-specific manner, and instead seemed to improve drug delivery to tumours regardless of agent administered. Further work in this chapter aims to explore the impact cavitation-facilitated drug delivery makes to drug binding and distribution which as of yet are not addressed.

Although IVIS as a modality provided relatively high-throughput assessment of drug delivery to the tumours, it measured only gross, tumour loading of drug, leaving unclear the extent to which drug delivered to the environment actually could bind or was distributed away from blood vessels. At worst, the signal could arise from burst intratumoural or superficial blood vessels in cavitation-treated mice. Regardless, the outcomes of these studies show that more drug physically accumulates about the tumours of cavitation treated mice. Put simply, the studies so far do not demonstrate if more drug is actually distributing and/or binding target in the tumour or tumour microenvironment. Studies presented in the next sections seek to address this limitation and clarify whether US-mediated cavitation may enhance the binding and/or distribution of drug to target.

4.5 Detection of *ex vivo* tumour-bound therapeutic antibody

It is clear from Figures 4.2 to 4.4 that ultrasound mediated cavitation can enhance the gross deposition of antibody-based drugs into tumours. However, it remains unclear whether cavitation increases the number of antibody-cell binding events within the tumour and what impact antibody specificity plays in dictating the frequency of such binding events. To address such questions flow cytometry (FCM) was adapted and tested to assess the intensity and frequency of antibody cell binding events.

FCM enables high-throughput measurement of cell-bound fluorescently-conjugated antibodies [O'Donnell et al. 2013]. Given the inability to directly visualize the near-infrared fluorescently conjugated antibodies utilized in the IVIS, drug accumulation/binding studies using FCM relied on a secondary antibody approach. Secondary antibodies, antibodies conjugated to a 'readable' tag (i.e. an FCM-compatible fluorochrome), bind the Fc domain of a primary, ligand-specific antibody (i.e. an unconjugated therapeutic antibody), thereby enabling detection of otherwise unconjugated agent. In this section the technique is evaluated for its ability to detect, *ex vivo* tumour-bound unconjugated aPDL1 antibody.

4.5.1 Experimental Overview

Four CT26 tumours were excised from sacrificed, tumour-bearing mice then dissociated into single cell suspensions. A portion of each tumour was then incubated *ex vivo* with unconjugated aPDL1 (Clone 10F9G2, an IgG2b antibody). Subsequently, all samples were incubated with a secondary, APC-channel compatible anti-IgG2b antibody (APC-aIgG2b) and then also stained for viability using 7AAD live/dead stain (Fig. 4.5a). For further detail regarding methods and reagents utilized see Section 2.6.1.

4.5.2 Results:

Tumour samples incubated *ex vivo* with aPDL1 showed an increase in average anti-IgG (APC channel) median fluorescence intensity (MFI) compared to tumour samples not incubated with aPDL1 (MFI 3083 vs. 199, p<.001), Fig. 4.5b. Likewise, the frequency of anti-IgG+ cells significantly (p<.0001) increased in aPDL1 *ex vivo* incubated samples compared to samples not incubated with aPDL1, (mean of 70.9 % v 2.8%, respectively), as shown in Fig. 4.5c. Gating hierarchy and representative APC vs. FSC plots are shown in Appx. 4.5a and b.

Fig. 4.5: Secondary Antibody Detection of Bound aPDL1 *Ex Vivo*

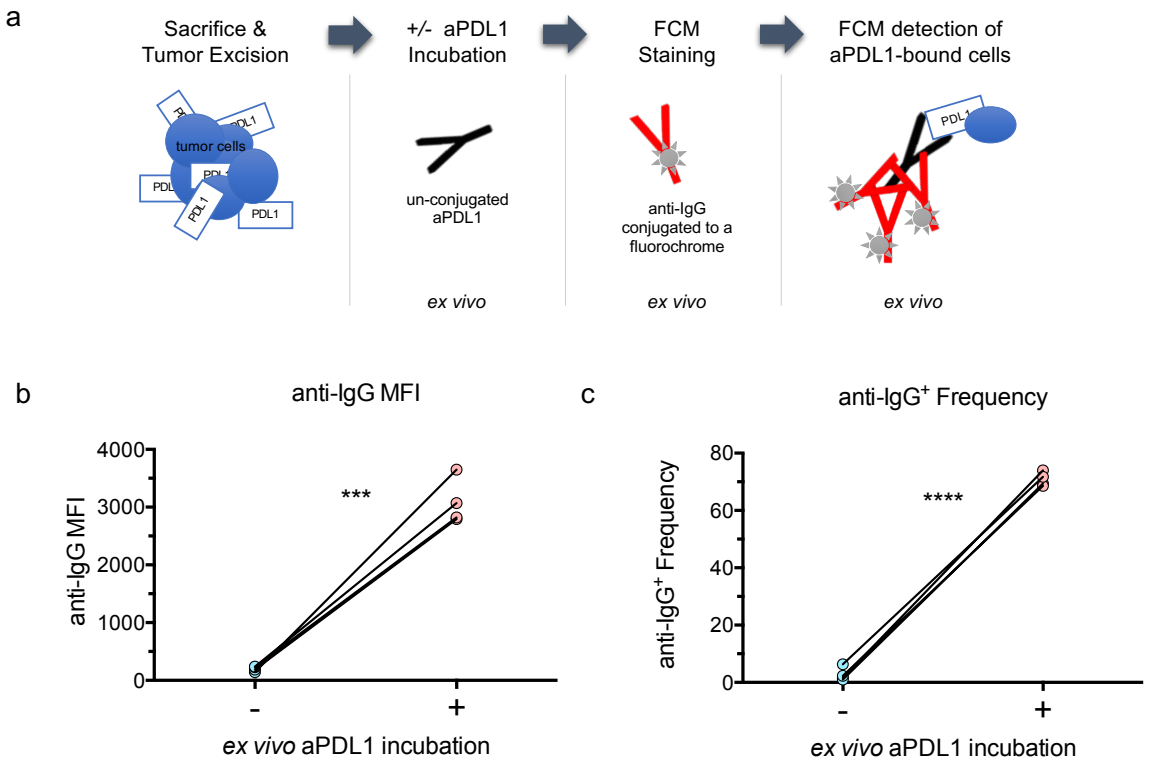


Figure 4.5:
a) Treatment naïve, CT26 tumour bearing mice were sacrificed and their tumours were excised (n=4). Tumours were prepared for FCM staining with or without prior ex vivo incubation with unconjugated aPDL1.
b) The anti-IgG median fluorescence intensity (MFI) of live, size-gated events (as per gating strategy shown in Appx. 4.5a). Connecting lines between two dots represent samples from the same tumour. Statistical analysis by paired t test
c) The anti-IgG+ frequency of live, size-gated events with or without aPDL1 incubation, as per gating strategy representation shown in (Appx. 4.5b). Connecting lines between two dots represent samples from the same tumour. Statistical analysis by paired t-test.

4.5.3 Discussion:

These studies confirm that secondary antibody detection via flow cytometry provides a means to quantify and detect therapeutic antibody bound cells, even those measured within complex heterogeneous samples such as tumours. In addition to increasing sensitivity, a secondary antibody approach allows these studies to be more closely aligned to survival studies whilst eliminating the possibility that antibody conjugation would change its size, charge, binding capability or biocompatibility compared to an unconjugated drug. This technique was therefore deemed sufficiently robust to assess whether cavitation could enhance the frequency and intensity of therapeutic drug binding.

4.6 Flow cytometry characterization of aPDL1 binding intensity and frequency with or without intratumoural cavitation

The therapeutic antibody detection techniques validated in 4.5 were used to characterize whether dosing of aPDL1 paired with intratumoural cavitation could enhance the binding of aPDL1 to target cells compared to tumours not exposed to cavitation.

4.6.1 Experimental Overview

In brief, to replicate conditions of survival studies (Chapter 4) in which mice bear single tumours, mice in this study were inoculated on a single flank and dosed unconjugated aPDL1 (Clone 10F9G2). Mice inoculated with a single CT26 tumour (15d post-inoculation) were dosed with 200μg of aPDL1 and SSPs. Six of the twelve mice were then treated with ultrasound (Fig. 4.6a). A pressure-adjustable cavitation strategy was utilized in this work (Section 2.2.2). Unpaired t test revealed no statistical difference in the assigned pre-intervention tumour volumes between ultrasound assigned and non-US mouse tumour volumes (Fig. 4.6b). The average tumour volumes across mice irrespective of assignment was 71.7mm^3 with a standard deviation of 16.1mm^3. The average pre-intervention tumour volume in aPDL1 grouped mice was 71.6mm^3 with an SD of 16.9 mm^3, whereas the average pre-intervention tumour volume was 71.9mm^3 and a standard deviation of 16.9mm^3.

Post-procedurally, mice were recovered and monitored and after approximately 24hrs they were sacrificed. Tumours were excised, processed to a single-cell suspension, Fc blocked to reduce non-specific antibody binding, and then stained with APC-aIgG2b. Cells were then thoroughly washed and stained with Pacific Blue (PB)-aCD45 to detect leukocytes and then 7-Aminoactinomycin D (7AAD) for live/dead stain assessment. For further clarification regarding methodology please see section 2.6.1. Taken together this protocol was designed to enable the assessment of the frequency and intensity of live leukocytes bound to therapeutic antibody.

FCM analysis was completed in *FlowJo*. After time-gating and down-sampling each sample to acquire a consistent number of events across all samples, all samples were *in silica* merged to create a concatenated file to form the basis of the gating strategy. Down-sampled populations are representative of their parent but enable an equal number of cells to contribute toward the *in silica* merged concatenated file utilized to inform gating strategy. Appx. 4.6c outlines the gating hierarchy that was applied to each sample after time-gating: singlet, size, then Live/Dead (7AAD) vs. CD45 (leukocyte common antigen) gating. Other than the time-gate, intended to exclude cytometric errors that can occur toward the end of tube acquisition owing to fluidics/sample running out, no other gates were manipulated on a per sample basis. Appx. 4.6d shows representative anti-IgG^+ gating. The threshold informing the anti-IgG+ gate was determined as the lowest florescent cut-off that resulted in a ≤2% positive frequency of live, leukocytes in all APC fluorescence minus one (FMO)-control samples from an alternate study conducted at the same voltages with a similar set of stains preformed (not shown).

4.6.2 Results & Discussion

Unpaired t test revealed no significant difference in sacrifice-day (i.e. ~24 hours) tumour volumes (Appx. 4.6a). Quantification of the integrated cavitation dose revealed the average, integrated cavitation dose was 3.722e-006 AUC with a standard deviation of 6.514e-007 AUC (Appx. 4.6b).

FCM revealed significant elevations in both the MFI of anti-IgG signal and frequency of drug-bound live leukocytes (anti-IgG+ leukocytes) in mice administered aPDL1 and SSPs paired with ultrasound compared to those that received aPDL1 and SSPs but no ultrasound (Fig. 4.6c-d, with gating strategies shown in Appx. 4.6c-d and additional populations quantified in Appx. 4.6e-h). For instance, FCM revealed that a significantly ($p<.01$) greater proportion (85.6% vs 63.6%) of live leukocytes were aPDL1-bound, in mice administered aPDL1 paired

with cavitation. Likewise, live leukocyte intensity of anti-IgG staining was significantly (p<.001) elevated (900.5 vs. 1571 APC MFI) in mice administered aPDL1 paired with cavitation.

Figure 4.6: FCM Detection of aPDL1 from Tumours Collected ~24hr-Post Intervention

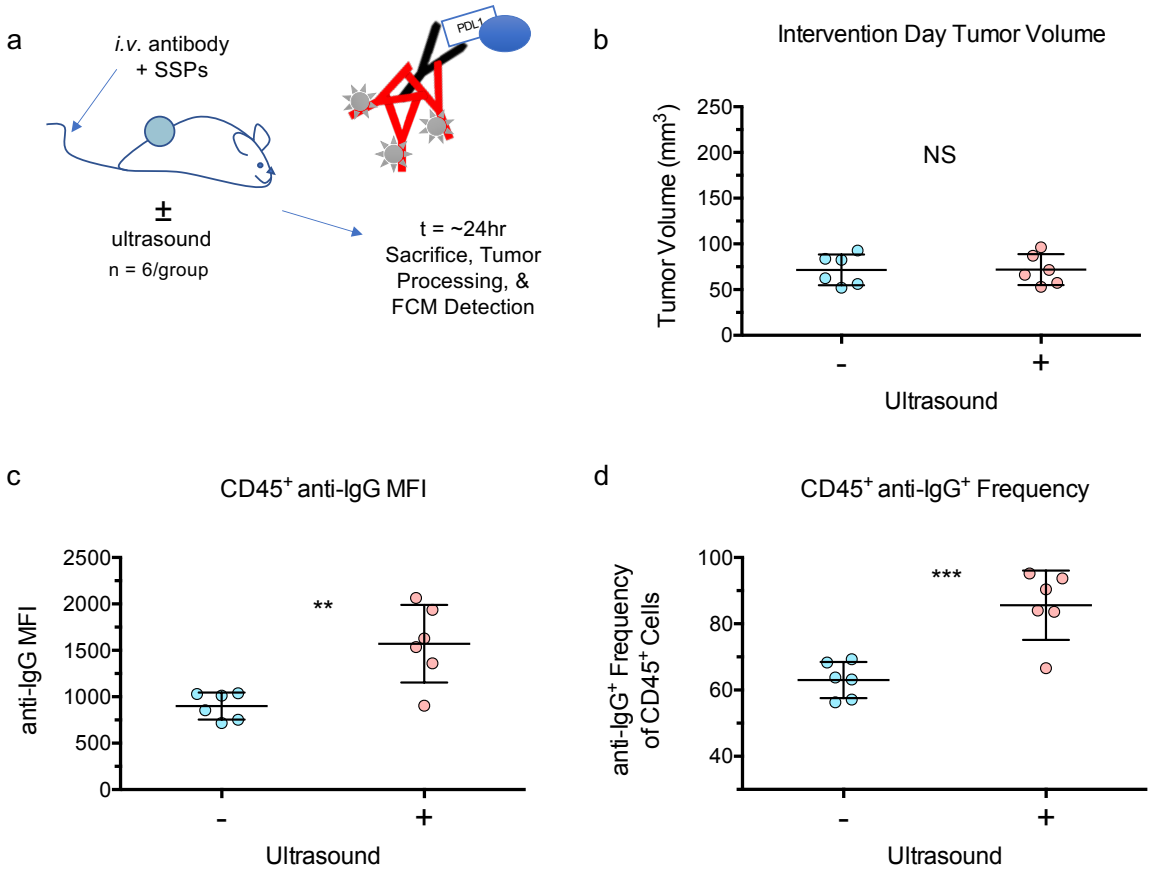


Figure 4.6
a) 12 single tumour bearing Balb/c mice were administered 200μg unconjugated aPDL1 and SSPs. Following i.v. dosing, 6 of the 12 mice were sonicated. Approximately 24hrs post-procedure, mice were sacrificed, and their tumours were queried for aPDL1 via FCM secondary antibody detection. Tumours were subjected to mechanical processing, washed, and blocked to retrieve a single-cell suspension which was then stained for the detection of bound therapeutic antibody by 'anti-IgG'—an APC-channel-compatible secondary antibody (anti-IgG2b)
b) Unpaired t test of pre-intervention tumour volumes between groups (n=6/group)
c) The anti-IgG median fluorescence intensity (MFI) of live, leukocytes (as per gating strategy of Appx. 4.6c). Statistical analysis by unpaired t-test (n=6/group)
d) The anti-IgG+ frequency of live, leukocytes with or without aPDL1 incubation, as per gating strategy examples shown in (Appx. 4.6d). Statistical analysis by unpaired t-test (n=6/group)

Limitations

There were three key limitations to the work in this study. The first limitation concerns live, non-leukocytes, the 7AAD$^-$, CD45$^-$ subset and, as a consequence, the live-total (7AAD$^-$)

population. Although these populations (Appx. 4.6e-h), behaved similarly to the live, leukocyte ($7AAD^-$, $CD45^+$) subset (Fig. 4.6c-d), the lack of a positive selection marker to define non-leukocytes, renders the results shown in Appx. 4.6e-h possibly unreliable. This was not a concern for the live, leukocyte population (Fig. 4.6c-d) where a positive selection marker, CD45, was utilized in the gating of live, leukocytes ($7AAD^-$, $CD45^+$). Future work should consider utilizing a positive selection marker to identify non-leukocytes, however, in this study no adequate extracellular marker of CT26 cells was found identified in time.

The second limitation in this study concerns the use of 7AAD to differentiate between live and dead cells. Although it is standard practice to utilize 7AAD in this capacity, it is important to consider the mechanism by which this agent functions. Mechanistically, 7AAD intercalates with nucleic acids (e.g. DNA), marking cells with compromised membranes as $7AAD^+$, allowing for their differentiation. Notably however, 7AAD is unable to mark anucleate debris or other particles as 'dead' if they altogether lack DNA/RNA. While singlet and size gating do enable selection of likely cellular events, the fact that 7AAD only marks nucleic-acid-containing dead cells remains a limitation of this technique. Future work should therefore consider utilizing a mechanistically different viability marker, as explored in the next section.

Lastly, the final limitation concerns the time-point at which tumours were collected. At ~24-hrs post-intervention although no significant changes in tumour volume were detected between groups, other biological changes could have taken place, including possibly the upregulation of PDL1 expression which could favour an increase in aPDL1 binding. Alternatively, the 24hr post therapy collection point may have reduced the difference in measured drug-enhancement, considering that over an increase in time, more drug would be able to passively accumulate in the non-US treatment group and/or drug actively pushed/pumped into the environment by cavitation could have been metabolized. Future work should therefore consider harvesting tissue at an earlier time-point after therapy.

Summary & Future Directions

This study revealed that pairing intravenous aPDL1 with intratumoural cavitation can enhance both the frequency and intensity of therapeutic antibody binding to live leukocytes. The results of this study are consistent with and extend previous observations that US-mediated cavitation can enhance the intratumoural accumulation of antibody in tumours determined through IVIS imaging of near-infrared conjugated immunomodulatory agents (Fig. 4.2 to 4.4). This study suggests that not only is there more drug in the tumour but also that the drug reaches more of its target in both the frequency of cells surveyed and intensity of binding to any given cell (ascertained via the increase in MFI).

Of note, while the study robustly queried how aPDL1-binding changes with respect to leukocytes, it did not conclusively query changes to non-leukocytes. While it would have added value to also assess drug binding to tumour cells, recent clinical and pre-clinical studies suggest that PDL1 expression on host immune populations could be as important or perhaps more important in dictating outcomes of PDL1/PD1 blocking therapy than the PDL1 expression on tumour cells [Munn 2018]. In fact, recent work Kleinovink et al. reports in the CT26 tumour model, that “PD-L1 expression on malignant cells is no prerequisite for checkpoint therapy.” [Kleinovink et al 2017]. Similarly, work by Lau et al. who also utilized the CT26 tumour model, found “Tumour and host cell PD-L1 is required to mediate suppression of anti-tumour immunity in mice” [Lau et al 2017].

There is mounting pre-clinical evidence that host cell (i.e. non-tumour cell) PDL1 expression may be in fact more important than tumour cell PDL1 expression [Tang et al. 2018, Lin et al. 2018]. Work by Lin et al. 2018 with elegant host and tumour cell PDL1 knockout models, observed that knocking-out host immune PDL1 expression abrogated the survival benefits conferred by aPDL1 therapy in mice with MC38 colon cancer, ID8 ovarian cancer, and B16-F10 melanoma tumours. On the other hand, mice bearing tumours propagated with PDL1 deficient tumours (e.g. PDL1 deficient MC38, ID8, and B16-F10) and treated with aPDL1 were

still responsive to aPDL1 therapy [Lin et al. 2018]. Lin et al. also corroborate their pre-clinical results with clinical correlate data, revealing that antigen presenting cell PDL1 expression correlated with checkpoint inhibitor efficacy better than tumour cell PDL1 expression [Lin et al. 2018]. Other clinical work has also highlighted the importance of leukocyte PDL1 expression, notably Herbst et al's *Nature* report "… show[ing] that across multiple cancer types, responses (as evaluated by Response Evaluation Criteria in Solid Tumours, version 1.1) were observed in patients with tumours expressing high levels of PD-L1, especially when PD-L1 was expressed by tumour-infiltrating immune cells*"* [Herbst et al. 2014]. Taken together, it is clear that "PD-L1 expressed on cancerous cells is not exclusively responsible for the therapeutic effect of PD-1/PD-L1 checkpoint blockade…" [Tang & Zheng 2018]. As such, this study, while not assessing tumour-cell binding, does address how delivery may be improved to leukocytes, cells that are not only a surrogate indicator of drug delivery to tumour cells, but also a cell type that is extremely relevant to PDL1-mediated carcinogenesis.

To further extend this work, an evaluation off what (if any) changes are present when cavitation is utilized to enhance accumulation of other agents, in particular aPD1, the complement agent to aPDL1 in block PD1-PDL1 signalling, and an IgG isotype should be considered. Additionally, as this study observed increases in the frequency and intensity of aPDL1 binding to leukocytes, it would be useful to understand better what leukocyte subpopulations the drug was binding to**.** Additionally, presented by caveat of the current FCM staining procedure, future work may consider switching to a membrane-based live/dead stain instead of a nuclear based stain (7AAD). Membrane-based dyes "…cannot penetrate live cell membranes, so only cell surface proteins are available to react with the dye, resulting in dim staining…" [ThermoFisher Scientific 2019]. On the other hand, "[T]he reactive dye can permeate the damaged membranes of dead cells and stain both the interior and exterior amines, resulting more intense staining work by reacting with free amines" [ThermoFisher Scientific 2019]. Although the membrane-based live/dead differentiation is also a viability dye of

exclusion, utilization of such a membrane-based stain offers perhaps more sensitive differentiation between real cells and membranous debris.

In summary, this study suggests that paring aPDL1 administration with intratumoural cavitation can enhance the intensity of therapeutic antibody binding and the frequency of live-leukocyte binding to antibody. The next study aims to address some of the limitations revealed in this work.

4.7 Comparative FCM of antibody binding frequency and intensity with respect to US treatment across the PD1/PDL1 axis

To better understand the improvements US-mediated cavitation can provide to the delivery of PD1/PDL1 axis blocking agents, this study queried the extent to which cavitation can improve the binding and intensity of aPDL1, aPD1, and isotype antibody binding frequency and intensity to leukocytes 1.5 hours after intervention. Likewise, assay improvements were implemented including the use of a membrane-based live/dead stain instead of DNA-based exclusion dye and the incorporation of additional markers during FCM to interrogate binding within the leukocyte compartment (CD11b to detect myeloid cells and CD3 to discern T cells). In short, this study aims to extend upon previous work to explore relationships between target cell binding, and drug mechanism of action.

4.7.1 Experimental Overview

Bilateral CT26 tumour bearing mice BALB/c mice were administered 200μg of unconjugated aPDL1, aPD1, or IgG2b (control isotype antibody) in addition to SSPs, followed by single-tumour sonication (Fig. 4.7a). The average pre-intervention tumour volume across mice irrespective of assignment was 74.5mm^3 with an SD of 21.4mm^3 (n=4 mice per group, 2-tumours per mouse, 24 tumours total). The mean (absolute value) of the difference between bilateral tumour volumes was 24.5mm^3 with a standard deviation of 15.8mm^3. The median (absolute value) of the difference between bilateral tumour volumes was 19.6mm^3 (ranging from 3.4mm^3 to 61.4mm^3) (Fig. 4.7b).

Approximately 1.5hrs after therapy mice were sacrificed and tumours were excised, processed to a single cell suspension, RBC-lysed, and stained by a membrane-based live/dead stain. Samples were then APC-aIgG2a (to detect aPD1) or APC-aIgG2b (to detect aPDL1 and IgG2b) stained, followed by staining to discern total leukocytes (CD45.2), T cells (CD3), and

myeloid cells (CD11b). In short, the APC channel, which detects APC-aIgG2a or APC-aIgG2b served as the 'reporter' ("anti-IgG") channel for the intensity therapeutic antibody binding while other fluorochromes allowed for the differentiation of leukocyte subsets and of live/dead status. Of note, the aIgG2a stain was accidentally applied to one aPDL1 treated, non-US tumour sample, however, the error was quickly corrected (thorough washing and re-application of the correct stain). The error would be expected to raise the APC signal of the sample (bias against hypothesis), but it did not, so the sample was not excluded from analysis. For additional detail regarding the methods utilized, please see Section 2.6.1.

Samples were acquired via BD FACS Canto II and subsequently gated and analysed in *FlowJo*. Appx. 4.7b outlines the gating hierarchy that was applied to each sample. Debris and dead cell particles were removed from analysis by singlet (FSC-H vs. FSC-A), width (FSC-H vs. FSC-W), size gating followed by differentiation of leukocytes by simultaneous live/dead and $CD45^+$ gating (as defined in Appx. 4.7b). The upper limit of $CD45^+$ expression was difficult to place, owing to an observation events highly expressing $CD45^+$ often co-expressed all other markers—including CD11b, CD3, and anti-IgG. Taken together such an expression pattern would indicate that such events are not true cells but rather a spectral issue. However, not all of the highly expressing $CD45^+$ events behaved in such a manner. In placing the upper limit of the CD45 gate it is acknowledged that it cannot be optimally placed.

Three tumours were harvested from two mice that received no drug injection nor ultrasound, and stained in a manner identical to that of other samples in this study. After FCM acquisition, these no-intervention samples were down-sampled and concatenated, yielding a 'concatenated no intervention controls' file. This file served as the negative control utilized to set gating thresholds of APC signal, the reporter channel for "anti-IgG" (APC-aIgG2a and APC-aIgG2b). The lower limit of the so-called anti-IgG^+ population, the drug-bound cell gate, was determined utilizing the concatenated no-intervention control file, as a negative control. The

lower limit of this gate was drawn to permit no more than a 2% false-positive rate of live, leukocytes ($CD45^+$ cells) (Appx. 4.7c).

Within the live, $CD45^+$ parent population, $CD3^+$, $CD11b^+$, and $CD11b^{++}$ were gated based upon population clustering patterns observed in the concatenated all samples file, then gated by the previously determined anti-IgG gate (Appx. 4.7d-e). Notably, the so termed $CD11b^{++}$ population highly expressed CD45, CD3, and CD11b in a manner suggestive that this population was heavily contaminated by spectral error rather than true marker expression.

4.7.2 Results

The mean CC-G2-calculated integrated cavitation doses were 3.118e-006, 3.910e-006, and 3.483e-006 AUC for IgG+US, aPD1+US, and aPDL1+US tumours respectively with standard deviations of 1.565e-006, 2.282e-006, and 1.178e-006 AUC. One-way ANOVA with Tukey multiple comparisons found no significant difference between groups (Appx. 4.7a). Significance in all other plots in this section were individually assessed by two-way ANOVA (US status and drug as factors; matching by mouse—bilateral tumours) with Sidak's multiple comparisons test (single pooled variance); further clarification provided in 2.8.

In aPDL1-dosed mice, it was evident that ultrasound-treated tumours had a significantly greater frequency and intensity of aPDL1 binding to live leukocytes (Fig. 4.7c-d) compared to contralateral, non-US-treated tumours. However, no similar enhancement was observed when mice were dosed with aPD1 or isotype control antibody (Fig. 4.7c-d). The anti-IgG florescence intensity of live leukocytes in aPDL1 administered mice significantly ($p<0.0001$) increased, with mean anti-IgG MFI increasing from 420 to 822 APC MFI when tumours were US treated. Likewise, the frequency of aPDL1-bound (anti-IgG+) live leukocytes significantly ($p<0.0001$) increased on average from a mean of 13.1% to 32.4% in non-US exposed vs. US-treated tumours. No robust changes were observed in the frequency or intensity of live leukocytes from

tumours of mice administered aPD1 or IgG with respect to ultrasound (Fig. 4.7c-d), though it is worthwhile to note that leukocyte (and/or leukocyte subset) counts were low in this study, even reaching <50 in certain aPD1 and IgG samples.

Figure 4.7 FCM Detection of Antibody Binding to Leukocytes +/- Cavitation

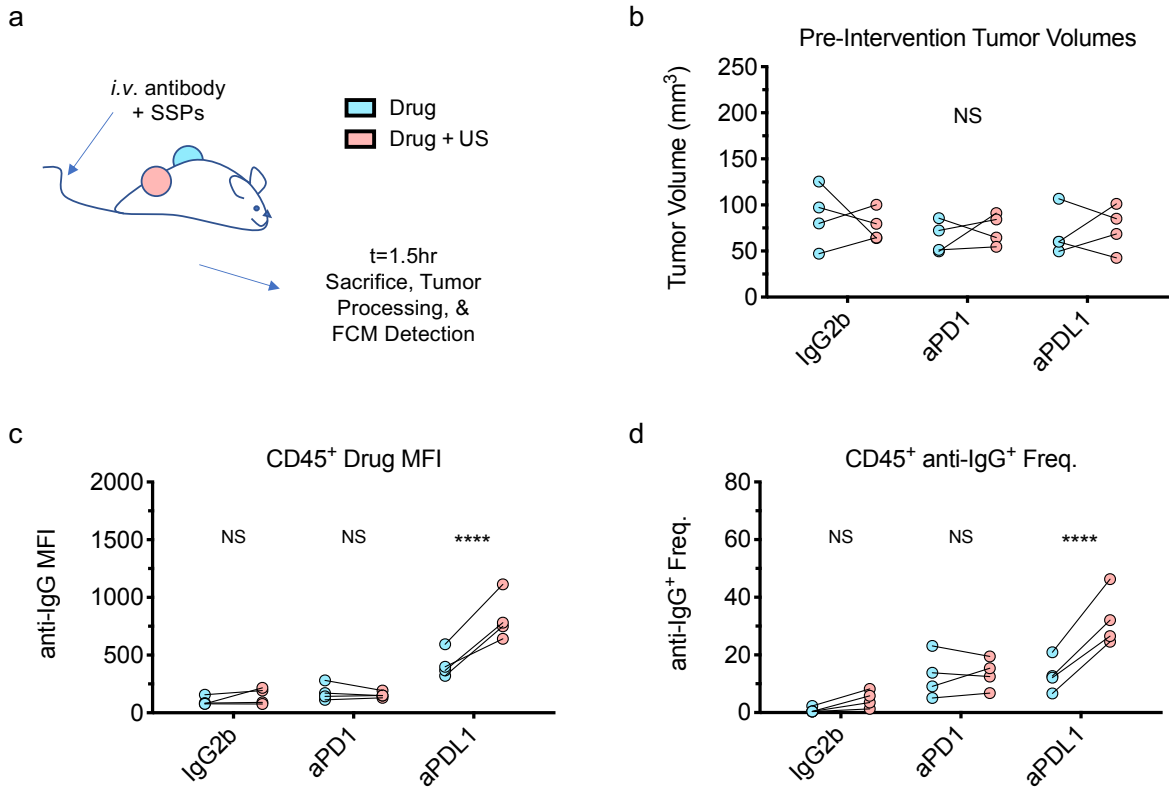


Figure 4.7:
a) 200μg of unconjugated IgG2b, aPD1, or aPDL1 were intravenously administered to bilateral CT26 tumour-bearing mice. One of two tumours was targeted with focused ultrasound, generating cavitation intratumorally monitored by PAM. Mice were sacrificed ~1.5hrs-post intervention and their tumours were excised, washed, weighted, washed, mechanically processed, washed, blocked, and stained for the assessment of live leukocyte-drug binding. Drug was detected by 'anti-IgG'—an APC-channel-compatible secondary antibody (anti-IgG2a for samples from aPD1 dosed mice or anti-IgG2b for samples from aPDL1 and IgG dosed mice).
b) Pre-intervention tumour volumes. Significance assessed by RM two-way ANOVA (US status and drug as factors; matching by mouse) with Sidak's multiple comparisons test (single pooled variance). Lines connect paired tumours
c-d) Live leukocyte anti-IgG (APC channel) median fluorescence intensity (MFI) and (d) the frequency of anti-IgG+ events out of live leukocytes (CD45+ events). Gating hierarchies are defined in Appx. 4.7b-c. MFI or frequency in each plot assessed by RM two-way ANOVA (US status and drug as factors; matching by mouse) with Sidak's multiple comparisons test (single pooled variance). Lines connect paired tumours

Immune subset analysis revealed even larger increases in the frequency and intensity of aPDL1 to T cells ($CD45^+CD3^+$ cells). In aPDL1-dosed mice, anti-IgG MFI increased from a mean of 295 to 778 in APC MFI, and the aPDL1-bound frequency (anti-IgG+ frequency) increased from a mean of 5.7% to 27.6% in US treated tumours compared to contralateral

tumours of aPDL1-dosed mice. Notably the MFI and frequency did not robustly change in tumours of mice dosed IgG or aPD1 irrespective of ultrasound treatment (Appx. 4.7f-g). Within the $CD45^{+}CD11b^{+}$ population, a mean increase in anti-IgG MFI (from 596 to 1094 APC MFI) and frequency of aPDL1-bound cells (from 17.15% to 46.80%) were observed in cells harvested from aPDL1+US treated tumours compared to contralateral aPDL1 (no US) tumours. No such significant changes in anti-IgG MFI nor anti-IgG+ frequency were observed in $CD45^{+}CD11b^{+}$ cells with respect to US treatment in IgG nor aPD1 dosed mice (Appx. 4.7h-i).

Changes in the APC MFI and the frequency of anti-IgG+ cells of the $CD11b^{++}$ subset of $CD45^{+}$ cells in aPDL1 administered mice were not consistent with changes observed in other populations (Appx. 4.7j-k). In fact, in this population, a decrease in US-treated tumours compared to contralateral controls was observed with respect to MFI and anti-IgG frequency. Further inspection of this population revealed that this population had a number of events which highly expressed CD45, CD3, and CD11b in a manner suggestive that this population is actually a spectral error and not real cells. In short, while there may be have some cells in it, there is little confidence that the acquired events are not artefact.

Notably, marked changes were not detected in the MFI or frequency of the total live or $CD45^{-}$ (live, non-leukocyte) populations across any drug group in this study (Appx. 4.7l-o). While these results seem to contradict previous findings (see Appx. 4.6e-h), it remains unclear as to whether the $CD45^{-}$ population defined in this, the previous FCM study, or both studies are actually valid. Given that both studies lack a positive selection marker it is not possible to definitely say what this population represents.

Although this study did present challenges to data analysis, taken together the data suggests that US-mediated cavitation significantly enhances aPDL1 but not aPD1 nor IgG binding intensity and frequency in total live leukocytes and $CD3^{+}$ and $CD11b^{+}$ leukocyte subsets recovered from ultrasound exposed tumours.

4.7.3 Discussion

Limitations

Given the limited number of mice in this study, if a given tumour was deemed too difficult (multinodular) to target with US, its contralateral side was assigned to US. The goal of assignment was to have overall tumour burdens distributed equally across drug-only and cavitation-enhanced groups. This practice likely biases the study against the hypothesis because it is likely that drug delivery to smaller tumours/multinodular masses would be better than in larger tumours which feature greater regions of necrosis/access barriers.

One caveat of this study and the previous FCM study emerged during review of this study. One possibility is that the improved drug binding intensity and bound-drug frequency of leukocytes could be attributed to *ex vivo* drug binding during tissue-processing rather than an *in vivo* drug binding as a result of better distribution of drug. In short, it is a possibility that unbound but tumour deposited drug bound cells during the tumour cell processing and isolation. Whereas in the previous study where tumours were collected from mice approximately 24hrs-post procedure, in this study tumours were collected 1.5hrs after the procedure, which means that the lymphatic system had less time to clear away perivascular trapped, unbound drug. Essentially by sacrificing the mice at 1.5hrs instead of 24hrs less time may have been provided for the tumours to be naturally *in vivo "*washed" to remove unbound drug. This earlier time point was selected intentionally, in order to better capture the influence of US while minimizing biological effects and passive accumulation that might evolve over 24hrs.

It would be very challenging to control for this limitation; one technique that would begin to address this issue would be to perfuse the tumours with saline in order to drive drug out of the vascular space, similar in technique to work by Madaio et al 1987 who saline-perfused kidneys for kidney staining [Madaio et al 1987]. However, unlike kidneys which have a tightly conserved anatomy, identifying a tumour feeding vessel may not be feasible.

Furthermore, it is notable that tumours in this study were effectively washed in buffer prior to tumour mashing, as the tumours were collected post-excision into buffer and then placed into fresh buffer after weights of the tumours were recorded. Likewise, after tumour homogenization, tumour suspensions were washed aggressively leaving minimal opportunity for post-processing binding of 'free' antibody.

Additionally, *in vivo* 1.5hr elapsed before mice were sacrificed. This may have allowed for sufficient time to elapse such that un-bound antibody was effectively 'washed-out' from the tumour environment. However, it is difficult to directly assert this given the lack of information regarding intratumoural, interstitial fluid flow rates in CT26 tumours. Work to measure or model interstitial fluid velocities often estimate velocities from 0.1 to 10um/second, though accurately predicting the interstitial fluid flow is challenging [Munson & Shieh 2014]. Additionally, it is unclear how these interstitial fluid rates might change owing to the increased presence of an antibody and/or disrupted or shear-stressed endothelia as a result. Although literature is sparse as it relates to the wash-out of cavitation-enhanced delivery of antibodies, a paper from 1992 reported some details regarding the local retention of a radiolabelled antibody administered intratumorally to antigen-expressing (SW116) and antigen-deficient (KB) tumours [Kitamura et al 1992]. Wash-out kinetics are reported as the percentage of injected dose divided by the grams of tumour; results show that there is greater antibody retention in tumours that express antigen (SW116) as compared to tumours that lack the antigen (KB) targeted by the antibody administered (Figure 2b of the paper). Unfortunately, the actual tumour weights for the mice of this figure could not be found in the manuscript and as such it is difficult to assert exactly how much of drug was locally retained in either condition. Nevertheless, the curves shown illustrate that local antibody decreases over time, in what appears to be an exponential fashion.

Microscopy may best hold the key in confirming whether or not aPDL1 binding is truly improved by cavitation. In the preparation of microscopy tissue, tumours can be excised and

then flash-frozen; eliminating the opportunity for *ex vivo* binding to occur. Such work is addressed in the next subsection.

Another point of further consideration was the use of RBC lysis buffer. The RBC lysis step was introduced to facilitate the removal of red blood cells to reduce noise in the data. Strikingly, in this study compared to the study in Fig. 4.6 where RBC lysis was not used, a dramatic reduction in the frequency and number of live, non-leukocyte events was observed. This could mean that there were many RBCs contaminating the study shown in Fig. 4.6 or that non-RBCs (i.e. tumour cells) were being lysed in this study. In either case, core to addressing this question is not only to assess tumour-cell sensitivity to RBC lysis, but more importantly, identifying a suitable tumour model (i.e. RFP-expressing tumour line) or marker in order to positively select for tumour cells [Carloni et al. 2013]. However, it is worthwhile to note the incorporation of a reporter, can change the intrinsic immunogenicity of the tumour cell-line [Yuzhakova et al. 2015].

Implications

This study observed that cavitation treated tumours of mice bearing two tumours dosed *i.v.* with aPDL1 had significantly greater aPDL1 (by drug intensity and degree of therapeutic aPDL1 binding to total leukocytes) as compared to contralateral tumours. Leukocyte subset analysis found similar enhancements in aPDL1 intensity and degree of aPDL1 binding to T cells (CD45+CD3+), and myeloid-like (CD45+CD11b+) leukocytes. Robust, similar trends were not observed in IgG or aPD1 administered mice. The results here directly extend the results of Fig. 4.6, where elevations in live-leukocyte, aPDL1-binding were observed as well. This study provides strong confirmatory proof not only because the experiments took place at different times, but also because the tumour model was improved (here a bilateral model was used), and the FCM staining protocol was refined. Given that leukocyte PDL1 expression is an important mediator of tumour immune evasion [Munn 2018] and that aPDL1 paired with cavitation can improve the frequency and intensity of drug binding to live leukocytes (as shown in this study

and the previous FCM-study), there is mounting mechanistic rationale for why pairing aPDL1 with cavitation could improve drug efficacy, as observed in survival studies.

Drug agnostic or agent-specific improvements in delivery?

Superficially, the results here seem to contradict the results of the IVIS studies, where drug accumulation also improved for aPD1 and IgG2b. However, closer inspection reveals that the differential effects are consistent with mechanistic differences between aPDL1 and IgG2b or aPD1.

The lack of a robust increase in IgG2b binding intensity and frequency aligns with its inability to specifically bind to antigens. By intention, the isotype control antibody is not expected to bind to any specific target [CrownBio 2018], and likewise, because it has no intratumoural antigen to bind, there is little to promote its capture by Fc receptors which are thought to preferentially bind antibodies that have clustered (bound to a target) [Zhao et al 2019]. In short, IgG2b has very few (if any) binding partners within the TME, though it can be reasoned that small increases in non-specific binding would occur in a dose-dependent manner. Work by Kitamura et al with radiolabelled, intratumorally-injected antibody is relevant to highlight. Their work shows that a greater concentration of antibody is retained in tumours that express antibody-recognizable antigen as compared to tumours that lack the antigen targeted by the antibody [Kitamura et al 1992]. Mechanistically they propose that, “[a]ntigen-specific monoclonal antibody can presumably retain a drug on the cancer cell surface by antigen-antibody interaction, inhibit the absorption of the drugs from the interstitial space into the blood, and maintain a high concentration of the drug at the target are” [Kitamura et al 1992]. This work begins to addresses the disconnect observed in the studies presented in this chapter, where the intratumoural aPDL1 and IgG2b could both be enhanced (i.e. analogous to intratumoural injection), yet, only a robust improvement in aPDL1 binding was observed—perhaps the only antibody with a widely-expressed binding partner within the TME.

In the case of aPD1, at least two phenomena could explain the results: 1) saturation of PD1 in both passively administered aPD1 and aPD1+US tumours—i.e. the drug's target is easily accessible even without the generation of cavitation, and 2) a lack of PD1 expression within the tumour (i.e. any observed increases in aPD1 binding could be related to non-specific binding interactions).

PD1 expression rises after T cell activation and is thought to decrease as antigen is cleared [Sharpe & Pauken 2018]. However, in the context of abundant, uncleared antigen, PD1 expression is maintained. What remains unclear mechanistically, is where exactly aPD1, a systemically administered drug, binds to the T cell expressed PD1. The results of this study, would seem consistent with aPD1 binding to its target in an environment unrestricted by drug delivery, as improving tumour-delivery (as shown in IVIS studies) did not robustly improve aPD1 binding frequency (as shown in this study). Beyond the tumour, there are ample opportunities for the T cell to easily engage with aPD1—including the lymph nodes where they are activated, systemic blood which they must travel in, and the perivascular space (where drug can easily accumulate) of tumours—each step of the cancer immunity cycle prior to the infiltration of the TIL to transport-challenged regions of tumour [Chen & Mellman 2013]. In fact, a 2019 study by Pluim et al. to assess the receptor occupancy of peripheral blood cells after aPD1 administration notes that "[s]hortly after infusion of nivolumab, receptor occupancy on CD8+-T-cells was 98%" [Pluim et al. 2019]. Put simply, one key reason no robust improvement in aPD1 binding was observed, could be that PD1 expressed in the tumour was already drug-saturated because the PD1 was able to bind to its target without a drug-delivery barrier restricting drug from accessing its target. To clarify the dominant factor (a lack of target expression OR target saturation), future work, could directly query tumour PD1 saturation, in a manner like that of Pluim et al. with peripheral blood [Pluim et al 2019], or similar work by Naing et al. 2019 and Fu et al 2019 [Naing et al. 2019, Fu et al 2019].

Curiously, within the lymphocyte (CD3) compartment of mice receiving aPDL1, increases in APC MFI and anti-IgG2b frequency were observed. This in itself is not surprising, given that PDL1 expression by T cells has been previously documented [Latchman et al 2004, Amarnath et al 2010, Mezache et al 2015]. However, what is curious is the disconnect between the improvement in T cell aPDL1 binding, but not aPD1 binding. One hypothesis that could explain the disconnect is that US-mediated cavitation induces PDL1 expression (but not PD1 expression). Recalling that mice in this study were sacrificed approximately 1.5hrs after therapy, this time interval could have allowed the development of an innate interferon response. In fact, it has been shown that Treg PDL1 expression can be partially induced via an IFNb mechanism [Chevalier et al 2018]. This brings to light another possible mechanism by which aPDL1+US improves efficacy outcomes of aPDL1—cavitation generates some degree of inflammation or cell stress that drives PDL1 expression. Drug present in that local environment is able to bind the cells that now express or highly express PDL1. As a result, greater cytotoxic effect is generated. Further mechanistic studies, assessing the immune populations up or downregulated in response to aPDL1+US are therefore critical—as explored in the last chapter.

In summary, in this study it was observed that cavitation could robustly improve the binding intensity and frequency of aPDL1 but not aPD1 nor IgG2b in live leukocytes. Likewise, this study suggests that mechanistic differences in drug specificity (i.e. aPD1 vs. aPDL1) dictate differential intratumoural binding ability despite drug-agnostic drug accumulation improvements that cavitation can provide.

4.8 Quantitative microscopy of aPDL1-treated, bilateral CT26 tumour bearing mice

While IVIS and flow cytometry studies each illustrated the extent to which US-mediated cavitation can improve drug accumulation and expand the breadth to which aPDL1 may engage with ligand within the TME, the distribution of the drug as of yet has not been fully addressed. To this end, microscopy can enable-direct visualization of drug post-treatment. In this study, microscopy is utilized to assess the delivery of aPDL1 in the CT26 bilateral tumour model.

4.8.1 Experimental Overview:

Four bilateral CT26 tumour bearing mice were administered 200μg of unconjugated aPDL1 and SSPs (Fig. 4.8a). One of two tumours was sonicated, and each mouse was sacrificed approximately 1.5hrs after therapy (see section 2.4). Paired, bilateral tumours from a given mouse were excised, OCT-embedded into a single block then gradually frozen by dry ice via isopentane (or equivalent). The paired, bilateral tumours were frozen adjacent to each other in a single block, to enable each cryosection to feature tissue from an US-treated tumour and its contralateral control tumour. Cryosections were cut, prepared for imaging, and quantified by *Oxford Nanoimaging Ltd*. In brief, three cryosections per block were washed, fixed, blocked, and sequentially stained to enable imaging of bound-aPDL1 (via aIgG2b), vasculature (via endothelial marker CD31), and nuclei (DAPI). Images were quantified utilizing Li thresholding of the non-US treated tumour tissue of a given cryosection by *Oxford Nanoimaging Ltd*.

The average overall tumour volume irrespective of group assignment was 78.2mm^3 with a standard deviation of 24.3mm^3 (n=4 mice total, 8 tumours). The mean absolute value of the difference between bilateral tumour volumes was 34mm^3 with a standard deviation of 32mm^3. The median absolute value difference between contralateral tumour volumes was 29.1mm^3

ranging from 5.7mm^3 to 72.2mm^3. Paired student t test of revealed no significant difference between pre-intervention tumour volumes (Fig. 4.8b).

Figure 4.8: Quantitative Microscopy of aPDL1-Treated, Bilateral CT26 Tumour Mice (1/3)

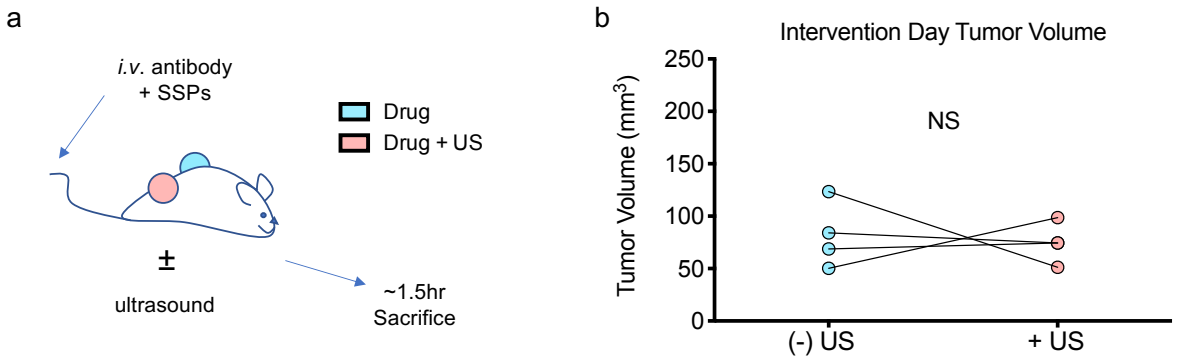
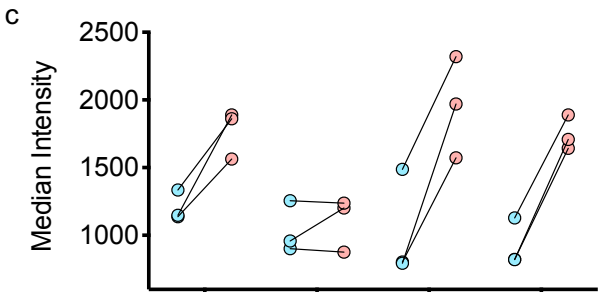


Figure 4.8:
a) aPDL1 was i.v. administered to (4) bilateral CT26 tumour-bearing BALB/c mice. One of two tumours was targeted with focused ultrasound, generating intratumoural cavitation. ~1.5hrs after intervention, mice were sacrificed, and their bilateral tumours were embedded into a single OCT block for cryosectioning
b) Pre-intervention tumour volumes were not significantly different as determined by paired t test. Lines connect paired tumours

4.8.2 Results

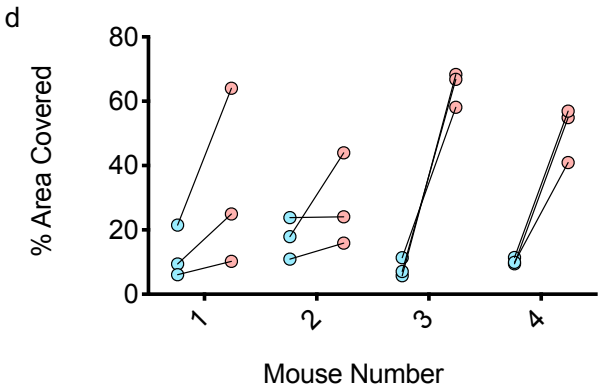
The average integrated cavitation dose, as calculated by CC-G2 analysis, was 3.323e-006 AUC with an SD of 1.458e-006 AUC (Appx. 4.8a). No clear correlation was observed between vasculature (as detected by anti-CD31) and aPDL1 (as detected by anti-IgG2b) stain intensity or area coverage. This suggests that that vasculature was similar between US-treated and non-sonicated tumours (Appx. 4.8b-c). Analysis of quantitative microscopy revealed that US-treatment has a highly significant effect upon both the intensity (a surrogate of quantity) and distribution of aPDL1 (area coverage) within tumour tissue, as per repeated measures two-way ANOVA analysis (Fig. 4.8c-d). The RM two-way ANOVA analysis defines treatment and mouse as factors and employs matching by cryosection (to account for the paired nature of the bilateral tumour tissue on a given cryosection). Representative images of the tumour sections, along with single-channel inlets are shown in Fig. 4.8e (prepared by Oxford Nanoimaging, Ltd).

Figure 4.8: Quantitative Microscopy of aPDL1-Treated, Bilateral CT26 Tumour Mice (2/3)



Source of Variation	% of total variation	P value	P value summary
Mouse x Treatment	14.96	0.0007	***
Mouse	15.86	0.1600	ns
Treatment	48.08	<0.0001	****
Cryosection	18.81	0.0037	**





Source of Variation	% of total variation	P value	P value summary
Mouse x Treatment	16.82	0.0125	*
Mouse	6.947	0.3599	ns
Treatment	54.81	<0.0001	****
Cryosection	15.04	0.1237	ns

Figure 4.8 continued:
c-d) The Oxford Nanoimaging-calculated MFI of anti-IgG2b (related to aPDL1 quantity within the tissue) (c), and the percentage of aPDL1 coverage in a given tissue (as detected by anti-IgG2b) (d) are shown on a per mouse basis. Tissue from a given cryosection is connected by a line (three cryosections per mouse). Each data set (median signal intensity or area coverage) was assessed by RM two-way ANOVA (treatment and mouse number as factors; matching by cryosection)

The paired fold change (FCs) in drug quantity (by MFI) was 1.62x and the paired FC in drug distribution was 4.47x. The paired FC in MFI was calculated by first calculating the FC in MFI on a per cryosection basis. Next, the mean paired FC of all cryosections from a given mouse was calculated, 'mPFC'. Lastly the mean of mPFC values (averaging across the four mice) was calculated, yielding the paired FC in drug quantity (by MFI). An equivalent process was utilized to calculate the paired FC in drug distribution. Across all images (no pairing), the anti-IgG2b MFI increased from a mean of 1049 to 1644 and aPDL1 area coverage (distribution) increased from a mean of 12% to 44.1% in non-US vs. US tumours.

Figure 4.8: Quantitative Microscopy of aPDL1-Treated, Bilateral CT26 Tumour Mice (3/3)

e

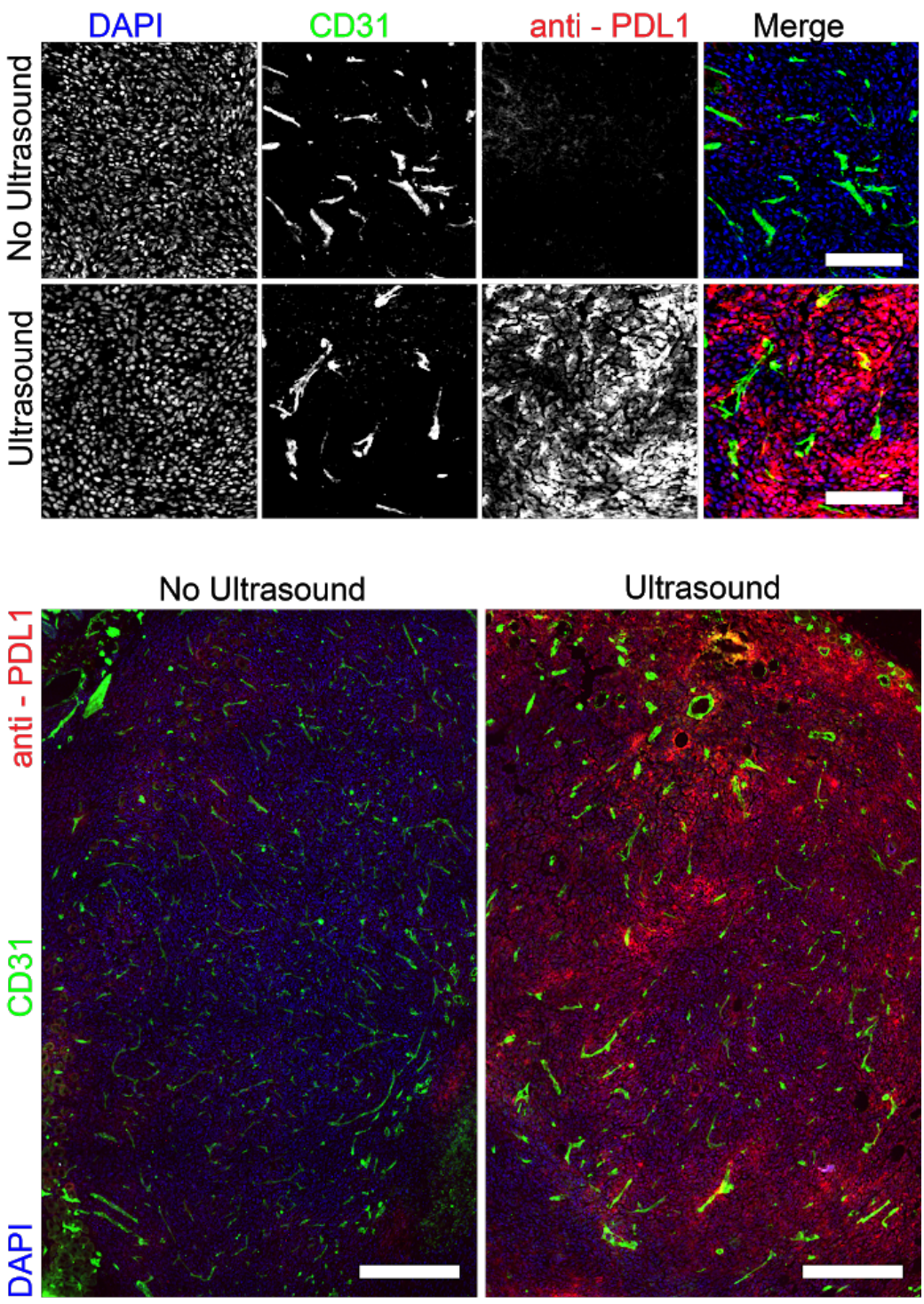


Figure 4.8 continued:
e) Representative single-channel images of DAPI (nuclei), CD31 (vasculature), and IgG2b (therapeutic aPDL1 drug detection), then merged together above representative images of tumours treated with or without sonication following the administration of aPDL1 and SSPs (prepared by Oxford Nanoimaging, Ltd.)

4.8.3 Discussion

This study observed that pairing aPDL1 with cavitation could improve the accumulation and distribution of tissue-bound aPDL1. These results are important for three core reasons. First, the results extend qualitative work by Kwan et al. 2015 who first illustrated that the cavitation of SSPs could enhance the distribution of an IgG antibody [Kwan et al. 2015]. In the present work, not only are similar qualitative changes are observed, but also quantitative increases in drug binding and coverage are documented, providing further evidence that cavitation can indeed bolster intratumoural drug delivery.

Second, the paired FC in drug distribution was 4.47x in US-treated tissue over contralateral non-sonicated ('drug-only') tissue. This number exceeds, though is consistent with the results of IVIS work, which observed paired FCs drug-accumulation ranging between 2.15 to 3.01-fold across the four agents tested in bilateral CT26-tumour bearing mice.

Third, it is important to highlight the wet-lab protocol utilized in this study. Notably, cryosections were washed prior to fixation and immunostaining in this study. This was done intentionally in order to query tissue-bound aPDL1 and minimize/eliminate the possibility that unbound aPDL1 could bind tissue *ex vivo* during processing. A caveat of previous flow cytometry work (Fig. 4.6 and 4.7) was uncertainty regarding whether cells were binding tumour-deposited, but unbound therapeutic antibody *ex vivo* during FCM-processing. In short, the microscopy results reinforce the findings of the FCM studies and suggest that *ex vivo* binding in the FCM studies likely not a driving factor of the observed results.

Beyond utilizing the microscopy approach implemented here to assess other time-points after intervention, and interventions utilizing other drugs, future work can begin to expand upon the findings here by improving the breadth of imaging and integrating additional markers. Approaches recently reported can allow for whole-organ imaging, such as recent work by Frétaud et al. to image zebrafish testis at a high-resolution [Frétaud et al. 2017]. The ability to

image drug-delivery in a whole-tumour would dramatically improve the quantitative characterization of drug-distribution throughout the tumour. Likewise, the ability to integrate additional markers (such as to detect immune subsets and un-bound PDL1 expression) to the microscopy strategy would allow for quantitative, cell-level based elucidation of drug-binding events. Recent work by Li et al. has demonstrated that multiplex immunofluorescence can in fact be integrated with tissue-clearing, allowing for quantitative analysis of large tissues [Li et al. 2017]. In short, improvements in the microscopy approach utilized could be of great value in characterizing the improvements in drug delivery SSP cavitation is able to drive.

4.9 Chapter Summary, Limitations, and Future Directions

Through a multi-modal approach, the results in this chapter suggest that US-mediated cavitation can enhance intratumoural drug delivery. After establishing that antibody could be near-infrared conjugated and imaged *in vivo* (4.1), the accumulation of NIR-conjugate aPDL1 was evaluated in mice bearing single tumours treated with or without cavitation (4.2). Although live-animal imaging did not resolve significant differences, IVIS-imaged excised tumours revealed that cavitation-treated tumours contained a significantly greater CBA, a surrogate for drug concentration within the tumour. 4.3 evaluated how the CBA of bilateral tumours from changed after single-sided sonication after the administration of four different agents. This study revealed that US-mediated cavitation could significantly increase drug accumulation in US-treated tumours over contralateral control tumours. In fact, this corresponded with paired ~2 to 3 fold increases in CBA (between all tumours of a given drug). Evaluating the generalizability of this drug-device approach, (4.4) observed that aPDL1 accumulation in bilateral EMT6 tumour bearing mice could also be enhanced by cavitation.

The results from IVIS studies motivated an evaluation of drug binding within the tumour microenvironment with respect to ultrasound treatment, utilizing a flow cytometry approach validated in (4.5). FCM analysis of tumours collected from mice administered aPDL1 with or without cavitation (4.6) suggested that live leukocytes harvested from US-treated tumours had a significantly greater number of cells (a greater frequency) that were aPDL1-bound and that these cells bound more drug (greater MFI intensity). This hypothesis generating work, drove interest in confirming the response in bilateral tumour bearing mice (4.7) across a broader range of agents (aPD1, aPDL1, and IgG2b). Consistent with the IVIS and ~24hr-sacrificed mouse studies, pairing aPDL1 administration with cavitation increased the frequency and intensity of aPDL1-bound (total) leukocytes compared to mice tumours that received the same systemic drug but no US. Notably, however, in this study it was observed that the intensity of drug binding

to total, live leukocytes did not robustly improve in the US-treated tumours of IgG2b or aPD1 dosed mice. Microscopy to assess aPDL1 distribution and intensity (4.8) addressed a question left unanswered by the FCM studies, in which it could not be ruled out that antibody had bound to cells *ex vivo.* Microscopy to detect tissue-bound aPDL1 observed that both drug intensity and distribution significantly increased in US-treated tumours compared to contralateral control tumour and re-confirmed previous results suggesting that cavitation does not create appreciable tissue damage as per H&E staining in (4.3).

Taken together, the results provide a strong mechanistic support for the hypothesis that cavitation can enhance intratumoural antibody accumulation, binding, and distribution provided that the drug's target is present. Limitations were identified and reviewed in each respective subsection, where many were addressed in subsequent studies. One of the most intriguing possibilities raised in this work was that of cavitation mediated PDL1 induction. This idea emerged out of work that revealed T cells bound aPDL1 with a greater frequency and intensity in US-treated tumours compared to contralateral controls, whereas a similar phenomenon was not observed in mice administered aPD1. The hypothesis that cavitation may drive aPDL1 expression can be further explored through a better characterization of the immune populations within the tumour and how they change with respect to cavitation. To this end, the next chapter aims to characterize biologic changes with respect to aPDL1+US therapy.

Future Directions

In addition to implementation of the recommendations of Chapter 3, there are several key directions for future work based on the results of this chapter. These largely break down into exploratory work to create new knowledge regarding mechanism and work to better define the already existing work.

To improve the depth in understanding cavitation-mediated drug dynamics future work should consider pursing: 1) Studies to intentionally query the relationship between cavitation dose and drug delivery. Cavitation of varying intensities could be administered allowing for elucidation of the role between cavitation and drug-dose. This work would be impactful because it could inform the acoustic strategy—allowing for the optimization of cavitation such that delivery is maximized. 2) A query of the temporal relationship between drug administration and cavitation. In other words, drug delivery studies in which cavitation is provided before or after drug administration could help clarify the exact physical mechanism by which drug delivery is improved.

To better define the already existing work 1) the development of ELISA or HPLC-based assays to quantify drug density should be considered. In addition to providing additional, multi-modal evidence to support the hypothesis, these modalities could enable an exact, instead of relative, measurement of antibody in tumour—enabling estimation of injected dose through use of a standard curve. 2) Studies should consider evaluating radiolabelled antibody distribution with or without cavitation. Radiolabelling is considered by some to be the gold-standard of bio distribution characterization [Cilliers et al 2017], enabling the accurate quantification over time; which unlike fluorescence it is not as subject to artefact issues. However “...such studies are labor intensive, costly, and require large numbers of animals” [Shah & Betts]. Additionally, the safety regulations and approval necessary could be limiting factors in the utilization of such an approach. of the temporal relationship.

5 Immunologic Correlates of Response

To better characterise the mechanism(s) by which aPDL1+US brings about the anti-tumour activity reported in Chapter 3, the studies described in this chapter were undertaken to understand immunological changes taking place as a result of the improved delivery and distribution of aPDL1 demonstrated in Chapter 4. Immune checkpoint modulation has been reported to influence a range of pathways at both the mRNA and protein level [Wei et al. 2017]. To best capture changes induced by the interventions applied here, techniques were required that allowed the level of a broad range of specific markers to be measured. Hence, through a combination of targeted mRNA transcript analysis (*Nanostring*) and flow cytometry the mechanistic basis of the therapeutic benefit provided by pairing aPDL1 with cavitation is explored in this chapter.

5.1 Gene-Level Changes Driven by aPDL1 Paired with Cavitation

To better understand the biological mechanism(s) by which aPDL1+US brings about anti-tumour immunity, gene-level changes were queried using *Nanostring* transcript profiling. *Nanostring's nCounter® PanCancer Mouse Immune Profiling* enables multiplexed gene expression analysis of 750 genes (and 20 house-keeping controls) related to innate and adaptive immune responses to cancer [Nanostring 2019]. This approach has been utilized by a number of groups to explore the mechanistic basis of other immunologically-active cancer treatments [Yu et al. 2018, Christmas et al. 2018, Zhao et al. 2018, Ghaffari et al. 2018].

The gene level changes are likely attributable to a combination of four factors: a) the administration of aPDL1, b) the presence of intratumoral cavitation, c) the improvement of aPDL1 delivery, and d) time. To investigate such factors, CT26 tumour bearing mice were assigned to 1 of 4 groups then sacrificed at two different time-points. IgG2b-adminsitered mice served as the baseline, no-treatment control and factors (a) and (b) were addressed with aPDL1 and IgG+US intervention groups. Mice were sacrificed either 24hr or 5-days post-intervention

for *Nanostring* evaluation of tumours in an effort to capture the plasticity of response (d). At the 5d-time point, additional tumour tissue not required for *Nanostring* analysis was also assessed by FCM for phenotypic and functional changes with panels modified and optimized from previous work (not shown).

5.1.1 Experimental Setup

A schematic of the study is shown in Fig. 5.1a. BALB/c mice were implanted with single CT26 tumours and treated by a single intervention (see Sections 2.3). Mice were assigned to 1 of 4 groups (IgG2b, IgG2b+US, aPDL1, aPDL1+US), the average pre-intervention tumour volume was 77.1mm^3 with an SD of 12.0mm^3 irrespective of intervention group, and there were therefore NS differences between groups as determined by one-way ANOVA with Tukey multiple comparisons correction (Fig. 5.1b). Throughout this chapter IgG2b (a subclass of IgG), is referred to as IgG. A PAM-informed, adjustable-pressure cavitation strategy was utilized in this study; for further detail, please refer to Section 2.4. Mice were sacrificed approximately 24-hours (“24hr-mice”, n=4/group) or 5-days (“5d-mice”, n=6/group) after their first (and only) intervention.

The post-hoc calculated, average CC-G2 calculated integrated cavitation doses were 4.611e-006 and 3.949e-006 AUC with SDs of 2.319e-006 and 1.955e-006 AUC for IgG+US and aPDL1+US treated mice, respectively (Section 2.2.3). The difference was NS as determined by unpaired student T test.

On day of sacrifice a sample of each tumour was collected in RNALater (Fisher Scientific), incubated overnight at 4°C, then frozen at -80°C for later Nanostring RNA query (see Section 2.7). Mice sacrificed 5-days after intervention were also queried by FCM. Tumour-draining lymph nodes (DLNs), non-tumour draining lymph nodes (NLNs), and extra tumour

tissue from 5d-mice was processed to single-cell suspensions, stained, then acquired via BD FACS Canto II, as per Section 2.6.2.

Figure 5.1: Gene-Level Changes Driven by aPDL1 Paired with Cavitation: Setup

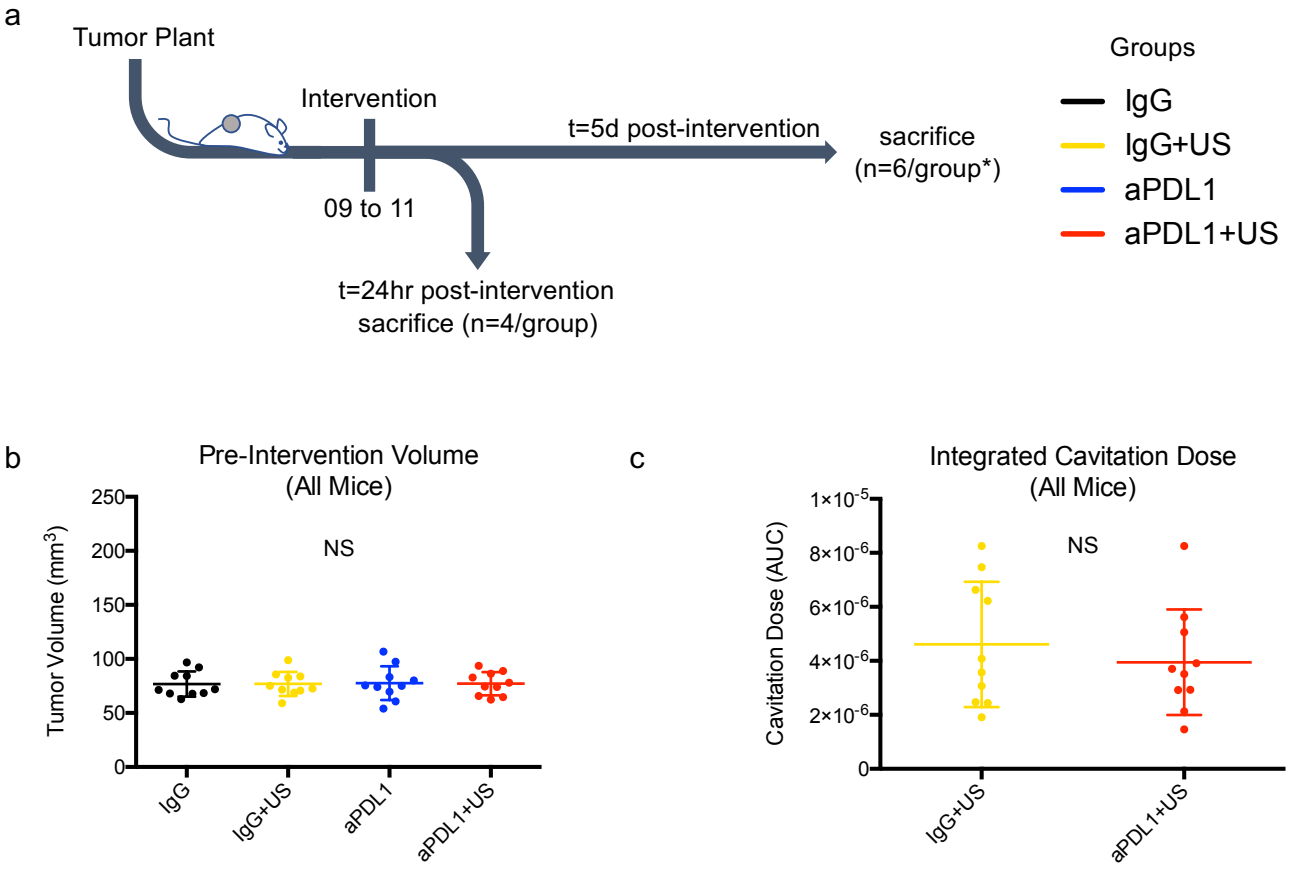


Figure 5.1:
a) BALB/c mice were implanted with a single CT26 tumour. 9 to 11 days after inoculation mice were assigned to 1 of 4 groups. After intervention mice were sacrificed approximately either 24hr (n=4/group) or 5 days post-intervention (n=6/group) for the collection of tumour tissue. *5 (instead of 6) IgG-treated mice were collected at the 5d-time point owing to requisite welfare-sacrifice*
b) Pre-intervention tumour volumes were not significantly different as determined by ordinary one-way ANOVA with Tukey's multiple comparisons test (single pooled variance). Mean and SD shown, n = 10/group
c) The integrated cavitation dose calculated by CC-G2 between IgG+US and aPDL1+US treated mice was NS different as determined by unpaired t test (n=10/group)

5.2 Gene-Level Changes 24hrs After Intervention

5.2.1 Results Overview

Approximately 24hrs post-intervention, mice were sacrificed for the assessment of gene-level changes using *Nanostring*. Although 4 mice per group were sacrificed at the 24hr-timepoint, only three of the four tumours were downstream processed for RNA Nanostring (chosen at random), therefore only 3-mice/group are shown in all subsequent figures for this time point. The excised tumour weights of this subset of mice are shown in Fig. 5.2a and were NS different as determined by one-way ANOVA with Tukey multiple comparisons correction. The integrated cavitation dose of this subset of mice is shown in Fig. 5.2b. The average integrated cavitation dose, as per CC-G2 analysis for IgG+US and aPDL1+US treated tumours averaged 6.43e-006 and 3.183e-006 AUC with standard deviations of 2.51e-006 and 4.48-007 AUC respectively, n=3. Although the cavitation dose was nearly double on average in IgG+US compared to aPDL1+US mice, the difference was NS as determined by unpaired student T test.

Figure 5.2: Gene-Level Changes 24hrs After Intervention (1/4)

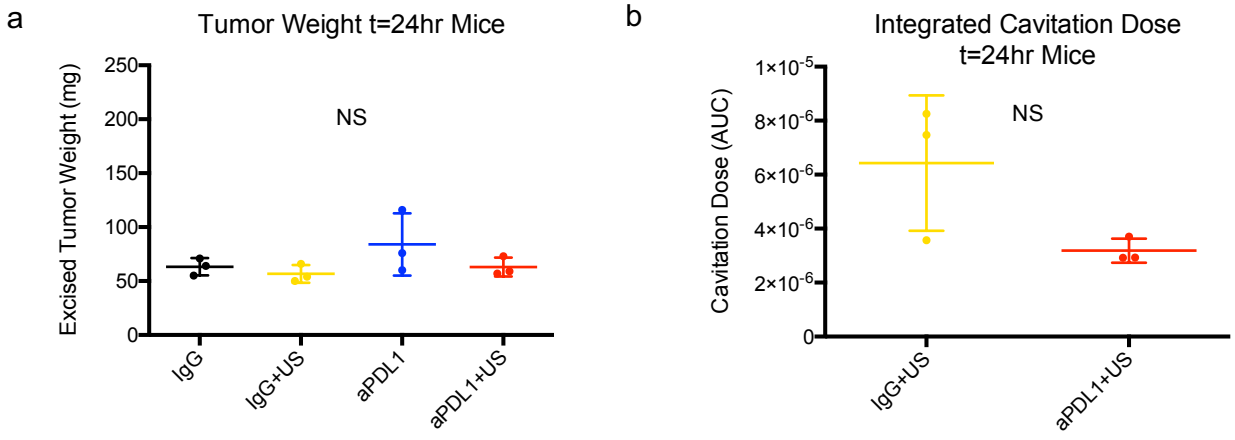


Figure 5.2:
a) Excised tumour weights of mice sacrificed approximately 24hr post-intervention and queried by downstream RNA analysis (n=3/group). Excised weights were compared by ordinary one-way ANOVA with Tukey's multiple comparisons test (single pooled variance)
b) The post-hoc, CC-G2-calculated integrated cavitation dose of mice sacrificed 24-hours post-intervention and queried by downstream RNA analysis (n=3/group), tested by unpaired t test (p = 0.0918), n=3/group.

Fig. 5.2c is a heatmap of pathway scores, which clusters samples (each tumour by column) based on their pathway scores (each row). A given pathway score reflects (summarizes) the changes in expression of a set of genes related to a putative pathway [Nanostring 2018, Zien et al. 2000].

Figure 5.2: Gene-Level Changes 24hrs After Intervention (2/4)

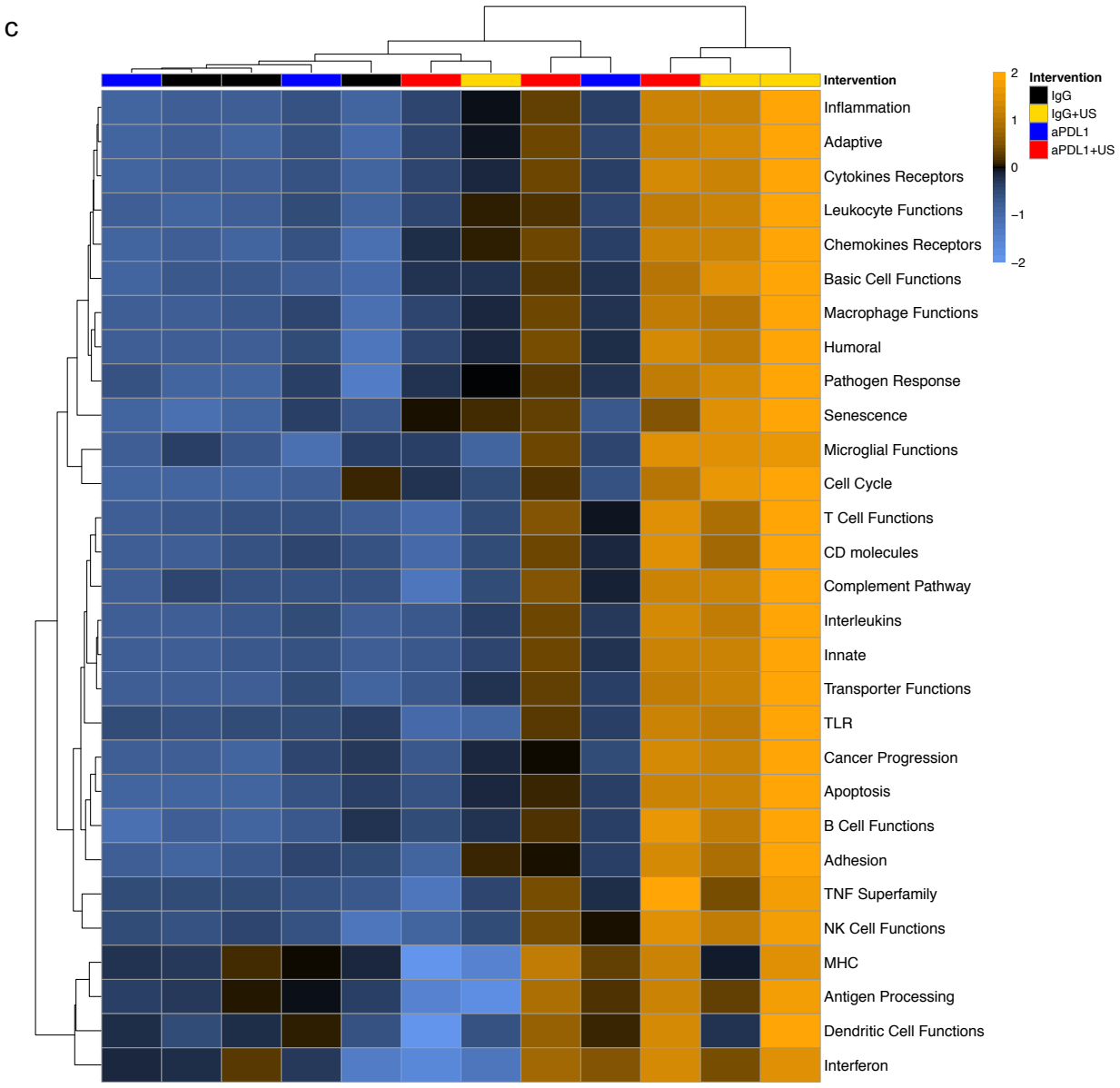


Figure 5.2 continued
c) A heatmap of pathway scores. Pathway scores were calculated in nSolver (Nanostring) then organized by unsupervised hierarchical clustering (Euclidian distance). Orange indicates increases in pathway score (enrichment), whereas blue indicates decreases in pathway score.

Fig. 5.2d-g explores how gene expression in experimental groups compares to that of expression in IgG-treated mice, so called differential gene expression at the 24hr-time point. Fig. 5.2d presents a heatmap of differentially expressed genes (DEGs) by group (compared to IgG control) across all transcripts.

Figure 5.2: Gene-Level Changes 24hrs After Intervention (3/4)

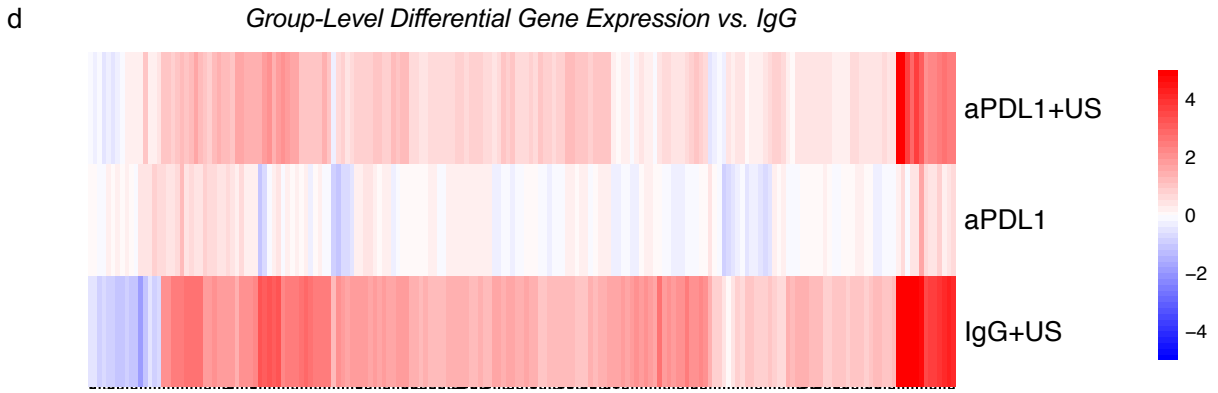


Figure 5.2 continued
d) A heatmap of differential gene expression comparing the gene expression of each transcript in aPDL1+US, aPDL1, or IgG+US treated tumours to that of IgG control treated mice. Upregulation of a gene compared to IgG control is represented by red, whereas down regulation of a given gene is indicated in blue.

Fig. 5.2e illustrates DEGs in a series of volcano plots—enabling direct visualization of the magnitude and significance of differential gene expression for each experimental group (aPDL1, IgG+US, or aPDL1+US) as it compares to IgG at the 24hr time-point. Genes very significantly ($p<0.01$) and differentially (fold change $FC>3$) expressed are labelled in these plots, “top DEGs.”

Figures 5.2f and 5.2g explores the degree to which DEGs are unique or shared between intervention groups as compared to IgG-treated mice. Fig. 5.2f summarizes such similarity/dissimilarity for DEGs that are significantly ($p<0.05$) and differentially (>1.1 fold-change) expressed compared to IgG-mice. Fig. 5.2g, applies more strict criteria, “top DEGs,” which are from here forward defined as DEGs that are very significantly ($p<0.01$) and differentially (>3 fold-change) expressed as compared to IgG-mice.

Figure 5.2: Gene-Level Changes 24hrs After Intervention (4/4)

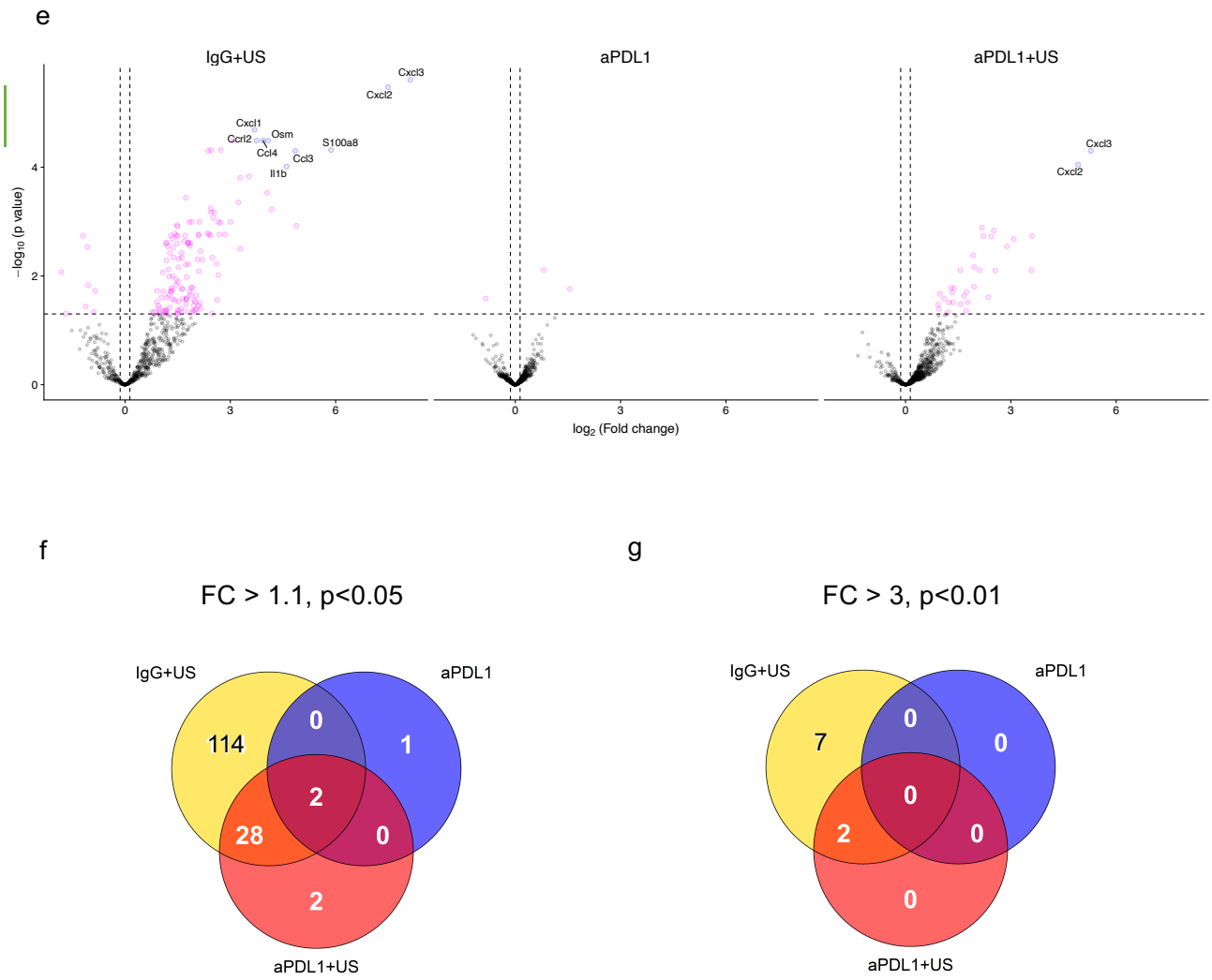


Figure 5.2 continued
e) Volcano plots to illustrate the magnitude and significance of differential gene expression as compared to IgG control. Labelled genes represent the top differentially expressed genes (top DEGs), genes which very significantly (p<0.01) and differentially expressed (>3 FC) compared to IgG. Gene are plotted based on FDR-corrected p-values with the dashed horizontal line representing an FDR-corrected p-value of 0.05. P-values calculated by FDR-adjusted TREAT [McCarthy & Smyth 2009] analysis with Benjamini-Hochberg (BH) Correction
f) Venn diagram summarizing the number of genes at the 24hr time-point that significantly (p<.05) and differentially (>1.1 FC) expressed compared to IgG. P-values calculated by FDR-adjusted TREAT analysis with BH Correction
g) Venn diagram summarizing the number of genes at the 24hr time-point that significantly (p<.01) and differentially (>3 FC) expressed compared to IgG. P-values calculated by FDR-adjusted TREAT analysis with BH correction

The most prominent DEGs are tabulated in Fig. 5.3a and their expression is shown in plots shown in Fig. 5.3b. To better put in context the results of d5 mice FCM data, genes that encode proteins detected FCM (or those closely related), are shown on a per-mouse basis in

Fig. 5.4. Fig. 5.5 displays the results of cell-type profiling for total leukocytes (CD45), macrophages, neutrophils, dendritic cells, NK cells, NK CD56dim cells, total T cells, and $CD8^+$ T cells. *Nanostring* cell-type profiling leverages the co-expression patterns of transcripts to predict cell-type scores [Sharpe et al. 2018, Nanostring 2016], a surrogate for infiltration.

5.2.2 Discussion

On a per-mouse basis, unsupervised pathway clustering (heat map) generally grouped cavitation-treated mice adjacent to each other and grouped IgG or aPDL1 treated mice together (Fig. 5.2c). This clustering pattern begins to suggest that cavitation at the 24hr-time point is a key driver of pathway score, or moreover differential gene expression. Differential gene analysis (Fig. 5.2d-g) further explored this hypothesis.

Qualitatively, the heatmap of differential gene expression across all 700+ transcripts on a per group basis (Fig. 5.2d), illustrated that there were few changes in transcript expression between aPDL1 and IgG mice, whereas a number of genes in cavitation-treated mice were changed. The genes that changed appeared similar in aPDL1+US and IgG+US treated mice (Fig. 5.2d), though not necessarily to same degree of significance or magnitude in fold-change (FC) over IgG control (Fig. 5.2e).

Fig. 5.2f-g quantitatively summarize the degree to which DEGs are unique or shared between intervention groups as compared to IgG-treated mice. As per Fig. 5.2f there were 3, 144, and 32 DEGs ($p<0.05$ and $FC>1.1$) after aPDL1, IgG+US, and aPDL1+US treatment respectively at the 24h-time point. Under stricter criteria, Fig. 5.2g, there were 0, 9, and 2 top DEGs ($p<0.01$ and >3 FC) in the aPDL1, IgG+US, and aPDL1+US groups respectively at the 24h-time point. Taken together, these preliminary results suggest that cavitation alone is a strong driver of differential gene expression, and that for some reason, IgG+US drives a greater number of changes in expression as compared to aPDL1+US, a topic further investigated.

5.3 Most Differentially Expressed Genes, 24hr-Post Intervention

There were 0, 9, and 2 prominent DEGs (p<0.01 and FC>3) in aPDL1, IgG+US, and aPDL1+US treated mice respectively (Fig. 5.2g). As per the table of Fig. 5.3a, the top DEGs of aPDL1+US therapy were not unique, and in fact those same genes were also top DEGs of IgG+US treated mice—Cxcl3 and Cxcl2.

Figure 5.3 Top Differentially Expressed Genes 24hr After-Intervention (1/2)

a

Group:	Top DEGs (compared to IgG): p<0.01 and FC>3									
aPDL1	None									
IgG+US	*Cxcl3*	*Cxcl2*	*S100a8*	*Ccl3*	*Il1b*	*Osm*	*Ccl4*	*Ccrl2*	*Cxcl1*	
aPDL1+US	*Cxcl3*	*Cxcl2*								

Figure 5.3
a) A table of the top differentially expressed genes between the given groups and IgG control. Top DEGs are genes that are very significantly (p<0.01) and differentially (FC>3) expressed.

Further investigation (Fig. 5.3b) of the top DEGs, revealed that all 9 of the IgG+US top DEGs were in fact also significantly upregulated in aPDL1+US treated mice. In short, although the magnitude of DEG FC was different between aPDL1+US and IgG+US treatments, all cavitation-treated mice significantly upregulated Cxcl3, Cxcl2, S100a8, Ccl3, Il1b, Osm, Ccl4, Ccrl2, and Cxcl1. This may reflect the raised (although not significantly so) level of cavitation in the IgG+US group (see Fig. 5.2b).

CXCL1, CXCL2, and CXLC3 are closely related chemokines [Zlotnik & Yoshie 2012] involved in the recruitment and activation of leukocytes, in particular neutrophils, in addition to a number of other functions. While these chemokines work together to promote leukocyte recruitment and activation, these chemokines do have some differential, non-redundant functions. For instance, work by Girbl et al carefully characterized how CXCL1 and CXCL2 act sequentially where CXCL1 supports neutrophil migration along endothelial cells and pericytes, whereas CXLCL2 guides neutrophil infiltration through endothelial junctions [Girbl et al 2018]. Additionally, it has been purported that these chemokines play a role in angiogenesis [Mehrad et al. 2007].

Figure 5.3 Top Differentially Expressed Genes 24hr After-Intervention (2/2)

b

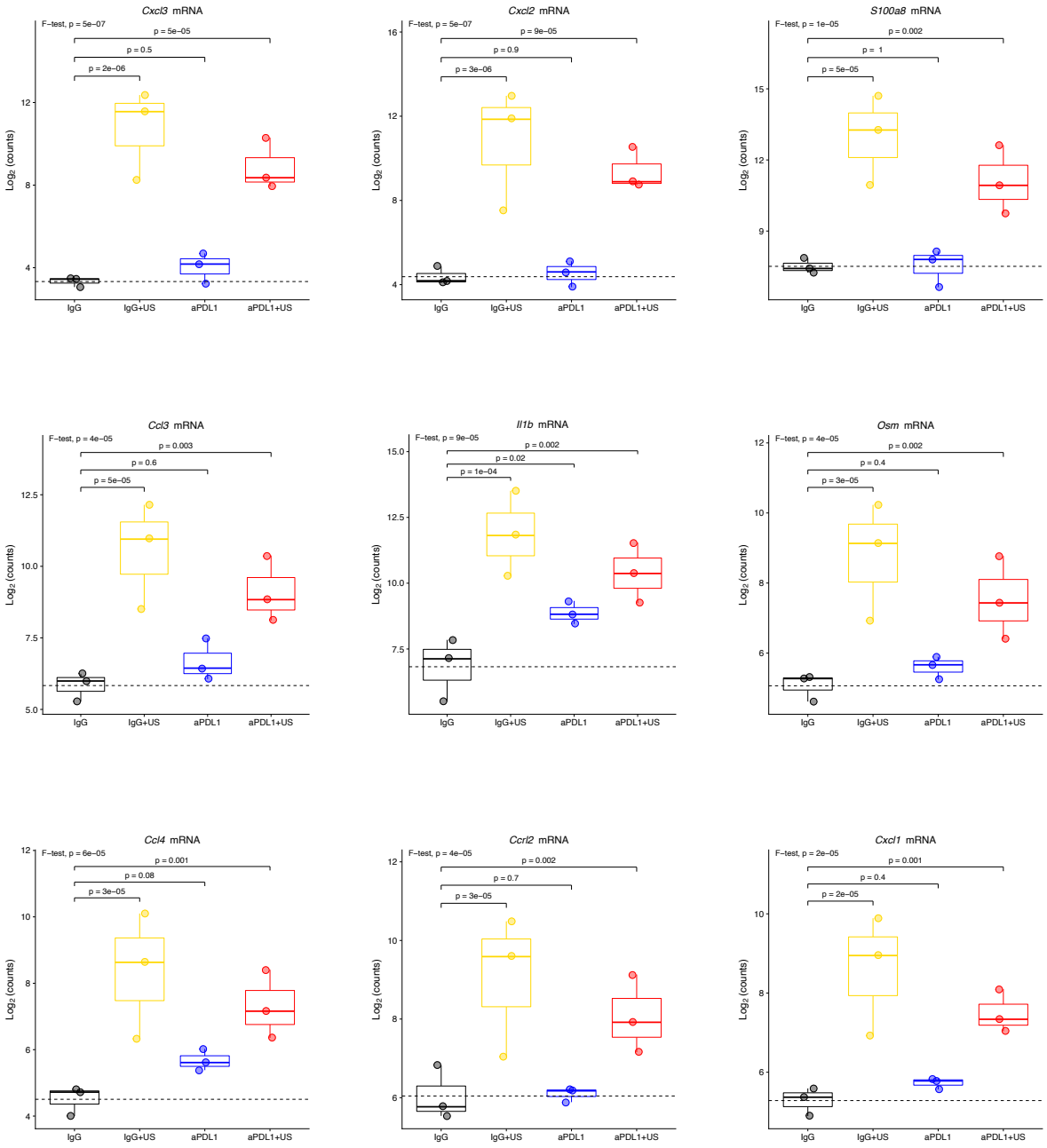


Figure 5.3 continued:
b) Break-out boxplots of top differentially expressed genes, genes very significantly (p<0.01) and differentially expressed (>3 FC) compared to IgG. Boxplot statistics calculated as per 2.7.

CCL3 and CCL4, also known as macrophage inflammatory protein-1 alpha and beta, are inflammatory chemokines, that “induce chemotactic mobilization of monocyte-lineage cells and lymphocytes into inflammatory tissues” [Baba & Mukaida 2014]. In short, the upregulation of CXC family chemokines, CCL3, and CCL4 suggests that innate and adaptive immune cells are being actively recruited in cavitation treated tumours. In a similar vein, cavitation treated tumours also significantly upregulated *Ccrl2*, a chemokine receptor [Del Prete et al. 2013].

Like the chemokines and their receptors reviewed, IL1b, a leukocyte pyrogen, also plays a role in regulating leukocyte infiltration—“promote[ing] the recruitment and retention of macrophages” [Rider et al. 2011]. Macrophages/monocytes are also a major source of oncostatin M (OSM), which was also a top DEG of IgG+US mice, and also significantly upregulated in aPDL1+US treated mice. Notably, “[m]onocyte/macrophages, a primary source of OSM, release OSM upon stimulation with agents such as TLR-ligands or prostaglandins” [Richards 2013]. Taken together, it seems that macrophage/monocyte and other leukocytes in cavitation treated tumours are activated. The role of *S100a8* is less clear, though its upregulation has been reported after US-mediated fractionation [Eranki et al. 2019], and others have shown that *S100a8* may play a role in neutrophil stimulation [Rycman et al. 2003] and NK cell activation [Narumi et al. 2015].

In summary, in cavitation treated mice, a number of genes related leukocyte infiltration or activation were significantly upregulated in cavitation treated tumours—suggesting that cavitation drives an acute, inflammatory response that drives innate and adaptive cells to the TME.

5.4 Effector-Response Related Genes 24hrs After Intervention

A subset of genes that putatively play a mechanistic role in mediating PD1/PDL1 blockade therapy were also plotted on a per-mouse basis. Their function is discussed in greater detail in Section 5.9. At the 24hr-time point, *Fas* and *Cd274* were upregulated in both cavitation groups IgG+US treated mice, and significantly so in the case of *Cd274* in IgG+US treated mice. *Cd274* encodes PDL1; this observation would be consistent with a hypothesis that robust cavitation can drive inflammatory programs, ultimately resulting in the upregulation of PDL1 expression, even as early as 24-hrs post-therapy.

Figure 5.4: Effector-Response Related Genes 24hrs After Intervention (1/2)

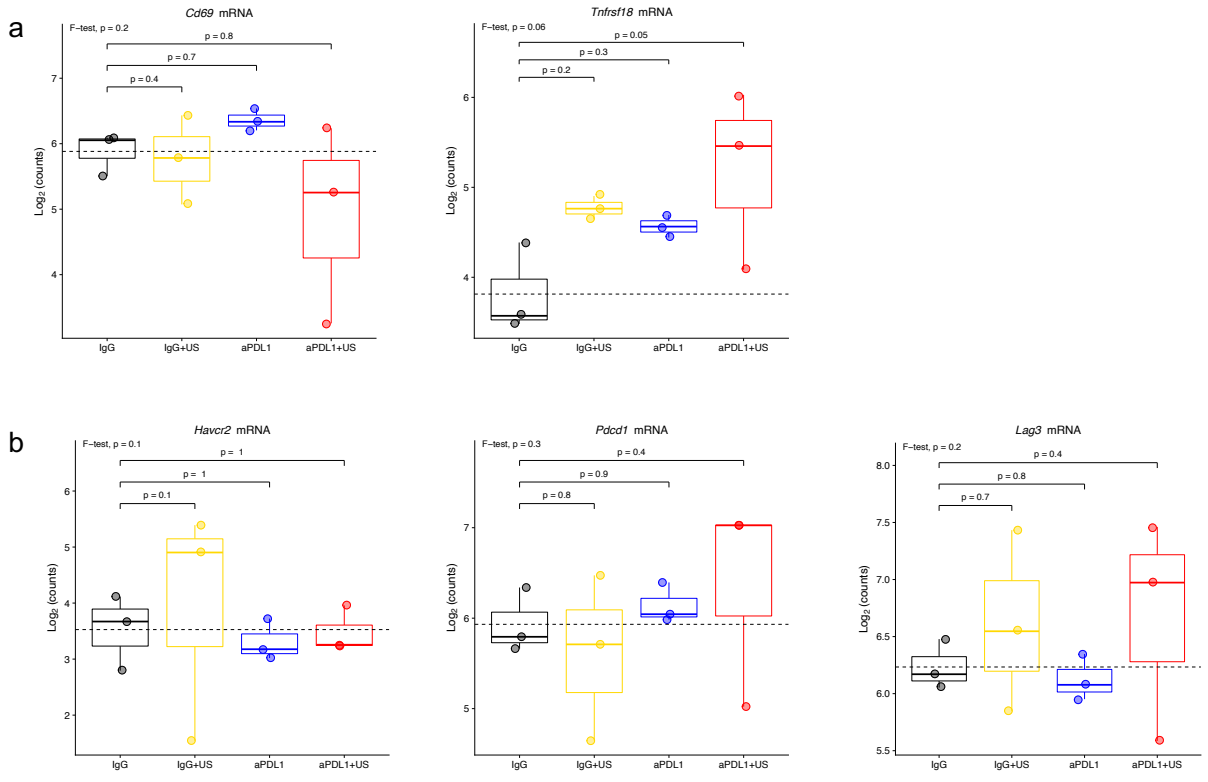


Figure 5.4:
a-b) Breakout boxplots of effector-response related genes. Genes are grouped by function, where (a) groups together genes encoding proteins related to T cell activation (CD69 and GITR) and (b) groups together genes encoding proteins related to T cell exhaustion and dysfunction (PD1, TIM3, and LAG3). Boxplot statistics calculated as per 2.7

Figure 5.4: Effector-Response Related Genes 24hrs After Intervention (2/2)

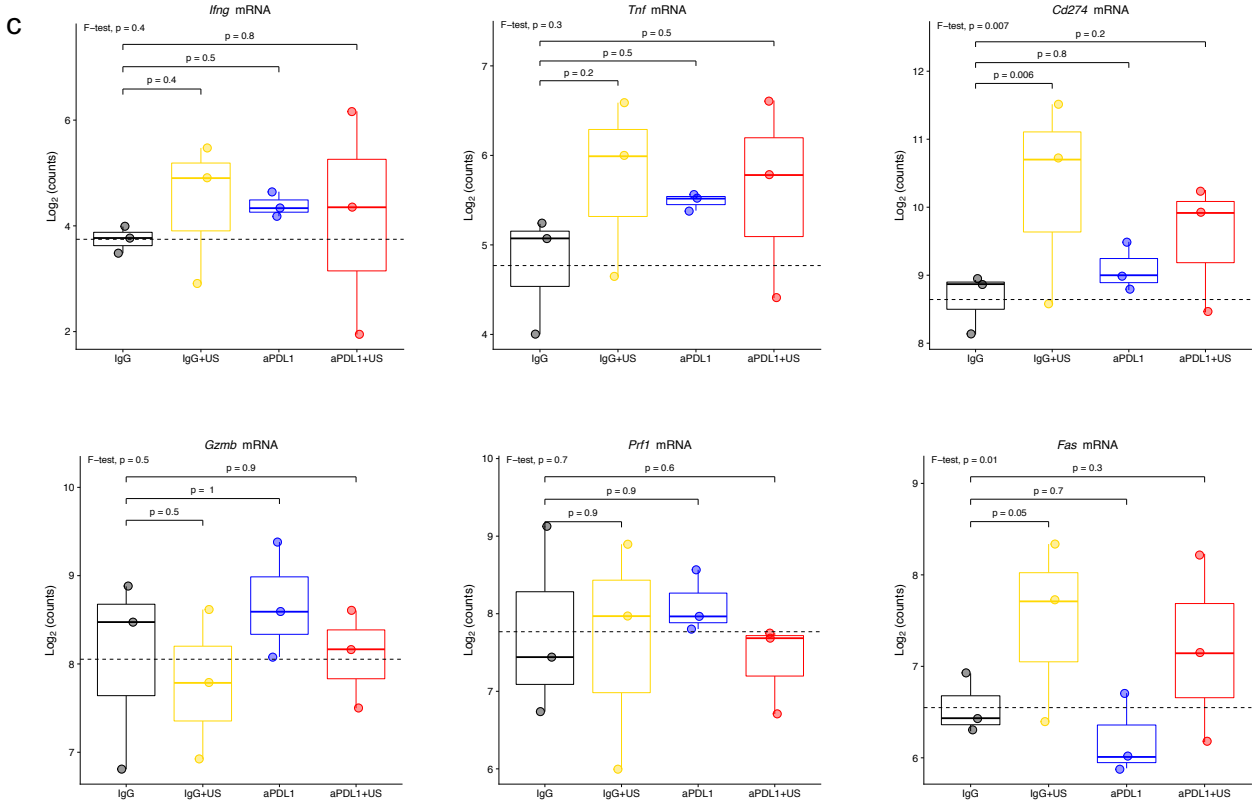


Figure 5.4 continued:
c) Breakout boxplots of genes that encode IFNg, TNFa, PDL1, GranzymeB, Perforin, and Fas. Boxplot statistics calculated as per 2.7

5.5 Cell Type Profiling 24hrs After Intervention

At the 24hr-timepoint, no significant changes in cell score were observed (Fig. 5.5). However, closer inspection may suggest that the cell scores of macrophages and neutrophils (PMN) increased in cavitation treated mice (aPDL1+US or IgG+US) as compared to mice receiving aPDL1 or IgG alone. This pattern is consistent with a hypothesis that this time-point captures an early snapshot of a growing inflammatory response—a moment in which chemoattractant signals are significantly upregulated, but macrophage and PMN infiltration are not yet robust.

Figure 5.5 Cell Type Profiling

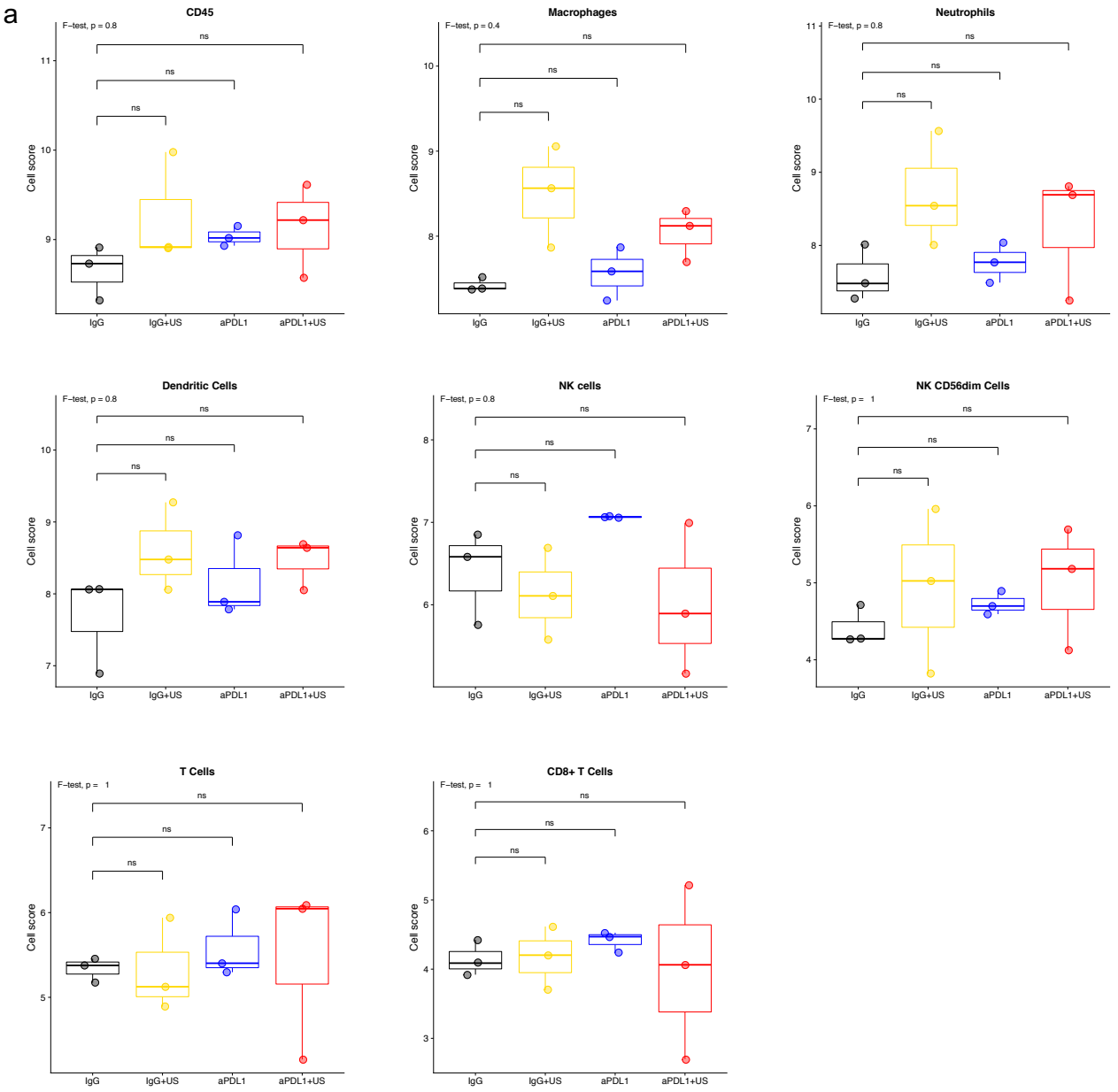


Figure 5.5:
a) Cell type profiling of innate and adaptive immune populations. Cell-scores estimate a given population's infiltration (abundance within the sample) through analysis of co-expressed genes. Cell type profiling of total leukocytes (CD45), macrophages, neutrophils, dendritic cells, NK cells, NK CD56dim cells T cells, and CD8+ T cells are shown (n=3/group). Cell scores were generated in nSolver (Nanostring). BH-adjusted p-values calculated by one-way ANOVA with Dunnett's test

Summary of gene-level changes 24hr-after intervention

Taken together, at the 24-hr time-point, gene-level data seems to suggest that cavitation drives an acute, injury-type inflammatory program—a program marked by significant upregulation of leukocyte attractants, which may lead to modest, insignificant, macrophage and neutrophil recruitment per *Nanostring* cell-type profiling. Tissue analysed 5-days post-therapy helps to better clarify the lasting impact, of the acute, inflammatory response likely generated by cavitation.

Limitations & the impact of cavitation to DEG expression

There are perhaps two caveats to the results described above, both of which relate to experimental variability. First, although mice were intended to be sacrificed exactly 24hs after therapy and best efforts were made to exactly do so, a 15% tolerance in sacrifice time was allowed (i.e. a mouse sacrificed 3hrs before its intended 24hrs sacrifice time was not excluded because this would represent only a 12.5% deviation from the intended sacrifice time). The second caveat to the data relates to cavitation and may in fact explain why a greater number of DEGs (in both FC and significance) were observed in IgG+US treated mice as compared to aPDL1+US treated mice.

Of the 24hr-mice analysed, an interesting post-hoc observation was that the CC-G2-calculated integrated cavitation dose was nearly double in IgG+US treated mice compared to the aPDL1+US treated mice (on average 6.430e-006 AUC vs. 3.183e-006 AUC respectively, Fig. 5.2b). Although this difference was not significant by unpaired student t test (Fig. 5.2b), this observation, may suggest that cavitation dose may be tied to the degree to which the acute inflammatory response is driven. This could explain why, although the upregulation pattern of genes in cavitation treated groups was similar, a greater number of DEGs had a higher FC in IgG+US treated mice over aPDL1+US treated mice (i.e. more top DEGs in IgG+US treated

mice, despite the fact that these top DEGs were also significantly elevated in aPDL1+US treated mice). Put simply, cavitation dose may have made an impact on DEGs, though cavitation dose was not intentionally manipulated in this study.

5.6 Gene-Level Changes 5d After Intervention

5.6.1 Results & Discussion

The early upregulation of an acute-phase, inflammatory reaction was intriguing. However, to better understand the sustained, lasting impact of therapy, mice were sacrificed 5-days after therapy and tumours assessed by *Nanostring*. There were six mice in each group except for the IgG group, where one mouse was sacrificed owing to a welfare concern. Excised tumour weights (n=5-6/group) were NS different as determined by one-way ANOVA with Tukey multiple comparisons correction (Fig. 5.6a). For mice in the 5d-subset, unpaired, student t test revealed a NS difference between the CC-G2 calculated, integrated cavitation doses between IgG+US and aPDL1+US treated (Fig. 5.6b). The average integrated cavitation dose for IgG+US and aPDL1+US treated mice were 3.433e-006 and 4.147e-006 AUC with SDs of 1.732e-006 and 2.480e-006 AUC respectively.

Figure 5.6: Gene-Level Changes 5d After Intervention (1/4)

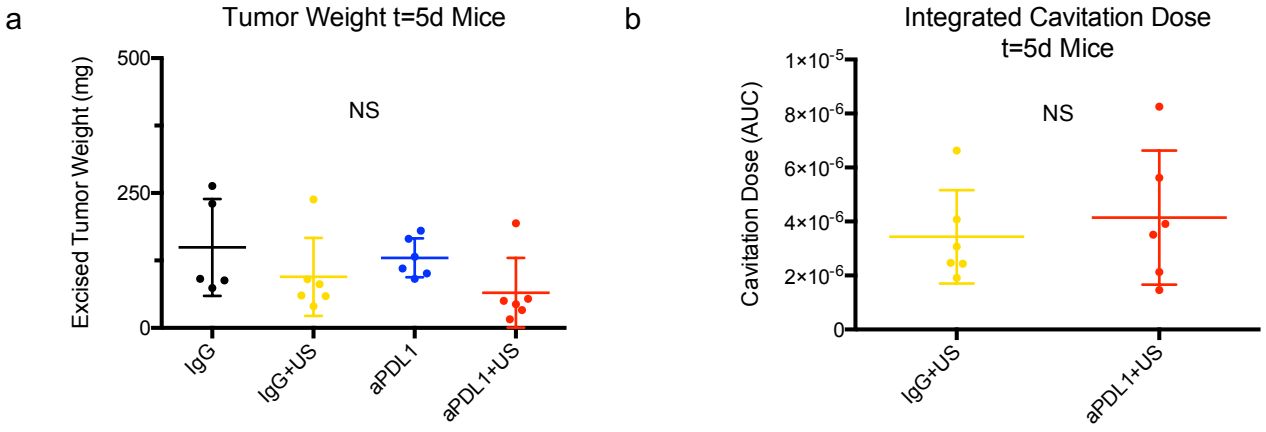


Figure 5.6
a) Excised tumour weights of mice sacrificed 5-days post-intervention and queried by downstream Nanostring analysis (n=5-6/group). Excised weights compared by ordinary one-way ANOVA with Tukey's multiple comparisons test (single pooled variance)
b) CC-G2 integrated cavitation dose of mice sacrificed 5d post-intervention and queried by downstream RNA analysis (n=6/group), compared by unpaired t test (p = 0.5763)

Fig. 5.6c is a heatmap of pathway scores and reveals that all but one of the aPDL1+US treated samples clustered together. Unsupervised, pathway clustering grouped together 5 out of the 6 aPDL1+US treated mice (Fig. 5.6c), suggesting that aPDL1+US treatment imparts tumours with a unique, conserved phenotype.

Figure 5.6: Gene-Level Changes 5d After Intervention (2/4)

c

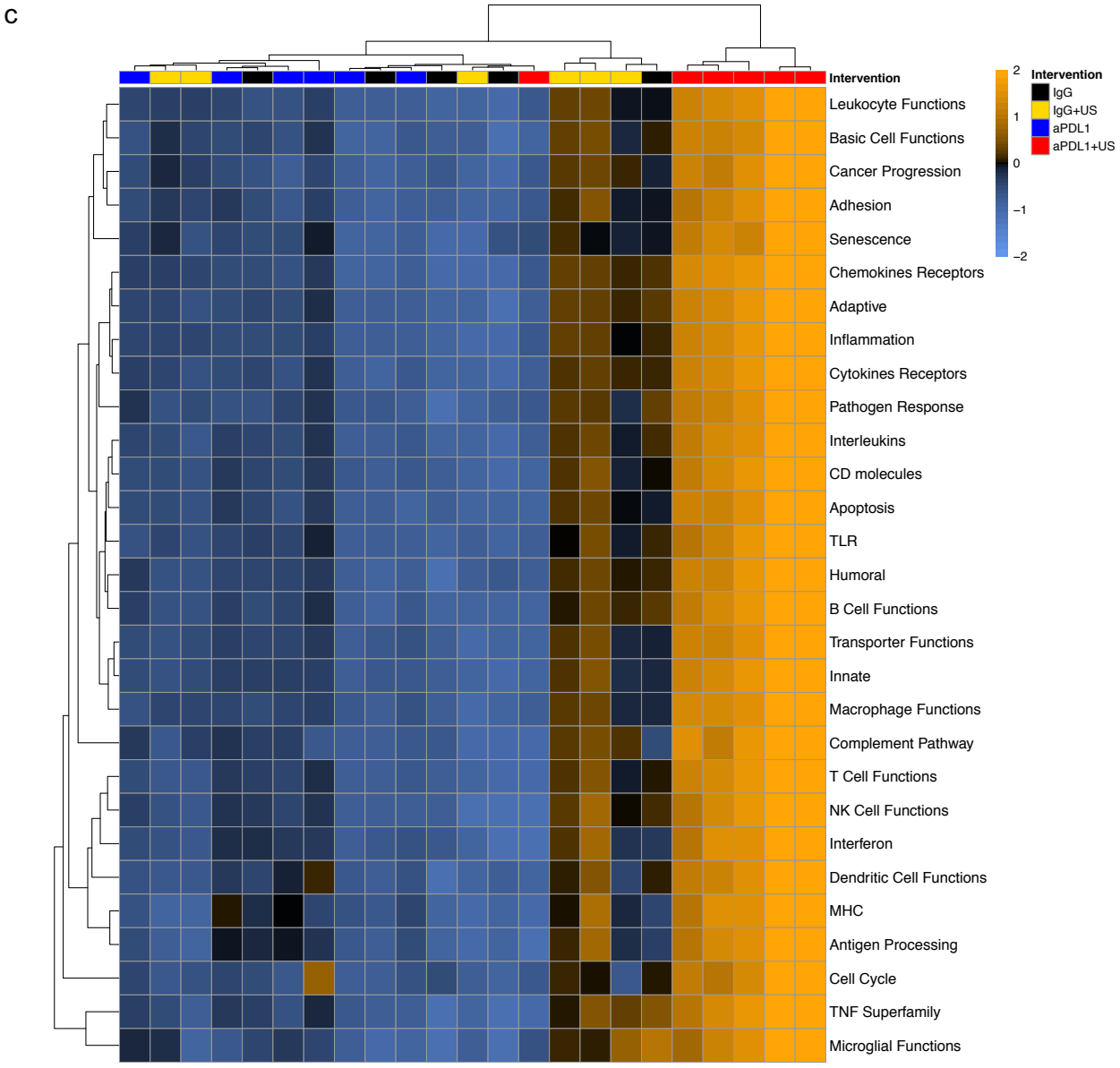


Figure 5.6 continued:
c) A heatmap of pathway scores of samples collected 5d-post-intervention. Orange indicates increases in pathway score (enrichment), whereas blue indicates decreases in pathway score. This figure was generated in a manner identical to that of Fig. 5.2c

Notably, the only aPDL1+US mouse that did not cluster with others of its group, received the lowest integrated cavitation dose, 1.46E-06 AUC, in comparison to the group average of 4.147e-006 AUC. The impact of cavitation to gene expression is further explored in the summary to this chapter.

Fig. 5.6d, illustrates group-level differential gene expression as compared to IgG control. Group-level query of differential gene expression (Fig. 5.6d), qualitatively suggests that aPDL1+US treatment results in strong, differential gene expression changes more so than aPDL1 or IgG+US treatments at the 5d time point.

Figure 5.6: Gene-Level Changes 5d Post-Intervention (3/4)

d

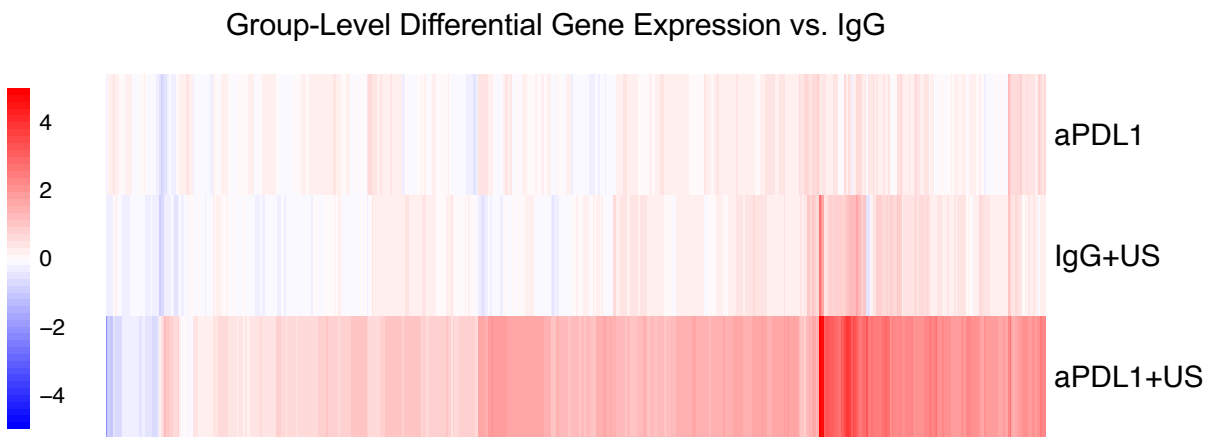


Figure 5.6 continued:
d) A heatmap of how upregulated (red) or downregulated (blue) genes in a given treatment group were expressed as compared to IgG control. This figure was generated in a manner identical to that of Fig. 5.2d

Volcano plots (Fig. 5.6e) and Venn diagrams (Fig. 5.6f and g) of differential gene expression (experimental groups vs. IgG control) further highlight the unique gene expression profile of aPDL1+US treated tumours. The volcano plots reinforce the hypothesis that aPDL1+US treatment results in strong, differential gene expression changes more so than aPDL1 or IgG+US treatments at the 5d time point. The biggest (by magnitude FC) and most significant changes in gene expression occurred in aPDL1+US treated mice (Fig. 5.6e), whose volcano plot is marked by a number of significant, highly differential (by FC), changes. Taken together these results begin to suggest that neither drug nor cavitation alone could drive

sustained, d5 gene expression changes—rather the culmination of both of these factors (aPDL1+US) was required to drive substantial DEG changes.

Figure 5.6: Gene-Level Changes 5d Post-Intervention (4/4)

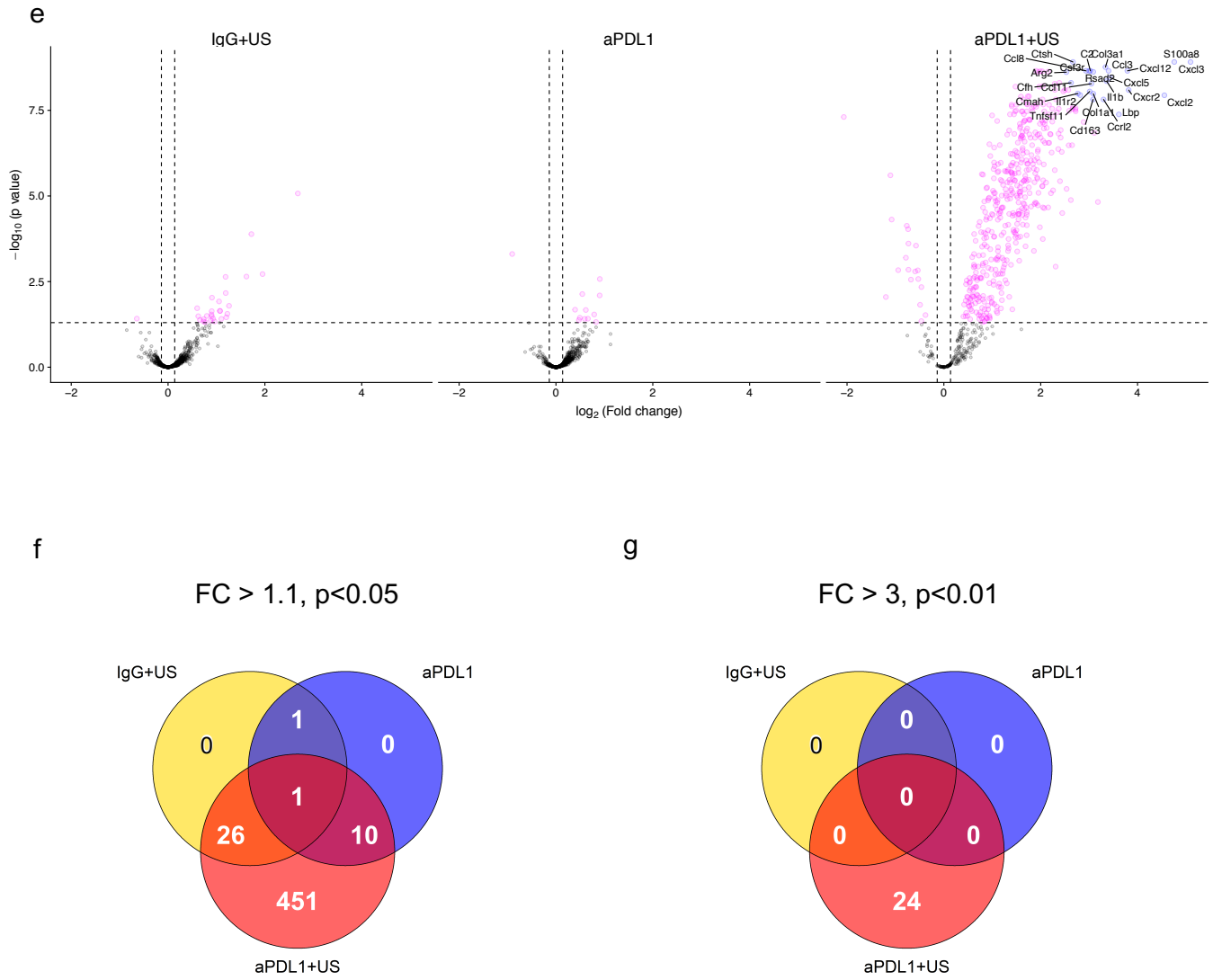


Figure 5.6 continued:
e) Volcano plots of differential gene expression. Labelled genes represent top DEGs, genes very significantly (p<0.01) and differentially (>3 FC) compared to IgG.
f) Venn diagram summarizing the number of genes at the 5d time-point that significantly (p<.05) and differentially (>1.1 FC) expressed compared to IgG.
g) Venn diagram summarizing the number of genes at the 5d time-point that significantly (p<.01) and differentially (>3 FC) expressed compared to IgG.
All statistics calculated in 5.6, were calculated in a manner identical to that of Fig. 5.2a-g

Further query into the similarity or dissimilarity of DEGs (p<0.05 and FC>1.1, Fig. 5.6f) between aPDL1, IgG+US, and aPDL1+US treated tumours found that aPDL1+US treatment

resulted in 488 DEGs compared to 28 and 12 DEGs in IgG+US and aPDL1 treated tumours respectively. The majority of IgG+US DEGs (27 of the 28 DEGs) were not unique to the IgG+US group—and in fact were also differentially expressed in aPDL1+US treated tumours. Likewise, the majority of DEGs in aPDL1 treated tumours (11 of 12 DEGs) were also DEGs of aPDL1+US. One gene, *Ccr1*, a chemokine receptor, was upregulated in all 3 groups. This indicates that the combination of aPDL1 and cavitation serves to amplify effects that would be achieved with either component in isolation and/or creating a range of novel responses.

Subsequent sections more closely explore the mechanism(s) putatively in play. Fig. 5.7 tabulates top DEGs and explicates the expression of the nine most differentially expressed (by FC) top DEGs on a per mouse basis. Additionally, the DEGs shared between aPDL1 and aPDL1+US mice are reviewed in Fig. 5.8. To better put in context the results of 5d-FCM data, genes that encode the proteins detected by FCM (or those closely related) are shown in boxplots of Fig. 5.9. Lastly, results of *Nanostring* cell-profiling are illustrated in Fig. 5.10.

5.7 Top DEGs 5d Post-Intervention

Whereas neither aPDL1 nor IgG+US treatment groups had a top DEG (p<0.01 and FC>3), aPDL1+US treatment had 24 top DEGs, as tabulated in Fig. 5.7 alphabetically. These 24 genes reflect the most differentially and significantly upregulated genes at the 5d time point.

Figure 5.7: Top Differentially Expressed Genes 5d Post-Intervention (1/2)

a

Group:	Top DEGs (compared to IgG): p<0.01 and FC>3							
aPDL1	none							
IgG+US	none							
aPDL1+US	*Arg2*	*C2*	*Ccl11*	***Ccl3***	*Ccl8*	*Ccrl2*	*Cd163*	*Cfh*
	Cmah	*Col1a1*	*Col3a1*	*Csf3r*	*Ctsh*	***Cxcl12***	***Cxcl2***	***Cxcl3***
	Cxcl5	***Cxcr2***	***Il1b***	*Il1r2*	***Lbp***	*Rsad2*	***S100a8***	*Tnfsf11*

Figure 5.7:
a) A table of the top differentially expressed genes (top DEGs) between the given groups and IgG control. Top DEGs are genes that are very significantly (p<0.01) and differentially (FC>3) expressed. The nine top DEGs with greatest differential expression (by FC) are bolded. There were no top DEGs for aPDL1 nor IgG+US mice compared to IgG control

Further investigation revealed that 15 of these 24 top DEGs were also significantly upregulated in IgG+US treated mice (compared to IgG control). In short, although the magnitude of DEG FC was different between aPDL1+US and IgG+US mice, the majority of aPDL1+US top DEGs were also significantly elevated after IgG+US treatment. In fact, out of the 9 most differentially expressed aPDL1+US top DEGs by FC (*Cxcl3, S100a8, Cxcl2, Cxcr2, Cxcl12, Lbp, Cxcl5, Ccl3,* and *Il1b*), all but one of the genes (*Il1b*) were also significantly upregulated in IgG+US-treated mice (Fig. 5.7b). In contrast, none of the 24 aPDL1+US top DEGs were significantly elevated after aPDL1 treatment. Although FC in gene expression is only one-way of looking at the data, it appears that cavitation—a shared feature of aPDL1+US and IgG+US treatment groups—was a strong driver of very significantly, and differentially (by FC) expressed genes—similar to observations of 24hr data.

In fact, 6 out of the 9 top DEGs from the 24hr time-point were also top DEGs 5-days after therapy (*Cxcl3, Cxcl2, S100a8, Ccl3, Il1b, Ccrl2*). As per the previous section, these genes play a variety of roles—however, together, they likely exert influence to recruit and activate innate and adaptive immune populations.

Figure 5.7: Top Differentially Expressed Genes 5d Post-Intervention (2/2)

b

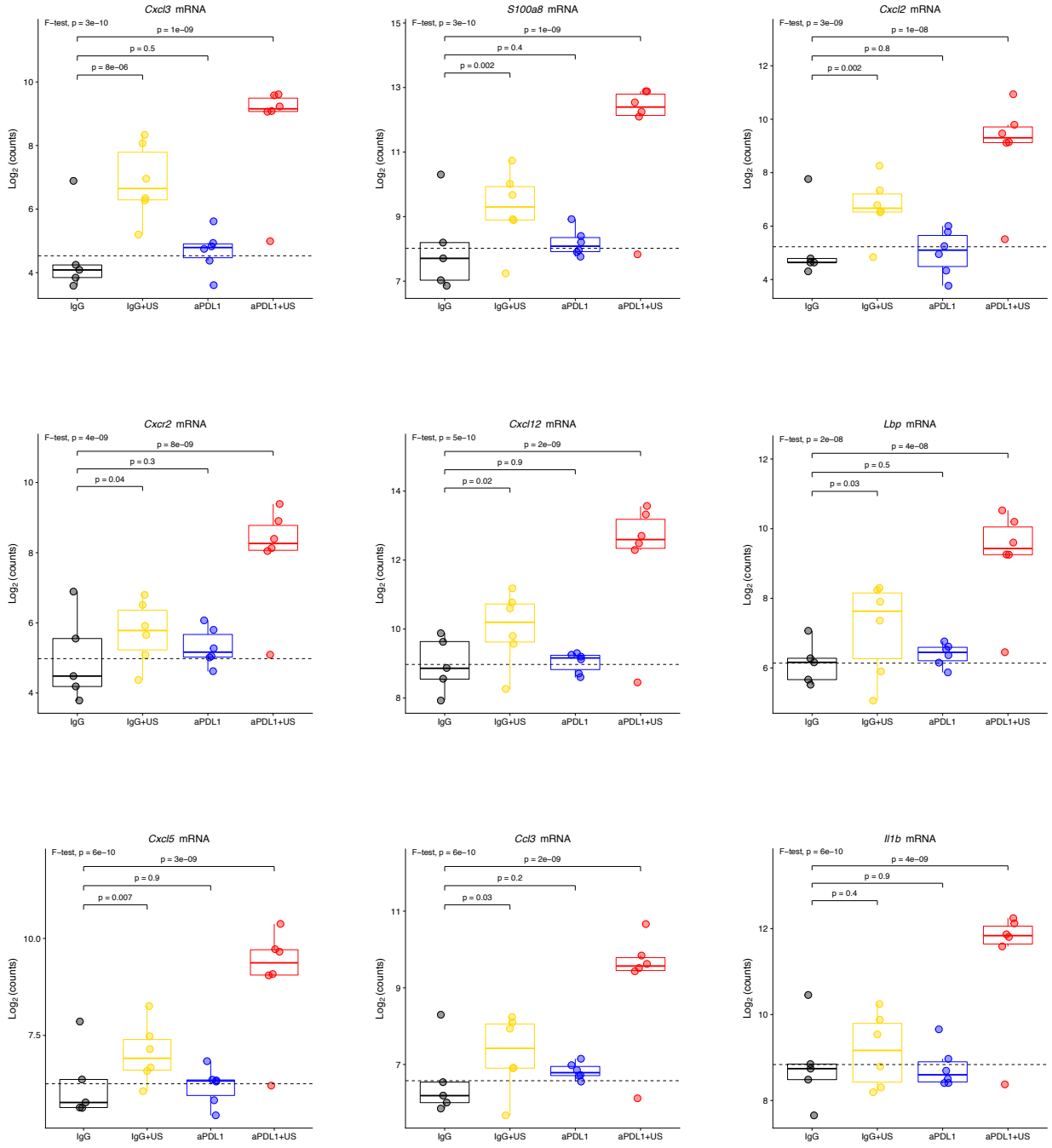


Figure 5.7 continued:
b) Break-out boxplots of 9 most differentially expressed, top DEGs. Boxplot statistics calculated as per 2.7

Other highly expressed (by FC) top DEGs at the 5d time-point, which were not evident at the 24hr time-point, were also implicated in chemoattractant roles—like leukocyte binding

protein (encoded by *Lbp*), chemokines (CXCL5 and CXCL12) and chemokine receptors (CXCL5's receptor is CXCR2). Leukocyte binding protein is an acute-phase protein classically thought to play a role in boosting pathogen clearance responses [Schumann et al 1990]. CXCL12 can act as a leukocyte chemoattractant that in fact becomes even more potent through cooperation with other chemokines—a processed termed chemokine synergy [Janssens et al. 2018]. CXCR2 is a chemokine receptor with a high affinity for CXCL5 and other CXC ligands, playing a role in neutrophil, monocyte/macrophage, and mast cell recruitment [Olson & Ley 2002, Stadtmann & Zarbock 2012, Sepuru et al. 2014]. For example, in an ischemia-reperfusion study, CXCR2 knockout resulted in a 44.3% reduction in inflammatory cells present [Tarzami e al. 2003], highlighting the critical role CXCR2 plays in enabling leukocyte recruitment.

In short, the most differentially expressed (by FC) top DEGs at the 5d time-point, were largely related to sustaining the recruitment and activation of an inflammatory response. Although top DEGs were generally significantly elevated in both cavitation groups, the fold-changes in gene expression were far greater after aPDL1+US treatment. At this time-point, on average, cavitation levels were only marginally higher in aPDL1+US treated mice (on average 4.147e-006 AUC vs. 3.433e-006 AUC in IgG+US treated mice). While this difference could partially explain why FC magnitude of differential gene expression is greater in aPDL1+US treated mice, it is also likely that the presence of aPDL1 in addition to cavitation further amplified differential gene expression, culminating in the sustained pro-inflammatory gene signature.

5.8 Shared genes between aPDL1 and aPDL1+US

Although many of the largest and most significant gene changes were likely related to cavitation, a number of other genes were significantly elevated after aPDL1+US treatment. Of particular interest, were a subset of DEGs ($p<0.05$ and $FC>1.1$) shared only between aPDL1-treated and aPDL1+US treated mice — specifically ten genes: *C6, Cd33, Gbp2b, Il15ra, Il34, Itgax, Jak3, Slamf6, Tap2,* and *Tnfsf13b* (Fig. 5.8). At the 24hr time point, there was no equivalent 'shared DEG' population—perhaps, a consequence of the delayed, necessary time for the drug to carry out its biologic function.

These 10 genes are putatively tied to the function of aPDL1, and, as observed in Fig. 5.8, 9 out of the 10 genes were far more expressed (by FC magnitude and significance) in aPDL1+US treated tumours vs. aPDL1 therapy. This would be consistent with a hypothesis that aPDL1+US therapy amplifies gene expression changes initiated by aPDL1 therapy. The function of these genes is reviewed; though functions overlap to an extent, the genes can be grouped into three rough categories: 1) innate immune system effector function, 2) adaptive immune system activity, and 3) general leukocyte activation and recruitment.

5.8.1 Innate immune system effector function (Fig. 5.8a)

C6 encodes a subunit of the membrane attack complex (MAC), an assembly of proteins that effectively create pores within target cell's membrane, bringing about cell lysis [Ragupathi et al. 2005, Rogers et al. 2014]. Put simply, the MAC complex is a direct means by which antibody and complement tagged cells are eliminated. MAC-attack can be triggered by any of the three complement pathways, including the antibody-dependent (IgG or IgM) classical complement pathway.

Itgax encodes CD11c, a critical component of complement receptor 4 (CR4), which mediates "the clearance of pathogen microbes, tumour- and apoptotic cells through

phagocytosis" [Lukácsi et al. 2017]. CR4 has also been shown to function through a receptor-mediated mechanism [Taborada & Casadevall 2002], akin to ADCC-mediated by Fc receptors. It has been shown that CR4 plays a role in the macrophage-mediated phagocytosis of antibody-opsonized *Cryptococcus neoformans* — principally the phagocytosis of cells bound by antibody [Taborda & Casadevall 2002].

Il15ra encodes the receptor for IL-15. It has been reported that "IL-15 enhance[s] antibody-dependent cellular cytotoxicity mediated by NK cells and macrophages" [Zhang et al. 2018]. Zhang et al's work has shown that the combination of IL-15 improved the efficacy of rituximab, by improving the NK and macrophage number and/or activation, thereby augmenting ADCC [Zhang et al. 2018]. Beyond its role in supporting ADCC, Il-15 has also been shown to drive NK and CD8 effector memory cell activation and expansion [Sneller et al. 2011]. *IL15ra's* overexpression suggests that there are more activated lymphocytes, and moreover, greater ADCC activity.

Figure 5.8 DEGs Shared Between aPDL1 and aPDL1+US Treated Tumours (1/4)

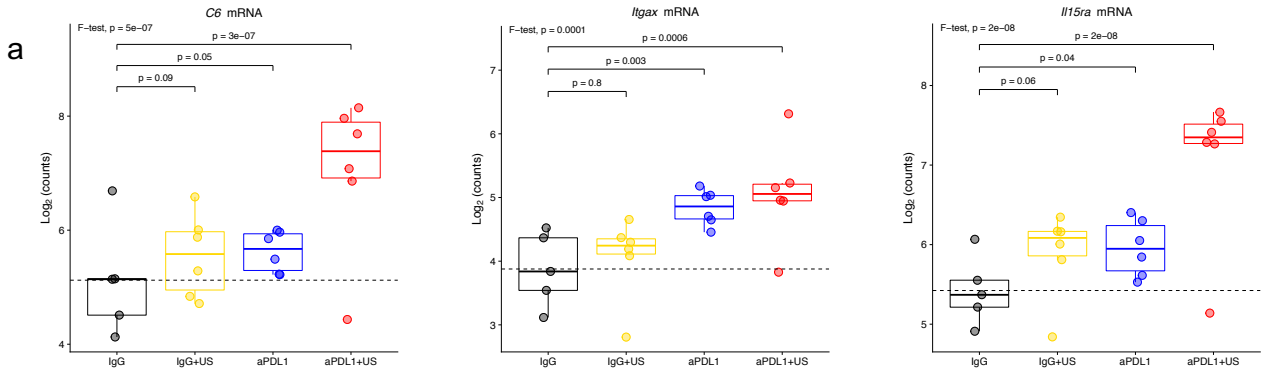


Figure 5.8
a) Differentially expressed genes (DEGs, p<0.05, and FC>1.1) shared between aPDL1 and aPDL1+US treated tumours vs. IgG control that encode proteins (C6, CD11c, and IL15Ra) related to innate immune system effector processes. Boxplot statistics calculated as per 2.7

In summary, the upregulation of *C6, Itgax, and IL15ra* suggests that aPDL1 and aPDL1+US treatment drives greater innate effector activity through non-redundant, antibody-mediated programs that can be both complement-dependent and independent—mechanisms that could explain how aPDL1 can bring about cell death via the innate immune system.

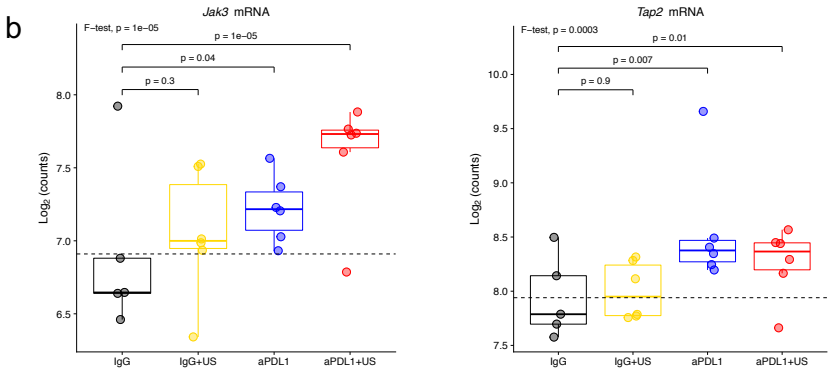
Activation of ADCC by aPDL1 has/has not been previously reported? It raises important issues regarding the potential importance of Fc competent status of aPDL1 antibodies.

5.8.2 Adaptive immune system activity (Fig. 5.8b)

T cells are activated and carry out their effector functions in an antigen-specific manner, through TCR-recognition of MHC-presented antigen. *Tap2* encodes a subunit of "transporter associated with antigen processing" (TAP). TAP loads antigen to major histocompatibility complex (MHC) I [Abele & Tampé 2004]. *Tap2* overexpression indicates more antigen is being presented by MHC-I; a feature which could facilitate T cell-mediated attack.

Jak3 plays a critical role in the activation and maturation of lymphocytes [Johnston et al. 1994], and in fact the phenotype of peripheral T cell Jak3 deficiency "…strongly resembles that observed in patients with a moderate combined immunodeficiency disease (XCID)" [Thomis & Berg 1997]. On the other hand, constitutive Jak3 activation can result in lymphoproliferative syndromes [Cornejo et al. 2009]. In summary, the *Tap2* and *Jak3* upregulation in aPDL1 and aPDL1+US treated mice, suggests that these treatments support the expansion and effector activities of adaptive immune cells.

Figure 5.8 DEGs Shared Between aPDL1 and aPDL1+US Treated Tumours (2/4)



b) Differentially expressed genes (DEGs, p<0.05, and FC>1.1) shared between aPDL1 and aPDL1+US treated tumours vs. IgG control that encode proteins related to adaptive immunity. Boxplot statistics calculated as per 2.7

5.8.3 Leukocyte activation and recruitment (Fig. 5.8c)

Gbp2 encodes guanylate-binding protein (GBP) 2, a protein known for its a role in intracellular pathogen clearance [Degrandi et al. 2013]. Importantly, like other murine GBPs, it is "specifically up-regulated by IFN-γ, other proinflammatory cytokines, toll-like receptor agonists…", [Degrandi et al. 2013], and in this sense, it can be perceived as a surrogate indicative of leukocyte activation. The role and function of SLAMF6 is emerging, though recent evidence points to its role in NK cell development [Wu et al. 2016] and T cell activation [Dragovich et al. 2019]. In this sense, it is both an innate and adaptive immune system activator, and its overexpression at the gene level suggest that pro-inflammatory signalling is upregulated.

Figure 5.8 DEGs Shared Between aPDL1 and aPDL1+US Treated Tumours (3/4)

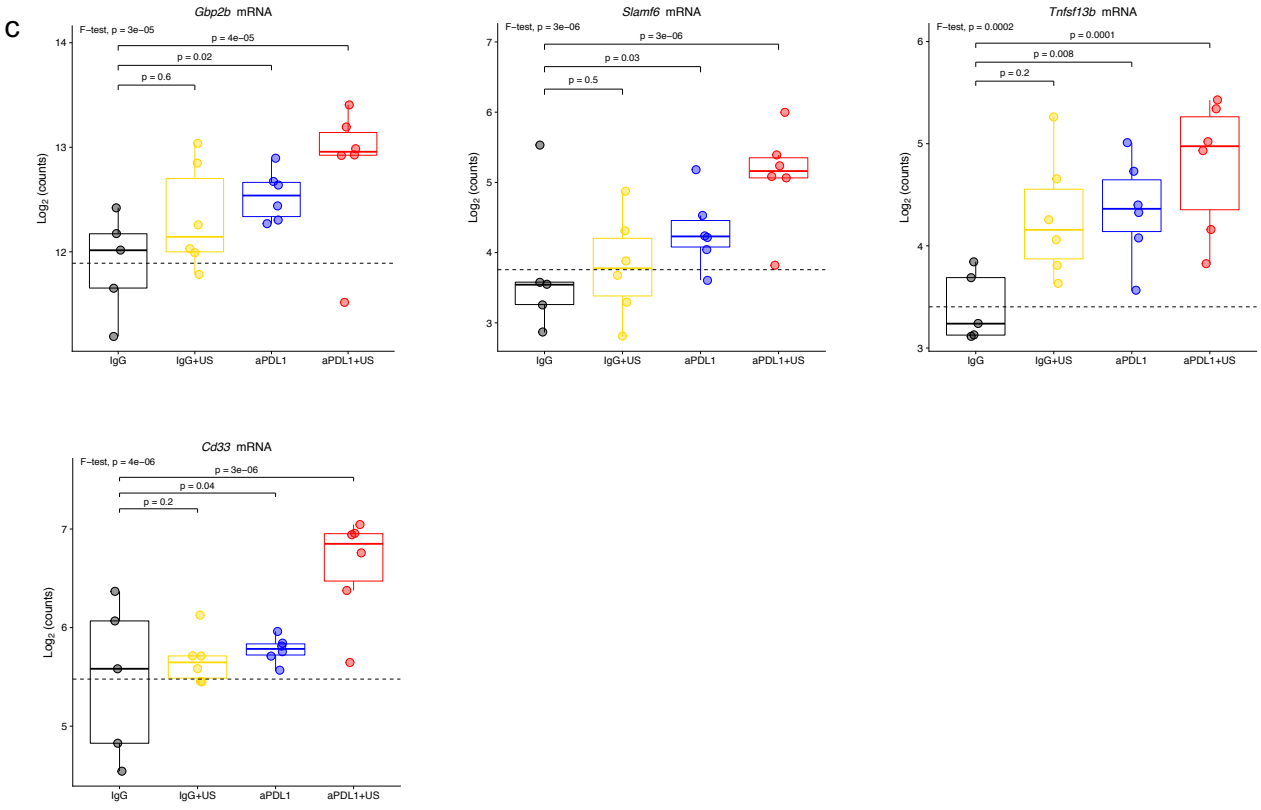


Figure 5.8 continued:
c) Differentially expressed genes (DEGs, p<0.05, and FC>1.1) shared between aPDL1 and aPDL1+US treated tumours vs. IgG control that encode proteins related to generalized leukocyte activation and recruitment (Interferon-induced guanylate-binding protein 2, SLAMF6, BAFF, CD33. Boxplot statistics calculated as per 2.7

Tnfsf13b encodes B-cell-activating factor (BAFF), which is canonically thought to support B-cell activation, maturation, and survival. BAFF is produced by IFNg-stimulated (activated) mononuclear phagocytes [Mackay & Browning 2002]. Although the exact role of B cells is unclear as it pertains to aPDL1 therapy, the upregulation of *Tnfsf13b* suggests that activated mononuclear phagocytes are present. CD33 is general considered a myeloid differentiation antigen, however, it can also be expressed by NK and T cells [Hernández-Caselles et al. 2006]. *CD33's* overexpression suggests that a greater number of myeloid and/or NK and T cells are present. Taken together the upregulation of *Gbp2*, *Slamf6, Tnfsf13b,* and *CD33* suggests that the tumour microenvironment of aPDL1 and aPDL1+US treated tumours contains inflammatory cues that attract and activate leukocytes.

5.8.4 Unclear role (Fig. 5.8d)

Unlike all other genes, where aPDL1+US amplified aPDL1 expression (in the same direction), *Il34* was significantly upregulated in aPDL1 treated tumours compared to IgG control, and, significantly downregulated in aPDL1+US treated mice.

Figure 5.8: DEGs Shared Between aPDL1 and aPDL1+US Treated Tumours (4/4)

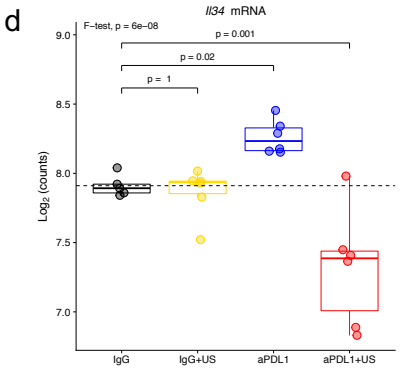


Figure 5.8 continued:
d) IL34 was the only outlier in the data set assessing for DEGs shared by both aPDL1 and aPDL1+US (DEGs, p<0.05, and FC>1.1. Boxplot statistics calculated as per 2.7

The discrepancy in expression could be tied to IL34's emerging role to drive monocytes toward an immunosuppressive fate [Foucher et al. 2013]. In other words, the decrease in *Il34* in

aPDL1+US treated mice suggests that the combination of aPDL1 with cavitation somehow decreases the likelihood that monocytes are driven to an immunosuppressive state.

5.8.5 Summary

In summary at the 5d time-point, the majority of DEGs uniquely shared between aPDL1 and aPDL1+US were related to leukocyte activation and effector functionality. Genes were generally more greatly expressed (by FC) in aPDL1+US treated mice as compared to aPDL1 treatment, which directly suggests that cavitation amplifies the gene-level changes driven by aPDL1, providing mechanistic insight into the manner by which aPDL1+US improves the efficacy of aPDL1 alone, including the upregulation of genes which directly play a role in bringing about cell death—the MAC complex, complement-independent CR4, antibody-mediated phagocytosis, ADCC, and adaptive immunity.

5.9 Effector-response related genes 5d after intervention

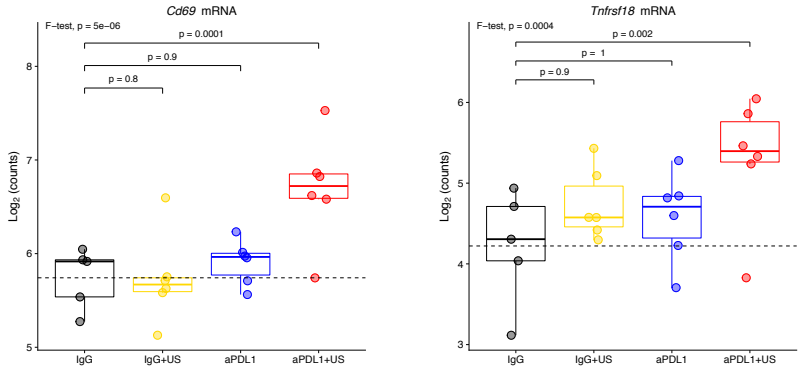
To better put in context the results of 5d FCM data, genes that encode the proteins detected by FCM in 5.11 (or those closely related) are shown in boxplots of Fig. 5.9. These genes at the 24hr-time point were not statistically different, however, at the 5d time point all of the genes were significantly elevated after aPDL1+US treatment compared to IgG except *Prf1*, which encodes perforin. None of these genes were significantly elevated as compared to IgG control after aPDL1 or IgG+US treatment. The genes encode proteins that play diverse roles, but they can loosely be broken down into three groups—those related to activation, dysfunction & resistance, and effector function (cytotoxicity).

5.9.1 Activation (Fig. 5.9a)

CD69 and GITR (*Tnfrsf18*) are markers of leukocyte activation for both innate (neutrophils, NK cells, and murine macrophages) and adaptive (B and T cells) populations [Simms & Ellis 1996, Nocentini et al. 2007, Cibrián & Sánchez-Madrid 2017]. The upregulation of *CD69* and *Tnfrsf18* suggests that aPDL1+US treated tumours are immunologically active.

Figure 5.9: Effector-Response Related Genes 5d After Intervention (1/3)

a



FFigure 5.9
a) Boxplots of genes related to T cell activation (CD69 and GITR). Box-plot statistics calculated as per 2.7

5.9.2 Dysfunction and Resistance (Fig. 5.9b)

PD1, LAG3, and TIM3 (encoded by *Havcr2*) can be considered activation markers, however, they have each also been purported as immunologic checkpoints that hinder anti-tumour immunity. Their inhibition is hypothesized to promote anti-tumour immunity. In fact, PD1 inhibitors are FDA approved cancer immunotherapies, and both LAG3 inhibitors [Solinas et al. 2019] and TIM3 inhibitors [He et al. 2018] are currently at differing stages of pre-clinical and clinical investigation as anti-cancer agents. The upregulation of these immunosuppressive checkpoints specifically in aPDL1+US may in particular suggest that anti-tumour immune responses are growing—invoking stronger upregulation of resistance mechanisms [Jacquelot et al 2019].

Figure 5.9: Effector-Response Related Genes 5d After Intervention (2/3)

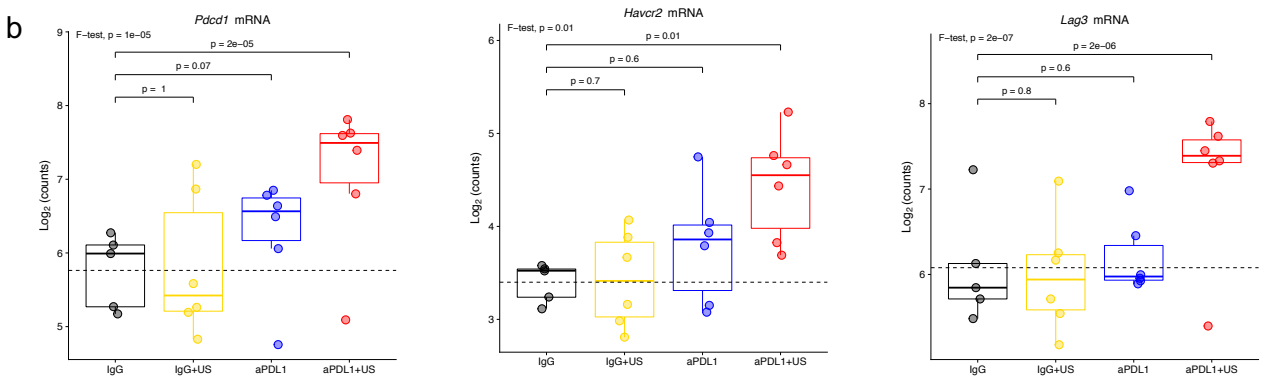


Figure 5.9 continued:
b) Boxplots of genes encoding proteins related to T cell exhaustion and dysfunction (PD1, TIM3, and LAG3). Boxplot statistics calculated as per 2.7

5.9.3 Effector function (Fig. 5.9c)

Ifng, Tnf, Cd274 encode IFNg, TNFa, and PDL1 respectively. Each protein has a direct role in cell-killing processes relevant to aPDL1 therapy. For example, IFNg can not only stimulate the expression of MHC-I, rendering tumour cells more susceptible to T-cell mediated

attack [Martini et al. 2010], but it can also drive PDL1 expression [Blank et al. 2004]. By increasing PDL1 expression, the cells may be more susceptible to aPDL1-mediated ADCC, CR4-mediated phagocytosis, even MAC-attack through classical complement pathway engagement. TNFa has also been purported to induce PDL1 expression [Wang et al. 2017]. In fact, *Cd274*, which encodes PDL1 was significantly upregulated in aPDL1+US treated mice—the same treatment group marked by increases in *Ifng* and *TNFa.*

Figure 5.9: Effector-Response Related Genes 5d After Intervention (2/3)

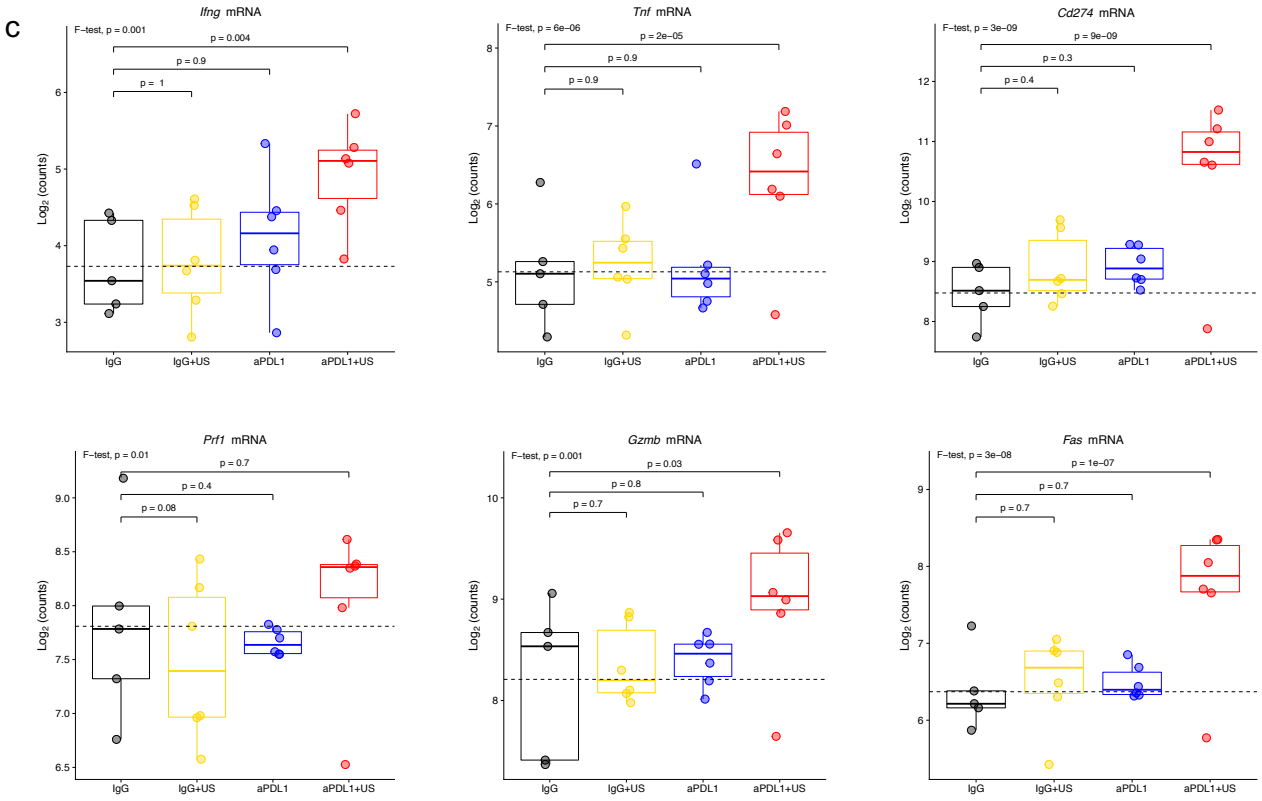


Figure 5.9 continued:
c) Boxplots of genes that encode IFNg, TNFa, PDL1, GranzymeB, Perforin, and FAS. Boxplot statistics calculated as per 2.7

Canonically perforin and GranzymeB were thought to work in tandem—whereby NK or T cell released perforin creates pores that allow for GranzymeB, a serine protease, to activate target cell caspases resulting in apoptosis [Trapani 1995]. However, GranzymeB B can also

work in a perforin-independent fashion [Gross et al. 2003] and can also play a role in mediating ADCC. Further, GranzymeB's expression is not restricted to lymphocytes, and work has highlighted that "…monocytes, much like NK cells, also utilize Granzyme B for ADCC" [Elavazhagan et al. 2015].

Monocyte-GranzymeB mediated ADCC may be particularly relevant in our studies given that *Gzmb* but not *prf1* (unlike all other markers) was significantly upregulated. This pattern of expression is consistent with monocyte *Gzmb* production, because in monocytes (unlike lymphocytes) *G*zmb is expressed "…generally without perforin" [Chowdhury & Liberman 2008]. Put simply because *Gzmb* but not *Prf1* was significantly elevated after aPDL1+US treatment, myeloid cells were likely the producers of *Gzmb.* Taken together, it can be reasoned that myeloid-mediated ADCC via *Gzmb* is important to aPDL1+US therapy because 1) myeloid cells are likely the producers of *Gzmb,* 2) myeloid cells mediate ADCC using *Gzmb.*

5.9.4 Summary

In summary, analysis of FCM-related genes revealed that aPDL1+US treatment resulted in the significant elevation of expression of proteins related to activation, immunologic resistance, and cytotoxic effector function. Perhaps the most intriguing observations here, were the increases in levels of protein related to innate and adaptive effector processes, including ADCC and T cell mediated attack, that fit with the observed, significant increase in T cell and antibody-mediated programs of Fig. 5.8. Taken together these changes begin to identify the mechanism underpinning tumour regression by aPDL1+US therapy observed in Chapter 3.

5.10 *Nanostring* Cell Scores 5d-Post Intervention

Unlike Nanostring cell-type profiling with 24hr-tissue, which showed no significant changes in any experimental group as compared to IgG control, tissue collected 5-days post therapy revealed highly significant increases in the infiltration of leukocytes, macrophages, neutrophils, DCs, NK CD56Dim, and T in aPDL1+US treated mice as compared to IgG control. No cell score changes were significantly elevated as compared to IgG control in the aPDL1 or IgG+US treatment groups (Fig. 5.10).

Figure 5.10: *Nanostring* Cell Scores 5d-Post Intervention

a

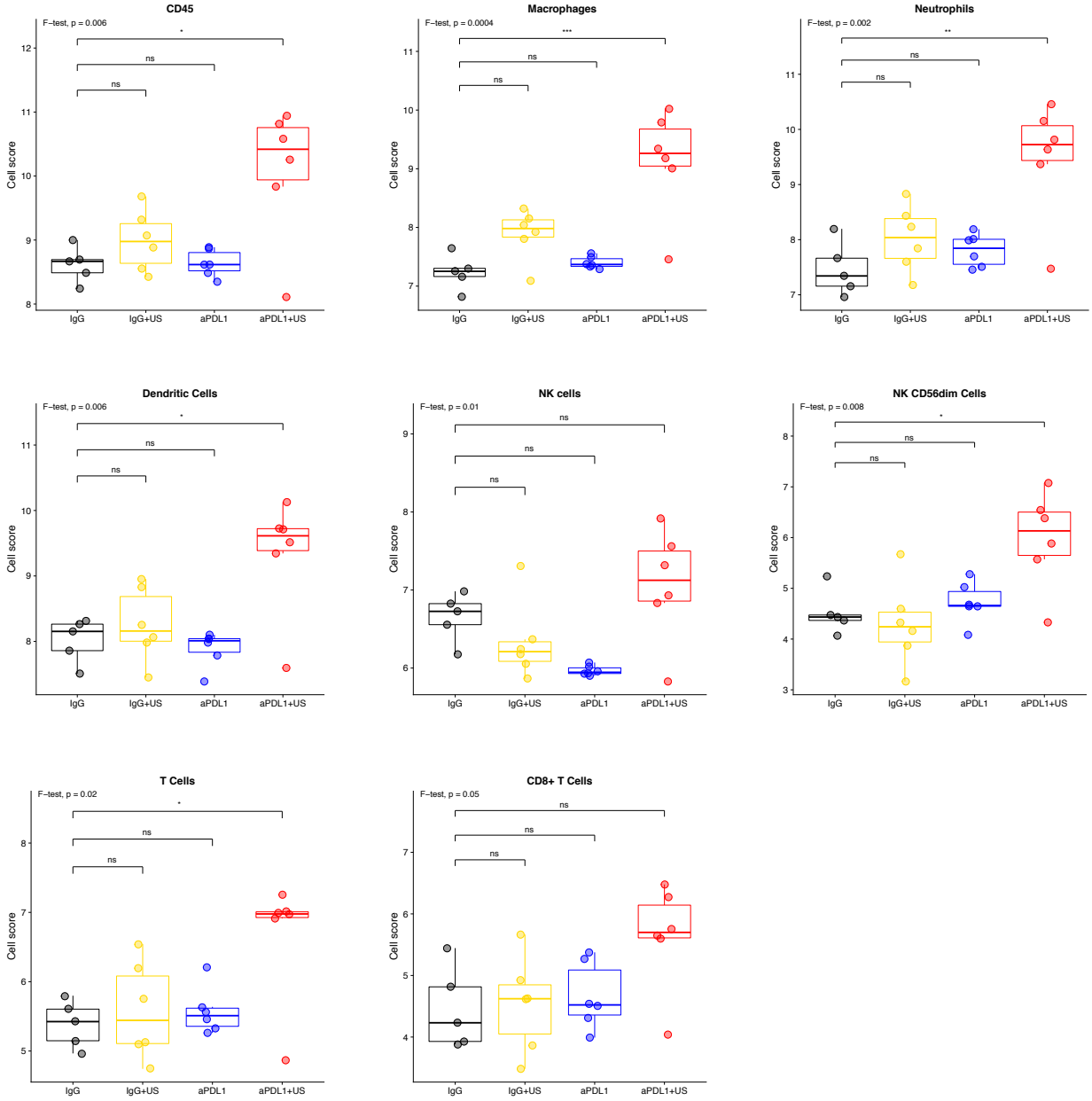


Figure 5.10:
a) Nanostring cell-type profiling scores for total leukocytes (CD45), macrophages, neutrophils, dendritic cells, NK cells, NK CD56dim, T Cells, and CD8+ T cells shown. Each samples' cell score for a particular population is reported. BH-adjusted p-values calculated by one-way ANOVA with Dunnett's test

As previously reviewed in the context of *Itgax* overexpression, macrophages can also phagocytose antibody-opsonized cells in an ADCC-independent, CR4-related process [Lukáski et al. 2017, Taborda & Casadevall 2002]. T cells, both CD4 and CD8 T subsets, can also bring about cell death through the antigen-specific release of cytotoxic granules (i.e. GranzymeB/perforin) [Lancki et al. 1991, Kägi et al. 1994, Kojima et al. 2000] and/or the expression of ligands (FAS-L) that drive target-cell apoptosis [Rouvier et al. 1993, Brown et al. 2009, Malyshkina et al. 2017]. In fact, significant *FasL* expression was observed in aPDL1+US treatment (data not shown), however, because CT26 tumours can also express *FasL* it is unclear whether the elevation in *FasL* represents anti-tumour activity of T cells or T cell attack by the tumour [Ryan et al. 2006].

However, it should be noted that certain subsets of these populations could alternatively play tumour-supportive roles (i.e. myeloid derived suppressor cells [Sevko & Umansky 2013], tumour-associated macrophages [Hu et al. 2019], and T regulatory cells [Facciabene et al. 2012]). However, put in the context of Chapter 3, where aPDL1+US therapy brought about an improvement in drug efficacy, it is likely that the cell-score suggested increases in the infiltration of innate and adaptive immune populations aided in tumour control.

5.10 Summary of Gene-Level Changes 5d After Intervention

Limitations

aPDL1+US treated mice had a greater number of DEGs, and DEGs of a greater FC compared to IgG+US treated mice at the 5d-time point. Unlike the 24hr-time point, the cavitation dose was comparable between IgG+US-treated mice and aPDL1+US treated mice. However, it was higher on average in the aPDL1+US treated mice. Given this post-hoc observation, it cannot be ruled out that reduced cavitation contributed to the reduced DEGs of IgG+US mice at the 5d time-point.

Key Take Home

High-level, clustering analysis identified that 5 of 6 aPDL1+US treated mice clustered together owing to their shared phenotype. Further inquiry revealed that aPDL1+US treatment drove the strongest and most significant number of DEGs as compared to IgG+US or aPDL1. The top DEGs ($p<0.01$ and $FC>3$) at the 5d time-point included 6 of the 9 top DEGs also identified in tumour tissue rescued at 24hr. The majority of other top DEGs played similar roles in further augmenting leukocyte recruitment and/or activation. The majority of these genes (15 of 24), were also upregulated in IgG+US treated mice, but not to the same degree (FC) nor level of significance. Cavitation levels were marginally lower after IgG+US vs. aPDL1+US treatment, however the cavitation doses were far more comparable, in contrast to the 24hr-study.

Investigation of DEGs uniquely shared between aPDL1 and aPDL1+US treatment, revealed these genes played roles in leukocyte activation, CDC, CR4-related mediated phagocytosis, ADCC, and T cell mediated attack via MHC I recognition. Likewise, for these shared DEGs, aPDL1+US treatment typically augmented the magnitude FC and significance in expression of the gene—suggesting that aPDL1+US therapy amplifies DEGs underpinning aPDL1's mechanism of action.

Analysis of genes encoding FCM-queried/related proteins, reinforced the hypothesis that aPDL1+US drives immune innate and adaptive effector processes (increasing *Gzmb*). For example, genes were expressed by aPDL1+US treated tumours that would suggest that IFNg or TNFa has induced PDL1 expression, which would make the cells prime targets for antibody (aPDL1) binding—in short, rendering the cells more sensitive to ADCC or other antibody-mediated effector mechanisms (like CDC or CR4-mediated phagocytosis). Lastly, cell type profiling suggested that aPDL1+US treatment, but not the other therapies, results in significant increases in the infiltration of both innate and adaptive immune populations that putatively play anti-tumour roles.

5.10.2 Summary of *Nanostring* Data

Leveraging *Nanostring* to query over 700+ genes related to cancer immunity, this study sought to better understand the mechanistic basis of aPDL1+US therapy. 24hrs-after therapy, gene-level changes were largely related to those of an acute, injury-like response and changes were observed in both IgG+US and aPDL1+US treated tumours. 5d-post therapy more DEGs were detected in aPDL1+US treated tumours compared to IgG+US or aPDL1-treated mice. Cavitation alone could have played a role in driving such DEG changes, however at the 5d time-point, where cavitation doses were more comparable between cavitation-treatment groups, it is also likely that the presence of drug (aPDL1) along with cavitation played a big role.

5-days post-therapy, genes related to leukocyte recruitment were again upregulated in IgG+US and aPDL1+US treated tumours. However, in addition to those changes, genes which were likely related to aPDL1's mechanism of action (aPDL1 DEGs) were significantly amplified in FC by aPDL1+US therapy. These genes drive processes including CDC, CR4-related phagocytosis, and ADCC—pathways by which tumour control can be achieved. Additionally, at the 5d-timepoint other genes related to effector mechanisms were upregulated—including the

induction of PDL1 expression which could render cells more sensitive to antibody-mediated attack. Cell score profiling at the 5d time-point, identified significant elevations of cell populations that could carry out the attack functions listed above. Altogether, *Nanostring* profiling identified putative mechanisms by which aPDL1+US could confer tumour control.

5.10.3 Time-Course of Biomarkers, A Working Hypothesis

Nanostring analysis identified a number of changes could play an important role in mediating the anti-tumour immunity conferred by aPDL1+US therapy. Schematic 5.10 aims to highlight a few of the intriguing biomarker changes and predict their importance over time.

Schematic 5.10: A Possible Time-Course of Biomarkers after aPDL1+US Therapy

Activity	t=24hr		t=5d		Time
Leukocyte recruitment *e.g. Cxcl2 and Cxcl3*	XXX	XXX	XXX	XXX	XX	X
Leukocyte activation *e.g. Il1b and S100a8*	XX	XXX	XXX	XXX	XXX	XX
Induction of adaptive immune processes *e.g. Jak3 and later Tap2 and Cd69*	X	XX	XX	XXX	XXX	XXX
Immunosuppression *e.g. Cd274 and Pdcd1*	X	XX	XX	XXX	XXX	XXX
Sustained activation & recruitment *e.g. Ifng, Tnf, Gbp2, Slamf6, and CD33*		X	X	XX	XXX	XXX
Anti-tumour effector activity *e.g. C6, Itgax, Il15ra, and Gzmb*		X	X	XX	XXX	XXX

Schematic 5.10:
*After aPDL1+US therapy, chemokines (e.g. Cxcl3) may drive **leukocyte recruitment** in tandem with **leukocyte activation** mediated by pro-inflammatory factors (e.g. Il1b). Driven by the pro-inflammatory cues, innate immune cells could **induce adaptive immune** processes, like antigen presentation (e.g. Tap2). In response to the upregulated anti-tumour activity, **immunosuppressive activity** might also increase (e.g. Cd274 which encodes PDL1). Despite this activity, in an ideal scenario, the **sustained activation & recruitment** of leukocytes (e.g. Ifng) may be able to reach a critical threshold, whereby innate and adaptive **effector processes** (e.g. Gzmb) could bring about tumour elimination. Xs are intended to represent the predicted importance of a given activity over time. Please note, this schematic reflects a working hypothesis; please see **limitations of Schematic 5.10***

Limitations of Schematic 5.10

Please note that Schematic 5.10 reflects prediction, a working-hypothesis, of biomarker importance that is informed by gene-expression data queried by *Nanostring* at only two time-points (24hrs and 5d post aPDL1+US therapy). Likewise, the genes and programs shown

represent only a fraction of those evaluated by *Nanostring* and other changes not tabulated could be playing an even more important role than those highlighted in the table. Additionally, the predicted importance (number of Xs) reflects an opinion rather than being defined by a significance and/or FC cut-off. Further, although genes are shown as belonging to a single functional area, in reality these genes often play pleiotropic roles across many of the activities shown. Additionally, because the gene expression data was evaluated in bulk (i.e. not on a single-cell basis) it is not possible to exactly attribute expression of a gene to a particular cell-type.

Gene-level changes were assessed in this study, and while *Nanostring* profiling and gene co-expression patterns have been shown to accurately correlate with protein-level changes [Sharpe et al. 2018], it was still desirable to try and directly-assess protein level changes. To better understand protein-level changes and increase the utility of the animal study, additional tissue collected at from 5d mice was assessed by FCM in the next subsection.

5.11 Flow Cytometry of 5-Day Tissue

After tumour tissue collection for *Nanostring* (the primary purpose of the study), remaining 5d-tumour tissue was processed and assessed via FCM. Although useful data was obtained it should be interpreted in the context of the very small quantities of tumour tissue which were available for FCM processing. This was a particular issue for samples from aPDL1+US treated mice owing to the very small tumour volumes at d5 given the efficacy of the treatment and the preferential, intentional prioritized allocation of tissue for *Nanostring*.

5.11.1 Experimental Overview

At sacrifice, in addition to tumour tissue, tumour-draining lymph nodes (DLNs) and non-draining lymph nodes (NLNs) were collected and stored in 5% FBS-PBS or equivalent. Tissues were processed to single-cell suspensions then stained with extracellular then intracellular markers. For additional detail, please refer to Section 2.6.2.

5.11.2 FCM Panel Design

FCM panel markers (FCM1, FCM2, and FCM3) and gating hierarchies are shown in Fig. 5.11 (FCM1) and Appx. 5.11 (FCM2 and FCM3). There were n=5-6 samples/intervention/tissue for most markers evaluated with the exception of tumour-tissue stained by the 3rd FCM panel which had only n=4 aPDL1+US treated tumour samples. Out of appropriately stained samples (198 samples), one sample was excluded due to a spectral compensation error (1 of 198 samples). On average, there were 68,941 size-gated events acquired per sample, therefore samples with fewer than 1000 size-gated events (7 of 197) were also excluded from analysis. Gating (when required) was informed by fluorescence-minus one (FMO) control.

Figure 5.11: Flow Cytometry (FCM) Panel and Gating Hierarchy

a

FITC	PE	PE-TxRed	PerCP	PE-Cy7	APC	APC-Cy7	Pacific Blue
CD3	CD62L	PD1	CD4	TIM3	GITR	CD8	CD44

b

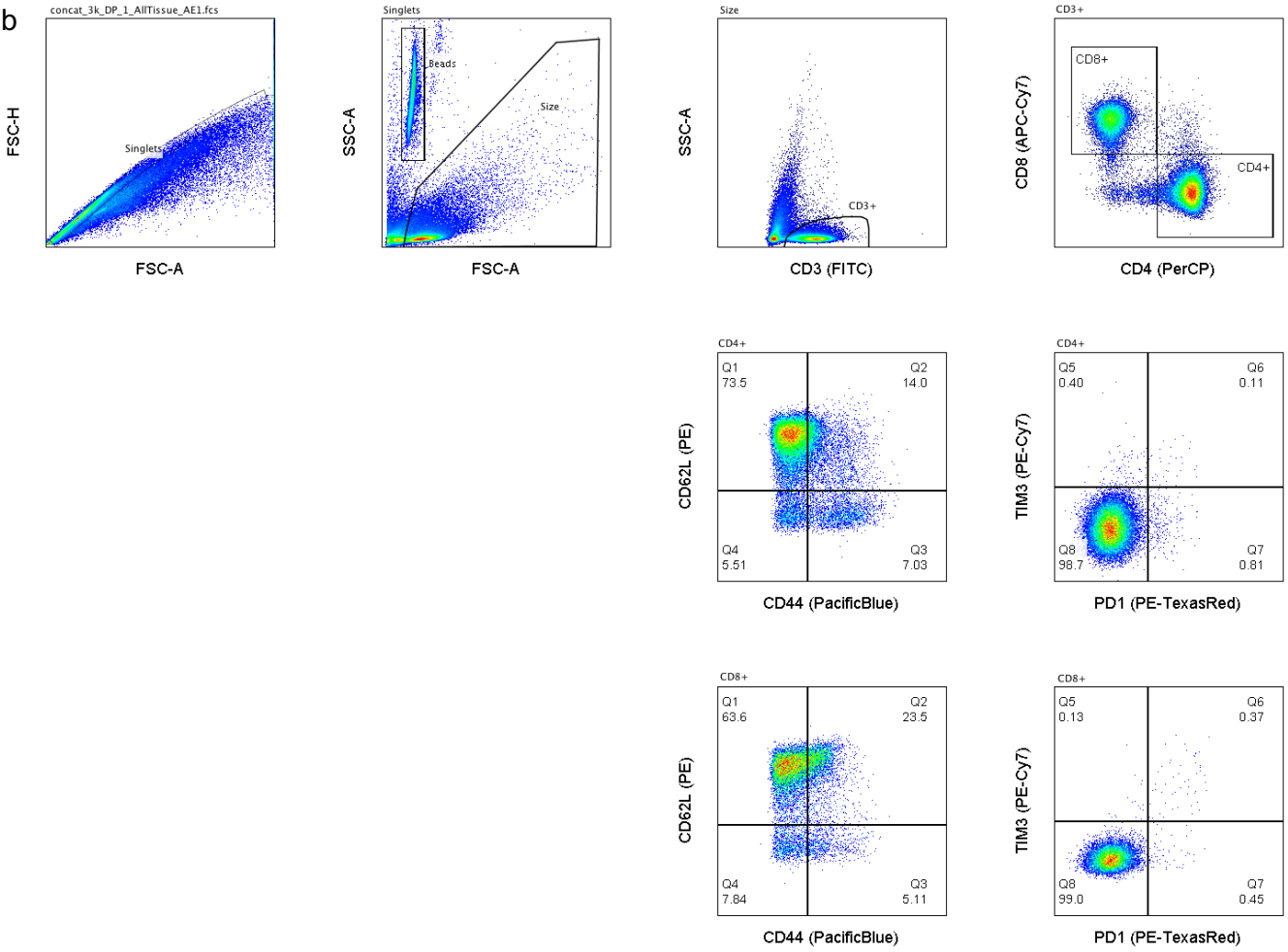


Figure 5.11
a) FCM Panel 1 (FCM1) evaluates changes to lymphocyte (T cell) functional state and memory status.
b) FCM1 gating hierarchy; first events were singlet gated, then FSC-A/SSC-A gated by size, then selected by CD3 (T cell) expression and subdivided to CD4 or CD8 subsets. CD4 GITR+ and CD8 GITR+ populations were determined based on FMO (negative) control. CD4 and CD8 T cells were gated based upon CD62L & CD44 co-expression or TIM3 & PD1 co-expression using quadrant gating. FCM2 and FCM3 gating is shown in Appx. 5.11

5.12 Distribution of Leukocytes Populations

5.12.1 Phenotypic comparisons across tissue-types irrespective of treatment

Preliminary analysis aimed to establish the high-level distributions of leukocyte populations between tumour and LN immune tissue, irrespective of treatment group. Data was aggregated by tissue-type, then the average leukocyte subsets frequencies were determined (Fig. 5.12a). Irrespective of treatment assignment, on average leukocytes (CD45+ cells) recovered from tumour-tissue primarily consisted of myeloid cells (~71%). In contrast, CD3+ T cells made up the majority of lymph node (LN) tissue leukocytes and just ~3.8% of tumour-tissue. NK cells were found in tumour samples (~4.6%) but were nearly absent in LN tissues.

Figure 5.12: Leukocyte Subset Analysis (1/2)

a

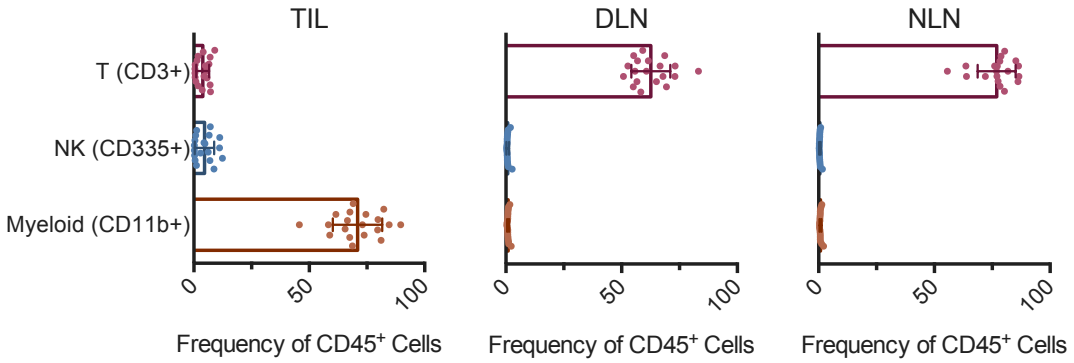


Figure 5.12
a) The average frequency of total T Cell (CD45+CD11b-CD3+), NK (CD45+CD11b-CD3-CD335), and myeloid (CD45+CD11b+) populations out of total leukocytes (CD45+), irrespective of treatment group across different tissue types: tumour (TIL), tumour-draining lymph node (DLN), or non-draining lymph node (NLN).

The observation that myeloid cells were the predominant population of immune cells recovered from tumour tissue is consistent with work reported by Elpek et al. who found that myeloid cells make up ~60% of tumour leukocytes—a frequency close to that which was observed here [Elpek et al. 2014]. Myeloid cells can facilitate immune evasion [Kusmartsev & Gabrilovich 2006], however, they can also play anti-tumour roles [Braster et al. 2014], typically

as determined by their environment. From a high-level, the predominance of myeloid cells within CT26 tumours suggests that the differential functional behaviour of these cells may play a key role in determining the differential responses observed between groups.

5.12.2 Phenotypic comparisons by treatment-group & tissue-type

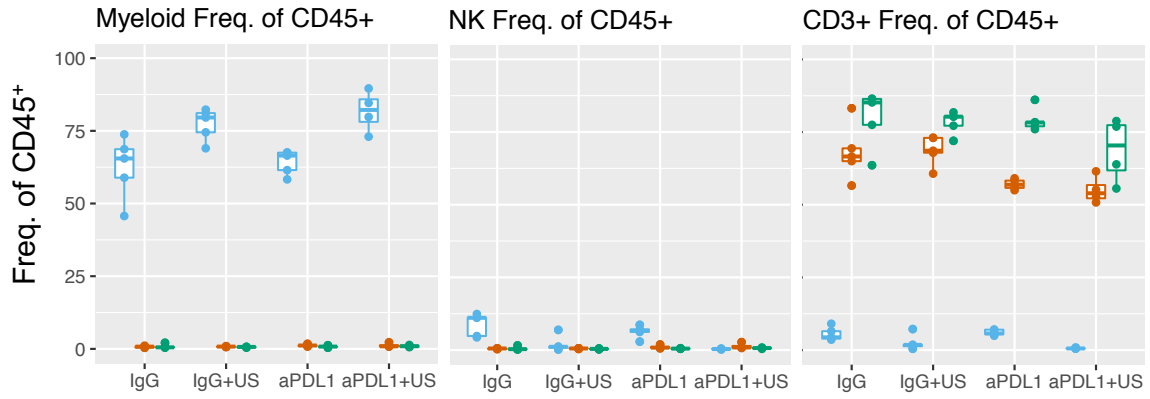
Fig. 5.12b presents the differences in myeloid, NK, and T cell frequency out of total leukocytes on a per-group basis across the 3-tissue types assessed. Statistical analysis of tumour tissue by means of ANOVA with Dunnett's post-hoc correction revealed that the frequency of myeloid cells was significantly elevated after cavitation-treatment compared to IgG control, with the greatest mean difference in myeloid frequency found between IgG and aPDL1+US treatment (Fig. 5.12d). Surprisingly, NK cell frequencies were significantly lower after cavitation treatment, with the greatest decrease in frequency found within aPDL1+US treated tumours. Likewise, the frequency of T cells out of leukocyte total were significantly decreased after aPDL1+US treatment, but not aPDL1 or IgG+US treatment.

However, it is worthwhile to note that the increases (myeloid cells) and decreases (NK and T cells) were relative to each other—the frequencies were calculated out of a shared, total leukocyte parent. Hence, this data does not estimate how the numbers of a particular immune population changed with respect to total tumour mass (infiltration). For example, in the case of aPDL1+US treatment (as compared to IgG control) the data suggests that 1 of 4 things could have taken place: 1) myeloid infiltration decreased, but NK and T cell infiltration decreased to a greater degree, 2) myeloid cell infiltration remained stable, while NK and T cell numbers decreased, 3) myeloid infiltration increased, whereas NK and T cell infiltration decreased, or 4) myeloid, NK, and T cell infiltration increased, however myeloid cell number increased most greatly. Preliminary analysis of infiltration data suggested (3), however, owing to FCM-processing artefact (i.e. disproportionate sample loss from smaller tumours during single-cell

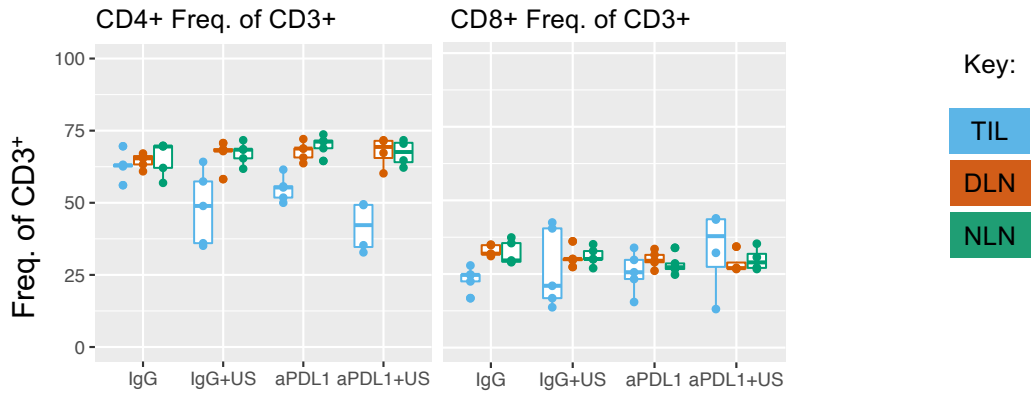
preparation, likely rendering normalized count to tumour-weight scaling unreliable), it was not feasible to accurately calculate infiltration using FCM. However, cell type profiling by *Nanostring*, a surrogate of infiltration, found significant increases in the cell scores of CD45 (total leukocytes), macrophages, neutrophils, DCs, NK CD56dim cells, and T cells—results most consistent with last (4) hypothesis—that leukocyte infiltration increased, however myeloid infiltration increased most greatly.

Figure 5.12: Leukocyte Subset Analysis (2/2)

b



c



d ANOVA of Tumor-Tissue Cell Subset Freq.

	Dunnett's test	Myeloid Freq. of CD45+	NK Freq. of CD45+	T Freq. of CD45+	CD4 T Freq. of CD3+	CD8 T Freq. of CD3+	CD4/CD8 Ratio
TIL	IgG vs. IgG+US	*	**	ns	*	ns	ns
	IgG vs. aPDL1	ns	ns	ns	ns	ns	ns
	IgG vs. aPDL1+US	**	***	**	**	ns	ns

Figure 5.12 continued:
b) The frequency of leukocytes of tumour (blue), draining lymph node (red), and non-draining lymph node (blue) across cell (green) that are myeloid (CD11b+), NK (CD335+) and CD3 T Cell in nature
c) The frequency of CD4 (CD45+CD11b-CD3+CD4+) and CD8 (CD45+CD11b-CD3+CD8+) T cells out of parent (CD45+CD11b-CD3+) by treatment group and tissue-type (by colour).
d) Statistical analysis of tumour-tissue as shown in (b-c) and CD4/CD8 ratio calculated using FCM3 data; each treatment is compared against IgG control by ordinary one-way ANOVA with Dunnett's correction for multiple comparisons (single pooled variance)

Put simply, the data suggests that while aPDL1+US therapy may benefit from increases in T and NK infiltration, myeloid cells may play a predominant role in efficacy benefits observed as they 1) are the biggest fraction of immune cells within the tumour, and 2) likely increase the most in number (infiltration) after aPDL1+US therapy.

With respect to tumour-tissue, T cell subset analysis (Fig. 5.12c) revealed that there were no significant differences in CD8 T cell frequency between groups, however, similar to their parent population (total T cells), CD4+ T cells were significantly lower in frequency in aPDL1+US treated tumours (Fig. 5.12d). This suggests that the drop in total T cell frequency can likely be ascribed to a decrease within the CD4 T cell compartment. There were NS changes with respect to the tumour-tissue CD4/CD8 frequency in any group.

5.13 Frequencies of T Regulatory Cells

5.13.1 T regulatory cells irrespective of treatment arm :

Regulatory T cells (T Regs) are a subset of CD4 T cells which can support tumour evasion of anti-tumour immune responses through multiple mechanisms. Physiologically they function to block aberrant immune attack (i.e. autoimmunity [Cvetanovich & Hafler 2010]), however, in the context of cancer, they enable tumorigenesis and immune escape through contact dependent (e.g. CTLA-4 expression to competitively capture B7 activation ligands) and contact independent mechanisms (the production of immunosuppressive factors like IL-10 and TGFb) [Tanaka & Sakaguchi 2017, Stockis et al. 2019]. Irrespective of treatment arm, greater T Regs made up a greater percentage of the CD4 compartment in tumour tissue compared to DLN or NLN tissue (Fig. 5.13a). In fact, T Regs made-up just over half of all CD4s within TIL tissue, a frequency nearly identical to the 56.7% frequency reported by Magnuson et al. with CT26 tumours [Magnuson et al. 2018]. This suggests that the CT26 tumours of our study were not immunologically silent; rather that they are immunogenic and marked by the upregulation of immune evasion programs to escape immune attack; in fact others have classified CT26 tumours as immunogenic [Lechner et al. 2013]

Figure 5.13: T Regulatory Cell Changes (1/2)

a

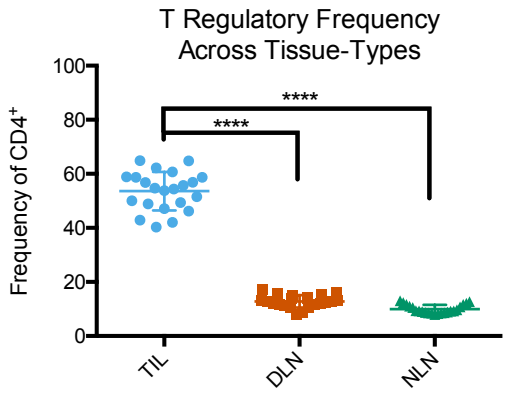


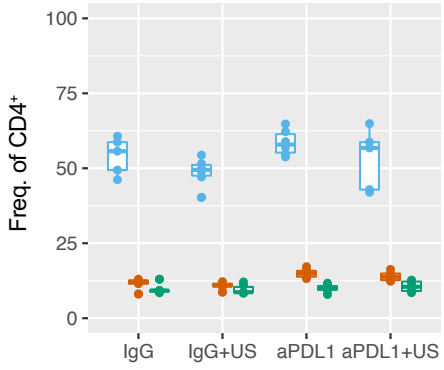
Figure 5.13a:
a) T reg. frequency (out of CD4 total) for each tissue-type, irrespective of treatment assignment. Statistical comparison by ordinary one-way ANOVA with Tukey's multiple comparisons test (single pooled variance) revealed a significantly greater frequency of Tregs in tumour-tissue as compared to DLN or NLN tissue

5.13.2 T Regulatory cells compared by treatment group

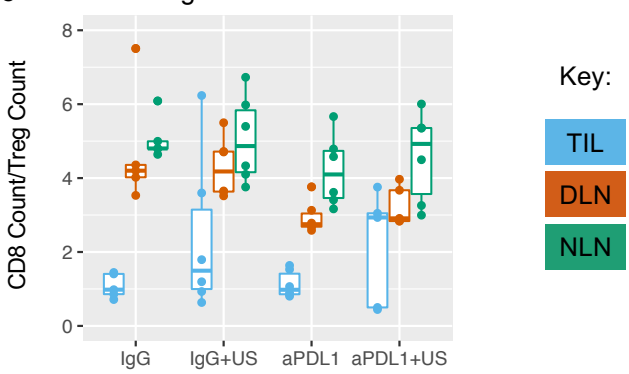
Fig. 5.13b presents the T reg. cell frequency on a per group basis by tissue-type. Given that CD4 T cells are not the only type of T cells, another commonly used metric to define lymphocyte activity is to assess the ratio of CD8 T cells to T Regs [Baras et al. 2016, Selby et al. 2016]. Fig. 5.13c calculates such ratios for each tissue-type by intervention. Comparison of tumour tissue T Reg frequency by treatment group to IgG control revealed no significant difference (Fig. 5.13d).

Figure 5.13: T Regulatory Cell Changes (2/2)

b



c



d

ANOVA of Tumor-Tissue Treg. Freq. & CD8/Treg Ratio

Dunnett's test	Treg. Freq. of CD4 T Cell	CD8 Count / Treg. Count
IgG vs. IgG+US	ns	ns
IgG vs. aPDL1	ns	ns
IgG vs. aPDL1+US	ns	ns

Figure 5.13 continued:
b) Box and whisker plots, overlaid by individual samples, explicating Treg frequency across tissue types and treatment groups as indicated.
c) The ratio of CD8 T cells to Tregs as calculated by dividing the CD8 T cell count by the Treg count.
c) Statistical analysis of tumour-tissue as shown in (b) and (c); each treatment is compared against IgG control by ordinary one-way ANOVA with Dunnett's correction for multiple comparisons (single pooled variance)

Tumour CD8/T Reg ratio changes were also insignificantly different by treatment, however although NS, cavitation-treated (IgG+US or aPDL1+US) tumours had greater mean CD8/T Reg ratios (Fig. 5.13d). This may suggest that tumours of cavitation treated mice are modestly tilted toward anti-tumour lymphocyte activity rather than an immunosuppressive program—perhaps as a consequence of pro-inflammatory cues, as suggested by *Nanostring* data.

.

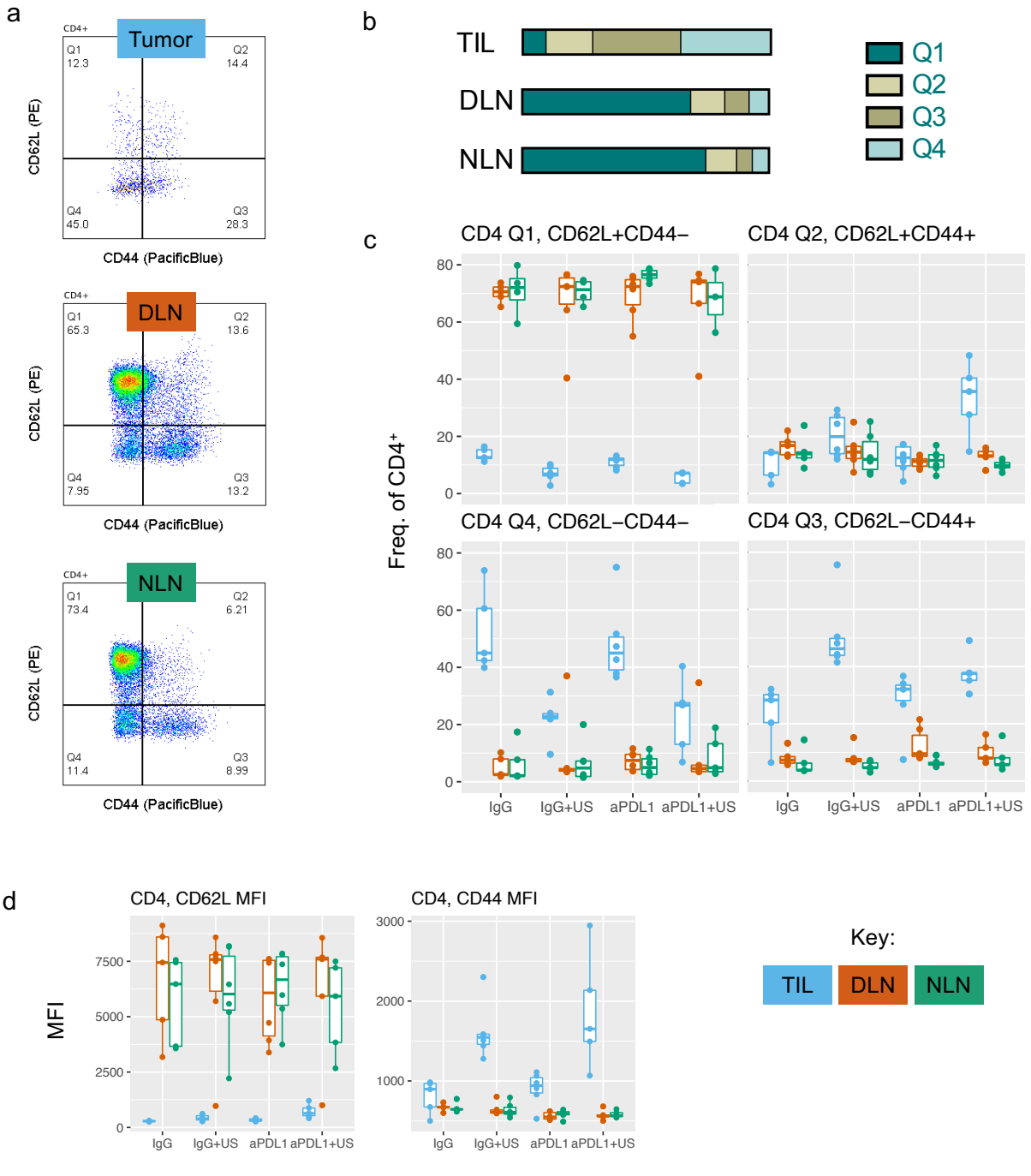
5.14 & 5.15 T Cell Memory Marker Expression: CD62L vs. CD44 Expression

Simultaneous T cell CD62L and CD44 evaluation enables the classical classification of T cell's memory status into naïve (Q1: CD62L+CD44-), central memory (Q2: CD62L+CD44+), and effector memory (Q3: CD62L-CD44+) compartments [Gerberick et al. 1997, Zhou et al. 2011]. Fig. 5.14a illustrates FCM gating of CD4 CD62L and CD44 of tumour (TIL), draining lymph node (DLN), and non-draining lymph node (NLN) tissue. Fig. 5.14b summarizes overall shifts in the average frequency of Q1-Q4 populations by tissue type for all treatment groups combined. Fig. 5.14c quantifies the Q1 through Q4 populations across treatment arms and tissue type (by colour, tumour blue, DLN orange, NLN green).

Irrespective of treatment, the majority of DLN and NLN CD4 T cells were naïve (Q1) whereas the majority of TILs expressed CD44 and were either central memory (Q2) or effector memory (Q3) cells irrespective of treatment group (Fig. 5.14b). On a per treatment-level, the most interesting changes were perhaps observed in tumour-tissue Q2, where it appeared that expansion had taken place. A statistical comparison of treatment arms within TIL tissue revealed that only aPDL1+US therapy resulted in a statistically significant increase of Q2 frequency as compared to IgG by ANOVA with Dunnett's testing. Put simply, aPDL1+US therapy significantly increased the frequency of central memory (Q2) CD4 T cells in tumour tissue.

FCM-data can be appreciated through gating and also an assessment of the median fluorescence intensity (MFI) of a given marker, especially relevant for functional markers where clear delineations between population subsets are less clear. Fig. 5.14d, corroborates the results from Q2 gating, revealing that both CD62L and CD44 MFI increased most greatly in aPDL1+US treated mice. Likewise, statistical testing revealed that both CD44 MFI and CD62L MFI independently were significantly elevated only in aPDL1+US treated mice (Fig. 5.14e).

Figure 5.14: CD4 T Cell Memory Status



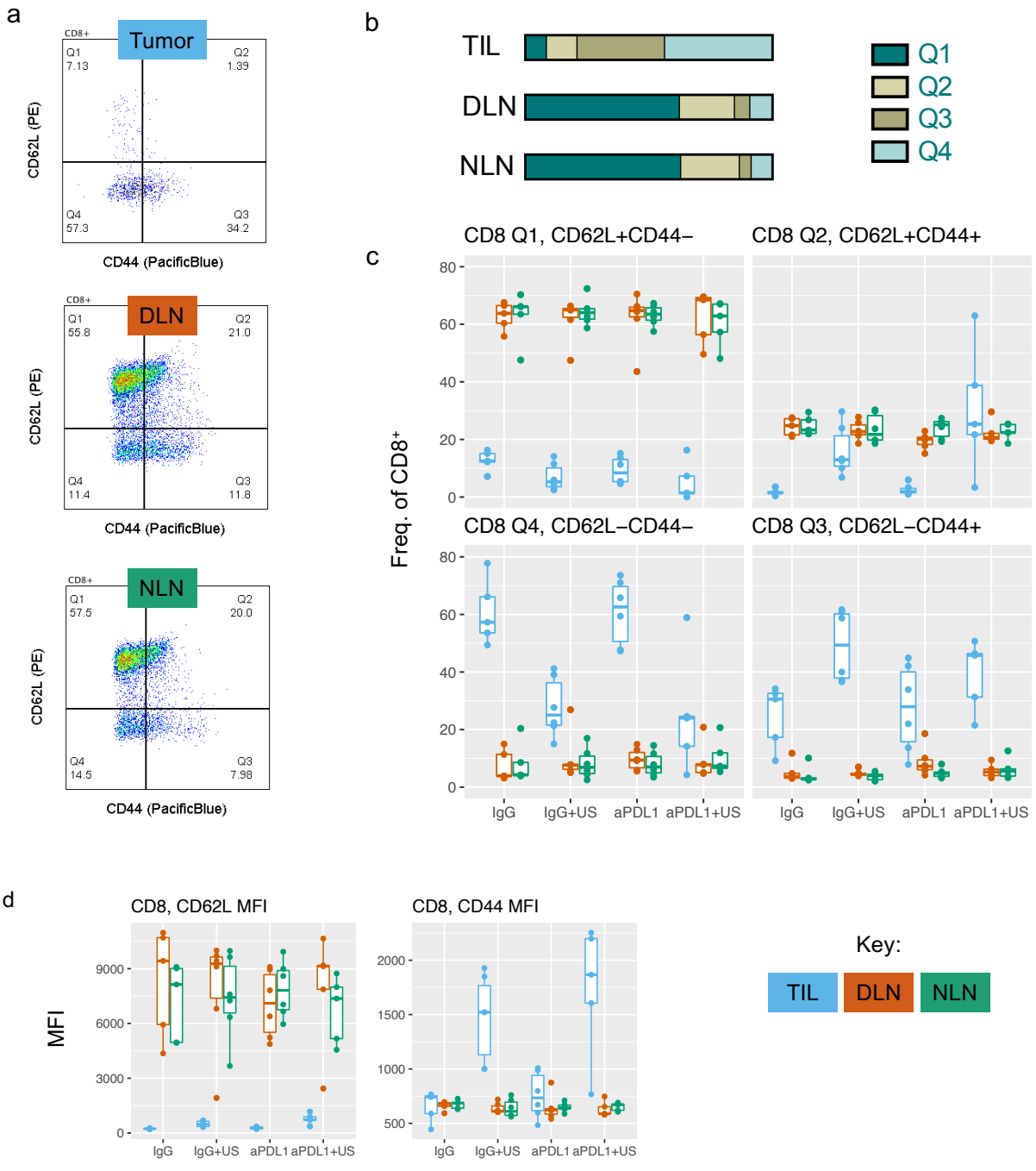
e ANOVA of Tumor-Tissue Subset (Quadrant) Freq. or MFIs

CD4	Dunnett's test	Q2 Freq.	CD62L MFI	CD44 MFI
TIL	IgG vs. IgG+US	ns	ns	*
	IgG vs. aPDL1	ns	ns	ns
	IgG vs. aPDL1+US	***	**	**

Figure 5.14
a) Example FCM gating of CD4 CD62L v. CD44 expression of tumour, draining lymph node (DLN), and non-draining lymph node (NLN) tissue.
b) Part-of-whole analysis illustrating the average breakdown of Q1, Q2, Q3, and Q4 contributions between different tissue types (irrespective of treatment)
c) Boxplots overlaid by individual data points of CD4 naïve (Q1: CD62L+CD44-), central memory (Q2: CD62L+CD44+), and effector memory (Q3: CD62L-CD44+) populations across tissue types and treatment groups. Each colour corresponds to a different tissue-type (light blue = tumour tissue, Red = tumour-draining lymph node tissue, Green = non-tumour draining lymph node tissue)
d) CD62L and CD44 median fluorescence intensity (MFI) for CD4 T Cells by group and tissue-type
e) Statistical analysis of the CD4 T cell Q2 (central memory) population frequency, CD62L MFI, and CD44 MFI for tumour-tissue; each treatment is compared against IgG control by ordinary one-way ANOVA with Dunnett's correction for multiple comparisons (single pooled variance)

Data as organized in Fig. 5.14 for CD4 T cells is similarly organized in Fig. 5.15 for the CD8 compartment. Changes to memory and differentiation classification of the CD4 compartment were mimicked in the CD8 compartment; with a notable a significant elevation of the tumour-tissue Q2 population in aPDL1+US treated mice compared to IgG controls was observed (Fig. 5.15e). Likewise, CD44 and CD62L MFI in CD8 cells was also highest on average in aPDL1+US mice compared to all other groups (Fig. 5.15d-e), and the greatest effect was seen when comparing IgG control to aPDL1+US treated mice.

Figure 5.15: CD8 T Cell Memory Status



e ANOVA of Tumor-Tissue Subset (Quadrant) Freq. or MFIs

CD8	Dunnett's test	Q2 Freq.	CD62L MFI	CD44 MFI
TIL	IgG vs. IgG+US	ns	*	**
	IgG vs. aPDL1	ns	ns	ns
	IgG vs. aPDL1+US	**	***	***

Figure 5.15
a) Example FCM gating of CD8 CD62L v. CD44 expression of tumour, draining lymph node (DLN), and non-draining lymph node (NLN) tissue.
b) Part-of-whole analysis illustrating the average breakdown of Q1, Q2, Q3, and Q4 contributions between different tissue types (irrespective of treatment)
c) Boxplots overlaid by individual data points of CD8 naïve (Q1: CD62L+CD44-), central memory (Q2: CD62L+CD44+), and effector memory (Q3: CD62L-CD44+) populations across tissue types and treatment groups. Each colour corresponds to a different tissue-type (light blue = tumour tissue, Red = tumour-draining lymph node tissue, Green = non-tumour draining lymph node tissue)
d) CD62L and CD44 median fluorescence intensity (MFI) for CD8 T Cells by group and tissue-type
e) Statistical analysis of the CD8 T cell Q2 (central memory) population frequency, CD62L MFI, and CD44 MFI for tumour-tissue; each treatment is compared against IgG control by ordinary one-way ANOVA with Dunnett's correction for multiple comparisons (single pooled variance).

The observed significant upregulation of Q2 central memory T cells across both the CD4 and CD8 compartments suggests that combination of aPDL1+US generates T cell anti-tumour memory. On this basis, it could be reasoned that improved delivery of an aPDL1 to one tumour can lead to abscopal-like benefits in distal, non-US treated tumours owing to T cell memory generated. Future work can further explore the potency of the immunological memory generated through tumour re-challenge studies or adoptive transfer studies, whereby immune cells from treated mice are administered to treatment naïve, tumour bearing mice.

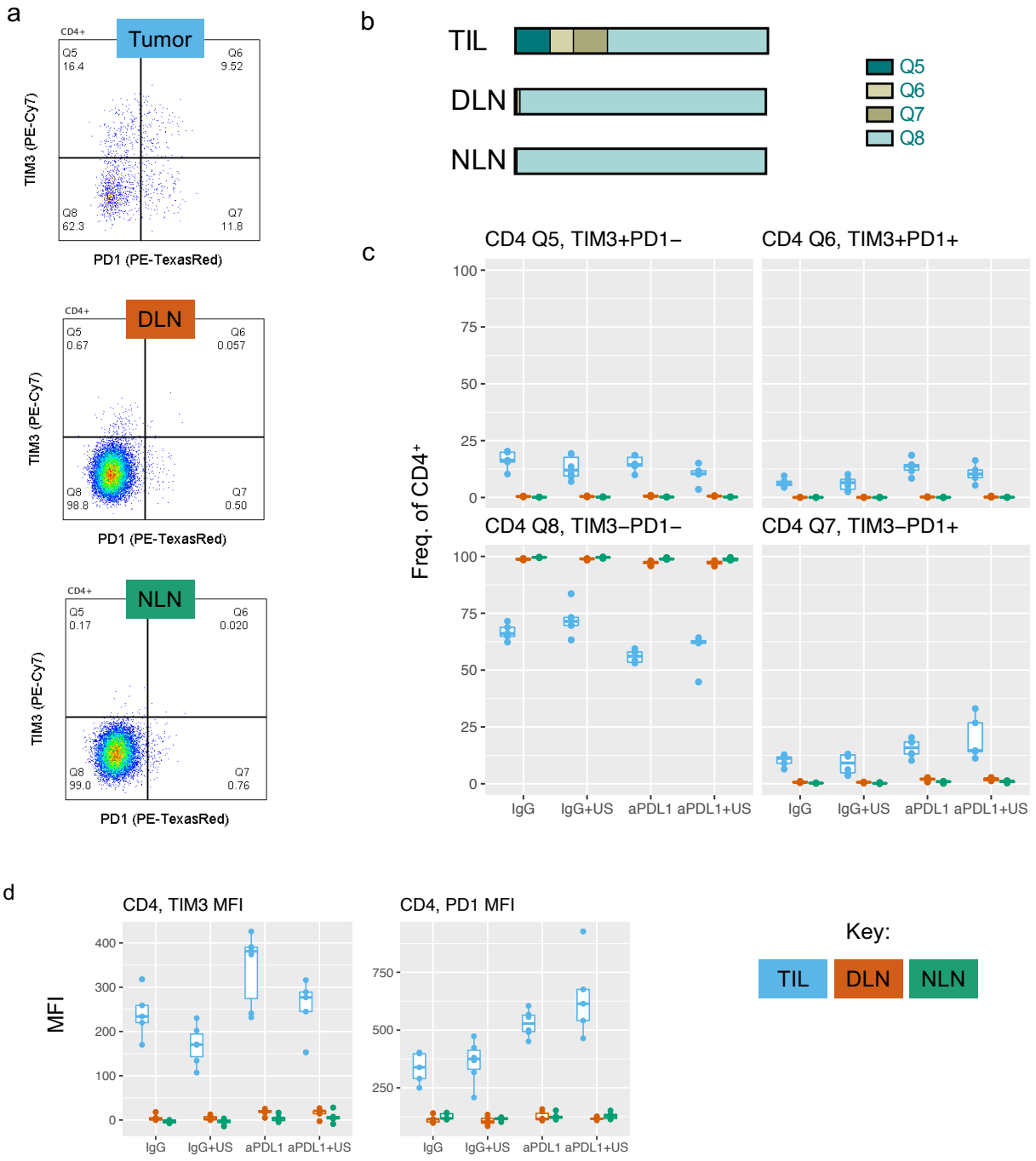
5.16 & 5.17 T Cell Exhaustion: TIM3 vs. PD1 Expression

Monney et. al first identified TIM3 as a negative regulator of immune responses [Monney et al. 2002]. Later, work to understand T cell responses in the context of viral infections, found that TIM3 could be used to define exhausted, dysfunctional CD8 T cells [Jones et al. 2008, Golden-Mason et al. 2009]. Sakuishi et al. later worked to define what TIM3's role in is cancer. In particular, Sakuishi *et. al* determined that the co-expression of TIM3 with PD1, another negative regulator of T cell responses, enabled the definition of an exhausted, dysfunctional cytotoxic tumour T cell population [Sakuishi et al. 2010]. It was observed that CD8 T cells bearing a PD1+TIM3+ signature are exhausted, dysfunctional, and unable to carry out effector T cell activities like producing pro-inflammatory cytokines IL-2, IFNg, and TNFa. Alternatively, the PD1+TIM3- signature was found to be of CD8 T cells most capable of mounting an anti-tumour immune response [Sakuishi et al. 2010].

Figures 5.16 and 5.17 explore the shifts in TIM3 and PD1 expression in CD4 (Fig. 5.16) and CD8 (Fig. 5.17) T cells by tissue-type and treatment-arm across with quadrants: Q5 (PD1-TIM3+), Q6 (PD1+TIM3+), Q7 (PD1+TIM-), and Q8 (PD1-TIM3-). For reference, Fig. 5.16d and Fig. 5.17d show MFI values of PD1 and TIM3 expression by tissue-type and treatment-group.

Comparing between tissue-types, irrespective of treatment arm, the data show PD1 and TIM3 expression in tumour tissue was robust across both CD4 and CD8 T cells (Fig. 5.16b and Fig. 5.17b). On the other hand, PD1 and TIM3 expression in LN tissues was nearly absent. This is consistent with the purported role of lymph nodes—sites where naïve T cell aggregate awaiting antigen-specific activation [Bousso 2008]. Given the paucity of expression in LNs, statistics related to this and other functional markers by treatment were not calculated for NLN or DLN tissue.

Figure 5.16: CD4 T Cell TIM3 and PD1 Expression

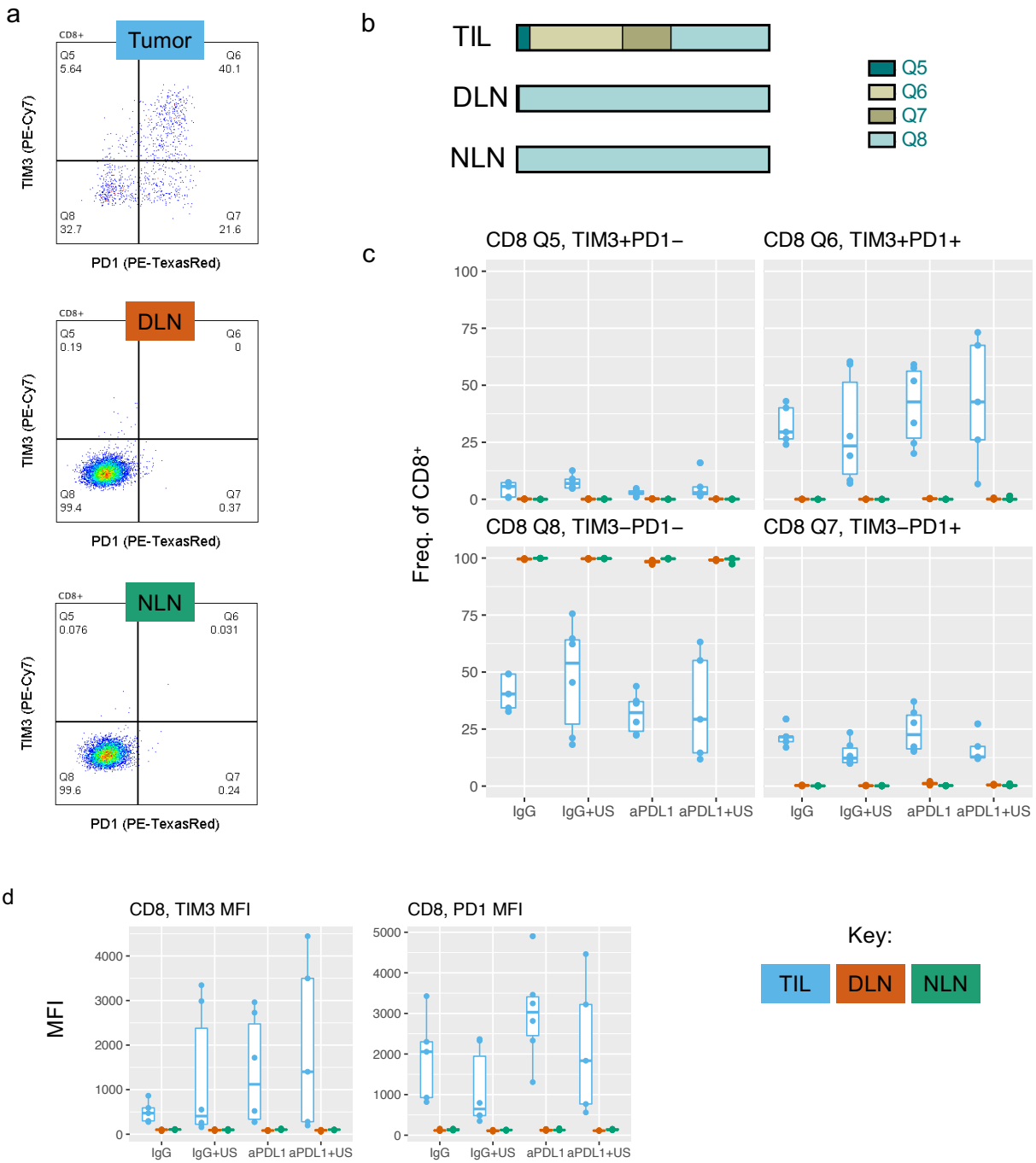


e ANOVA of Tumor-Tissue Subset (Quadrant) Freq. or MFIs

CD4	Dunnett's test	Q7 Freq.	TIM3 MFI	PD1 MFI
TIL	IgG vs. IgG+US	ns	ns	ns
	IgG vs. aPDL1	ns	*	*
	IgG vs. aPDL1+US	*	ns	***

Figure 5.16
a) Example FCM gating of CD4 TIM3 v. PD1 expression of tumour, draining lymph node (DLN), and non-draining lymph node (NLN) tissue.
b) Part-of-whole analysis illustrating the average breakdown of Q5, Q6, Q7, and Q8 contributions between different tissue types (irrespective of treatment)
c) Box plots of Q5 (TIM3+PD1), exhausted (Q6: TIM3+PD1+), activated (Q7: CD62L+CD44-), and inactive (Q8: TIM3-PD1-) CD8 T cells by treatment and color-coded by tissue-type
d) TIM3 and PD1 median fluorescence intensity (MFI) for CD4 T Cells by group and tissue-type for reference
e) Statistical analysis of the CD4 T cell Q7 (activated) frequency, TIM3 MFI, and PD1 MFI for tumour-tissue; each treatment is compared against IgG control by ordinary one-way ANOVA with Dunnett's correction for multiple comparisons (single pooled variance)

Figure 5.17: CD8 T Cell TIM3 and PD1 Expression



e ANOVA of Tumor-Tissue Subset (Quadrant) Freq. or MFIs

CD8	Dunnett's test	Q7 Freq.	TIM3 MFI	PD1 MFI
TIL	IgG vs. IgG+US	ns	ns	ns
	IgG vs. aPDL1	ns	ns	ns
	IgG vs. aPDL1+US	ns	ns	ns

Figure 5.17
a) Example FCM gating of CD8 TIM3 v. PD1 expression of tumour, draining lymph node (DLN), and non-draining lymph node (NLN) tissue.
b) Part-of-whole analysis illustrating the average breakdown of Q5, Q6, Q7, and Q8 contributions between different tissue types (irrespective of treatment)
c) Box plots of Q5 (TIM3+PD1), exhausted (Q6: TIM3+PD1+), activated (Q7: CD62L+CD44-), and inactive (Q8: TIM3-PD1-) CD8 T cells by treatment and color-coded by tissue-type
d) TIM3 and PD1 median fluorescence intensity (MFI) for CD4 T Cells by group and tissue-type for reference
e) Statistical analysis of the CD8 T cell Q7 (activated) frequency, TIM3 MFI, and PD1 MFI for tumour-tissue; each treatment is compared against IgG control by ordinary one-way ANOVA with Dunnett's correction for multiple comparisons (single pooled variance).

Comparing between tumour-tissue treatment arms and IgG control, revealed that the CD4 T cell Q7 population (CD4+PD1+TIM3-) was significantly greater in aPDL1+US mice compared to IgG control (ANOVA with Dunnett's testing), with no other significant changes observed (Fig. 5.16e). This suggests that treatment facilitated either the expansion or maintenance of PD1+TIM3- cells, cells which likely bear a phenotype indicative of activation but not exhaustion. However, it is noteworthy that Sakuishi et. al's work explored CD8 T cells but not CD4 T cells (Sakuishi et. al. An assessment of the CD8 TIL compartment did not reveal a similar Q7 expansion (Fig. 5.17e).

5.18 T Cell Activation

5.18.1 CD69, OX40, ICOS, and GITR

CD69, OX40, ICOS, GITR expression were utilized to further query the activation state of lymphocytes with respect to tissue-type and treatment group. In general, irrespective of treatment, marker expression was more robust in tumour-tissue lymphocytes in comparison to DLN or NLN tissue (Fig. 5.18a-c). Hence, the remainder of analysis is focused upon tumour-tissue expression.

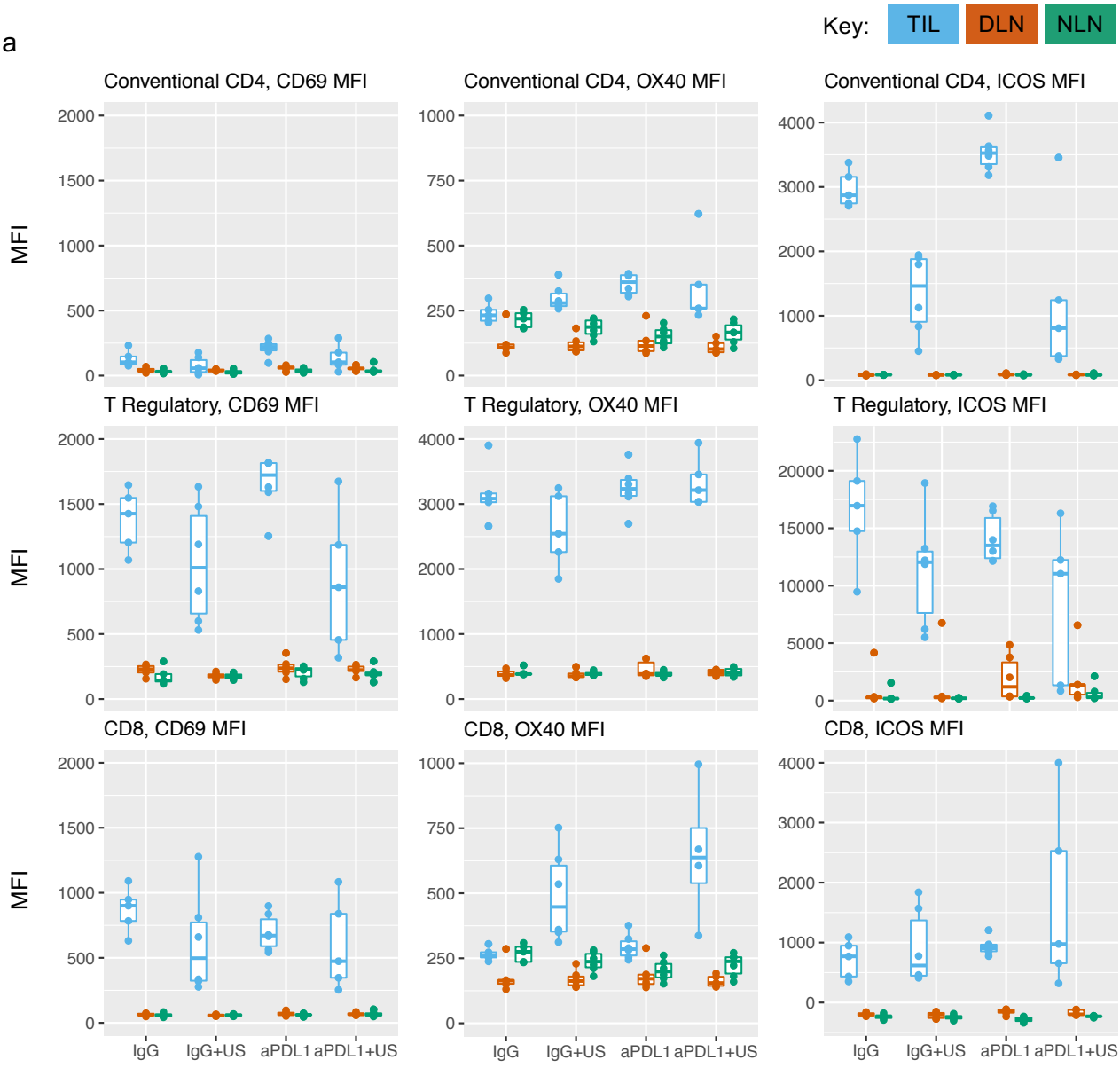
5.18.2 Tumour-tissue changes in CD69, OX40, and ICOS Expression

Out of lymphocyte subsets (conventional CD4, T Reg, and CD8 T cells), T Regs generally expressed greater CD69, OX40 and ICOS (as per MFI) in comparison to conventional CD4 and CD8 T cells (Fig. 5.18a). Tumour-tissue ANOVA analysis with Dunnett's correction, comparing the lymphocyte subset's MFI of a given marker between IgG and IgG+US, aPDL1, or aPDL1+US treatments are summarized in Fig. 5.18b.

CD69 was not significantly modulated in a treatment-specific fashion by any lymphocyte-subset. OX40 expression significantly increased in the CD8 compartment (by MFI) in aPDL1+US treated mice but was not significantly modulated by treatment in any of the CD4 subsets. In CD8 T cells, OX40 expression has been shown to support CD8 T cell survival, proliferation, and memory development [Bansal-Pakal et al. 2004, Song et al. 2005, Croft et al. 2009]. The significant OX40 expression of CD8 T cells is consistent with an improving CD8 T cell function in tumours of aPDL1+US treated mice.

Figure 5.18: T Cell Activation (1/2)

a



b ANOVA of Tumor-Tissue MFIs for Each Cell Subset

MFI	Conventional CD4 T Cell			Regulatory CD4 T Cell			CD8 T Cell		
Dunnett's test	CD69	OX40	ICOS	CD69	OX40	ICOS	CD69	OX40	ICOS
IgG vs. IgG+US	ns	ns	**	ns	ns	ns	ns	ns	ns
IgG vs. aPDL1	ns	ns	ns	ns	ns	ns	ns	ns	ns
IgG vs. aPDL1+US	ns	ns	**	ns	ns	*	ns	**	ns

Figure 5.18
a) The median fluorescence intensities of CD69, OX40, and ICOS (from left to right) of Conventional CD4 T cells (CD3+CD4+FOXP3-), Regulatory T cells (CD3+CD4+FOXP3-), and CD8 T cells (CD3+CD8+) percentage (frequency) of each sample, grouped together by intervention and color-coded by tissue-type.
b) Ordinary one-way ANOVA with Dunnett's multiple comparisons test (single pooled variance) was utilized to compare a given marker's MFI (CD69, OX40, or ICOS) between intervention groups and IgG for each lymphocyte subset (conventional CD4 T cells, T regulatory cells, and CD8 T cells).

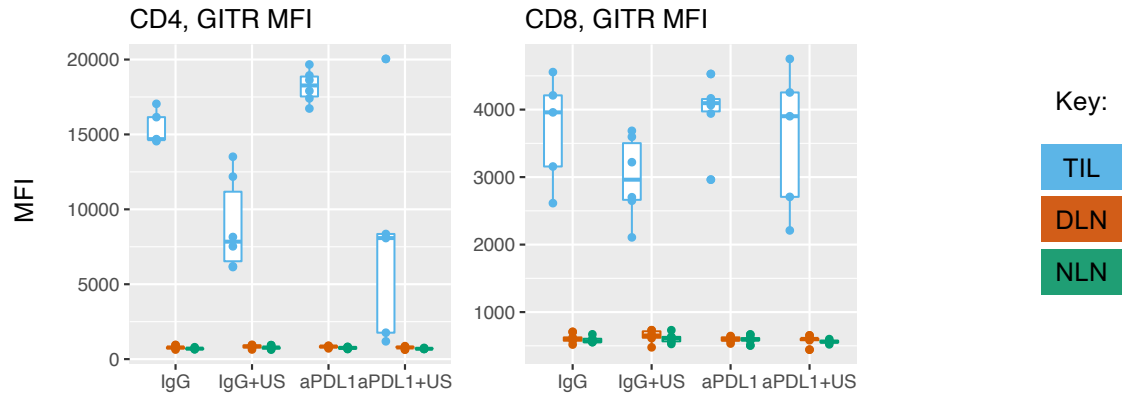
ICOS on the other hand was significantly modulated by both CD4 subsets. ICOS expression acts to amplify the T cell's intrinsic function, whether it bolstering the suppressive activities of a T Reg or, alternatively supporting the inflammatory activities of a conventional T cell [Dong et al 2001, Chen et al. 2018]. The significant loss of T Reg ICOS expression suggests that the T Regs of aPDL1+US treated mice are less functional/suppressive; a feature consistent with improving anti-tumour immunity. However, ICOS MFI also significantly decreased in conventional CD4 T cells treated by aPDL1+US (and IgG+US). These decreases are difficult to reconcile mechanistically, though, it is notable that ICOS expression in conventional T cells was much lower than that of T Reg ICOS expression.

5.18.3 Tumour-tissue changes in GITR Expression

Owing to the panel (FCM) in which GITR was assessed, GITR expression could be delineated between CD8 and CD4 subsets broadly, however, its expression could not be further subdivided into conventional and regulatory CD4 GITR expression (Fig. 5.18c-d).

Figure 5.18: T Cell Activation (2/2)

c



d ANOVA of Tumor-Tissue GITR MFI

Dunnett's test	CD4 T Cell	CD8 T Cell
IgG vs. IgG+US	*	ns
IgG vs. aPDL1	ns	ns
IgG vs. aPDL1+US	*	ns

Figure 5.18
c) The median fluorescence intensities of GITR for CD4 T cells (CD3+CD4+) and CD8 T cells (CD3+CD8+) of each sample, grouped together by intervention and color-coded by tissue-type. Owing to the FCM panel GITR was assessed in, it was not feasible to differentiate between conventional and regulatory CD4 T cell expression of GITR in other words, the CD4 population here contains a mixture of both T rags and conventional CD4 T cells.
d) Ordinary one-way ANOVA with Dunnett's multiple comparisons test (single pooled variance) was utilized to compare GITR MFI between intervention groups and IgG of either CD4 or CD8 T cells in tumour tissue.

GITR expression (by MFI) was far greater in tumour CD4 T cells compared to CD8 T cells. Statistical analysis observed that CD4 GITR MFI was significantly elevated as compared to IgG control in both cavitation (IgG+US or aPDL1+US) groups. No significant differences in tumour-tissue CD8 GITR MFI were observed. GITR acts in a manner very similar to that of ICOS; therefore, unfortunately, because this panel could not discern between conventional CD4 and Treg GITR expression it is not clear what the impact of total CD4 GITR loss is.

5.19 Cytotoxic Function: GranzymeB

As reviewed in 5.9, GranzymeB (Gzb) is a serine protease that is directly implicated in eliciting cell death via innate and adaptive immune cells. As per Fig. 5.19a, GranzymeB (Gzb) expression was observed in myeloid, NK, and T cell subsets, with generally greater Gzb expression in tumour-tissue immune populations over LN-sourced lymphocytes.

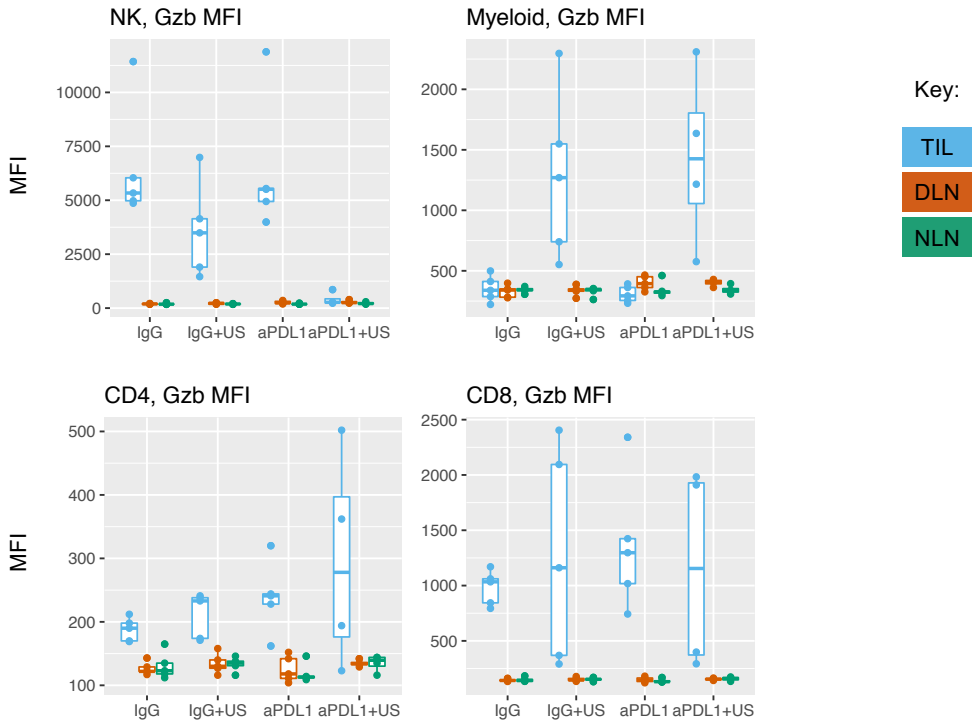
ANOVA analysis of tumour-tissue Gzb MFI by immune subset, revealed that Gzb was significantly elevated in myeloid cells of cavitation treated mice and significantly decreased in NK cells of aPDL1+US treated (Fig. 5.19b). While the decrease in NK cell Gzb MFI in aPDL1+US treated mice is perplexing, it is worthwhile to consider that NK cells represented less than 5% of the tumour leukocytes on average, and an even smaller fraction (<0.6%) of total leukocytes in aPDL1+US treated tumours (as per Fig. 5.12)—suggesting that although a decrease in NK Gzb occurred, it was not likely very meaningful given how few NK cells there actually were in aPDL1+US treated tumours.

In contrast, myeloid cells, were the dominant immune population in all tumours (~71% on average), as per Fig. 5.12. GranzymeB MFI was highest in aPDL1+US treated mice—an observation reinforcing *Nanostring* data which has suggested monocytes-derived *Gzmb* plays a critical role in mediating cytotoxicity.

While conventionally, GranzymeB expression is thought to be confined to lymphocytes, it can in fact be expressed by myeloid cells [Chowdhury & Liberman 2008]. In fact, a recently approved RO1 NIH grant is studying the potential anti-tumour function of myeloid cell-produced GranzymeB [Tridandapani et. al 2017]. Taken in the context of the Nanostring data, which revealed a dramatic increase in a myeloid cell score (a surrogate of infiltration), and the induction of gene-pathways related myeloid-mediated Gzb attack it seems more and more clear that some of the anti-tumour immunity generated by aPDL1+US therapy could be ascribed to the myeloid cells.

Figure 5.19: Granzyme B Expression

a



b

ANOVA of Tumor-Tissue GranzymeB B MFI for Each Cell Type

Dunnett's test	Total CD45	Myeloid Cell	CD4 T Cell	CD8 T Cell	NK Cell
IgG vs. IgG+US	ns	*	ns	ns	ns
IgG vs. aPDL1	ns	ns	ns	ns	ns
IgG vs. aPDL1+US	ns	*	ns	ns	**

Figure 5.19
a) GranzymeB MFI across tissue types & treatment arms for different immune cell populations (NK, myeloid cells, CD4 T cells, and CD8 T cells).
b) Ordinary one-way ANOVA with Dunnett's correction (single pooled variance) was utilized to compare GZB MFI between intervention groups of different cell subsets in tumour tissue. Analysis compared the significance (if any) between an intervention group (IgG+US, aPDL1, or aPDL1+US) and IgG.

5.20 Summary of FCM Data

Extra tissue, collected from day 5 mice of Section 5.1, was assessed here by FCM. The data presented here should be interpreted in the context of the very small quantities of tumour tissue which was available for FCM processing. FCM panels were designed to broadly quantify the distribution of basic innate and adaptive immune populations and query the functional characteristics of T cells based on an assumption that checkpoint inhibitors modulate T cell behaviour [Sakuishi et al. 2010, Duraiswamy et al. 2013, Wei et al. 2017]. There were a few interesting observations regarding tumour T cells of mice treated with aPDL1+US including: 1) an increase in the frequency of central memory cells across both the CD4 and CD8 subsets, 2) an increase in the frequency of activated but not exhausted (PD1+TIM3-) CD4 T cells, 3) an increase in CD8 activation as per increases in CD8 OX40 MFI, and 4) a decrease in Treg. ICOS MFI, suggesting that Tregs are less immunosuppressive.

However, beyond these significant changes, the majority of changes explored by FCM of tumour-tissue were not significant or, for that matter, consistent; for example, there was no significant change in the frequency of Tregs, CD8/Treg ratio, or production of GranzymeB by CD4 or CD8 T cells. Taken together, T cells changes may have contributed toward the anti-tumour effect of aPDL1+US therapy, however, when it is also considered that T cells made up less than 1% of aPDL1+US tumour leukocytes (frequency CD45+CD3+ cells out of total CD45+ leukocytes as per Fig. 5.12), two hypothesis may be drawn: 1) that 5d is ‘too late’ to capture T cell changes in aPDL1+US treated tumours as the T cells mediating the response have achieved their goals, and have either ‘left’ the tumour—a hypothesis supported by the fact that of the T cells found in aPDL1+US, there was significant enrichment of the central memory subset—T cells canonically retained within lymphatic tissue after a pathogen has been cleared in preparation for future infection [Gray et al. 2018]. Alternatively, 2) perhaps tumour-eradication activities were carried out by a more dominant population, such as myeloid cells.

Notably, myeloid cells made up the majority of tumour-leukocytes (Fig. 5.12). Although FCM data related to myeloid cells was sparse, as the panels were intended to characterize T cell changes, it was observed that myeloid GranzymeB production was significantly upregulated in cavitation treated tumours. This observation, in addition to the fact that myeloid cell frequencies were most upregulated in aPDL1+US treated tumours, suggests that myeloid cell GranzymeB could be an important mediator of the anti-tumour activity conferred by aPDL1+US therapy. In summary, the significant upregulation of myeloid cell frequency in aPDL1+US treated tumours, the upregulation of GranzymeB in said myeloid cells, and GranzymeB's role in mediating cell-death, are consistent with myeloid cells playing an important role in mediating aPDL1+US efficacy. This hypothesis is also consistent with the *Nanostring* data.

5.21 Chapter Summary

Pairing aPDL1 with cavitation has been shown to improve drug efficacy (Chapter 3) and delivery (Chapter 4). In this chapter, the mechanistic and immunological basis by which the tumour-control is mediated was further investigated through flow cytometry (FCM) and gene-level transcript analysis by *Nanostring*. The four factors hypothesized to contribute to the therapeutic effect were a) the administration of aPDL1, b) the presence of intratumoral cavitation, c) the improvement of aPDL1 delivery, and d) time.

5.21.1 Nanostring Analysis

Mice were sacrificed either 24-hrs or 5-days post-intervention and queried at the gene-level in an effort to capture the plasticity of response across 700+ cancer immunotherapy-related mRNA transcripts. 24hrs-after therapy, differentially expressed genes (DEGs) were observed in both IgG+US and aPDL1+US treated tumours (5.2). At this early time-point the number and fold changes (FC) of DEGs, were more pronounced in IgG+US treated tumours compared to aPDL1+US treated tumours, perhaps as consequence of cavitation dose, (average cavitation dose after IgG+US treatment was more than double than that of aPDL1+US treatment at this time point (6.43e-006 vs. 3.183e-006 AUC with standard deviations of 2.51e-006 and 4.48-007 AUC respectively, n=3/group) (5.2). This study did not intend to manipulate and evaluate the role cavitation plays in dictating the number and magnitude of differential gene expression, but this tentative observation nevertheless warrants future investigation.

At the 24hr-time point, top DEGs ($p<0.01$ and $FC>3$) were largely related to those of an acute, injury-like response, including the upregulation of genes encoding proteins that stimulate leukocyte infiltration (i.e. chemokines, cytokines, and their receptors) and amplify local inflammatory signalling (5.3). However, despite upregulation of genes that mediate leukocyte recruitment and general inflammation, most genes related directly to anti-tumour processes

were not significantly upregulated with exception to those encoding PDL1 and FAS suggestive that cavitation alone can assist in their upregulation (5.4). *Nanostring* cell scores, surrogate metrics for leukocyte infiltration, were also not significantly changed at the 24-hr time point, however trends in cell score suggested that macrophage and neutrophil recruitment would be modestly greater in cavitation-treated mice—consistent with a hypothesis that the 24hr-time point represents a snapshot of a growing inflammatory process driven by cavitation (5.5). Therefore, it seems that cavitation leads to drug-agnostic increases in the expression of genes related to leukocyte recruitment to bring about an acute, injury-like inflammatory program.

5d-post therapy more DEGs were detected in aPDL1+US treated tumours compared to IgG+US or aPDL1-treated mice (5.6). Cavitation was NS lower in IgG+US treated mice compared to aPDL1+US treated mice (on average 3.433e-006 and 4.147e-006 AUC with SDs of 1.732e-006 and 2.480e-006 AUC respectively). However, while it cannot be ruled out that the decrease in cavitation contributed to the decrease in DEGs of IgG+US treated mice, the level of cavitation between IgG+US and aPDL1+US were much more comparable at the 5d-time point.

5-days post-therapy, top DEGs ($p<0.01$ and $FC>3$) from the 24hr-time point were again DEGs of IgG+US and aPDL1+US treated tumours. In short, many of the top DEGs observed at 5d were largely related to sustaining the recruitment of immune cells and the growth of an inflammatory response (5.7). Although 5d top DEGs were generally significantly elevated in both cavitation groups, the FC in gene expression was far greater in aPDL1+US treated tumours as compared to IgG+US treatment.

However, in addition to those changes, at the 5d time-point DEGs were uniquely shared between aPDL1 and aPDL1+US treated tumours (10 genes). Notably this population of shared DEGs was not detected at the 24hr time-point. These genes were generally greater in FC in aPDL1+US treated mice as compared to aPDL1 treated mice; these genes were not only tied to leukocyte activation, but also effector functions. For example, CDC, CR4-related phagocytosis, ADCC, and antigen presentation (5.8). A range of genes which have previously been reported

to be involved in aPDL1 activity and also raise important questions about the value of Fc competency in the design of aPDL1 therapeutics. Crucially, other genes related to activation, immunologic resistance, and cytotoxic effector function were found to be significantly upregulated only in aPDL1+US treated tumours, taken together suggesting that: 1) PDL1 expression was induced—which would render the tumour more susceptible to antibody targeting, and 2) GranzymeB was being produced without perforin—consistent with monocyte production and utilization of this cytotoxic protease for ADCC (5.9). This raises the important question of whether the responses seen are an amplification of aPDL1 activity that would also be achieved by higher dosing or are unique to the combination of aPDL1+US due to improved distribution and/or a combination of MOAs. Cell type profiling at the 5d-time point, observed significant increases in the cell scores of macrophages, neutrophils, DCs, NK CD56Dim, and T cells—increases in leukocytes capable of carrying out effector pathways implicated elsewhere (5.10).

Taken together, the Nanostring data suggested that cavitation can drive an inflammatory program that wanes over time, but can be sustained when an IO-drug is present, and that while T cell mediated responses could be important to the benefit conferred by aPDL1+US therapy, changes in the innate compartment likely also make a meaningful contribution. This is exemplified by the upregulation of genes related to innate immune system effector mechanisms (PDL1-induction, CDC, CR4-related phagocytosis, and ADCC) and the likely nature of GranzymeB production and utilization by monocytes.

5.21.2 Flow Cytometry with Additional Tumour Tissue

Extra tissue from 5d-mice sacrificed as per (5.1), was also analysed by FCM for phenotypic and functional changes, largely focused upon the T cell compartment, but also incorporating stains to delineate changes in the frequency of innate and adaptive populations

more broadly (5.11). Perhaps the most striking observation from basic, leukocyte subset characterization, was that leukocytes from aPDL1+US treated tumours were largely comprised of myeloid cells, whereas NK (<1% of total leukocytes) and T cells (<1% of leukocytes) made up only a small fraction of the leukocytes present (5.12).

T cells from aPDL1+US treated tumours were significantly unique in some aspects of function, i.e. increased central memory expansion (5.14-5.15), however in others (i.e. activation, dysfunction, or effector function) the significance (or insignificance) of changes varied as function of cell subtype and marker queried—all together painting a more convoluted picture as to the implication of T cell changes (5.16-5.18). This lack of clarity, in addition to the fact that T cells comprised less than 1% of aPDL1+US tumour leukocytes might suggest either that by 5 days T cells have 'left' the TME after completing their duties (which would be supported by the fact that aPDL1+US tumour T cells were significantly enriched for the central memory phenotype) or that innate populations played an even larger role in mediating anti-tumour responses.

Although the panels were not intended to characterize myeloid cells, it was observed that aPDL1+US treated, tumour-myeloid cells significantly upregulated GranzymeB expression (5.19). Taking into account the significant upregulation of myeloid cell frequency in aPDL1+US treated tumours, the detected increase myeloid-cell GranzymeB, and GranzymeB's role in mediating cell-death, there is a growing hypothesis that myeloid cells play a key role in mediating aPDL1+US efficacy.

In summary, both innate and adaptive responses play an important role in the tumour control provided by aPDL1+US therapy. The data suggests that inertial cavitation events immunologically prime the tumours for leukocyte recruitment and activation which, when combined with the increased presence of aPDL1 within the TME, results in amplification of aPDL1-driven adaptive and innate anti-tumour effector processes. In these models at the doses

of antibody and cavitation applied this results in robust tumour control benefits not observed when aPDL1 or cavitation are administered independently of each other.

5.21.3 Future Directions

Beyond the recommendations of Chapters 3 and 4, work in this chapter points toward several areas of future investigation, which can be organized into two general categories—

1) improving the characterization of mechanistic changes that may be present, and

2) directly evaluating mechanisms proposed in this chapter.

To improve the characterization of mechanistic changes, future work should consider (a) utilizing single-cell RNA sequencing—which would enable capture of not only cancer-immunotherapy related transcripts, but also changes across the transcriptome at the resolution of single-cells [Pan et al. 2019, Song et al. 2019]. This would better define the mechanistic changes undergone by immune cells, stromal elements, and tumour cells of the CT26 tumours with respect to therapy. Further, (b) improving and modifying FCM panels encompass a broader range of phenotypic and functional markers, especially those related to the characterization of innate populations. The utilization of higher-plexed cytometry would be useful to achieve such a goal. Lastly, future studies should consider (c) characterizing changes using cytometry time-of-flight (CyTof). CyTof, unlike FCM, relies on mass/charge ratios rather than fluorescence in order to differentiate between proteins of a single-cell [Leipold et al. 2015]. In doing so, CyTof can enable the simultaneous detection of 40+ proteins in a given cell. Although CyTof tends to be more expensive and slower at processing samples than FCM [Gadalla et al. 2019], characterization by CyTof may provide a higher resolution of detail related to cell-processes at the protein-level compared to use of FCM.

To directly evaluate mechanisms proposed in this chapter, future work could consider evaluating the contribution of a particular leukocyte subsets to the therapeutic efficacy. The

questions of how important the immune system is to the response observed, and which components of the immune system (myeloid cells? lymphocytes?) are most important, are important to address. These questions could be addressed through the use of immunocompromised mice via genetic manipulation [e.g. Shultz et al. 2005, Walzer et al. 2007] the application of cell-depleting antibodies [Kruisbeek 1992], or administration of agents that selectively regulate leukocyte subsets (such clodronate to deplete macrophages) [Weisser et al. 2012]. At a more granular level, inhibitors of specific pathways suspected of mediating the response could be queried through knockout, knockdown, or overexpression of particular genes of interest (i.e. IFNg KO transgenic mice [Nakajima et al. 2001]). Alternatively administration of pathway specific inhibitors, such as anti-Fc receptor antibodies to block Fc action, or use of Fc incompetent versions of the aPDL1 used would provide revealing data with important clinical ramifications [Arlauckas et al. 2017].

Lastly, the relationship between cavitation dose, particularly intratumoral cavitation, and biological and immunological changes should be queried. Of particular interest would be to determine whether intentionally varied cavitation dose makes an impact upon gene or protein-level changes in a dose-dependent fashion, as suggested by the 24hr-gene-level data of this chapter.

6 Conclusion

Despite clinical promise aPDL1 is effective only a fraction of patients treated [Mariathasan et al. 2018]. Poor intratumoural delivery could be a factor limiting aPDL1's efficacy, as a consequence of factors including tumour vascular heterogeneity, elevated interstitial pressures, and stromal barriers. In fact, studies by Deng et al. have demonstrated that the distribution of a radiolabelled aPDL1 within tumours is "primarily associated with tumor vasculature with little or no diffusion into the tumor parenchyma" [Deng et al. 2016].

In the studies reported here, the impact of pairing aPDL1 administration with ultrasound-mediated cavitation of submicron, sonosensitive particles was evaluated on the basis that drug delivery is a factor limiting the efficacy of aPDL1 and that US-mediated cavitation could improve the delivery of antibody-based drugs like aPDL1. Evidence that cavitation can enhance anti-cancer agent delivery into tumours had been previously reported [Carlisle et al. 2013, Bazan-Peregrino et al 2013, Kwan et al 2015, and Myers et al. 2016], but the studies reported here represent the first detailed analysis of the impact of cavitation on the delivery and efficacy of an antibody. The aims of this thesis are to:

1. Pair aPDL1 with submicron, tumour-penetrating cavitation nucleation agents (SSPs) and focused ultrasound to improve the efficacy of aPDL1
2. Enhance the intratumoural delivery of immunotherapy with SSP-nucleated cavitation
3. Characterize the biological and immunological changes induced by intratumoural cavitation in the absence or in the presence of a checkpoint inhibitor

6.1 Efficacy Studies Chapter Summary

Chapter 3 directly queried whether pairing aPDL1 with cavitation could improve its anti-tumour efficacy. The first study of this thesis (3.1), observed that survival of CT26-tumor bearing mice could be extended by treating mice with a sub-clinical-equivalent dose (100μg per dose) of aPDL1 and cavitation, but not through the administration of drug alone nor drug with ultrasound and cavitation-incompetent nuclei. Subsequent evaluation (3.2), found that pairing aPDL1 with cavitation could realize a similar benefit in drug efficacy, even when aPDL1 drug-dose was doubled—more aligned with what is clinically administered. This study also showed that benefits provided by cavitation alone were modest, and that, pairing aPD1 with cavitation did not yield a similar improvement in survival. Studies in 3.3 confirmed the essentiality of cavitation, wherein a lack of sufficient cavitation likely resulted in survival outcomes not consistent with previous work. This work motivated a change in acoustic strategy—one that took advantage of real-time cavitation feedback to inform real-time pressure adjustment—improving the consistency of intratumoral cavitation in 3.4.

The results of 3.4 were very consistent with 3.1 and 3.2; finding that aPDL1 paired with cavitation could significantly improve survival. In fact, perhaps as a consequence of improved cavitation, more than 40% of mice treated by aPDL1 and cavitation (aPDL1+US) were tumour free at the end of the study. No significant survival benefit was observed by pairing aPD1 with cavitation. Furthermore, pilot work (3.5) in a different tumour model (EMT6), known for its rich stroma [Mariathasan et al. 2018] suggested, albeit insignificantly, that aPDL1+US therapy would decrease tumour burden more than aPDL1 alone. In summary, the data of Chapter 3 suggests that: 1) aPDL1 paired with cavitation can improve drug efficacy and that 2) sufficient cavitation is critical in mediating the benefit conferred by pairing aPDL1 with cavitation.

6.2 Drug Delivery Studies Chapter Summary

Chapter 4 explored whether cavitation of submicron cavitation nuclei (SSPs) could indeed improve antibody delivery through (a) the near-infrared (NIR)-imaging of drug in excised, whole-tumours, (b) flow cytometry to detect cell-bound drug, and (c) quantitative microscopy. Imaging of whole-tumours excised from mice dosed with aPDL1 conjugated to a NIR-fluorochrome via NHS-linker chemistry (4.1), indicated that the ultrasound exposed tumours, had significantly greater fluorescence—a surrogate for drug concentration within the tumours—than those not exposed to ultrasound (US) (4.2). In fact, across four different NIR-conjugate antibodies (aPD1, aPDL1, aICOS, or isotype control antibody—IgG2b), cavitation was able to significantly improve drug-accumulation with 2-3-fold increases in drug-accumulation in cavitation treated tumours as compared to the contralateral control tumours not exposed to US (4.3). Similar benefits were also observed in bilateral EMT6 tumour bearing mice (4.4).

Flow cytometry (FCM) was also utilized to probe the degree to which drug delivery could be improved. This was achieved by utilizing a secondary antibody capable of detecting cell-bound therapeutic antibody (4.5). Cavitation increased both the frequency and intensity of live-leukocyte aPDL1-binding in cells from tumours collected roughly one day after intervention as compared to drug-only control tumours (4.6). Similar improvements in aPDL1 binding intensity and frequency were found in the US-treated tumours of bilateral tumour bearing mice collected ~1.5 hours after intervention. In contrast improvements in aPD1 or IgG2b binding were not as pronounced (4.7). Quantitative microscopy utilizing a secondary antibody for the detection of tissue-bound aPDL1, further validated the IVIS and FCM results, observing that the quantity and distribution of aPDL1 was improved in cavitation-treated tumours of bilateral tumour bearing mice administered with aPDL1 (4.8).

6.3 Immunologic Correlates of Response Chapter Summary

Chapter 5 explored the immunological mechanism(s) underpinning the efficacy benefits observed by pairing aPDL1 with cavitation which improved aPDL1 delivery. Gene-level changes were queried by *Nanostring*, enabling characterization of 700+ genes related to cancer immunotherapy at two-time points (24hr and 5d) after intervention.

Approximately 24hrs after intervention, cavitation (irrespective of drug administered) was likely the dominant driver of differential gene expression as compared to IgG control (DEGs), with nearly all of the most significantly and differentially expressed genes (top DEGs) related to the activation and/or recruitment of leukocytes to the TME. In fact, at the 24hr-time point, IgG+US treated mice had a greater number of DEGs than aPDL1+US treated mice; possibly a consequence of on average greater (though insignificant) cavitation levels in IgG+US over aPDL1+US treated mice on average at this time point. 5d post-intervention, cavitation treatment was still a major driver of top DEGs. However, there were a substantially greater number of DEGs in aPDL1+US treated mice. Although the IgG+US treated mice at this time point received an insignificantly lower cavitation dose than aPDL1+US treated mice, the average cavitation doses between groups were comparable, suggesting that the increase in DEGs of aPDL1+US treated tumours was a consequence of aPDL1 being administered.

A subset of DEGs upregulated in aPDL1+US treated tumours could be traced to innate and adaptive effector mechanisms including complement-dependent cytotoxicity (CDC), CR4-related phagocytosis of antibody opsonized cells, antibody-dependent cell-mediated cytotoxicity (ADCC), and T cell mediated cytotoxicity. Many of these same effector pathways were significantly upregulated in aPDL1 (no cavitation) treated mice as well, though not to the same degree of amplification. Likewise, only in aPDL1+US therapy were cell scores, a surrogate for leukocyte infiltration, of immune populations capable of carrying out such effector mechanisms, significantly upregulated. Exploratory FCM of tumour tissue from these mice, revealed that T

cells from aPDL1+US treated tumours did have greater frequencies of central memory T cells, however, the T cells accounted for <1% of the leukocytes in aPDL1+US tumours. This suggests that either T cells were important to therapy, but were 'leaving' after clearing tumour, and/or T cells are not the only population important in mediating tumour control observed after aPDL1+US therapy. Notably, FCM revealed that aPDL1+US therapy most greatly skewed the distribution of leukocytes toward myeloid cells (already the predominate leukocyte population of control tumours). Likewise, the myeloid cells of aPDL1+US treated tumours most greatly upregulated GranzymeB (a serine protease). This suggests that myeloid-mediated effector programs (like ADCC or CR4-related phagocytosis) were important to aPDL1+US efficacy. In short, biological characterization suggests that aPDL1+US therapy engages both the innate and adaptive immune system, which leverage the improved aPDL1 delivery and modest, cavitation-induced inflammation to yield amplification of effector mechanisms that facilitate tumour and TME elimination.

Beyond the US strategy utilized here, it is important to highlight that other types of US (alone or in combination with other therapies) hold promise in driving tumour antigen and immunogenic stimuli release, supporting APC maturation, and inducing adaptive immunity [Sheybani et al. 2019]. These other types of US include, for example, the use of US to generate acoustic stress [Skalina et al. 2019], thermally ablate [Silvestrini et al 2017, Han et al 2019], mechanically fractionate [Eranki et al. 2019], and modulate and/or compromise the vasculature of tumours [Czarnota et al. 2012, Bulner et al. 2019]. Broadly speaking, the work here adds to a growing body of evidence that therapeutic US can support innate and adaptive anti-tumour immunity.

6.4 Limitations

Key limitations to the work were outlined in each respective chapter. Some of the most important limitations to the work are summarized here. They include:

1) a lack of diversity in the tumour model, restricting the generalizability of the findings (although initial work in EMT6 does seem to support the findings in CT26)

2) the ability to accurately measure and quantify cavitation dose owing to the potential for extra-tumoral (skin/fur) cavitation to be detected as intratumoral cavitation. The contribution of extra-tumoral cavitation is especially problematic in studies where pressure was adjusted in real-time in accordance to PAM-feedback, potentially opening up the possibility that therapy was incorrectly modulated.

3) the lack of a positive selection marker for tumour cells in FCM drug delivery studies, resulting in a necessity to limit the scope of analysis to leukocytes, a surrogate of total drug binding/delivery.

4) the narrow scope of genes assessed by *Nanostring*. Unlike other modalities to assess gene expression (i.e. single cell RNA sequencing), the analysis here is restricted to analysis of bulk populations and is further limited to a defined selection genes. Hence, there is a possibility that other pathways or significant genes may have been overlooked.

6.5 Future Work

Future directions can be found at the end of each chapter. The majority of these recommendations relate to improving experimental design, not only to address the aforementioned limitations, but also to improve quality or scope of how a given efficacy, delivery, or mechanistic study is conducted. Additional future work would be aimed at extending current findings to support the translation of this technology to the clinic, and could include the following:

1) Expanding the generalizability of findings by testing in higher order species with tumours that better recapitulate human carcinogenesis (e.g. VX2 rabbits, WHV woodchucks).

2) Evaluating the relationship between cavitation dose and drug delivery, biologic tissue re-programming, and survival.

3) Querying the safety and tolerability of cavitation *in vivo* with special attention to the metabolism of the cavitation nuclei.

4) Developing more user-friendly software-hardware interfaces to facilitate R&D activities, including the capability to automatically sustain and control cavitation activity to pre-defined levels within the tumour.

5) Exploring the utility of pairing US-mediated cavitation with chemotherapeutics, other immunomodulatory agents (including adjuvants and next generation checkpoint inhibitors), and/or tumour-targeted therapies like irreversible electroporation, radiofrequency ablation, cryoablation, and radiotherapy.

6.6 Synthesis and Proposed Mechanism

Taken together, this work suggests that aPDL1+US therapy confers a survival benefit over aPDL1 alone because (i) aPDL1 delivery is restricted in the tumour microenvironment, (ii) US-mediated cavitation can improve the delivery and distribution of aPDL1, and that (iii) cavitation induces modest acute inflammation that primes the tumour microenvironment for sustained, drug-related effector responses. Based on the work presented here, the following working hypothesis could be suggested:

1. Cavitation improves intratumoral antibody accumulation. Such improvement is especially beneficial for a drug like aPDL1, whose increased delivery improves its ability to bind an intratumoral target (PDL1). *This is exemplified by the improved distribution of tissue-bound aPDL1 as observed by quantitative microscopy*.
2. Cavitation also drives a modest, acute inflammatory program marked by the upregulation of cytokines and chemokines which attract leukocytes. Leukocyte infiltration and activation within the TME start to increase, but in response so does immunosuppressive activity, such as PDL1 expression. *Snapshots of such changes were captured by Nanostring*
3. Leukocytes within the TME recognize antibody-opsonized cells. Leukocytes within aPDL1+US treated tumours carry out potent cell-mediated (ADCC, CR4-related phagocytosis, and T-cell mediated attack) and cell-independent (CDC) effector processes that bring about the death of PDL1-expressing cells. *Such aPDL1-related effector processes are less robust in aPDL1 (no cavitation) treated mice, given the absence of the modest cavitation-induced leukocyte infiltration and insufficient drug delivery within the TME. This is consistent with the relative amplification of most aPDL1 DEGs in fold-change by aPDL1+US therapy at 5d.*

4. The innate and adaptive effector processes within aPDL1+US treated tumours continue to build, acting akin to a positive-feedback loop. *FCM data suggests that myeloid cells are the key players, given their increasing predominance out of the leukocyte population and notable GranzymeB production in aPDL1+US treated tumours*.
5. Further immunologic activation induces IFNg and other inflammatory processes in aPDL1+US treated tumours, driving even greater neoantigen and PDL1 expression by target cells. This renders the cells even more sensitive to T cell and aPDL1-mediated innate effector attack.
6. The cell death generated by aPDL1+US therapy drives further inflammation that results in the recruitment and activation of even greater numbers of leukocytes. *In the absence of aPDL1, the modest inflammation of cavitation-alone (IgG+US) fades. This is evidenced by the relative paucity of gene-level changes observed in IgG+US treated mice at 5d, and the absence of a robust survival benefit conferred by cavitation alone.*
7. Cavitation-mediated drug delivery improves aPDL1 efficacy owing to improvements in drug-delivery and modest cavitation-induced inflammation. Tumour growth impedance or tumour regression is grossly observed as long as the anti-tumour response outpaces tumour-mediated resistance programs.

References:

Abele, R. & Tampé, R. The ABCs of immunology: Structure and function of TAP, the transporter associated with antigen processing. Physiology 19, 216–224 (2004).

Adkins, C. E. et al. Characterization of passive permeability at the blood–tumor barrier in five preclinical models of brain metastases of breast cancer. Clin. Exp. Metastasis 33, 373–383 (2016).

Alexandrakis, G. et al. Two-photon fluorescence correlation microscopy reveals the two-phase nature of transport in tumors. Nat. Med. 10, 203–207 (2004).

Amarnath, S. et al. Regulatory T cells and human myeloid dendritic cells promote tolerance via programmed death ligand-1. PLoS Biol. 8, (2010).

Anderson, A. C., Joller, N. & Kuchroo, V. K. Lag-3, Tim-3, and TIGIT: Co-inhibitory Receptors with Specialized Functions in Immune Regulation. Immunity 44, 989–1004 (2016).

Apolo, A. B. et al. Avelumab, an anti-programmed death-ligand 1 antibody, in patients with refractory metastatic urothelial carcinoma: Results from a multicenter, Phase Ib study. J. Clin. Oncol. 35, 2117–2124 (2017).

Arlauckas, S. P. et al. In vivo imaging reveals a tumor-associated macrophage-mediated resistance pathway in anti-PD-1 therapy. Sci. Transl. Med. 9, (2017).

AstraZeneca (IMFINZI). Durvalumab label. FDA 1–27 (2018).

Atchley, A. A. & Prosperetti, A. The crevice model of bubble nucleation. J. Acoust. Soc. Am. 86, 1065–1084 (1989).

Azuma, K. et al. Association of PD-L1 overexpression with activating EGFR mutations in surgically resected nonsmall-cell lung cancer. Ann. Oncol. 25, 1935–1940 (2014).

Azuma, T. et al. B7-H1 is a ubiquitous antiapoptotic receptor on cancer cells. Blood 111, 3635–3643 (2008).

Baaten, B. J. G. et al. CD44 Regulates Survival and Memory Development in Th1 Cells. Immunity 32, 104–115 (2010).

Baba, T. & Mukaida, N. Role of macrophage inflammatory protein (MIP)-1α/CCL3 in leukemogenesis. Mol. Cell. Oncol. 1, 1–5 (2014).

Baeriswyl, V. & Christofori, G. Seminars in Cancer Biology The angiogenic switch in carcinogenesis. 19, 329–337 (2009).

Bansal-Pakala, P., Halteman, B. S., Cheng, M. H.-Y. & Croft, M. Costimulation of CD8 T Cell Responses by OX40. J. Immunol. 172, 4821–4825 (2004).

Baras, A. S. et al. The ratio of CD8 to Treg tumor-infiltrating lymphocytes is associated with response to cisplatin-based neoadjuvant chemotherapy in patients with muscle invasive urothelial carcinoma of the bladder. Oncoimmunology 5, 1–7 (2016).

Bazan-Peregrino, M. et al. Cavitation-enhanced delivery of a replicating oncolytic adenovirus to tumors using focused ultrasound. J Control Release 169, 40–47 (2013).

Benci, J. L. et al. Tumor Interferon Signaling Regulates a Multigenic Resistance Program to Immune Checkpoint Blockade. Cell 167, 1540-1554.e12 (2016).

Bhatnagar, N. et al. FcγRIII (CD16)-mediated ADCC by NK cells is regulated by monocytes and FcγRII (CD32). Eur. J. Immunol. 44, 3368–3379 (2014).

Blank, C. et al. PD-L1/B7H-1 Inhibits the Effector Phase of Tumor Rejection by T Cell Receptor (TCR) Transgenic CD8+ T Cells. Cancer Res. 64, 1140–1145 (2004).

Bourgeois-Daigneault, M. C. et al. Neoadjuvant oncolytic virotherapy before surgery sensitizes triple-negative breast cancer to immune checkpoint therapy. Sci. Transl. Med. 10, (2018).

Bousso, P. T-cell activation by dendritic cells in the lymph node: Lessons from the movies. Nat. Rev. Immunol. 8, 675–684 (2008).

Boyerinas, B. et al. Antibody-Dependent Cellular Cytotoxicity Activity of a Novel Anti-PD-L1 Antibody Avelumab (MSB0010718C) on Human Tumor Cells. Cancer Immunol. Res. 3, 1148–1157 (2015).

Braster, R., O'Toole, T. & Van Egmond, M. Myeloid cells as effector cells for monoclonal antibody therapy of cancer. Methods 65, 28–37 (2014).

Brown, D. M., Kamperschroer, C., Dilzer, A. M., Roberts, D. M. & Swain, S. L. IL-2 and antigen dose differentially regulate perforin- and FasL-mediated cytolytic activity in antigen specific CD4+ T cells. Cell. Immunol. 257, 69–79 (2009).

Brown, J. M. & Giaccia, A. J. The unique physiology of solid tumors: Opportunities (and problems) for cancer therapy. Cancer Res. 58, 1408–1416 (1998).

Brunet, J. F. et al. A new member of the immunoglobulin superfamily-CTLA-4. Nature 328, 267–270 (1988).

Bulner, S., Prodeus, A., Gariepy, J., Hynynen, K. & Goertz, D. E. Enhancing Checkpoint Inhibitor Therapy with Ultrasound Stimulated Microbubbles. Ultrasound Med. Biol. 45, 500–512 (2019).

Butte, M. J., Keir, M. E., Phamduy, T. B., Sharpe, A. H. & Freeman, G. J. Programmed death-1 ligand 1 interacts specifically with the B7-1 costimulatory molecule to inhibit T cell responses. Immunity 27, 111–22 (2007).

Cancer Research Institute. PD-1/PD-L1 Landscape Analysis. Cancer Research Institute vol. 11 1–20 https://www.cancerresearch.org/scientists/immuno-oncology-landscape/pd-1-pd-l1-landscape (2019).

Carlisle, R. et al. Enhanced tumor uptake and penetration of virotherapy using polymer stealthing and focused ultrasound. J Natl Cancer Inst 105, 1701–1710 (2013).

Carlisle, R. & Coussios, C. C. Mechanical approaches to oncological drug delivery. Ther. Deliv. 4, 1213–1215 (2013).

Carloni, V., Mazzocca, A., Mello, T., Galli, A. & Capaccioli, S. Cell fusion promotes chemoresistance in metastatic colon carcinoma. Oncogene 32, 2649–2660 (2013).

Carretero-González, A. et al. Analysis of response rate with ANTI-PD1/PDL-1 monoclonal antibodies in advanced solid tumors: A meta-analysis of randomized clinical trials. Oncotarget 9, 8706–8715 (2018).

Chang, Y. S. et al. Mosaic blood vessels in tumors: Frequency of cancer cells in contact with flowing blood. Proc. Natl. Acad. Sci. U. S. A. 97, 14608–14613 (2000).

Chattopadhyay, P. K. & Roederer, M. Cytometry: Today's technology and tomorrow's horizons. Methods 57, 251–258 (2012).

Chauhan, V. P., Stylianopoulos, T., Boucher, Y. & Jain, R. K. Delivery of Molecular and Nanoscale Medicine to Tumors: Transport Barriers and Strategies. Annu. Rev. Chem. Biomol. Eng. 2, 281–298 (2011).

Chemnitz, J. M., Parry, R. V., Nichols, K. E., June, C. H. & Riley, J. L. SHP-1 and SHP-2 Associate with Immunoreceptor Tyrosine-Based Switch Motif of Programmed Death 1 upon Primary Human T Cell Stimulation, but Only Receptor Ligation Prevents T Cell Activation. J. Immunol. 173, 945–954 (2004).

Chen, D. S. & Mellman, I. Elements of cancer immunity and the cancer-immune set point. Nature 541, 321–330 (2017).

Chen, D. S. & Mellman, I. Oncology meets immunology: The cancer-immunity cycle. Immunity 39, 1–10 (2013).

Chen, H. & Hwang, J. H. Ultrasound-targeted microbubble destruction for chemotherapeutic drug delivery to solid tumors. J. Ther. Ultrasound 1, 1 (2013).

Chen, Q. et al. ICOS signal facilitates Foxp3 transcription to favor suppressive function of regulatory T cells. Int. J. Med. Sci. 15, 666–673 (2018).

Chen, X., Song, X., Li, K. & Zhang, T. FCλ-binding is an important functional attribute for immune checkpoint antibodies in cancer immunotheraphy. Front. Immunol. 10, 1–13 (2019).

Chevalier, M. F. et al. Conventional and PD-L1-expressing Regulatory T Cells are Enriched During BCG Therapy and may Limit its Efficacy. Eur. Urol. 74, 540–544 (2018).

Chowdhury, D. & Lieberman, J. Death by a Thousand Cuts: Granzyme Pathways of Programmed Cell Death. Annu. Rev. Immunol. 26, 389–420 (2008).

Chowdhury, S. M., Lee, T. & Willmann, J. K. Ultrasound-guided drug delivery in cancer. Ultrasonography 36, 171–184 (2017).

Christmas, B. J. et al. Entinostat converts immune-resistant breast and pancreatic cancers into checkpoint-responsive tumors by reprogramming tumor-infiltrating MDSCs. Cancer Immunol. Res. 6, 1561–1577 (2018).

Cibrián, D. & Sánchez-Madrid, F. CD69: from activation marker to metabolic gatekeeper. Eur. J. Immunol. 47, 946–953 (2017).

Cilliers, C., Nessler, I., Christodolu, N. & Thurber, G. M. Tracking Antibody Distribution with Near-Infrared Fluorescent Dyes: Impact of Dye Structure and Degree of Labeling on Plasma Clearance. Mol. Pharm. 14, 1623–1633 (2017).

Collins, J. M. & Gulley, J. L. Product review: avelumab, an anti-PD-L1 antibody. Hum. Vaccines Immunother. 15, 891–908 (2019).

Cornejo, M. G. et al. Constitutive JAK3 activation induces lymphoproliferative syndromes in murine bone marrow transplantation models. Blood 113, 2746–2754 (2009).

Couzin-Frankel, J. Cancer immunotherapy. Science (80-.). 342, 1432–1433 (2013).

Coviello, C. et al. Passive acoustic mapping utilizing optimal beamforming in ultrasound therapy monitoring. J. Acoust. Soc. Am. 137, 2573–2585 (2015).

Croft, M. Costimulation of T cells by OX40, 4-1BB, and CD27. Cytokine Growth Factor Rev. 14, 265–273 (2003).

Croft, M., So, T., Duan, W. & Soroosh, P. The Significance of OX40 and OX40L to T cell Biology and Immune Disease OX40 and OX40L are Induced on Lymphoid and Non-lymphoid Cells. Immunol Rev 229, 173–191 (2009).

CrownBio. Why to Use Isotype Control Antibodies. https://blog.crownbio.com/why-isotype-control-antibodies (2018).

Cvetanovich, G. L. & Hafler, D. A. Human regulatory T cells in autoimmune diseases. Curr. Opin. Immunol. 22, 753–760 (2010).

Czarnota, G. J. et al. Tumor radiation response enhancement by acoustical stimulation of the vasculature. Proc. Natl. Acad. Sci. U. S. A. 109, (2012).

Dahan, R. et al. FcγRs Modulate the Anti-tumor Activity of Antibodies Targeting the PD-1/PD-L1 Axis. Cancer Cell 28, 285–295 (2015).

Degrandi, D. et al. Murine Guanylate Binding Protein 2 (mGBP2) controls Toxoplasma gondii replication. Proc. Natl. Acad. Sci. U. S. A. 110, 294–299 (2013).

Del Prete, A., Bonecchi, R., Vecchi, A., Mantovani, A. & Sozzani, S. CCRL2, a fringe member of the atypical chemoattractant receptor family. Eur. J. Immunol. 43, 1418–1422 (2013).

Deng, L. et al. Irradiation and anti – PD-L1 treatment synergistically promote antitumor immunity in mice Find the latest version : Irradiation and anti – PD-L1 treatment synergistically promote antitumor immunity in mice. J. Clin. Invest. 124, 687–695 (2014).

Deng, R. et al. Preclinical pharmacokinetics, pharmacodynamics, tissue distribution, and tumor penetration of anti-PD-L1 monoclonal antibody, an immune checkpoint inhibitor. MAbs 8, 593–603 (2016).

Dewhirst, M. W. & Secomb, T. W. Transport of drugs from blood vessels to tumour tissue. Nat. Rev. Cancer 17, 738–750 (2017).

Dieterich, L. C. et al. Tumor-associated lymphatic vessels upregulate PDL1 to inhibit T-cell activation. Front. Immunol. 8, 1–13 (2017).

Dong, C. et al. ICOS co-stimulatory receptor is essential for T-cell activation and function. Nature 409, 97–101 (2001).

Dong, H. et al. Tumor-associated B7-H1 promotes T-cell apoptosis: A potential mechanism of immune evasion. Nat. Med. 8, 793–800 (2002).

Dragovich, M. A. et al. SLAMF6 clustering is required to augment T cell activation. PLoS One 14, 1–17 (2019).

Duan, J. et al. Use of Immunotherapy With Programmed Cell Death 1 vs Programmed Cell Death Ligand 1 Inhibitors in Patients With Cancer: A Systematic Review and Meta-analysis. JAMA Oncol. (2019) doi:10.1001/jamaoncol.2019.5367.

Duraiswamy, J., Kaluza, K. M., Freeman, G. J. & Coukos, G. Dual blockade of PD-1 and CTLA-4 combined with tumor vaccine effectively restores T-cell rejection function in tumors. Cancer Res. 73, 3591–3603 (2013).

Elavazhagan, S. et al. Granzyme B Expression Is Enhanced in Human Monocytes by TLR8 Agonists and Contributes to Antibody-Dependent Cellular Cytotoxicity. J. Immunol. 194, 2786–2795 (2015).

Elpek, K. G. et al. The tumor microenvironment shapes lineage, transcriptional, and functional diversity of infiltrating myeloid cells. Cancer Immunol. Res. 2, 655–667 (2014).

EMD Serono (BAVENCIO). Avelumab label. FDA 1–34 (2019).

Eranki, A. et al. High Intensity Focused Ultrasound (HIFU) Triggers Immune Sensitization of Refractory Murine Neuroblastoma to Checkpoint Inhibitor Therapy. Clin. Cancer Res. clincanres.1604.2019 (2019) doi:10.1158/1078-0432.ccr-19-1604.

Facciabene, A., Motz, G. T. & Coukos, G. T-Regulatory Cells: Key Players in Tumor Immune Escape and Angiogenesis. Cancer Res. 72, 2162–2171 (2012).

FDA. List of Cleared or Approved Companion Diagnostic Devices (In Vitro and Imaging Tools). 1–7 http://www.fda.gov/MedicalDevices/ProductsandMedicalProcedures/InVitroDiagnostics/ucm301431.htm (2019).

FDA. Center for Drug Evaluation and Research Approval Package for: Application Number: 125514Orig1s000. 1–12 https://www.accessdata.fda.gov/drugsatfda_docs/nda/2014/125514Orig1s000Approv.pdf (2014).

FDA. FDA grants accelerated approval to pembrolizumab for advanced gastric cancer. fda.gov https://www.fda.gov/drugs/resources-information-approved-drugs/fda-grants-accelerated-approval-pembrolizumab-first-tissuesite-agnostic-indication (2017) doi:10.31525/fda1-ucm577093.htm.

Foucher, E. D. et al. IL-34 Induces the Differentiation of Human Monocytes into Immunosuppressive Macrophages. Antagonistic Effects of GM-CSF and IFNγ. PLoS One 8, (2013).

Freeman, G. J. et al. Engagement of the PD-1 immunoinhibitory receptor by a novel B7 family member leads to negative regulation of lymphocyte activation. J. Exp. Med. 192, 1027–1034 (2000).

Frétaud, M. et al. High-resolution 3D imaging of whole organ after clearing: Taking a new look at the zebrafish testis. Sci. Rep. 7, 1–11 (2017).

Fu, J. et al. Receptor occupancy measurement of anti-PD-1 antibody drugs in support of clinical trials. Bioanalysis 11, 1347–1358 (2019).

Fukumura, D. & Jain, R. K. Tumor microvasculature and microenvironment: Targets for anti-angiogenesis and normalization. Microvasc. Res. 74, 72–84 (2007).

Gadalla, R. et al. Validation of CyTOF against flow cytometry for immunological studies and monitoring of human cancer clinical trials. Front. Oncol. 9, 1–13 (2019).

Gajewski, T. F. et al. Cancer immunotherapy strategies based on overcoming barriers within the tumor microenvironment. Curr. Opin. Immunol. 25, 268–276 (2013).

Gascard, P. & Tlsty, T. D. Carcinoma-associated fibroblasts: Orchestrating the composition of malignancy. Genes Dev. 30, 1002–1019 (2016).

Gerberick, G. F., Cruse, L. W., Miller, C. M., Sikorski, E. E. & Ridder, G. M. Selective modulation of t cell memory markers CD62L and CD44 on murine draining lymph node cells following allergen and irritant treatment. Toxicol. Appl. Pharmacol. 146, 1–10 (1997).

Ghaffari, A. et al. Sting agonist therapy in combination with pd-1 immune checkpoint blockade enhances response to carboplatin chemotherapy in high-grade serous ovarian cancer. Br. J. Cancer 119, 440–449 (2018).

Girbl, T. et al. Distinct Compartmentalization of the Chemokines CXCL1 and CXCL2 and the Atypical Receptor ACKR1 Determine Discrete Stages of Neutrophil Diapedesis. Immunity 49, 1062-1076.e6 (2018).

Girotra, M. et al. The Current Understanding of the Endocrine Effects From Immune Checkpoint Inhibitors and Recommendations for Management. JNCI Cancer Spectr. 2, 1–9 (2018).

Goel, S. et al. Normalization of the Vasculature for Treatment of Cancer and Other Diseases. Physiol. Rev. 91, 1071–1121 (2011).

Golden-Mason, L. et al. Negative Immune Regulator Tim-3 Is Overexpressed on T Cells in Hepatitis C Virus Infection and Its Blockade Rescues Dysfunctional CD4+ and CD8+ T Cells. J. Virol. 83, 9122–9130 (2009).

Gormley, A. J. et al. Guided delivery of polymer therapeutics using plasmonic photothermal therapy. Nano Today 7, 158–167 (2012).

Graham, S. M. et al. Inertial cavitation to non-invasively trigger and monitor intratumoral release of drug from intravenously delivered liposomes. J Control Release 178, 101–107 (2014).

Gray, J. I., Westerhof, L. M. & MacLeod, M. K. L. The roles of resident, central and effector memory CD4 T-cells in protective immunity following infection or vaccination. Immunology 154, 574–581 (2018).

Gray, M. D., Stride, E. P. & Coussios, C.-C. Snap, Crackle, and Pop: Theracoustic Cavitation. Acoust. Today 15, 19–27 (2019).

Grilo, A. L. & Mantalaris, A. The Increasingly Human and Profitable Monoclonal Antibody Market. Trends Biotechnol. 37, 9–16 (2019).

Gross, C., Koelch, W., DeMaio, A., Arispe, N. & Multhoff, G. Cell Surface-bound Heat Shock Protein 70 (Hsp70) Mediates Perforin-independent Apoptosis by Specific Binding and Uptake of Granzyme B. J. Biol. Chem. 278, 41173–41181 (2003).

Grosso, J. F. & Jure-Kunkel, M. N. CTLA-4 blockade in tumor models: An overview of preclinical and translational research. Cancer Immun. 13, 1–14 (2013).

Gyöngy, M. & Coussios, C. C. Passive cavitation mapping for localization and tracking of bubble dynamics. J. Acoust. Soc. Am. 128, (2010).

Han, X. et al. In situ thermal ablation of tumors in combination with nano-adjuvant and immune checkpoint blockade to inhibit cancer metastasis and recurrence. Biomaterials 224, 119490 (2019).

Hanahan, D. & Weinberg, R. A. The hallmarks of cancer. Cell 100, 57–70 (2000).

Hanahan, D. & Folkman, J. Patterns and Emerging Mechanisms of the Angiogenic Switch during Tumorigenesis. 86, 353–364 (1996).

Hanahan, D. & Weinberg, R. A. Hallmarks of cancer: The next generation. Cell 144, 646–674 (2011).

Hanley, B. P., Xing, L. & Cheng, R. H. Variance in multiplex suspension array assays: Microsphere size variation impact. Theor. Biol. Med. Model. 4, 1–8 (2007).

Hashizume, H. et al. Openings between Defective Endothelial Cells Explain Tumor Vessel Leakiness. Am J Pathol 156, 1363–1380 (2000).

Haslam, A. & Prasad, V. Estimation of the Percentage of US Patients With Cancer Who Are Eligible for and Respond to Checkpoint Inhibitor Immunotherapy Drugs. JAMA Netw. open 2, e192535 (2019).

Haymaker, C. L. et al. Metastatic melanoma patient had a complete response with clonal expansion after whole brain radiation and PD-1 blockade. Cancer Immunol. Res. 5, 100–105 (2017).

He, Y. et al. OncoTargets and Therapy Dovepress TiM-3, a promising target for cancer immunotherapy. Onco. Targets. Ther. 11–7005 (2018) doi:10.2147/OTT.S170385.

Herbst, R. S. et al. Predictive correlates of response to the anti-PD-L1 antibody MPDL3280A in cancer patients. Nature 515, 563–567 (2014).

Hernández-Caselles, T. et al. A study of CD33 (SIGLEC-3) antigen expression and function on activated human T and NK cells: two isoforms of CD33 are generated by alternative splicing. J. Leukoc. Biol. 79, 46–58 (2006).

Hillen, F. & Griffioen, A. W. Tumour vascularization : sprouting angiogenesis and beyond. 489–502 (2007) doi:10.1007/s10555-007-9094-7.

Hodi, F. S. et al. Improved Survival with Ipilimumab in Patients with Metastatic Melanoma. N. Engl. J. Med. 363, 711–723 (2010).

Hu, G. et al. Nanoparticles targeting macrophages as potential clinical therapeutic agents against cancer and inflammation. Front. Immunol. 10, 1–14 (2019).

Hughes, C. S., Postovit, L. M. & Lajoie, G. A. Matrigel: a complex protein mixture required for optimal growth of cell culture. Proteomics 10, 1886–1890 (2010).

Hunt, J. W., Arditi, M. & Foster, F. S. Ultrasound transducers for medical imaging. IEEE Trans. Biomed. Eng. BME-30, 453 (1983).

Hutloff, A. et al. Hutloff Icos Structure 1999. 100, 263–266 (1999).

Iglesias, P. Cancer immunotherapy-induced endocrinopathies: Clinical behavior and therapeutic approach. Eur. J. Intern. Med. 47, 6–13 (2018).

Ignee, A., Atkinson, N. S. S., Schuessler, G. & Dietrich, C. F. Ultrasound contrast agents. Endosc. Ultrasound 5, 355–362 (2016).

Ishida, Y., Agata, Y., Shibahara, K. & Honjo, T. Induced expression of PD-1, a novel member of the immunoglobulin gene superfamily, upon programmed cell death. EMBO J. 11, 3887–3895 (1992).

Iwai, Y. et al. Involvement of PD-L1 on tumor cells in the escape from host immune system and tumor immunotherapy by PD-L1 blockade. Proc. Natl. Acad. Sci. 99, 12293–12297 (2002).

Jacquelot, N. et al. Sustained Type I interferon signaling as a mechanism of resistance to PD-1 blockade. Cell Res. 29, 846–861 (2019).

Jain, R. K. Normalizing tumor vasculature with anti-angiogenic therapy: A new paradigm for combination therapy. Nat. Med. 7, 987–989 (2001).

Janssens, R., Struyf, S. & Proost, P. The unique structural and functional features of CXCL12. Cell. Mol. Immunol. 15, 299–311 (2018).

Jiang, T., Zhou, C. & Ren, S. Role of IL-2 in cancer immunotherapy. Oncoimmunology 5, 1–10 (2016).

Jiang, X. et al. Role of the tumor microenvironment in PD-L1/PD-1-mediated tumor immune escape. Mol. Cancer 18, 1–17 (2019).

Johnston, J. A. et al. Phosphorylation and activation of the Jak-3 Janus kinase in response to interleukin-2. Nature 370, 151–153 (1994).

Jones, R. B. et al. Tim-3 expression defines a novel population of dysfunctional T cells with highly elevated frequencies in progressive HIV-1 infection. J. Exp. Med. 205, 2763–2779 (2008).

Juliá, E. P., Amante, A., Pampena, M. B., Mordoh, J. & Levy, E. M. Avelumab, an IgG1 anti-PD-L1 immune checkpoint inhibitor, triggers NK cell-mediated cytotoxicity and cytokine production against triple negative breast cancer cells. Front. Immunol. 9, 1–12 (2018).

Kägi, D. et al. Fas and perforin pathways as major mechanisms of T cell-mediated cytotoxicity. Science (80-.). 265, 528–530 (1994).

Kaufman, H. L. et al. Avelumab in patients with chemotherapy-refractory metastatic Merkel cell carcinoma: a multicentre, single-group, open-label, phase 2 trial. Lancet Oncol 17, 1374–1385 (2016).

Kaufman, H. L., Kohlhapp, F. J. & Zloza, A. Oncolytic viruses: A new class of immunotherapy drugs. Nat. Rev. Drug Discov. 14, 642–662 (2015).

Keir, M. E., Butte, M. J., Freeman, G. J. & Sharpe, A. H. PD-1 and Its Ligands in Tolerance and Immunity. Annu. Rev. Immunol. 26, 677–704 (2008).

Kelly, Z. R. & Davar, D. The Financial and Physical Toxicity of Immune Checkpoint Inhibitors in Cancer. ASCO Daily News https://dailynews.ascopubs.org/do/10.1200/ADN.19.190405/full/ (2019).

Kelz, R. R. et al. Time-of-Day Effects on Surgical Outcomes in the Private Sector: A Retrospective Cohort Study. J. Am. Coll. Surg. 209, 434-445.e2 (2009).

Khalil, D. N., Smith, E. L., Brentjens, R. J. & Wolchok, J. D. The future of cancer treatment: Immunomodulation, CARs and combination immunotherapy. Nat. Rev. Clin. Oncol. 13, 273–290 (2016).

Kitamura, K. et al. Local Administration of Monoclonal Antibody-Drug Conjugate: A New Strategy to Reduce the Local Recurrence of Colorectal Cancer. Cancer Res. 52, 6323–6328 (1992).

Kleinovink, J. W., van Hall, T., Ossendorp, F. & Fransen, M. F. PD-L1 immune suppression in cancer: Tumor cells or host cells? Oncoimmunology 6, 1–2 (2017).

Kojima, H., Toda, M. & Sitkovsky, M. V. Comparison of Fas- versus perforin-mediated pathways of cytotoxicity in TCR- and Thy-1-activated murine T cells. Int. Immunol. 12, 365–374 (2000).

Kruisbeek, A. M. In Vivo Depletion of CD4- and CD8-Specific T Cells. Curr. Protoc. Immunol. 1, 4.1.1-4.1.5 (1992).

Krummel, M. F., Sullivan, T. J. & Allison, J. P. Superantigen responses and co-stimulation: CD28 and CTLA-4 have opposing effects on T cell expansion in vitro and in vivo. Int. Immunol. 8, 519–523 (1996).

Kuai, R. et al. Elimination of established tumors with nanodisc-based combination chemoimmunotherapy. Sci. Adv. 4, 1–14 (2018).

Kusmartsev, S. & Gabrilovich, D. I. Role of immature myeloid cells in mechanisms of immune evasion in cancer. Cancer Immunol. Immunother. 55, 237–245 (2006).

Kwan, J. J. et al. Ultrasound-Propelled Nanocups for Drug Delivery. Small 11, 5305–5314 (2015).

Lan, Y. et al. Enhanced preclinical antitumor activity of M7824, a bifunctional fusion protein simultaneously targeting PD-L1 and TGF-. Sci. Transl. Med. 10, (2018).

Lancki, D. W., Hsieh, C. S. & Fitch, F. W. Mechanisms of lysis by cytotoxic T lymphocyte clones: Lytic activity and gene expression in cloned antigen-specific CD4+ and CD8+ T lymphocytes. J. Immunol. 146, 3242–3249 (1991).

Latchman, Y. E. et al. PD-L1-deficient mice show that PD-L1 on T cells, antigen-presenting cells, and host tissues negatively regulates T cells. Proc. Natl. Acad. Sci. U. S. A. 101, 10691–10696 (2004).

Lau, J. et al. Tumour and host cell PD-L1 is required to mediate suppression of anti-tumour immunity in mice. Nat. Commun. 8, (2017).

Leach, D. R., Krummel, M. F. & Allison, J. P. Enhancement of antitumor immunity by CTLA-4 blockade. Science (80-.). 271, 1734–1736 (1996).

Lechner, M. G. et al. Immunogenicity of Murine Solid Tumor Models as a Defining Feature of In Vivo Behavior and Response to Immunotherapy. J. Immunother. 36, 477–489 (2013).

Lee, H. T., Lee, S. H. & Heo, Y. S. Molecular interactions of antibody drugs targeting PD-1, PD-L1, and CTLA-4 in immuno-oncology. Molecules 24, 1–16 (2019).

Lee, J. W., Komar, C. A., Bengsch, F., Graham, K. & Beatty, G. L. Genetically engineered mouse models of pancreatic cancer: The KPC model (LSL-KrasG12D/+;LSL-Trp53R172H/+;Pdx-1-Cre), its variants, and their application in immuno-oncology drug discovery. Curr. Protoc. Pharmacol. 2016, 14.39.1-14.39.20 (2016).

Leipold, M. D., Newell, E. W. & Maecker, H. T. Multiparameter Phenotyping of Human PBMCs Using Mass Cytometry. in Methods in molecular biology (Clifton, N.J.) vol. 1343 81–95 (2015).

Lenschow, D. J., Walunas, T. L. & Bluestone, J. A. Cd28/B7 System of T Cell Costimulation. Annu. Rev. Immunol. 14, 233–258 (1996).

Less, J. R., Skalak, T. C., Sevick, E. M. & Jain, R. K. Microvascular architecture in a mammary carcinoma: branching patterns and vessel dimensions. Cancer Res. 51, 265–73 (1991).

Li, C. H. & Tam, P. K. S. An iterative algorithm for minimum cross entropy thresholding. Pattern Recognit. Lett. 19, 771–776 (1998).

Li, W., Germain, R. N. & Gerner, M. Y. Multiplex, quantitative cellular analysis in large tissue volumes with clearing-enhanced 3D microscopy (C e 3D). Proc. Natl. Acad. Sci. U. S. A. 114, E7321–E7330 (2017).

Lin, H. et al. Host expression of PD-L1 determines efficacy of PD-L1 pathway blockade-mediated tumor regression. J. Clin. Invest. 128, 1708 (2018).

Ling, B. et al. A novel immunotherapy targeting MMP-14 limits hypoxia, immune suppression and metastasis in triple-negative breast cancer models. Oncotarget 8, 58372–58385 (2017).

Lu, C., Redd, P. S., Lee, J. R., Savage, N. & Liu, K. The expression profiles and regulation of PD-L1 in tumor-induced myeloid-derived suppressor cells. Oncoimmunology 5, 1–13 (2016).

Lu, D., Wientjes, M. G., Lu, Z. & Au, J. L. S. Tumor priming enhances delivery and efficacy of nanomedicines. J. Pharmacol. Exp. Ther. 322, 80–88 (2007).

Lukácsi, S., Nagy-Baló, Z., Erdei, A., Sándor, N. & Bajtay, Z. The role of CR3 (CD11b/CD18) and CR4 (CD11c/CD18) in complement-mediated phagocytosis and podosome formation by human phagocytes. Immunol. Lett. 189, 64–72 (2017).

Lyon, P. C. et al. Safety and feasibility of ultrasound-triggered targeted drug delivery of doxorubicin from thermosensitive liposomes in liver tumours (TARDOX): a single-centre, open-label, phase 1 trial. Lancet Oncol. 19, 1027–1039 (2018).

Mackay, F. & Browning, J. L. BAFF: A fundamental survival factor for B cells. Nat. Rev. Immunol. 2, 465–475 (2002).

Madaio, M. P. et al. Murine monoclonal anti-DNA antibodies bind directly to glomerular antigens and form immune deposits. J. Immunol. 138, 2883–2889 (1987).

Maecker, H. T., Frey, T., Nomura, L. E. & Trotter, J. Selecting fluorochrome conjugates for maximum sensitivity. Cytom. Part A 62, 169–173 (2004).

Maeda, H. The enhanced permeability and retention (EPR) effect in tumor vasculature: the key role of tumor-selective macromolecular drug targeting. Adv Enzym. Regul 41, 189–207 (2001).

Maeda, H., Wu, J., Sawa, T., Matsumura, Y. & Hori, K. Tumor vascular permeability and the EPR effect in macromolecular therapeutics: a review. J. Control. Release 65, 271–84 (2000).

Magnuson, A. M. et al. Identification and validation of a tumor-infiltrating Treg transcriptional signature conserved across species and tumor types. Proc. Natl. Acad. Sci. U. S. A. 115, E10672–E10681 (2018).

Malyshkina, A. et al. Fas Ligand-mediated cytotoxicity of CD4+ T cells during chronic retrovirus infection. Sci. Rep. 7, 1–10 (2017).

Marabelle, A., Tselikas, L., de Baere, T. & Houot, R. Intratumoral immunotherapy: Using the tumor as the remedy. Ann. Oncol. 28, xii33–xii43 (2017).

Mariathasan, S. et al. TGFβ attenuates tumour response to PD-L1 blockade by contributing to exclusion of T cells. Nature 554, 544–548 (2018).

Martin, J. D., Seano, G. & Jain, R. K. Normalizing Function of Tumor Vessels: Progress, Opportunities, and Challenges. Annu. Rev. Physiol. 81, 505–534 (2019).

Martini, M. et al. IFN-γ-mediated upmodulation of MHC class I expression activates tumor-specific immune response in a mouse model of prostate cancer. Vaccine 28, 3548–3557 (2010).

Matlung, H. L. et al. Neutrophils Kill Antibody-Opsonized Cancer Cells by Trogoptosis. Cell Rep. 23, 3946-3959.e6 (2018).

Maude, S. L. et al. Tisagenlecleucel in children and young adults with B-cell lymphoblastic leukemia. N. Engl. J. Med. 378, 439–448 (2018).

McBain, S. C., Yiu, H. H. P. & Dobson, J. Magnetic nanoparticles for gene and drug delivery. Int. J. Nanomedicine 3, 169–180 (2008).

McCarthy, D. J. & Smyth, G. K. Testing significance relative to a fold-change threshold is a TREAT. Bioinformatics 25, 765–771 (2009).

McDonald, D. M. & Choyke, P. L. Imaging of angiogenesis: From microscope to clinic. Nat. Med. 9, 713–725 (2003).

Mehrad, B., Keane, M. P. & Strieter, R. M. Chemokines as mediators of angiogenesis. Thromb. Haemost. 97, 755–762 (2007).

Merck & Co. (Keytruda). Keytruda Label. FDA https://www.accessdata.fda.gov/drugsatfda_docs/label/2017/125514s014lbl.pdf (2017).

Mezache, L., Paniccia, B., Nyinawabera, A. & Nuovo, G. J. Enhanced expression of PD L1 in cervical intraepithelial neoplasia and cervical cancers. Mod. Pathol. 28, 1594–1602 (2015).

Minchinton, A. I. & Tannock, I. F. Drug penetration in solid tumours. Nat. Rev. Cancer 6, 583–592 (2006).

Mitragotri, S. Healing sound: The use of ultrasound in drug delivery and other therapeutic applications. Nat. Rev. Drug Discov. 4, 255–260 (2005).

Mocellin, S. TNF and cancer: the two sides of the coin. Front. Biosci. 13, 2774 (2008).

Monney, L. et al. Th1-specific cell surface protein Tim-3 regulates macrophage activation and severity of an autoimmune disease. Nature 415, 536–541 (2002).

Munn, D. H. The host protecting the tumor from the host — targeting PD-L1 expressed by host cells. J. Clin. Invest. 128, 570–572 (2018).

Munson, J. M. & Shieh, A. C. Interstitial fluid flow in cancer: Implications for disease progression and treatment. Cancer Manag. Res. 6, 317–318 (2014).

Myers, R. et al. Polymeric Cups for Cavitation-mediated Delivery of Oncolytic Vaccinia Virus. Mol. Ther. 24, 1627–1633 (2016).

Myers, R. et al. Ultrasound-mediated cavitation does not decrease the activity of small molecule, antibody or viral-based medicines. Int J Nanomedicine 13, 337–349 (2018).

Myers, R. et al. Ultrasound-mediated cavitation does not decrease the activity of small molecule, antibody or viral-based medicines. Int. J. Nanomedicine 13, 337–349 (2018).

Naing, A. et al. Anti-PD-1 monoclonal antibody MEDI0680 in a phase i study of patients with advanced solid malignancies. J. Immunother. Cancer 7, 1–15 (2019).

Nakahara, T., Norberg, S. M., Shalinsky, D. R., Hu-Lowe, D. D. & McDonald, D. M. Effect of inhibition of vascular endothelial growth factor signaling on distribution of extravasated antibodies in tumors. Cancer Res. 66, 1434–1445 (2006).

Nakajima, C. et al. A role of interferon-γ (IFN-γ) in tumor immunity: T cells with the capacity to reject tumor cells are generated but fail to migrate to tumor sites in IFN-γ-deficient mice. Cancer Res. 61, 3399–3405 (2001).

Nanostring. nCounter Advanced Analysis 2.0 User Manual. vol. MAN-10030- www.nanostring.com (2018).

Nanostring. nCounter PanCancer Immune Profiling Panel. https://www.nanostring.com/products/gene-expression-panels/gene-expression-panels-overview/hallmarks-cancer-gene-expression-panel-collection/pancancer-immune-profiling-panel (2019).

Nanostring. Gene expression markers of tumor-infiltrating leukocytes. https://www.nanostring.com/download_file/944/7274 (2016).

Narumi, K. et al. Proinflammatory Proteins S100A8/S100A9 Activate NK Cells via Interaction with RAGE. J. Immunol. 194, 5539–5548 (2015).

Netti, P. A., Berk, D. A., Swartz, M. A., Grodzinsky, A. J. & Jain, R. K. Role of extracellular matrix assembly in interstitial transport in solid tumors. Cancer Res. 60, 2497–2503 (2000).

Nichols, J. W. & Bae, Y. H. EPR: Evidence and fallacy. J Control Release 190, 451–464 (2014).

Nishimura, H. et al. Autoimmune dilated cardiomyopathy in PD-1 receptor-deficient mice. Science (80-.). 291, 319–322 (2001).

Nishimura, H., Nose, M., Hiai, H., Minato, N. & Honjo, T. Development of lupus-like autoimmune diseases by disruption of the PD-1 gene encoding an ITIM motif-carrying immunoreceptor. Immunity 11, 141–151 (1999).

Nocentini, G., Ronchetti, S., Cuzzocrea, S. & Riccardi, C. GITR/GITRL: More than an effector T cell co-stimulatory system. Eur. J. Immunol. 37, 1165–1169 (2007).

Nomura, L., Maino, V. C. & Maecker, H. T. Standardization and optimization of multiparameter intracellular cytokine staining. Cytom. Part A 73, 984–991 (2008).

Nurieva, R. et al. T-cell tolerance or function is determined by combinatorial costimulatory signals. EMBO J. 25, 2623–2633 (2006).

O'Donnell, E. A., Ernst, D. N. & Hingorani, R. Multiparameter Flow Cytometry: Advances in High Resolution Analysis. Immune Netw. 13, 43 (2013).

Oeffinger, B. E. & Wheatley, M. A. Development and characterization of a nano-scale contrast agent. Ultrasonics 42, 343–347 (2004).

Olson, T. S. & Ley, K. Chemokines and chemokine receptors in leukocyte trafficking. Am. J. Physiol. Integr. Comp. Physiol. 283, R7–R28 (2002).

Paefgen, V., Doleschel, D. & Kiessling, F. Evolution of contrast agents for ultrasound imaging and ultrasound-mediated drug delivery. Front. Pharmacol. 6, 1–16 (2015).

Pahk, K. J. et al. Boiling Histotripsy-induced Partial Mechanical Ablation Modulates Tumour Microenvironment by Promoting Immunogenic Cell Death of Cancers. Sci. Rep. 9, 1–12 (2019).

Pan, Y. et al. Single-cell RNA sequencing reveals compartmental remodeling of tumor-infiltrating immune cells induced by anti-CD47 targeting in pancreatic cancer. J. Hematol. Oncol. 12, 124 (2019).

Park, J. J. et al. B7-H1/CD80 interaction is required for the induction and maintenance of peripheral T-cell tolerance. Blood 116, 1291–1298 (2010).

Park, J. Y., Kim, S. H., Lee, S. M., Lee, J. S. & Han, J. K. CT volumetric measurement of colorectal cancer helps predict tumor staging and prognosis. PLoS One 12, 1–15 (2017).

Parry, R. V. et al. CTLA-4 and PD-1 Receptors Inhibit T-Cell Activation by Distinct Mechanisms. Mol. Cell. Biol. 25, 9543–9553 (2005).

Parsa, A. T. et al. Loss of tumor suppressor PTEN function increases B7-H1 expression and immunoresistance in glioma. Nat. Med. 13, 84–88 (2007).

Passaniti, A. et al. A simple, quantitative method for assessing angiogenesis and antiangiogenic agents using reconstituted basement membrane, heparin, and fibroblast growth factor. Lab. Investig. 67, 519–528 (1992).

Patsoukis, N., Li, L., Sari, D., Petkova, V. & Boussiotis, V. A. PD-1 Increases PTEN Phosphatase Activity While Decreasing PTEN Protein Stability by Inhibiting Casein Kinase 2. Mol. Cell. Biol. 33, 3091–3098 (2013).

Pereno, V. et al. Layered acoustofluidic resonators for the simultaneous optical and acoustic characterisation of cavitation dynamics, microstreaming, and biological effects. Biomicrofluidics 12, 1–14 (2018).

PerkinElmer. Technical Data Sheet, NIR Fluorochrome Labeling Kit. 1–2 (2010).

Pluim, D., Ros, W., Miedema, I. H. C., Beijnen, J. H. & Schellens, J. H. M. Multiparameter Flow Cytometry Assay for Quantification of Immune Cell Subsets, PD-1 Expression Levels and PD-1 Receptor Occupancy by Nivolumab and Pembrolizumab. Cytom. Part A 95, 1053–1065 (2019).

Postow, M. A. et al. Nivolumab and ipilimumab versus ipilimumab in untreated melanoma. N. Engl. J. Med. 372, 2006–2017 (2015).

Pries, A. R., Höpfner, M., le Noble, F., Dewhirst, M. W. & Secomb, T. W. The shunt problem: control of functional shunting in normal and tumour vasculature. Nat. Rev. Cancer 10, 587–593 (2010).

Radhakrishnan, K. et al. Relationship between cavitation and loss of echogenicity from ultrasound contrast agents. Phys. Med. Biol. 58, 6541–63 (2013).

Ragupathi, G. et al. Antibodies against Tumor Cell Glycolipids and Proteins, but Not Mucins, Mediate Complement-Dependent Cytotoxicity. J. Immunol. 174, 5706–5712 (2005).

Redmond, W. L., Ruby, C. E. & Weinberg, A. D. Role of OX40 in T cell costim and survival. Crit. Rev. Immunol. 29, 187–201 (2009).

Ribas, A. & Wolchok, J. D. Cancer immunotherapy using checkpoint blockade. Science (80-.). 359, 1350–1355 (2018).

Ribatti, D., Nico, B., Crivellato, E. & Vacca, A. The structure of the vascular network of tumors. Cancer Lett. 248, 18–23 (2007).

Richards, C. D. The Enigmatic Cytokine Oncostatin M and Roles in Disease. ISRN Inflamm. 2013, 1–23 (2013).

Rider, P. et al. IL-1α and IL-1β Recruit Different Myeloid Cells and Promote Different Stages of Sterile Inflammation. J. Immunol. 187, 4835–4843 (2011).

Ritchie, M. E. et al. Limma powers differential expression analyses for RNA-sequencing and microarray studies. Nucleic Acids Res. 43, e47 (2015).

Rogers, L. M., Veeramani, S. & Weiner, G. J. Complement in monoclonal antibody therapy of cancer. Immunol. Res. 59, 203–210 (2014).

Rouvier, E., Luciani, M. F. & Golstein, P. Fas involvement in Ca(2+)-independent T cell-mediated cytotoxicity. J. Exp. Med. 177, 195–200 (1993).

Ryan, A. E., Lane, S., Shanahan, F., O'Connell, J. & Houston, A. M. Fas ligand expression in human and mouse cancer cell lines; a caveat on over-reliance on mRNA data. J. Carcinog. 5, 1–7 (2006).

Ryckman, C., Vandal, K., Rouleau, P., Talbot, M. & Tessier, P. A. Proinflammatory Activities of S100: Proteins S100A8, S100A9, and S100A8/A9 Induce Neutrophil Chemotaxis and Adhesion. J. Immunol. 170, 3233–3242 (2003).

Sakuishi, K. et al. Targeting Tim-3 and PD-1 pathways to reverse T cell exhaustion and restore anti-tumor immunity. J. Exp. Med. 207, 2187–2194 (2010).

Samson, A. et al. Intravenous delivery of oncolytic reovirus to brain tumor patients immunologically primes for subsequent checkpoint blockade. Sci. Transl. Med. 10, (2018).

Schumacher, T. N. & Schreiber, R. D. Neoantigens in cancer immunotherapy. Science (80-.). 348, 69–74 (2015).

Schumann, R. et al. Structure and function of lipopolysaccharide binding protein. Science (80-.). 249, 1429–1431 (1990).

Schütze, F. et al. Inhibition of Lysyl Oxidases Improves Drug Diffusion and Increases Efficacy of Cytotoxic Treatment in 3D Tumor Models. Sci. Rep. 5, 1–13 (2015).

Selby, M. J. et al. Preclinical development of ipilimumab and nivolumab combination immunotherapy: Mouse tumor models, In vitro functional studies, and cynomolgus macaque toxicology. PLoS One 11, 1–19 (2016).

Selby, M. J. et al. Anti-CTLA-4 antibodies of IgG2a isotype enhance antitumor activity through reduction of intratumoral regulatory T cells. Cancer Immunol. Res. 1, 32–42 (2013).

Sepuru, K. M., Poluri, K. M. & Rajarathnam, K. Solution Structure of CXCL5 — A Novel Chemokine and Adipokine Implicated in Inflammation and Obesity. PLoS One 9, e93228 (2014).

Sevko, A. & Umansky, V. Myeloid-derived suppressor cells interact with tumors in terms of myelopoiesis, tumorigenesis and immunosuppression: Thick as thieves. J. Cancer 4, 3–11 (2013).

Shah, D. K. & Betts, A. M. Antibody biodistribution coefficients. MAbs 5, 297–305 (2013).

Sharma, P., Hu-Lieskovan, S., Wargo, J. A. & Ribas, A. Primary, Adaptive, and Acquired Resistance to Cancer Immunotherapy. Cell 168, 707–723 (2017).

Sharpe, A. H. & Pauken, K. E. The diverse functions of the PD1 inhibitory pathway. Nat. Rev. Immunol. 18, 153–167 (2018).

Sharpe, C. et al. Comparison of gene expression and flow cytometry for immune profiling in chronic lymphocytic leukaemia. J. Immunol. Methods 463, 97–104 (2018).

Sheybani, N. D. & Price, R. J. Perspectives on recent progress in focused ultrasound immunotherapy. Theranostics 9, 7749–7758 (2019).

Shi, L. et al. PD-1 Blockade Boosts Radiofrequency Ablation–Elicited Adaptive Immune Responses against Tumor. Clin. Cancer Res. 22, 1173–1184 (2016).

Shin, D. S. et al. Primary resistance to PD-1 blockade mediated by JAK1/2 mutations. Cancer Discov. 7, 188–201 (2017).

Shultz, L. D. et al. Human Lymphoid and Myeloid Cell Development in NOD/LtSz- scid IL2R γ null Mice Engrafted with Mobilized Human Hemopoietic Stem Cells . J. Immunol. 174, 6477–6489 (2005).

Silvestrini, M. T. et al. Priming is key to effective incorporation of image-guided thermal ablation into immunotherapy protocols. JCI Insight 2, 1–16 (2017).

Simms, P. E. & Ellis, T. M. Utility of flow cytometric detection of CD69 expression as a rapid method for determining poly- and oligoclonal lymphocyte activation. Clin. Diagn. Lab. Immunol. 3, 301–304 (1996).

Simpson, T. R. et al. Fc-dependent depletion of tumor-infiltrating regulatory T cells co-defines the efficacy of anti–CTLA-4 therapy against melanoma. J. Exp. Med. 210, 1695–1710 (2013).

Skalina, K. A., Singh, S., Chavez, C. G., Macian, F. & Guha, C. Low Intensity Focused Ultrasound (LOFU)-mediated Acoustic Immune Priming and Ablative Radiation Therapy for in situ Tumor Vaccines. Sci. Rep. 9, 1–12 (2019).

Skeate, J. G., Woodham, A. W., Einstein, M. H., Da Silva, D. M. & Kast, W. M. Current therapeutic vaccination and immunotherapy strategies for HPV-related diseases. Hum. Vaccines Immunother. 12, 1418–1429 (2016).

Smith, A. M., Mancini, M. C. & Nie, S. NIH Public Access: Second window for in vivo imaging. Nat. Nanotechnol. 4, 710–711 (2010).

Smith, A. M., Mancini, M. C. & Nie, S. Bioimaging: Second window for in vivo imaging. Nat. Nanotechnol. 4, 710–711 (2009).

Sneller, M. C. et al. IL-15 administered by continuous infusion to rhesus macaques induces massive expansion of CD8+ T effector memory population in peripheral blood. Blood 118, 6845–6848 (2011).

Solinas, C., Migliori, E., De Silva, P. & Willard-Gallo, K. LAG3: The biological processes that motivate targeting this immune checkpoint molecule in human cancer. Cancers (Basel). 11, (2019).

Song, A., Tang, X., Harms, K. M. & Croft, M. OX40 and Bcl-x L Promote the Persistence of CD8 T Cells to Recall Tumor-Associated Antigen . J. Immunol. 175, 3534–3541 (2005).

Song, Q. et al. Dissecting intratumoral myeloid cell plasticity by single cell RNA-seq. Cancer Med. 8, 3072–3085 (2019).

Stadtmann, A. & Zarbock, A. CXCR2: From bench to bedside. Front. Immunol. 3, 1–12 (2012).

Stockis, J., Roychoudhuri, R. & Halim, T. Y. F. Regulation of regulatory T cells in cancer. Immunology 157, 219–231 (2019).

Stride, E. & Coussios, C. Nucleation, mapping and control of cavitation for drug delivery. Nat. Rev. Phys. 1, 495–509 (2019).

Sun, C., Mezzadra, R. & Schumacher, T. N. Regulation and Function of the PD-L1 Checkpoint. Immunity 48, 434–452 (2018).

Taborda, C. P. & Casadevall, A. CR3 (CD11b/CD18) and CR4 (CD11c/CD18) are involved in complement-independent antibody-mediated phagocytosis of Cryptococcus neoformans. Immunity 16, 791–802 (2002).

Takeda, Y. et al. A TLR3-Specific Adjuvant Relieves Innate Resistance to PD-L1 Blockade without Cytokine Toxicity in Tumor Vaccine Immunotherapy. Cell Rep. 19, 1874–1887 (2017).

Tanaka, A. & Sakaguchi, S. Regulatory T cells in cancer immunotherapy. Cell Res. 27, 109–118 (2017).

Tang, F. & Zheng, P. Tumor cells versus host immune cells: Whose PD-L1 contributes to PD-1/PD-L1 blockade mediated cancer immunotherapy? Cell Biosci. 8, 1–8 (2018).

Tang, H. et al. Facilitating T Cell Infiltration in Tumor Microenvironment Overcomes Resistance to PD-L1 Blockade. Cancer Cell 30, 500 (2016).

Tang, J. et al. The clinical trial landscape for PD1/PDl1 immune checkpoint inhibitors. Nat. Rev. Drug Discov. 17, 854–855 (2018).

Tarzami, S. T. et al. Opposing Effects Mediated by the Chemokine Receptor CXCR2 on Myocardial Ischemia-Reperfusion Injury: Recruitment of Potentially Damaging Neutrophils and Direct Myocardial Protection. Circulation 108, 2387–2392 (2003).

Tennant, B. C. et al. Hepatocellular carcinoma in the woodchuck model of hepatitis B virus infection. Gastroenterology 127, 283–293 (2004).

Ter Haar, G. R. High intensity focused ultrasound for the treatment of tumors. Echocardiography 18, 317–322 (2001).

ter Haar, G. & Coussios, C. High intensity focused ultrasound: Physical principles and devices. Int. J. Hyperth. 23, 89–104 (2007).

ThermoFisher Scientific. Fixable Viability Stains for Flow Cytometry. https://www.thermofisher.com/us/en/home/life-science/cell-analysis/flow-cytometry/flow-cytometry-assays-reagents/cell-viability-assays-flow-cytometry/fixable-viability-dyes-flow-cytometry.html (2019).

Thomis, D. C. & Berg, L. J. Peripheral expression of Jak3 is required to maintain T lymphocyte function. J. Exp. Med. 185, 197–206 (1997).

Tian, T., Olson, S., Whitacre, J. M. & Harding, A. The origins of cancer robustness and evolvability. Integr. Biol. (Camb). 3, 17–30 (2011).

Tie, Y. et al. Safety and efficacy of atezolizumab in the treatment of cancers: A systematic review and pooled-analysis. Drug Des. Devel. Ther. 13, 523–538 (2019).

Tivol, E. A. et al. Loss of CTLA-4 leads to massive lymphoproliferation and fatal multiorgan tissue destruction, revealing a critical negative regulatory role of CTLA-4. Immunity 3, 541–547 (1995).

Tong, R. T. et al. Vascular normalization by vascular endothelial growth factor receptor 2 blockade induces a pressure gradient across the vasculature and improves drug penetration in tumors. Cancer Res. 64, 3731–3736 (2004).

Tontonoz, M. In a First , FDA Approves Immunotherapy Combination for Advanced Melanoma. CRI vol. 2 19–21 https://www.cancerresearch.org/blog/october-2015/fda-approves-immunotherapy-combination-melanoma (2015).

Trapani, J. A. Target cell apoptosis induced by cytotoxic T cells and natural killer cells involves synergy between the pore-forming protein, perforin, and the serine protease, granzyme B. Aust. N. Z. J. Med. 25, 793–799 (1995).

Treffers, L. W. et al. FcγRIIIb restricts antibody-dependent destruction of cancer cells by human neutrophils. Front. Immunol. 10, 1–13 (2019).

Tridandapani, S., Butchar, J. P. & Byrd, J. C. NIH Research Project (R01): Myeloid cell-derived Granzyme B as an inducible enhancer of cancer immunotherapy. http://grantome.com/grant/NIH/R01-CA203584-01A1 (2018) doi:1R01CA203584-01A1.

Truffi, M. et al. Nano-strategies to target breast cancer-associated fibroblasts: Rearranging the tumor microenvironment to achieve antitumor efficacy. Int. J. Mol. Sci. 20, (2019).

Trujillo, J. A., Sweis, R. F., Bao, R. & Luke, J. J. T Cell–Inflamed versus Non-T Cell–Inflamed Tumors: A Conceptual Framework for Cancer Immunotherapy Drug Development and Combination Therapy Selection. Cancer Immunol. Res. 6, 990–1000 (2018).

Utoguchi, N. et al. Effect of tumour cell-conditioned medium on endothelial macromolecular permeability and its correlation with collagen. Br. J. Cancer 73, 24–28 (1996).

Van Der Vlist, M., Kuball, J., Radstake, T. R. D. & Meyaard, L. Immune checkpoints and rheumatic diseases: What can cancer immunotherapy teach us? Nat. Rev. Rheumatol. 12, 593–604 (2016).

Vargas, F. A. et al. Fc Effector Function Contributes to the Activity of Human Anti-CTLA-4 Antibodies. Cancer Cell 33, 649-663.e4 (2018).

Walzer, T. et al. Identification, activation, and selective in vivo ablation of mouse NK cells via NKp46. Proc. Natl. Acad. Sci. U. S. A. 104, 3384–3389 (2007).

Wang, S. et al. Intratumoral injection of a CpG oligonucleotide reverts resistance to PD-1 blockade by expanding multifunctional CD8+ T cells. Proc. Natl. Acad. Sci. U. S. A. 113, E7240–E7249 (2016).

Wang, X. et al. Inflammatory cytokines IL-17 and TNF-α up-regulate PD-L1 expression in human prostate and colon cancer cells. Immunol. Lett. 184, 7–14 (2017).

Wang, Y. et al. Adjuvant effect of the novel TLR1/TLR2 agonist Diprovocim synergizes with anti–PD-L1 to eliminate melanoma in mice. Proc. Natl. Acad. Sci. U. S. A. 115, E8698–E8706 (2018).

Waterhouse, P. et al. Lymphoproliferative disorders with early lethality in mice deficient in Ctla-4. Science (80-.). 270, 985–988 (1995).

Webster, R. M. The immune checkpoint inhibitors: Where are we now? Nat. Rev. Drug Discov. 13, 883–884 (2014).

Wei, S. C. et al. Distinct Cellular Mechanisms Underlie Anti-CTLA-4 and Anti-PD-1 Checkpoint Blockade. Cell 170, 1120-1125.e17 (2017).

Weisser, S. B., van Rooijen, N. & Sly, L. M. Depletion and reconstitution of macrophages in mice. J. Vis. Exp. 5–11 (2012) doi:10.3791/4105.

Weissleder, R. A clearer vision for in vivo imaging. Nat. Biotechnol. 19, 316–317 (2001).

Wherry, E. J., Blattman, J. N., Murali-Krishna, K., van der Most, R. & Ahmed, R. Viral Persistence Alters CD8 T-Cell Immunodominance and Tissue Distribution and Results in Distinct Stages of Functional Impairment. J. Virol. 77, 4911–4927 (2003).

WHO. Cancer. Cancer vol. 7 2018 https://www.who.int/news-room/fact-sheets/detail/cancer (2018).

Wolchok, J. D. et al. Nivolumab plus Ipilimumab in advanced melanoma. N. Engl. J. Med. 369, 122–133 (2013).

Woo, S.-R. et al. Immune Inhibitory Molecules LAG-3 and PD-1 Synergistically Regulate T-cell Function to Promote Tumoral Immune Escape. Cancer Res. 72, 917–927 (2012).

Wu, N. et al. A hematopoietic cell-driven mechanism involving SLAMF6 receptor, SAP adaptors and SHP-1 phosphatase regulates NK cell education. Nat. Immunol. 17, 387–396 (2016).

Xiao, Y. et al. RGMb is a novel binding partner for PD-l2 and its engagement with PD-l2 promotes respiratory tolerance. J. Exp. Med. 211, 943–959 (2014).

Yamazaki, T. et al. Expression of Programmed Death 1 Ligands by Murine T Cells and APC. J. Immunol. 169, 5538–5545 (2002).

Yarchoan, M. et al. PD-L1 expression and tumor mutational burden are independent biomarkers in most cancers. JCI Insight 4, 1–10 (2019).

Yu, J. X., Hodge, J. P., Oliva, C., Neftelinov, S. T. & Hubbard-lucey, V. M. Trends in clinical development for PD-1 / PD-L1 inhibitors. Nat. Rev. Drug Discov. 18, 1–3 (2019).

Yu, J. W. et al. Tumor-immune profiling of murine syngeneic tumor models as a framework to guide mechanistic studies and predict therapy response in distinct tumor microenvironments. PLoS One 13, 1–27 (2018).

Yu, W.-H. et al. ADCC-Mediated CD56dim NK Cell Responses Are Associated with Early HBsAg Clearance in Acute HBV Infection. Pathog. Immun. 3, 2 (2018).

Yue, W. et al. Checkpoint blockade and nanosonosensitizer-augmented noninvasive sonodynamic therapy combination reduces tumour growth and metastases in mice. Nat. Commun. 10, 1–15 (2019).

Yuzhakova, D. V. et al. CT26 murine colon carcinoma expressing the red fluorescent protein KillerRed as a highly immunogenic tumor model. J. Biomed. Opt. 20, 088002 (2015).

Yuzhakova, D. V. et al. CT26 murine colon carcinoma expressing the red fluorescent protein KillerRed as a highly immunogenic tumor model. J. Biomed. Opt. 20, 088002 (2015).

Zaretsky, J. M. et al. Mutations associated with acquired resistance to PD-1 blockade in melanoma. N. Engl. J. Med. 375, 819–829 (2016).

Zeng, J. et al. Anti-PD-1 blockade and stereotactic radiation produce long-term survival in mice with intracranial gliomas. Int. J. Radiat. Oncol. Biol. Phys. 86, 343–349 (2013).

Zhang, M. et al. IL-15 enhanced antibody-dependent cellular cytotoxicity mediated by NK cells and macrophages. Proc. Natl. Acad. Sci. U. S. A. 115, E10915–E10924 (2018).

Zhao, J., Nussinov, R. & Ma, B. Antigen binding allosterically promotes Fc receptor recognition. MAbs 11, 58–74 (2019).

Zhao, J. et al. Irreversible electroporation reverses resistance to immune checkpoint blockade in pancreatic cancer. Nat. Commun. 10, 1–14 (2019).

Zhao, X. et al. B Cell Lymphoma Immunotherapy Using TLR9-Targeted Oligonucleotide STAT3 Inhibitors. Mol. Ther. 26, 695–707 (2018).

Zheng, X. et al. Increased vessel perfusion predicts the efficacy of immune checkpoint blockade. J. Clin. Invest. 128, 2104–2115 (2018).

Zhou, J., Nagarkatti, P., Zhong, Y. & Nagarkatti, M. Characterization of T-cell memory phenotype after in vitro expansion of tumor-infiltrating lymphocytes from melanoma patients. Anticancer Res. 31, 4099–109 (2011).

Zhou, P., L'italien, L., Hodges, D. & Schebye, X. M. Pivotal Roles of CD4 + Effector T cells in Mediating Agonistic Anti-GITR mAb-Induced-Immune Activation and Tumor Immunity in CT26 Tumors . J. Immunol. 179, 7365–7375 (2007).

Zien, A., Küffner, R., Zimmer, R. & Lengauer, T. Analysis of gene expression data with pathway scores. Proc. Int. Conf. Intell. Syst. Mol. Biol. 8, 407–417 (2000).

Zitvogel, L. & Kroemer, G. Targeting PD-1/PD-L1 interactions for cancer immunotherapy. Oncoimmunology 1, 1223–1225 (2012).

Zlotnik, A. & Yoshie, O. The Chemokine Superfamily Revisited. Immunity 36, 705–716 (2012).

Appendices

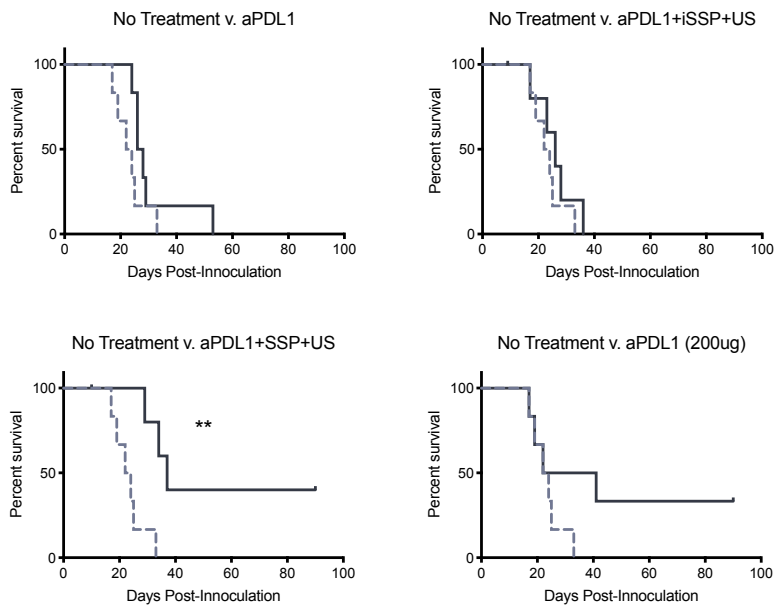
Appendix 3.1 - Extended Data Related to 3.1

Appendix 3.1 (1 of 2)

a 2-Way ANOVA with Tukey's Multiple Comparisons Test

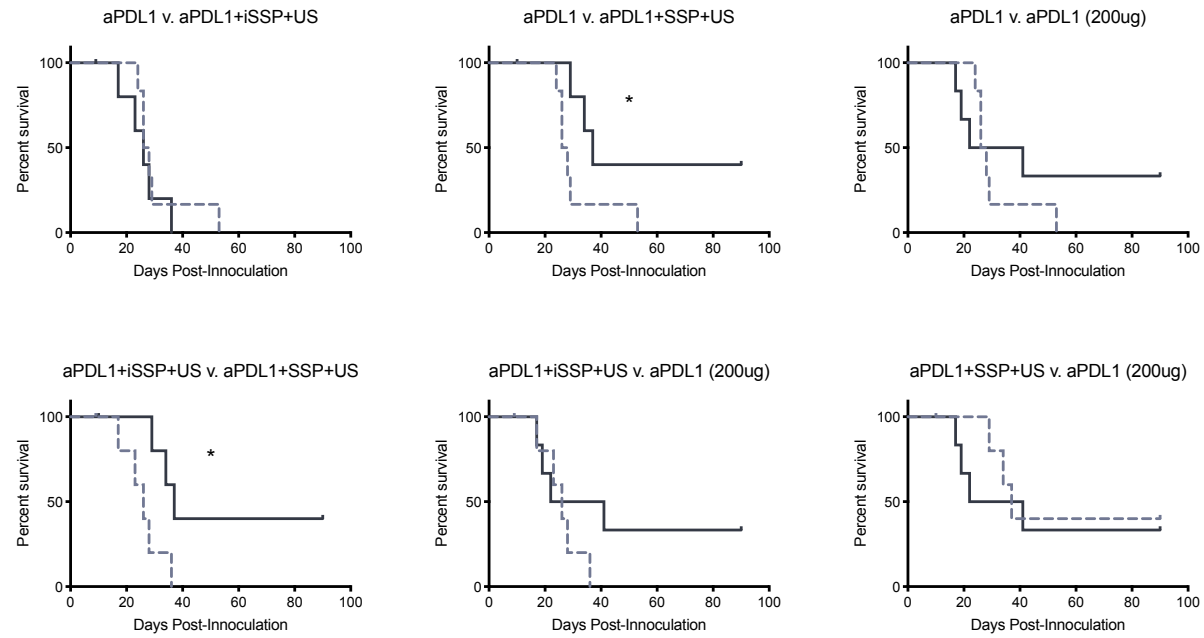
Comparison & Day	11	12	13	14	15	16	17
No Treatment vs. aPDL1	ns	ns	ns	ns	ns	ns	ns
No Treatment vs. aPDL1+iSSP+US	ns	ns	ns	ns	ns	ns	ns
No Treatment vs. aPDL1+SSP+US	ns	ns	ns	ns	ns	***	****
No Treatment vs. aPDL1 (200ug)	ns	ns	ns	ns	ns	ns	ns
aPDL1 vs. aPDL1+iSSP+US	ns	ns	ns	ns	ns	ns	ns
aPDL1 vs. aPDL1+SSP+US	ns	ns	ns	ns	ns	ns	ns
aPDL1 vs. aPDL1 (200ug)	ns	ns	ns	ns	ns	ns	ns
aPDL1+iSSP+US vs. aPDL1+SSP+US	ns	ns	ns	ns	ns	ns	ns
aPDL1+iSSP+US vs. aPDL1 (200ug)	ns	ns	ns	ns	ns	ns	ns
aPDL1+SSP+US vs. aPDL1 (200ug)	ns	ns	ns	ns	ns	ns	ns

b

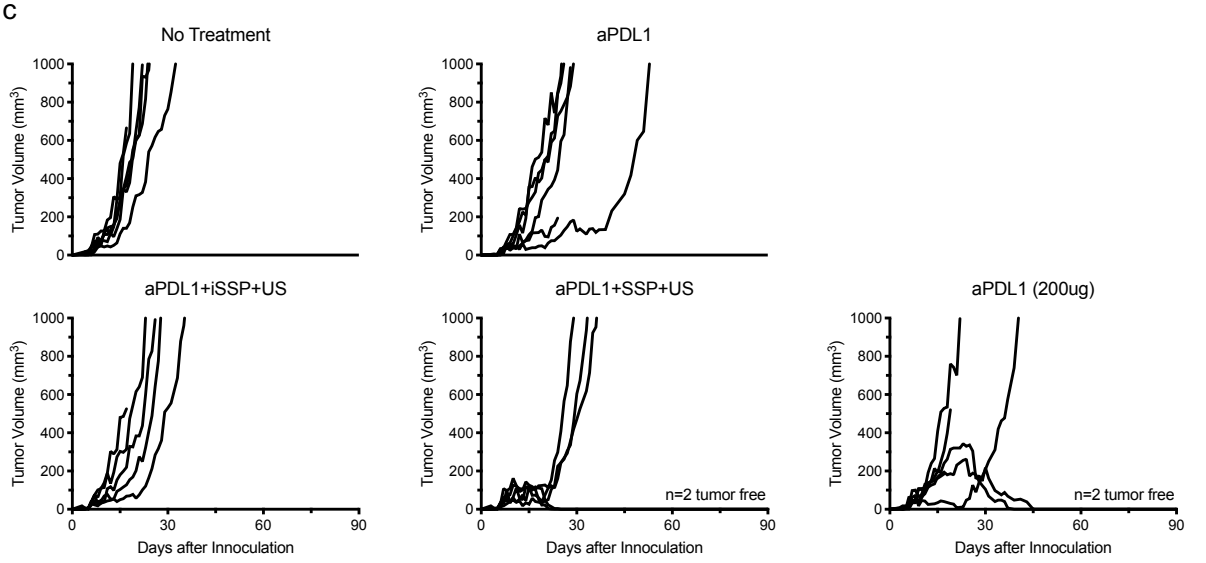


Extended data related to 3.1:
a) Statistical analysis of tumour volumes between groups (from day 11 to day 17). Note, a majority but not necessarily all mice were measured on each day. Significance determined by ordinary two-way ANOVA (factors: day and group) with Tukey's multiple comparisons test (single pooled variance)
b) Uncorrected, log-rank (Mantel-Cox) pairwise comparisons (corresponding to tabulation in Fig. 3.1e). In each plot, the dashed grey line represents the first named group, and the solid line represents the second named group

b (continued)

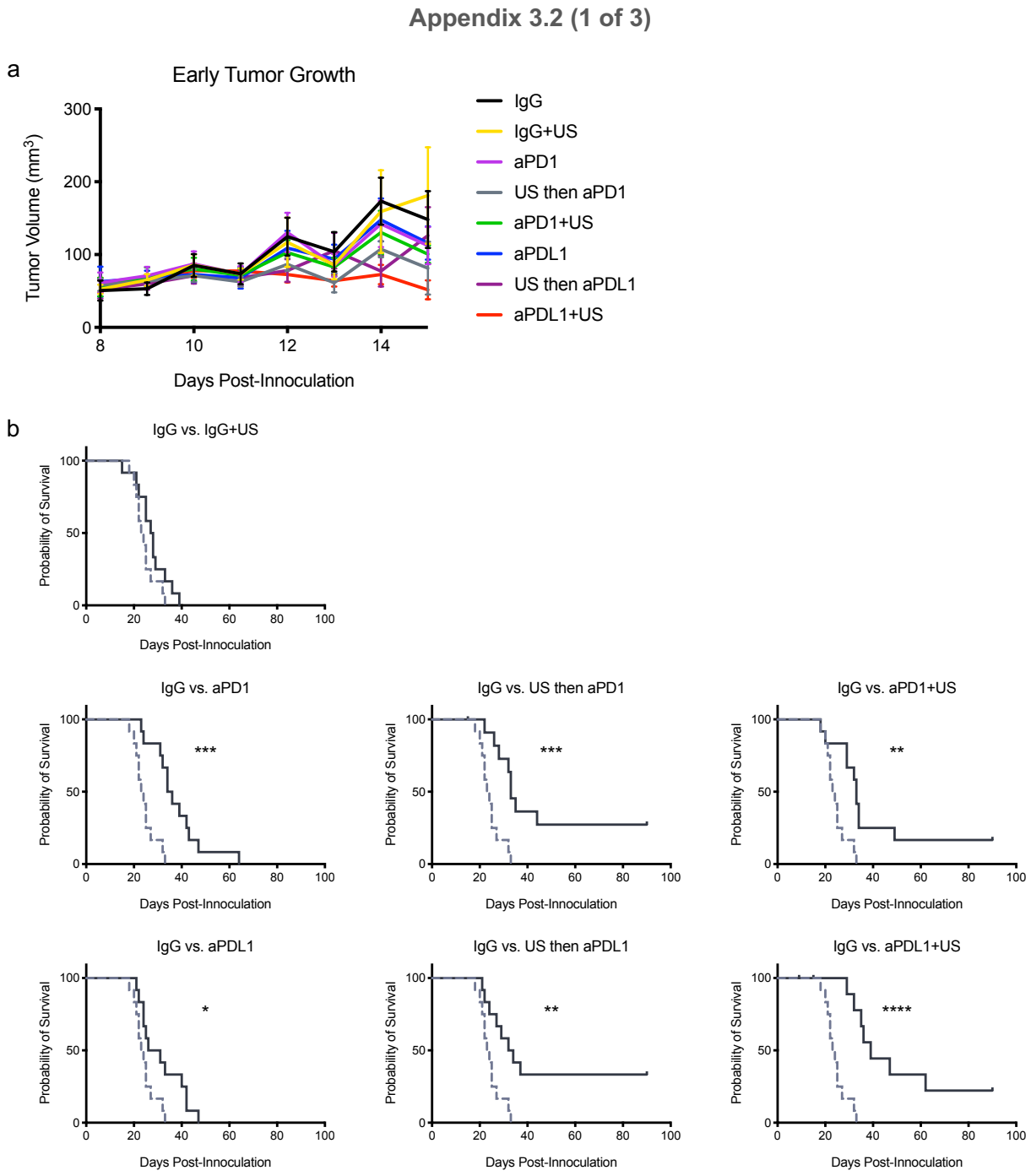


c



Extended data related to 3.1 continued:
b) Uncorrected, log-rank (Mantel-Cox) pairwise comparisons (corresponding to tabulation in Fig. 3.1e). In each plot, the dashed grey line represents the first named group, and the solid line represents the second named group
c) Individual tumour growth curves of study-enrolled mice arranged by group

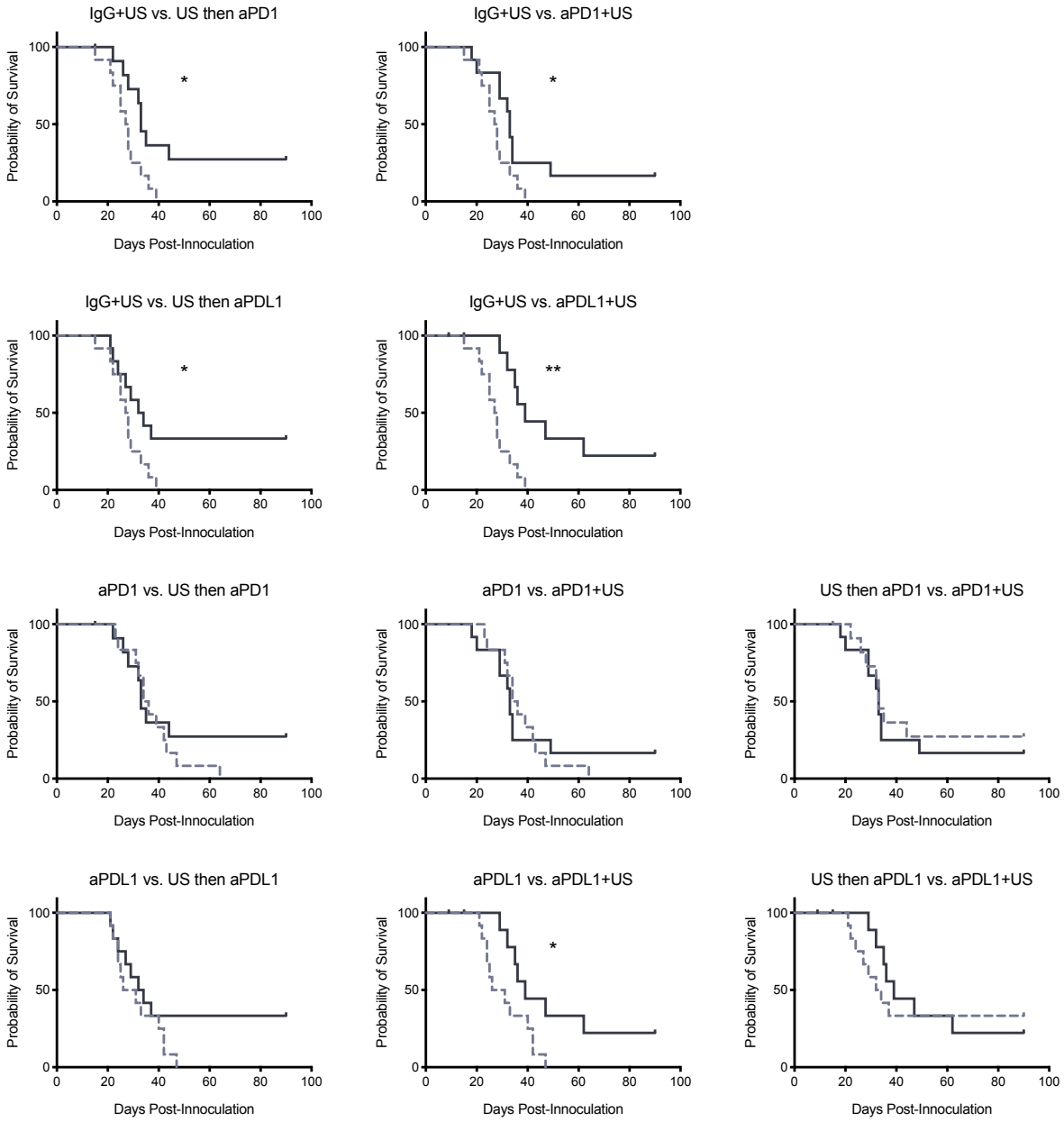
Appendix 3.2 - Extended Data Related to 3.2



Extended data related to 3.2:
a) Early tumour growth curves. Lines connect the average of tumour volumes measured (by group) on a given day (mean and SEM shown). Note, on most days only about half of the mice in each group were measured. Different colours correspond to each of the groups
b) Uncorrected, log-rank (Mantel-Cox) pairwise comparisons (corresponding to tabulation in Fig. 3.2e). In each plot, the dashed grey line represents the first named group, and the solid line represents the second named group

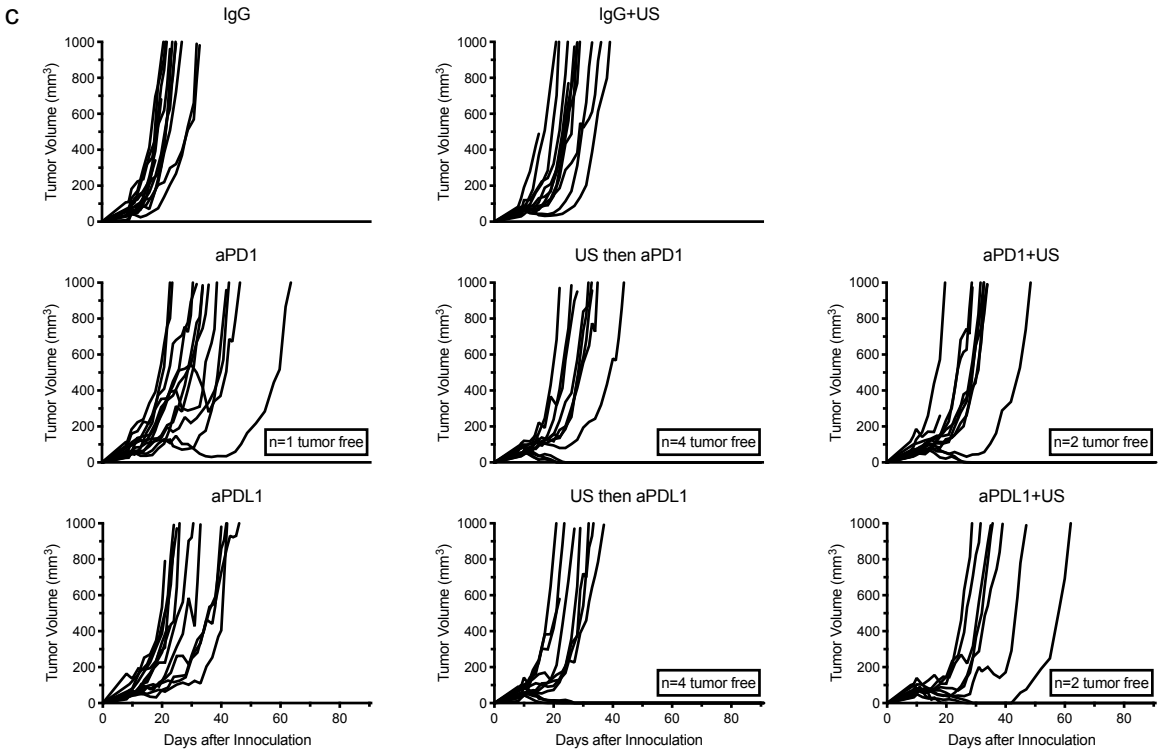
Appendix 3.2 (2 of 3)

b (continued)



Extended data related to 3.2 continued:
b) Uncorrected, log-rank (Mantel-Cox) pairwise comparisons (corresponding to tabulation in Fig. 3.2e). In each plot, the dashed grey line represents the first named group, and the solid line represents the second named group

Appendix 3.2 (3 of 3)



Extended data related to 3.2 continued:
c) Individual tumour growth curves of study-enrolled mice stratified by group

Appendix 3.3 - Extended Data Related to 3.3

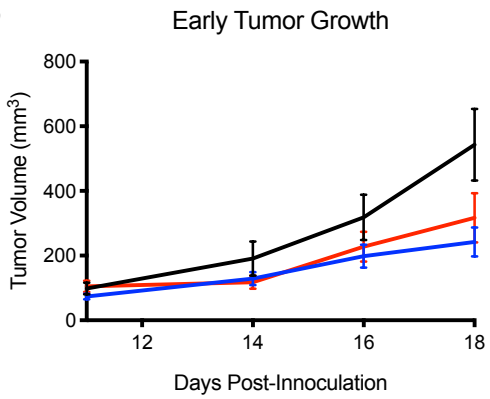
Appendix 3.3 (1 of 1)

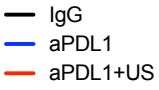
a

Pre-Intervention Tumour Volumes

	Mean (mm^3)	SD (mm^3)
IgG	62.1	12.1
aPDL1	61.6	12.8
aPDL1+US	60.3	10.5
Overall	61.3	11.4

b

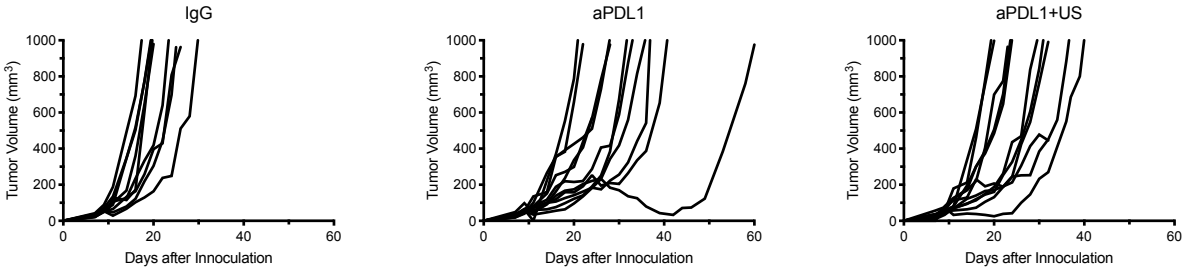




2-Way ANOVA with Tukey's Multiple Comparisons Test

Comparison & Day	11	14	16	18
IgG vs. aPDL1	ns	ns	ns	***
IgG vs. aPDL1+US	ns	ns	ns	**
aPDL1 vs. aPDL1+US	ns	ns	ns	ns

c



Extended data related to 3.3:
a) Tabulation of pre-intervention tumour volumes on a per-group basis. In this study, tumours not ideal for US-treatment (i.e. bimodal, multinodular tumours, non-spherical/ellipsoid in shape) were assigned to the IgG control group.
b) Average tumour volumes by group (mean and SEM). Note, a majority but not necessarily all mice were measured on each day. Adjacent is a tabulation of the significance (or lack thereof) between tumour volumes by group assessed on days shown in the table. Significance determined by ordinary two-way ANOVA (factors: day and group) with Tukey's multiple comparisons test (single pooled variance)
c) Individual tumour growth curves of study-enrolled mice *arranged by group*

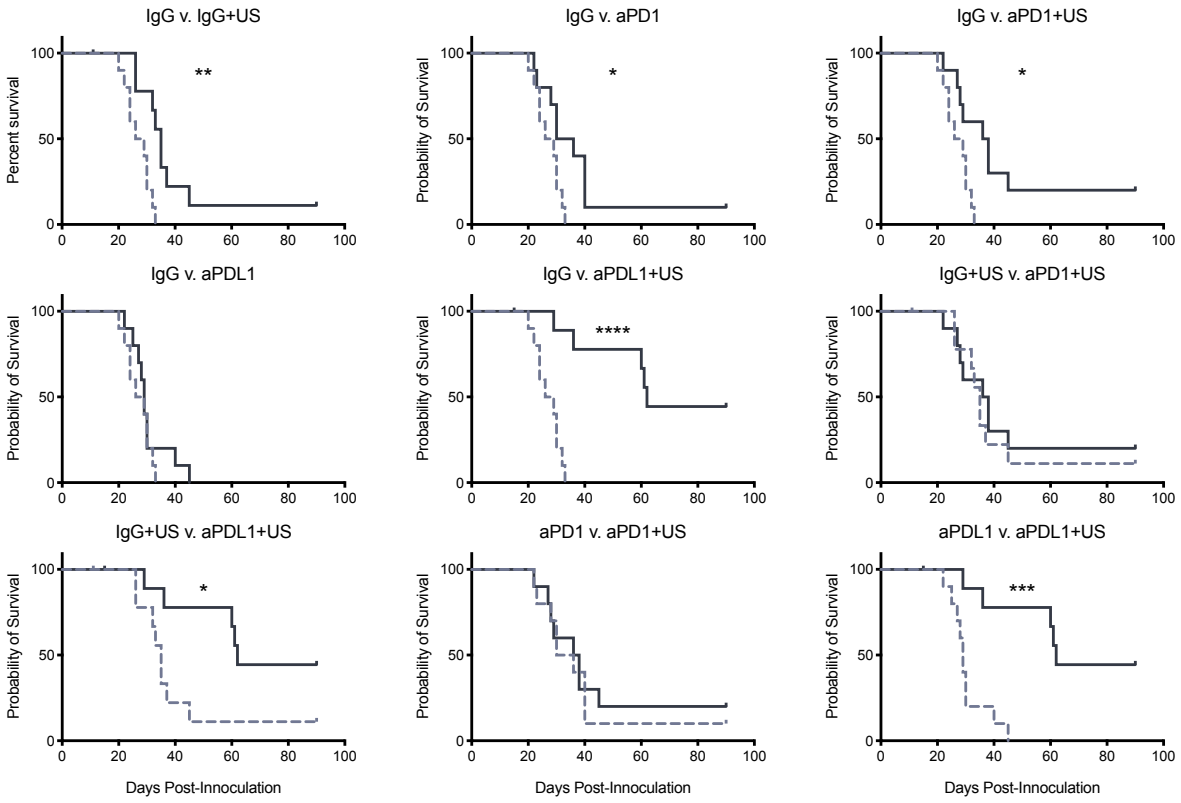
Appendix 3.4 - Extended Data Related to 3.4

Appendix 3.4 (1 of 2)

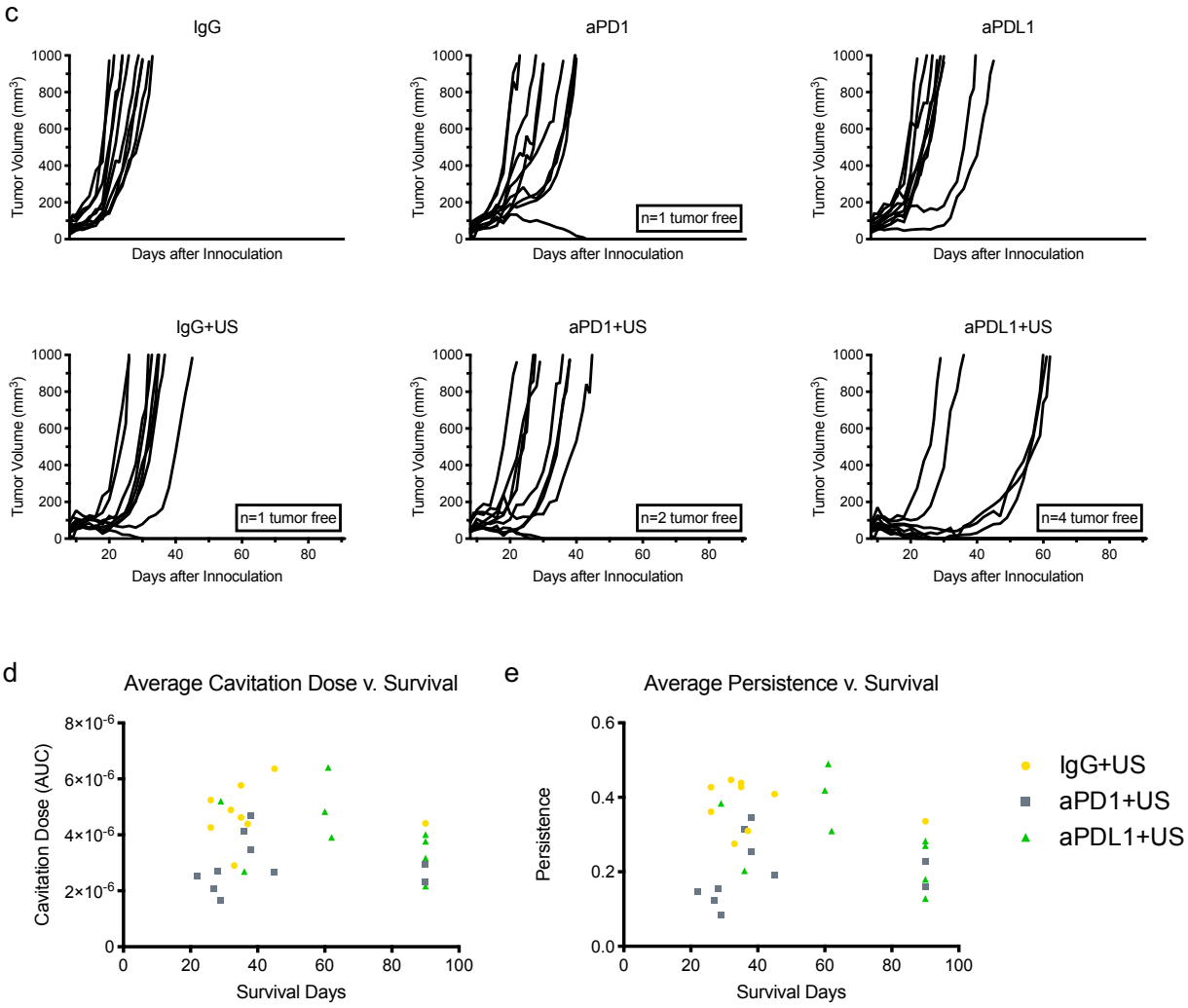
a 2-Way ANOVA with Tukey's Multiple Comparisons Test

Comparison & Day	12	14	16	18	20
IgG vs. IgG+US	ns	ns	ns	ns	****
IgG vs. aPD1	ns	ns	ns	ns	ns
IgG vs. aPD1+US	ns	ns	ns	ns	***
IgG vs. aPDL1	ns	ns	ns	ns	ns
IgG vs. aPDL1+US	ns	ns	ns	**	****
IgG+US vs. aPD1	ns	ns	ns	ns	***
IgG+US vs. aPD1+US	ns	ns	ns	ns	ns
IgG+US vs. aPDL1	ns	ns	ns	ns	**
IgG+US vs. aPDL1+US	ns	ns	ns	ns	ns
aPD1 vs. aPD1+US	ns	ns	ns	ns	ns
aPD1 vs. aPDL1	ns	ns	ns	ns	ns
aPD1 vs. aPDL1+US	ns	ns	ns	ns	****
aPD1+US vs. aPDL1	ns	ns	ns	ns	ns
aPD1+US vs. aPDL1+US	ns	ns	ns	ns	ns
aPDL1 vs. aPDL1+US	ns	ns	ns	ns	****

b



Extended data related to 3.4:
a) Analysis of differences between tumour volumes (by group) of study-enrolled mice measured on even days from day 12 to day 20. Significance determined by ordinary two-way ANOVA (factors: day and group) with Tukey's multiple comparisons test (single pooled variance)
b) Uncorrected, log-rank (Mantel-Cox) pairwise comparisons (corresponding to tabulation in Fig. 3.4f). In each plot, the dashed grey line represents the first named group, and the solid line represents the second named group

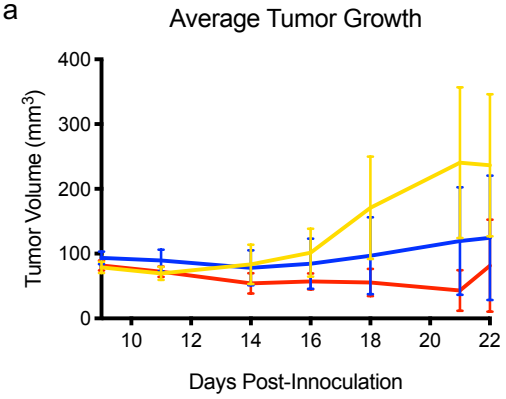


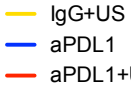
Extended data related to 3.4 continued:
c) Individual *tumour* growth curves of study-enrolled mice *stratified by group*
d) Scatter plot of the average, integrated cavitation dose versus the survival outcomes. The integrated cavitation dose was calculated on a per mouse basis by CC-G2 then averaged between the two interventions. Censored mice were excluded from analysis
e) Scatter plot of the average, persistence versus the survival outcomes. The persistence was calculated on a per mouse basis by CC-G2 then averaged between the two interventions. Censored mice were excluded from analysis

Appendix 3.5 - Extended Data Related to 3.5

Appendix 3.5 (1 of 1)

a

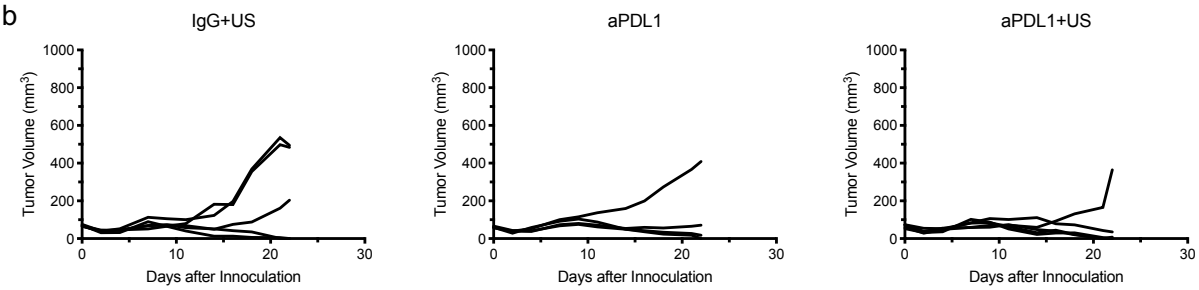




2-Way ANOVA with Tukey Multiple Comparisons

Comparison & Day	9	11	14	16	18	21	22
IgG+US vs. aPDL1	ns	ns	ns	ns	ns	ns	ns
IgG+US vs. aPDL1+US	ns	ns	ns	ns	ns	*	ns
aPDL1 vs. aPDL1+US	ns	ns	ns	ns	ns	ns	ns

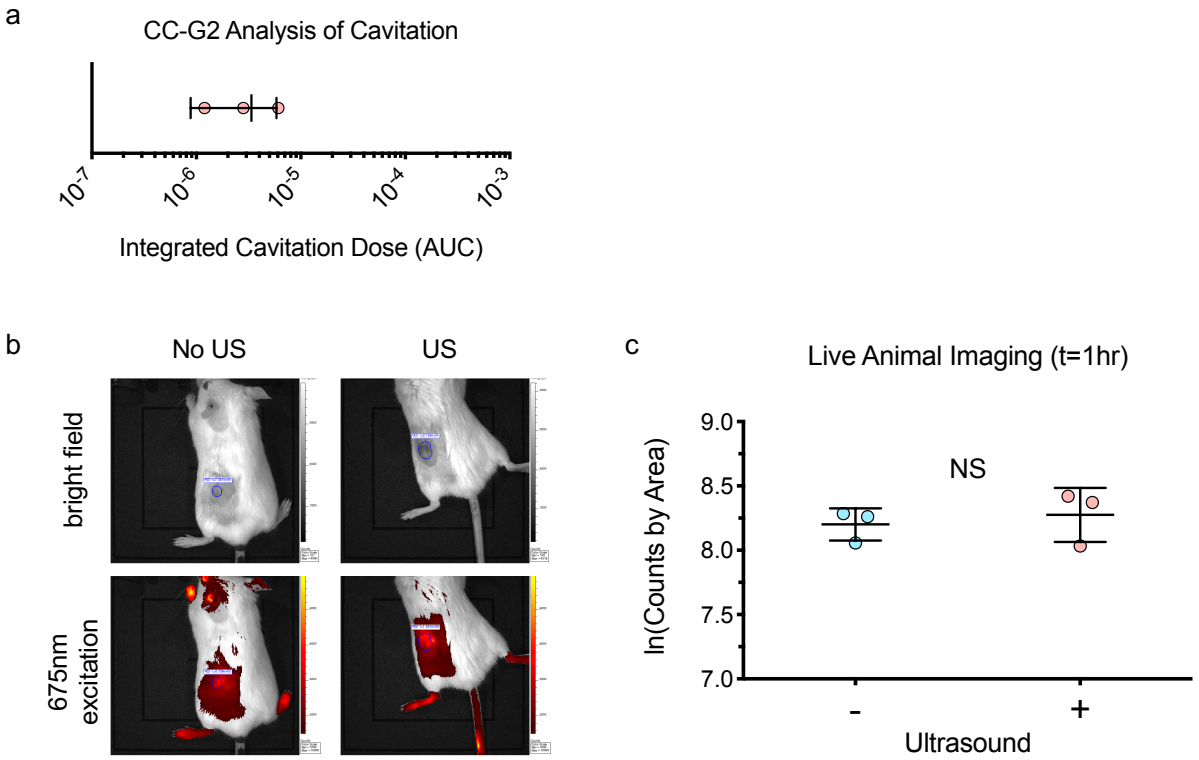
b



Extended data related to 3.5:
a) Early tumour growth curves. Lines connect the average of tumour volumes measured (by group) on a given day (mean and SEM shown). Note, a majority but not necessarily all mice were measured on each day shown. Different colours correspond to each of the groups. Differences in tumour volumes by group (from day 9 to day 22, on days shown in the table) were assessed by ordinary two-way ANOVA (factors: group and day) with Tukey's multiple comparisons test (single pooled variance)
b) Individual tumour growth curves of study-enrolled mice. Note, at early time-points it is likely that Matrigel (used in tumour propagation) was measured in addition to any true-tumour volume

Appendix 4.2 - Extended Data Related to 4.2

Appendix 4.2 (1 of 1)

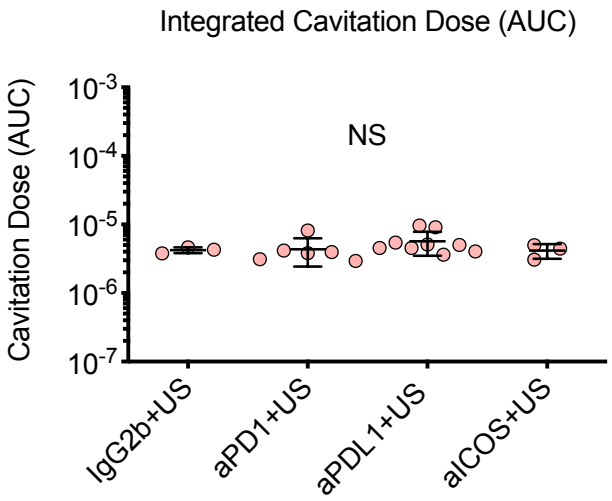


Extended data related to 4.2:
a) CC-G2 integrated cavitation dose (AUC) of US-treated tumours. Mean: 3.367e-006 AUC, SD: 2.486e-006 AUC
b) Representative bright field and NIR imaging of mice dosed aPDL1-680 +/- US. Imaging parameters: FOV: 7.5, f-stop: 8, exposure = 0.25s, Ex = 675, Em: Cy5. It is worthwhile to note that we observe signal from feet (likely wet) and tail-markings (permanent marker) in mice irrespective of US treatment assignment. Closer examination revealed that water on the skin was the cause of signal. Skin + water = large florescence signal.
c) Quantified CBA of tumours from live-animal imaging (natural-log transformed). Significance assessed by unpaired t test of ln(CBA). Mean and SD shown.

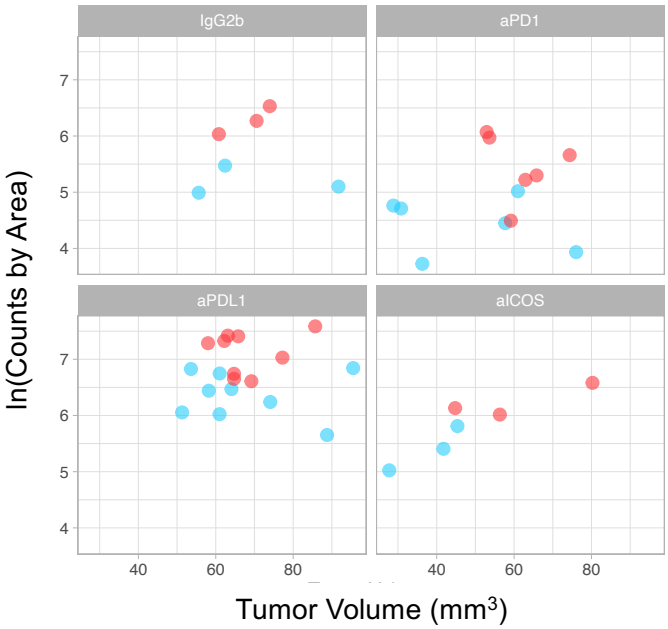
Appendix 4.3 - Extended Data Related to 4.3

Appendix 4.3 (1 of 1)

a



b

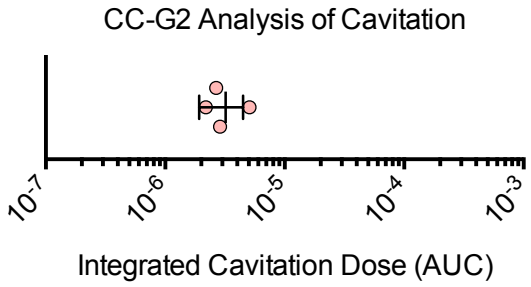


Extended data related to 4.3:
a) The CC-G2 calculated integrated cavitation dose for each US-treated tumour. AUC values by drug were compared to each other by ordinary one-way ANOVA with Tukey's multiple comparisons test (single pooled variance)
b) Scatter plot to illustrate the relationship (or lack thereof) between ln(CBA) and pre-intervention tumour volume

Appendix 4.4 - Extended Data Related to 4.4

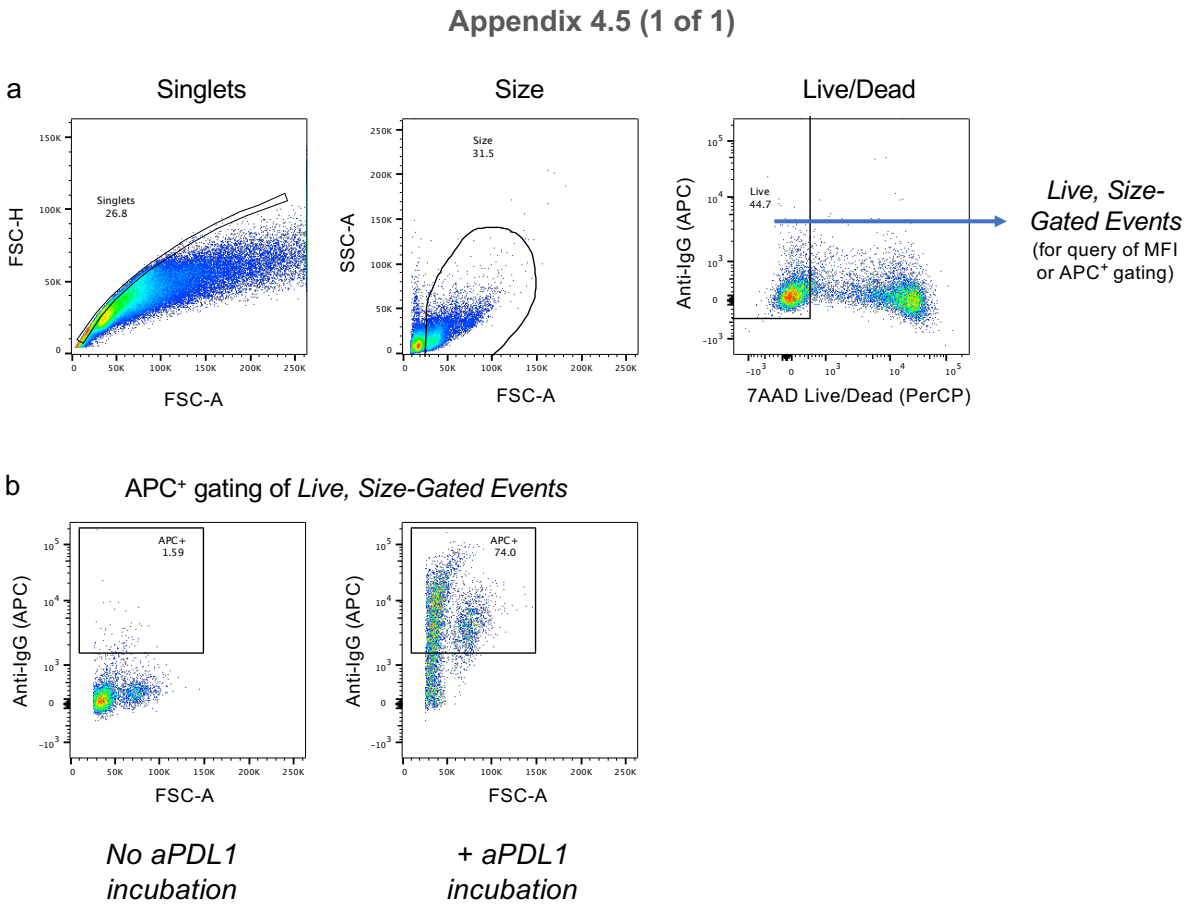
Appendix 4.4 (1 of 1)

a



Extended data related to 4.4:
a) *CC-G2-calculated integrated cavitation dose of sonicated tumours. The mean cavitation dose was 3.203e-006 AUC with an SD 1.278e-006 AUC*

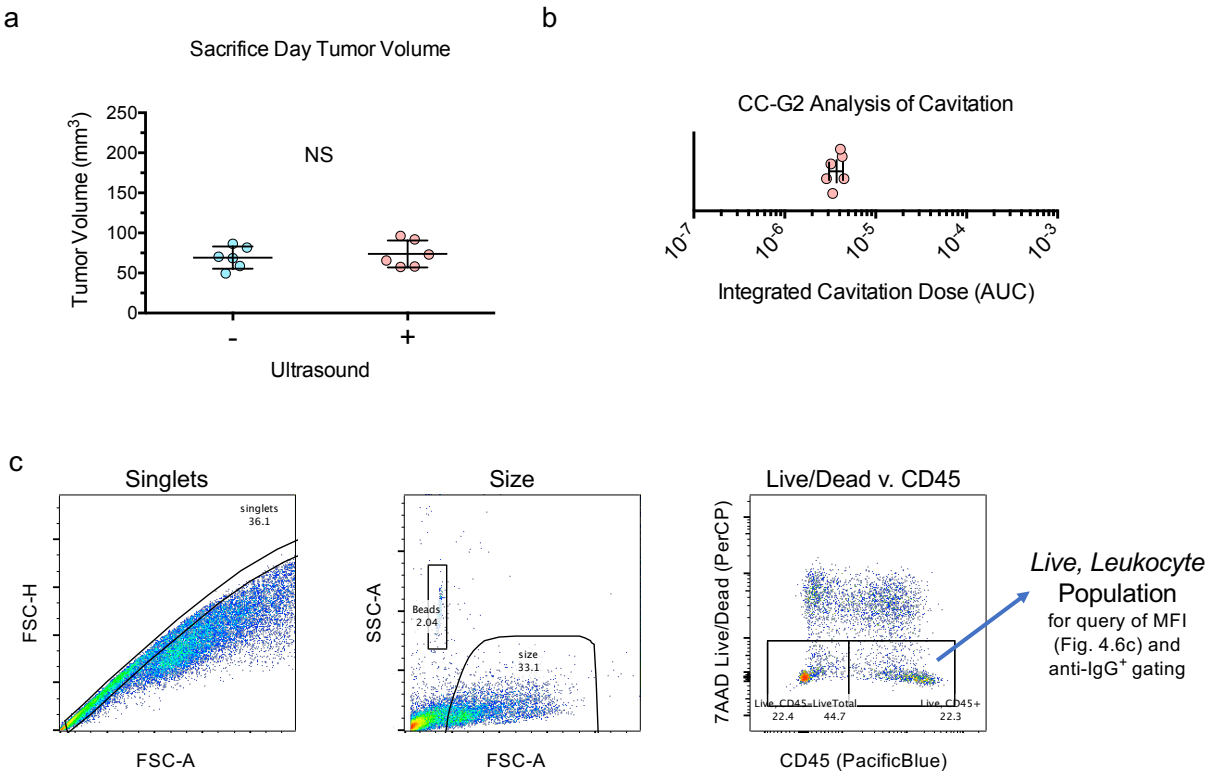
Appendix 4.5 - Extended Data Related to 4.5



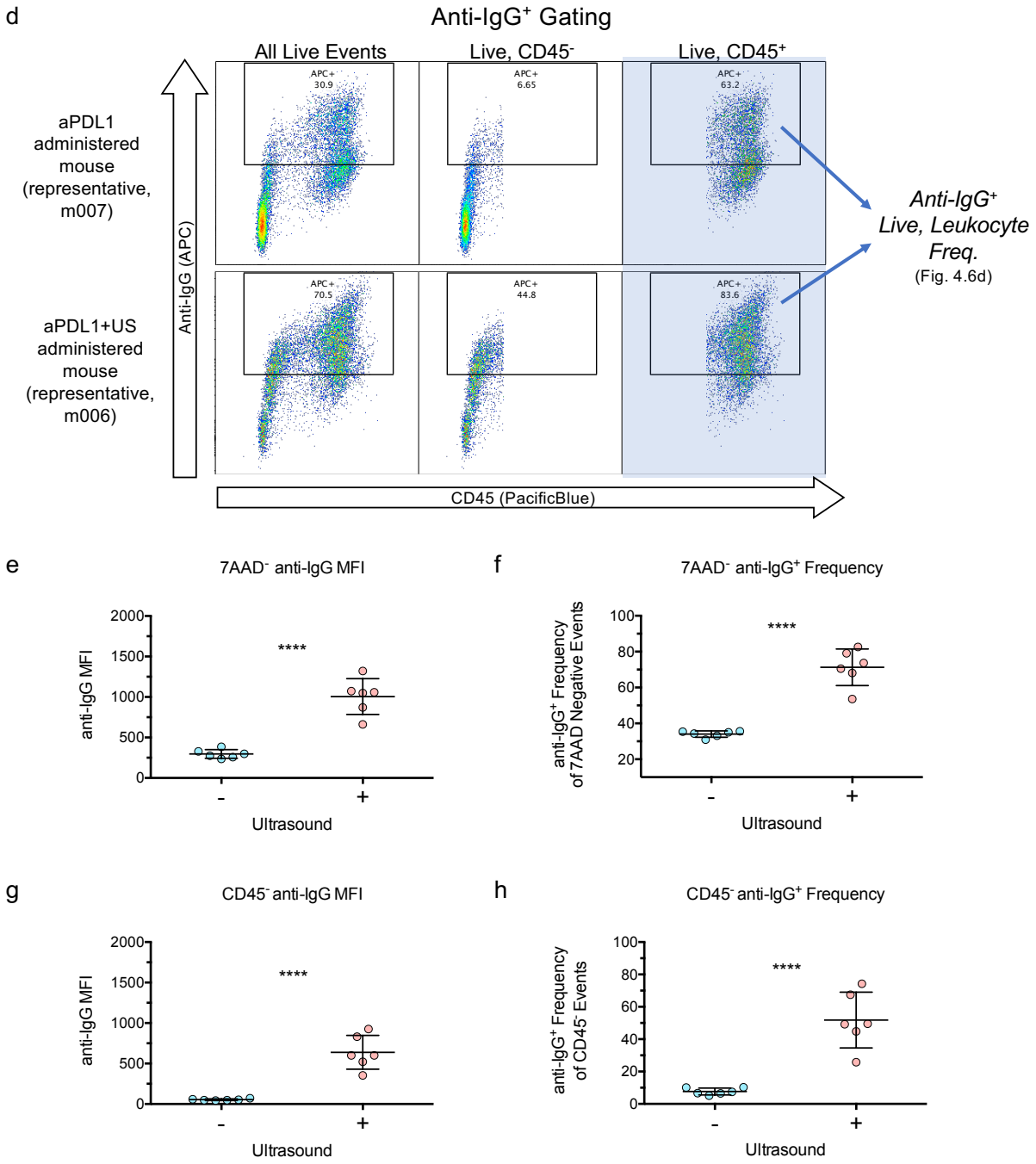
Extended data related to 4.5:
a) Gating hierarchy of ex vivo incubated CT26 tumour tissue. Briefly, cells were singlet, size, then live/dead gated, yielding the 'Live, Size-Gates events" population.
b) An APC+ subpopulation of "Live, Size-Gated' events were determined by an APC+ gate drawn in the APC vs. FSC-A space, such that the lower threshold of this gate was set such that the median APC+ population in the no-incubation control group would not exceed 2%

Appendix 4.6 - Extended Data Related to 4.6

Appendix 4.6 (1 of 2)



Extended data related to 4.6:
a) Sacrifice-day tumour volumes. Significance assessed by unpaired t test (n=6/group)
b) The average, integrated cavitation dose was 3.722e-006 AUC with a standard deviation of 6.514e-007 AUC
c) After sample-specific time-gating, the following gating hierarchy was applied to each sample. Time-gated samples were singlet, size, then live/CD45 gated. Gating hierarchy shown on a concatenation of all time-gated files acquired.

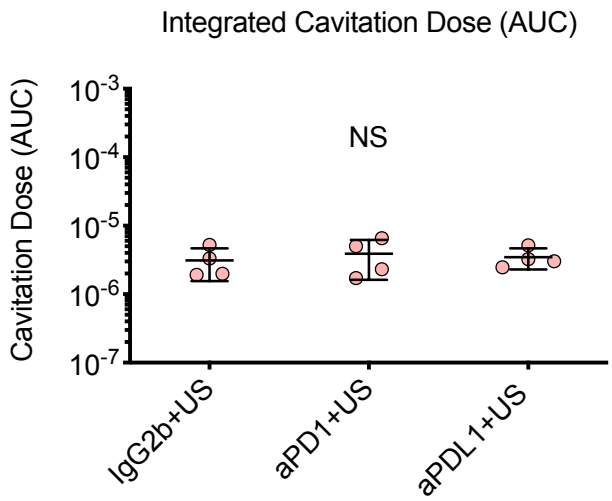


Extended data related to 4.6 continued:
d) Representative anti-IgG+ population (APC reporter channel) gating of the live events total, 7AAD-CD45- events, and 7AAD-CD45+ populations (from left to right) of aPDL1 (top) and aPDL1+US (bottom) treated mice (m3 and m7 shown). The anti-IgG+ gate was kept consistent across all samples and its lower limit was set based upon another experiment (not shown) as there was no APC-FMO control.
e-h) Quantified anti-IgG median florescence intensity (MFI) and anti-IgG+ gated frequency of aPDL1 vs. aPDL1+US treated tumours for live total (7AAD- events) and live, non-leukocyte (7AAD- and CD45- events). Statistically analysed by unpaired t test.

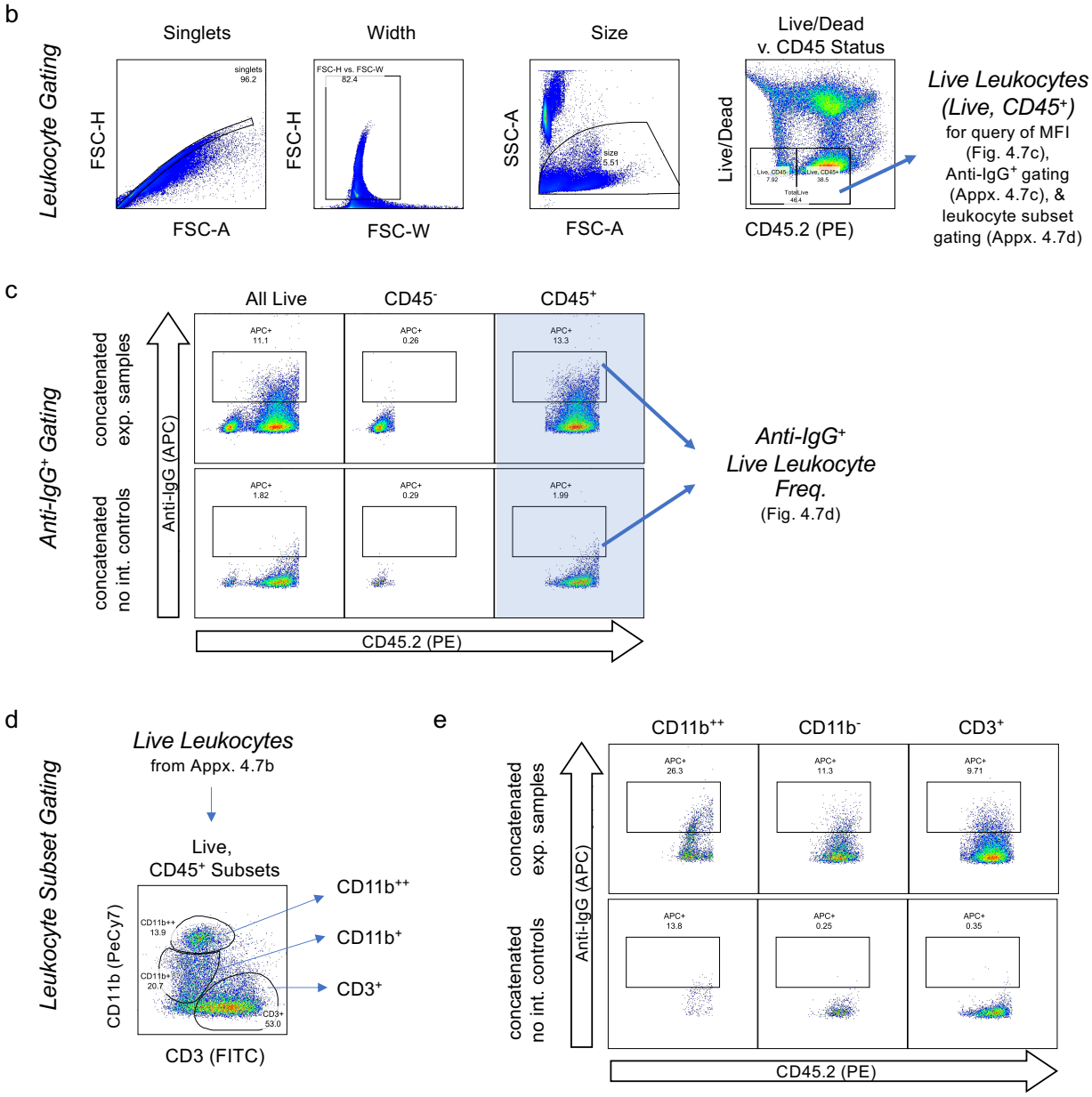
Appendix 4.7 - Extended Data Related to 4.7

Appendix 4.7 (1 of 4)

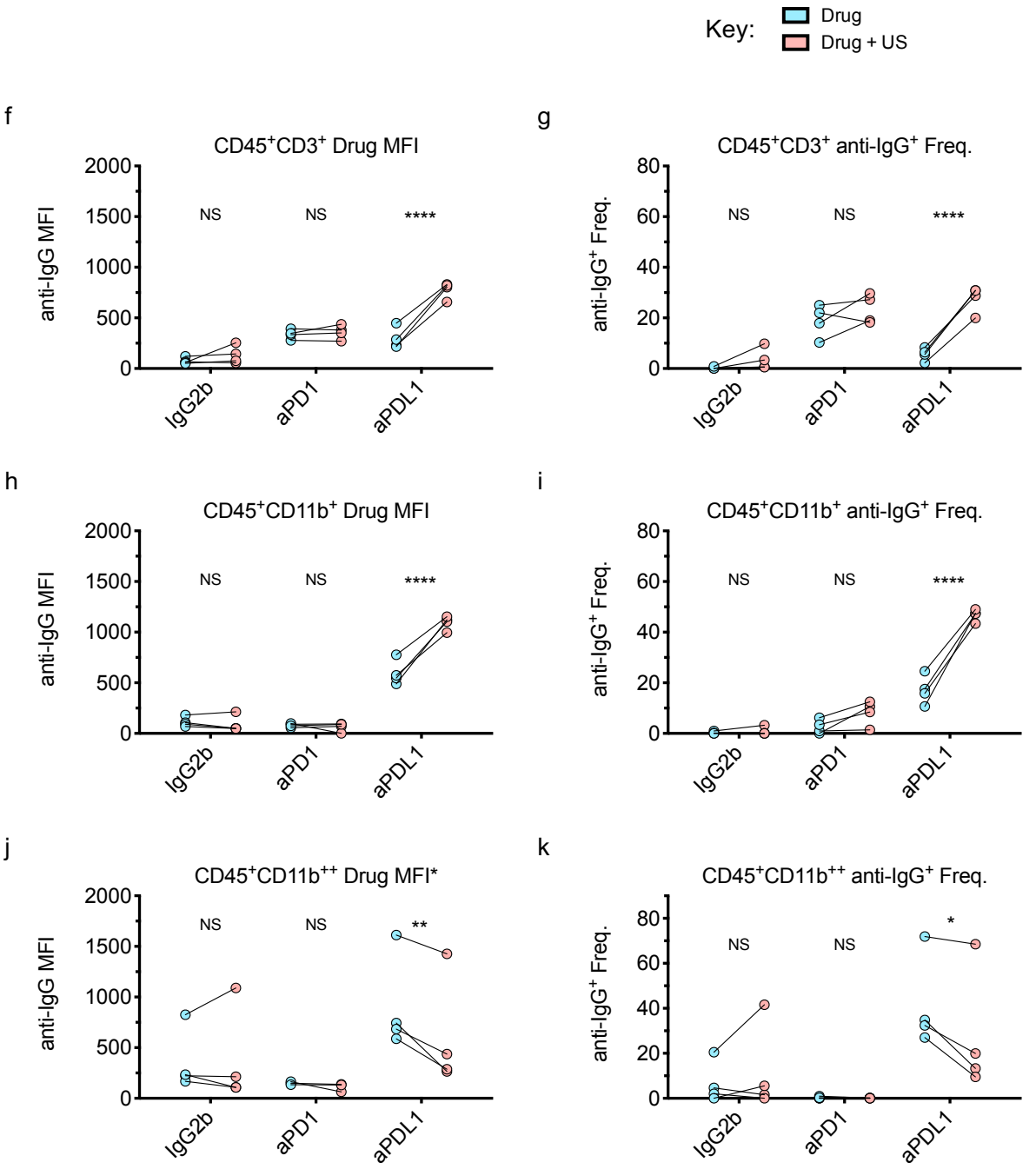
a



Extended data related to 4.7:
a) The CC-G2 calculated integrated cavitation dose (AUC). AUC differences between groups assessed by ordinary one-way ANOVA with Tukey's multiple comparisons test (single pooled variance). The average integrated cavitation doses were 3.118e-006, 3.910e-006, and 3.483e-006 AUC for IgG, aPD1, and aPDL1 respectively with SDs of 1.565e-006, 2.282e-006, and 1.178e-006 AUC



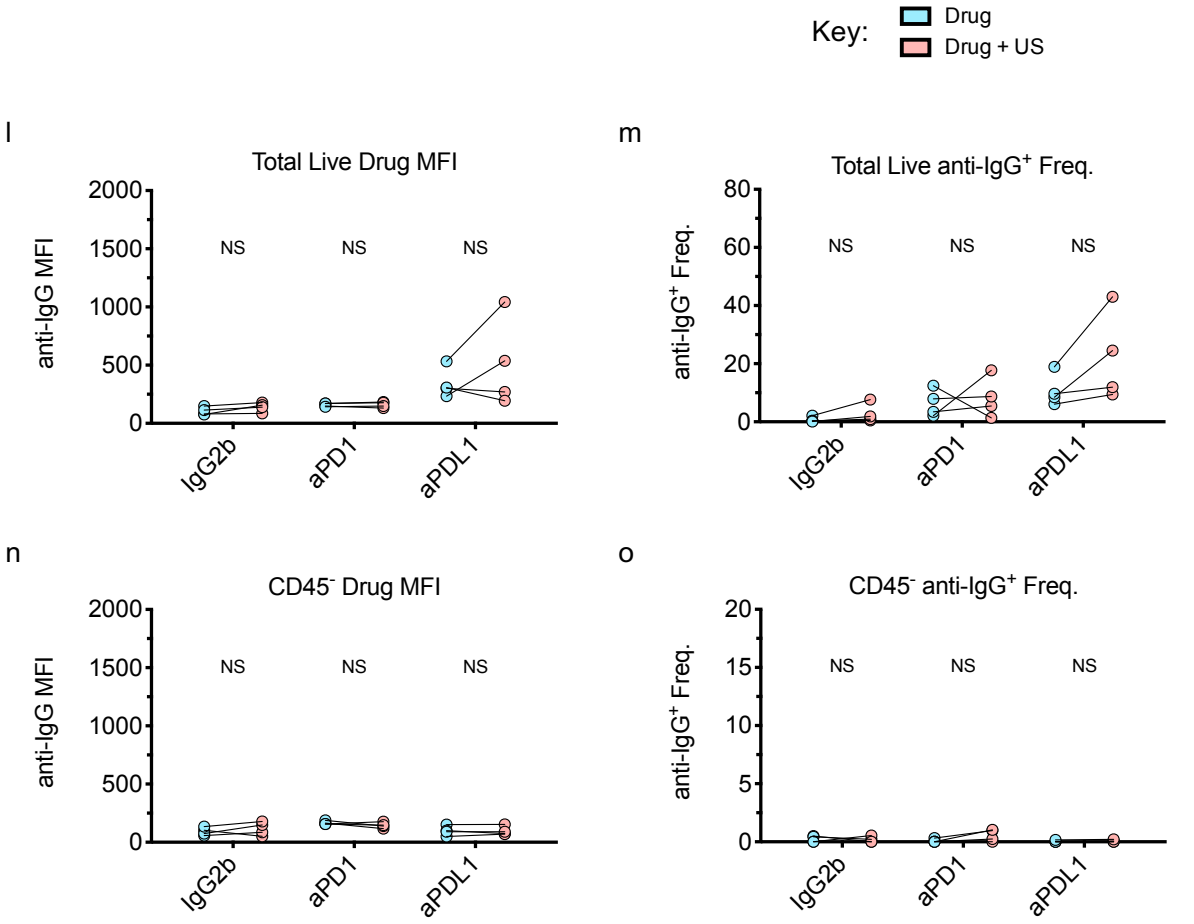
Extended data related to 4.7 continued:
b) Leukocyte gating strategy; events were singlet, width, size, then live & CD45+ gated. Gating hierarchy is shown on a concatenation of down-sampled experimental samples (n=24 tumours from n=12 mice).
c) Anti-IgG+ gating of all live events, CD45- events, and CD45+ events (live leukocytes) in the anti-IgG (APC) vs. CD45.2 (PE) space. A concatenation of down-sampled experimental samples is shown in the top row and a concatenation of down-sampled no-intervention control samples (n=3 tumours, from n=2 mice not administered antibody nor US) in the bottom row. The lower limit of the anti-IgG+ gate, was set to permit no more than a 2% false-positive frequency in the no-intervention control concatenation file of total, live leukocytes (bottom right, CD45+).
d) The live leukocyte population from Appx. 4.7b, was further gated to resolve the CD3+, CD11b+, and CD11b++ populations (gating shown utilizing a concatenation of down-sampled experimental samples)
e) Anti-IgG+ gating strategy of live leukocyte subsets (CD11b+, CD11b++, CD3+, from left to right) in the anti-IgG (APC) vs. CD45.2 (PE) space organized in a manner to (Appx. 4.7c), with the top row comprised a concatenation of down sampled 'experimental samples' and the bottom row a concatenation of down-sampled 'no intervention' control samples. The APC+ threshold, lower limit of the anti-IgG gate was set to permit no more than a 2% false-positive frequency in the no-intervention control concatenation file of total, live leukocytes (from Appx. 4.7c).



Extended data related to 4.7 continued:
*f-i) The anti-IgG median fluorescence intensity (MFI) and anti-IgG+ frequency of myeloid-like (CD45+CD11b+, l-m) and T (CD45+CD3+, n-o), and CD45+CD11b++ (j-k) populations. Drug was detected by 'anti-IgG'—an APC-channel-compatible secondary antibody (anti-IgG2a for samples from aPD1 dosed mice or anti-IgG2b for samples from aPDL1 and IgG2b dosed mice. MFI or frequency in each plot assessed by RM two-way ANOVA (US status and drug as factors; matching by mouse) with Sidak's multiple comparisons test (single pooled variance). Lines connect paired tumours. *Unlike all other plots, in (j) one aPD1 mouse (one pair of tumours) was excluded from analysis because it lacked a CD11b++ drug MFI value for its no-US tumour (n=3), but n=4 for all other conditions.*

Appendix 4.7 (4 of 4)

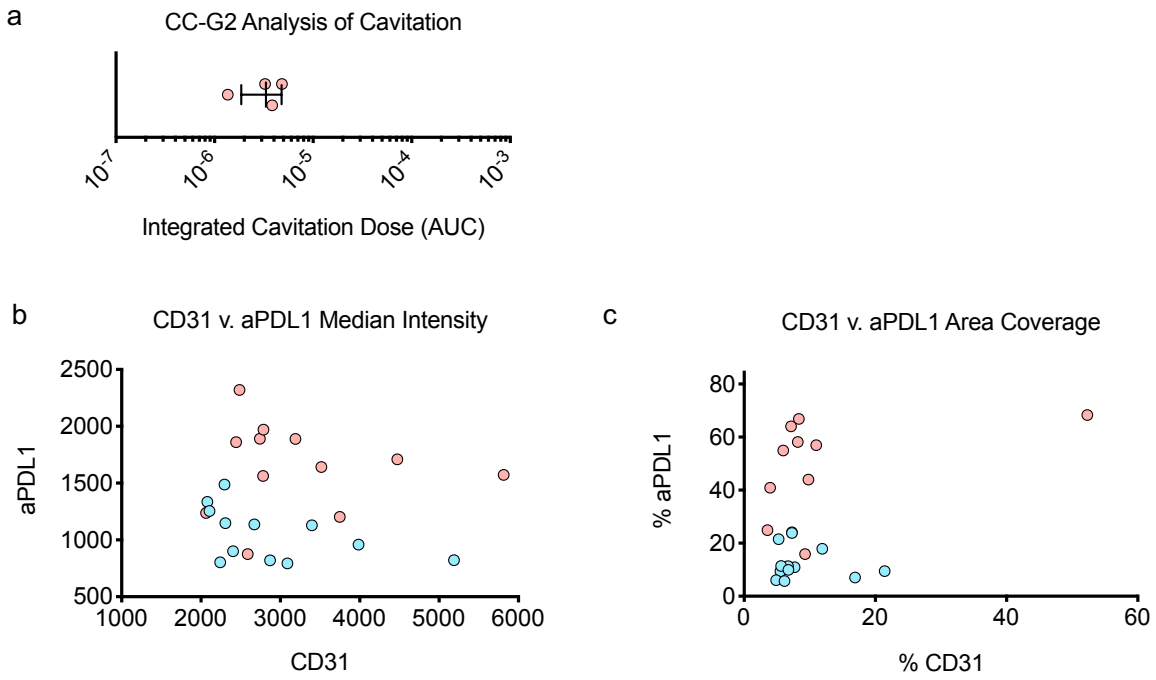
Extended data related to 4.7 continued:



l-m) The anti-IgG median fluorescence intensity (MFI) and anti-IgG+ frequency across in total live (l-m) and CD45- (n-o) populations (n=4/condition). Populations are defined in gating hierarchies as shown in Appx. 4.7b-e. Drug was detected by 'anti-IgG'—an APC-channel-compatible secondary antibody (anti-IgG2a for samples from aPD1 dosed mice or anti-IgG2b for samples from aPDL1 and IgG2b dosed mice. MFI or frequency in each plot assessed by RM two-way ANOVA (US status and drug as factors; matching by mouse) with Sidak's multiple comparisons test (single pooled variance). Lines connect paired tumours

Appendix 4.8 - Extended Data Related to 4.8

Appendix 4.8 (1 of 1)



Extended data related to 4.8
a) The mean, CC-G2-calculated integrated cavitation dose was 3.323e-006 AUC with an SD of 1.458e-006 AUC
b-c) The aPDL1 signal intensity (as detected by anti-IgG2b) and aPDL1 area coverage bear no clear relationship with the intensity of CD31 staining. Each dot represents a stained tumour section. Blue dots represent sections from tumours that did not receive US (systemic aPDL1 only), whereas pink dots represent sections from tumours treated with sonication and aPDL1.

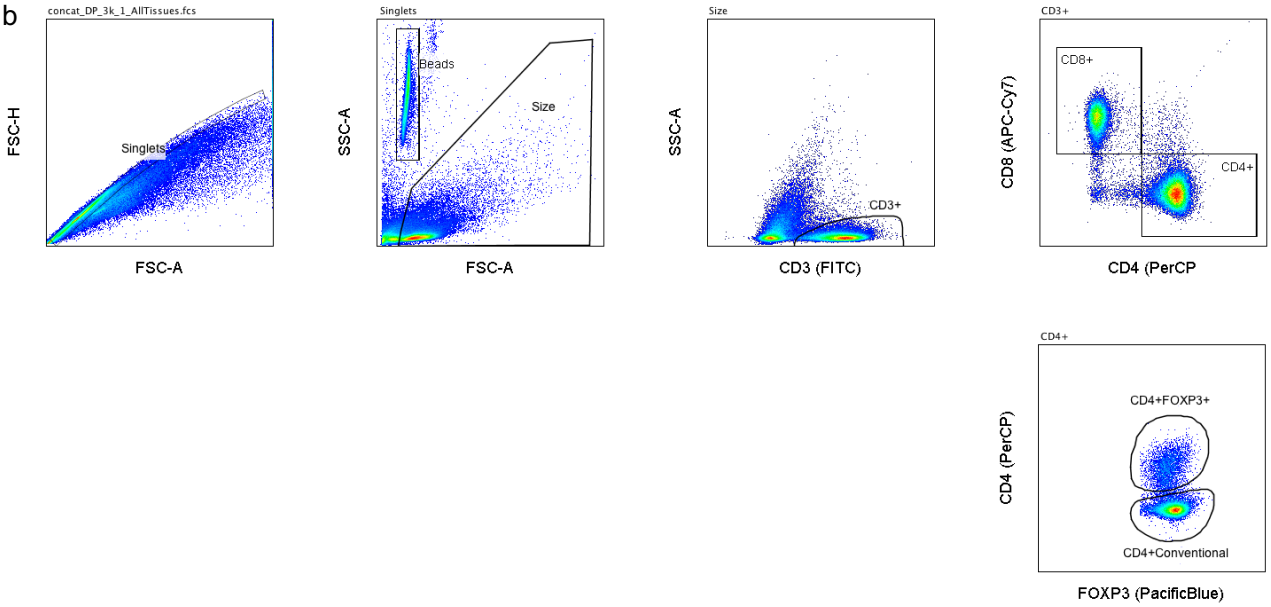
Appendix 5.11 - Extended Data Related to 5.11

Appendix 5.11 (1 of 2)

a

FITC	PE	PE-TxRed	PerCP	PE-Cy7	APC	APC-Cy7	Pacific Blue
CD3	OX40		CD4	CD69	ICOS	CD8	(FOXP3)

b



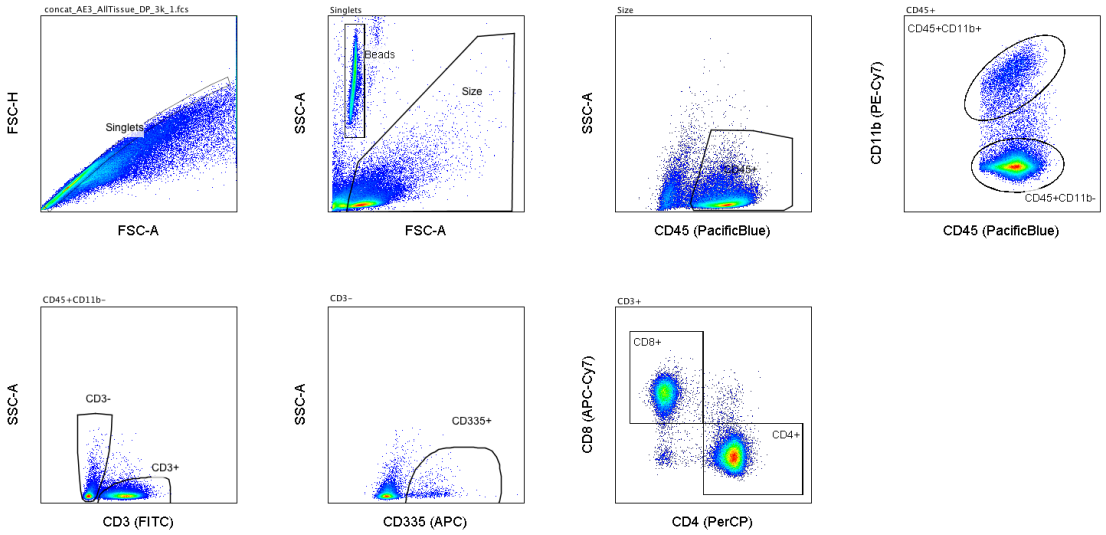
Extended data related to 5.11:
a) FCM Panel 2 (FCM2) explores changes to lymphocyte (T cell) frequencies among conventional and regulatory T cell populations in addition to evaluating how the functional status (activation) of these populations' changes.
b) FCM2 gating hierarchy; events were singlet, size, then gated based upon CD3 expression. T cells were then subdivided into CD4 and CD8 groups, then the CD4 compartment was further subdivided into conventional and regulatory subsets based upon FOXP3 expression. Terminal populations (CD8, conventional CD4 T cell, regulatory CD4 T cells) gated for OX40+, CD69+, or ICOS+ populations based upon on respective FMO-control

Appendix 5.11 (2 of 2)

c

FITC	PE	PE-TxRed	PerCP	PE-Cy7	APC	APC-Cy7	Pacific Blue
CD3	(Gzb)		CD4	CD11b	CD335	CD8	CD45

d



Extended data related to 5.11 continued:
c) FCM Panel 3 (FCM3) looks to characterize the relative frequencies of different leukocyte populations in addition to assessing the level of GranzymeB produced by each subset (myeloid, NK, or T cell)
d) FCM3 gating hierarchy; Events were singlet and size gated, then gated upon CD45 expression (the pan-leukocyte marker). Leukocytes were then subdivided based on their expression of CD11b, with myeloid cells comprising the CD11b+ population and CD11b- cells further gated for CD3 expression. CD3+ T cells were then subdivided into CD4 and CD8 subsets. CD3- cells were then gated upon their CD335 expression, yielding NK cells (CD45+CD11b-CD3-CD335+)